Research Group
Scanning Probe Methods

Triannual Report
2011 - 2013

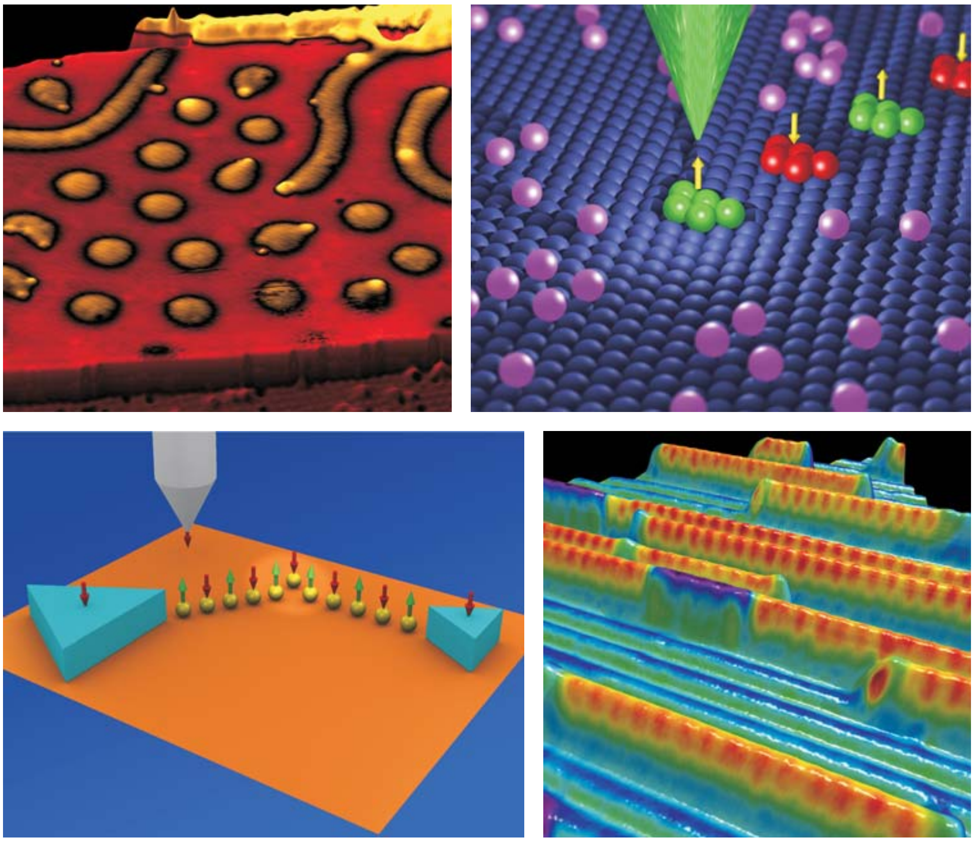

University of Hamburg

Gate to the World of Science

Triannual Report 2011 – 2013

Research Group "Scanning Probe Methods"

University of Hamburg
Institute of Applied Physics

Microstructure Advanced
Research Center Hamburg (MARCH)

Interdisciplinary Nanoscience Center
Hamburg (INCH)

Hamburg Cluster of Excellence
"NANOSPINTRONICS"

Sonderforschungsbereich 668
(DFG Collaborative Research Center)

ERC Advanced Grant Group
"FURORE"

Contact:
Prof. Dr. Roland Wiesendanger
Tel. (++49) 40-42838-5244 (direct)
(++49) 40-42838-3203/-7045 (secretary)
FAX (++49) 40-42838-6188
e-mail `wiesendanger@physnet.uni-hamburg.de`
WWW www.nanoscience.de

Contents

Chapter 1

Preface

This is the seventh triannual report of the research group „Scanning Probe Methods“ at the Institute of Applied Physics of the University of Hamburg. Based on the strategic development of nanoscience-related infrastructure at the University of Hamburg over a time period of more than 20 years, several Centers and international networks of scientific excellence could be established in recent years and are recognized worldwide:

Since 2006 we have established a Collaborative Research Center, DFG-Sonderforschungsbereich (SFB 668), entitled „Magnetism from the single atom to the nanostructure“ (chairman: Prof. Dr. Roland Wiesendanger). The SFB 668 is focussed on fundamental studies of magnetic properties of nanostructures in contact with a substrate, including spin structures in thermal equilibrium as well as transport and dynamic properties. It involves research groups from the Institute of Applied Physics, from the I. Institute of Theoretical Physics, from the Institute of Experimental Physics, from the Institute of Inorganic and Applied Chemistry (all from Hamburg University), and from the Institute of Experimental Physics of the University of Kiel. In total more than 100 researchers are working within the SFB 668. In 2013 the SFB 668 was evaluated with great success and received funding for the third period (2014 – 2017).

In 2006 also a Research Training Network on “Tailored metal-semiconductor hybrid systems” (chairman: Prof. Dr. Ulrich Merkt) could be established with participation of groups from the departments of physics and informatics, including our research group. It will continue to run till 2015. Within the framework of such Research Training Groups about 20 to 25 Ph.D. students obtain an excellent education and training in an interdisciplinary scientific environment.

In 2009 the State Government of the Free and Hanseatic City of Hamburg started an Excellence Initiative in order to support outstanding Research Clusters and Graduate Schools. We were successful in the competition and could establish a Cluster of Excellence in the topical field of “Nanospintronics” (chairman: Prof. Dr.

Roland Wiesendanger). In total about 200 scientists from the University of Hamburg and the Helmholtz Centers DESY and Geesthacht were involved in this Cluster which received funding for a time period of 3,5 years.

In Europe we have become partners within numerous research networks funded by the European Community in recent years. In addition, an ERC Advanced Grant of the European Research Council (ERC) was awarded to Roland Wiesendanger in 2008 for “Fundamental studies and innovative approaches of research on magnetism”. This new type of funding program allows individual researchers to build up a significant activity in an innovative field of science based on previous outstanding research achievements. While the first ERC Advanced Grant project is ending in 2013, a second ERC Advanced Grant for five years has been awarded to Roland Wiesendanger in 2013 for a project on “Atomic-scale studies of the nature of and conditions for inducing superconductivity at high-temperatures”.

In 2013, Dr. Alexander Khajetoorians was awarded with an Emmy Noether Grant by the DFG which allows him setting up an independent Young Investigator Group at the University of Hamburg focussing on innovative approaches in the field of “Nanospintronics”. In the same year, Dr. Jens Wiebe successfully applied for a project in the framework of the new DFG Priority Program on “Topological Insulators” with the goal of combining advanced scanning tunnelling spectroscopy techniques, angle-resolved photoemission, and XMCD measurements in order to correlate structural, electronic, and magnetic properties of this novel class of materials.

In the present triannual report 2011-2013 the scientific achievements of the research group "Scanning Probe Methods" are summarized covering the following topics: magnetic nanostructures, semiconductor quantum structures, insulators, molecular systems, and instrumental developments. The research activities of our group in the time period 2011-2013 resulted in 66 scientific publications (among them 7 in Science and Nature Journals, 17 in "Physical Review Letters") and 275 presentations at conferences, colloquia or seminars (including 90 plenary and invited talks at international meetings).

Several prizes and awards were given to members of our group in the past three years, including the Chinese Government Award for Outstanding PhD Students Abroad in 2011 (Lihui Zhou), the ECOSS Prize 2011 (Matthias Menzel), the Gerhard Ertl Young Investigator Award 2012 (Dr. Alexander Khajetoorians), the ECOSS Prize 2012 (Anika Schlenhoff), the Young Scientist Award of the Physical Society of Japan (Dr. Yasuo Yoshida), and the Gaede Prize 2013 (Dr. Kirsten von Bergmann). In 2012, Roland Wiesendanger became Honorary Professor of the Harbin Institute of Technology (HIT), China. Furthermore, Roland Wiesendanger has been elected as Fellow of the American Vacuum Society (AVS) in 2012 and as Foreign Member of the

Polish Academy of Sciences in 2013.

This research report provides a good opportunity to thank all funding agencies including the DFG, the ERC, the Stifterverband für die Deutsche Wissenschaft, the Alexander von Humboldt Foundation, the DAAD, the Konrad-Adenauer-Stiftung, the "Forschungs- und Wissenschafts-Stiftung Hamburg" as well as several industrial companies for their financial support of our research activities. In particular we would like to thank the Ministry of Science and Research (BWF) of the Free and Hanseatic City of Hamburg and the University of Hamburg for their continuous support of our activities in nanoscience and nanotechnology. I would also like to take the opportunity to thank all the past and present members of the research group „Scanning Probe Methods" for their strong devotion to scientific excellence. Finally, we gratefully acknowledge the great support by our central mechanical and electronic workshops, as well as by our secretaries and administration staff.

Hamburg, December 2013

Prof. Dr. Roland Wiesendanger

(Chairman of the DFG Collaborative Research Center SFB 668 and Scientific Coordinator of the Interdisciplinary Nanoscience Center Hamburg)

Chapter 2

Staff Members

Head

Prof. Dr. Roland Wiesendanger

Secretary

Andrea Beese
Ute Brenger
Sigrid Schmidtke

Public Relations Office

Dipl.-Chem. Heiko Fuchs

Technical Support

PTA Norbert Dix
Dipl.-Ing. Michael Langer
Dipl.-Ing. Jörg Völkel

Senior Scientists

Dr. Makoto Ashino (until March 2013)
Dr. Maciej Bazarnik
Dr. Kirsten von Bergmann
Dr. Jessica Bickel (until July 2012)
Dr. Jens Brede
Dr. Anna Butenko
Dr. Régis Decker
Dr. Yingshuang Fu (until July 2011)
Dr. Mahboubeh Hortamani (until March 2012)

Dr. Alexander Khajetoorians
Dr. Stefan Krause
Dr. André Kubetzka
Dr. Safia Ouazi
Dr. Oswald Pietzsch (until June 2013)
Dr. René Schmidt (until March 2013)
Dr. Alexander Schwarz
Dr. Elena Vedmedenko
Dr. Marta Wasniowska (until December 2012)
Dr. Jens Wiebe
Dr. Robert Wieser
Dr. Shiro Yamazaki (until January 2012)
Dr. Yasuo Yoshida (until March 2011)
Dr. Hai Zhong
Dr. Lihui Zhou

Ph. D. Students

Henning von Allwörden
David Altwein
Bruno Chilian (until August 2011)
Liudmila Dzemiantsova (until May 2013)
Thomas Eelbo
Andreas Eich
Johannes Friedlein
Josef Grenz
Mike Gyamfi (until December 2012)
Christian Hannecken
Gabriela Herzog (until December 2011)
Arne Köhler
Knud Lämmle (until May 2011)
Peter Löptien
Matthias Menzel (until November 2012)
Niklas Romming
Kai Ruschmeier
Anika Schlenhoff
Jörg Schwöbel
Andreas Sonntag
Tobias Schlenk (until August 2013)
Thim Stapelfeldt
Manuel Steinbrecher
Kolja Them
Boris Wolter

Diploma/Master Students

André Engel (until July 2011)
Lasse Cornils
Benjamin Ehlers (until October 2012)
Gotthold Fläschner
Julian Hagemeister
Jonas Harm
Jan Hermenau
Jonas Warmuth
Qingchui Zhu (until April 2011)

Chapter 3

Research Activities 2011-2013

3.1 Overview

R. Wiesendanger

Our research activities are concentrated on nanometer-scale probe methods. In particular, emphasis is put on the investigation of the fundamental relationship between nanostructure and nanophysical properties. Scanning probe methods are ideally suited for such investigations because they provide atomic-scale spatial resolution combined with spectroscopical capabilities at low energy scales (down to micro-eV). By choosing an appropriate type of interaction between probe tip and sample, almost any kind of nanophysical property can be studied by scanning probe methods. We apply scanning probe methods (SPM) to various classes of materials, including metals, semiconductors, insulators, superconductors, magnetic materials, as well as organic thin films and molecular materials.

To be able to make significant contributions to this rapidly developing field, a major part of our activities is devoted to new developments or further improvements on SPM instrumentation, including the development of new positioning devices with nanometer-scale accuracy, the development of new types of sensors, or the development of dedicated SPM instruments which can operate under extreme conditions (e.g. UHV, low temperatures and high magnetic fields). Special emphasis is also put on the development of new experimental methods based on the local probe geometry, which usually requires adjustments of the hardware and software for SPM data acquisition. These developments are often made in close collaboration with European companies specialized in SPM instrumentation.

In the following, a brief summary of the highlights of our research activities in the time period of 2011 - 2013 is provided. For further information, please do not hesitate to contact us. We will be glad to provide reprints of publications on specific topics.

3.2 Magnetic atoms and artificial nanostructures on metallic substrates

A.A. Khajetoorians, J. Wiebe, and R. Wiesendanger

This section deals with the experimental investigation of the magnetic properties of individual atoms adsorbed on the surface of nonmagnetic metals. The first focus of our interest was to gain a fundamental understanding of how the adatom and substrate electronic properties affect the magnetic moment, magnetic anisotropy, g-factor, Kondo screening and magnetization dynamics of the combined system. For this purpose, the 3d transition metal element Fe was deposited on the (111) surfaces of different metals, i.e. of 3d (Cu), 4d (Ag) and 5d (Pt) transition metals. Subtle effects, e.g. of the Shockley surface state, which is occupied on some of these surfaces, have been revealed. Moreover, it has been observed, which role these surface states play in the so called Ruderman-Kittel-Kasuya-Yosida (RKKY) indirect exchange interaction, which is mediated between adatoms by the itinerant substrate electrons over nanometer distances. We were able to directly measure the distance dependence of the RKKY interaction and compare to first principles calculations. A second focus was to investigate how this knowlege can be used to build artificial arrays from RKKY coupled adatoms, so called *dilute nanostructures*, with interesting properties related to the fundamental physics of nanomagnetism or even to nanospintronics applications. Different from direct magnetic exchange interaction, the weaker RKKY interaction is oscillating between ferromagnetic and antiferromagnetic coupling over distances of several lattice spacings. It is therefore possible to use the method of STM-tip induced atom manipulation to tailor the topology of, and the strength and sign of the magnetic interaction within, such dilute nanostructures almost arbitrarily in a bottom up approach.

The experimental techniques we used for these investigations are the two complementary methods of spin-resolved scanning tunneling spectroscopy (SP-STS) and inelastic STS (ISTS), which we successfully applied to the sample system of magnetic atoms on nonmagnetic metal surfaces within this triannual research period (Sec. 3.2.1). For the system of Fe/Pt(111), which is known to almost fulfill the Stoner criterion for ferromagnetism, we were able to reveal the effect of the Fe adsorption site dependence of the large Pt polarization cloud on the magnetic anisotropy, g-factor and magnetization dynamics (Sec. 3.2.1). Section 3.2.2 shows the investigation of the magnetic properties of different artificial dilute magnetic nanostructures, which vary in size, coupling strength and topology. Finally, Sec. 3.2.3 focuses on the construction and investigation of all-spin based logic gates which were build from only eleven Fe atoms and two Co islands.

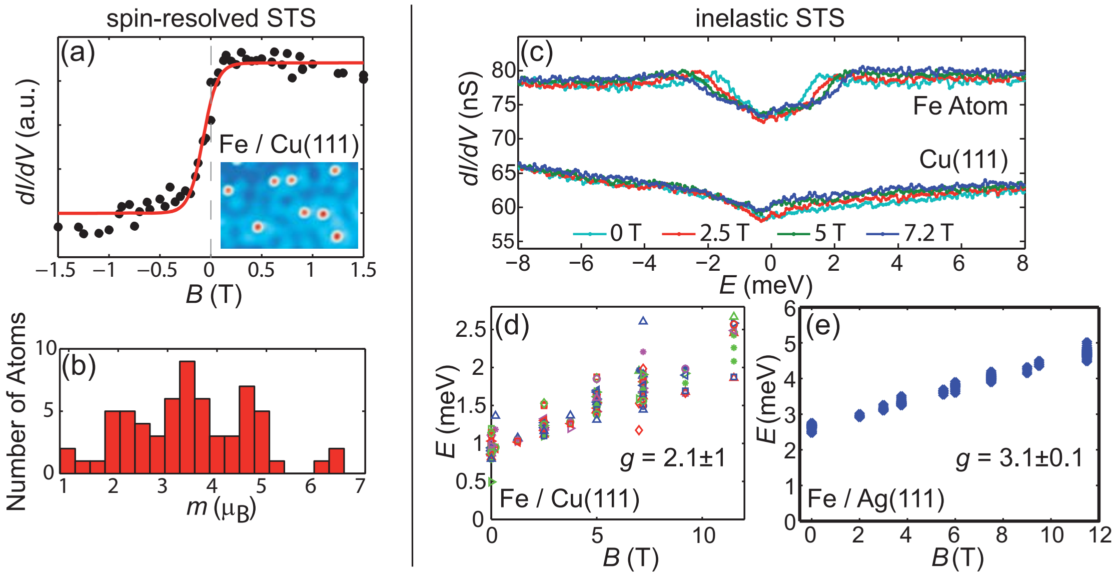

Figure 3.1: Fe atoms on Cu(111) and Ag(111): (a) Magnetization curve of an Fe atom on Cu(111) (black) and fit to a Langevin model (red). (b) Histogram of the fitted magnetic moments [1]. (c) ISTS spectra of an Fe atom and of the Cu(111) substrate at different magnetic fields as indicated. (d,e) Spin excitation energy as a function of the B-field for Fe atoms on Cu(111) [1] and on Ag(111) [2]. The g-factors determined from the slope are indicated.

3.2.1 Spin resolved and inelastic scanning tunneling spectroscopy

A. A. Khajetoorians, J. Wiebe, M. Steinbrecher, L. Zhou, B. Chilian, T. Schlenk, B. Schweflinghaus, M. dos Santos Dias, M. Bouhassoune, S. Lounis, A. T. Costa, D. L. Mills, and R. Wiesendanger

Fe atoms on Cu(111)

We developed the combination of the two methods of SPSTS and ISTS and were able to apply it in a single experiment to the same sample of Fe adatoms on Cu(111) [Fig. 3.1(a-d)]. The single atom magnetization curves measured via SPSTS reveal a broad distribution of magnetic moments of the Fe atoms with 3.5 μ_B being the mean value. ISTS reveals a magnetization excitation with a lifetime of 200 fsec which decreases by a factor of two upon application of a magnetic field of 12 T. The experimental observations are quantitatively explained by the decay of the magnetization excitation into Stoner modes (spin-flip scattering) of the itinerant electron system as shown by newly developed theoretical modeling [1].

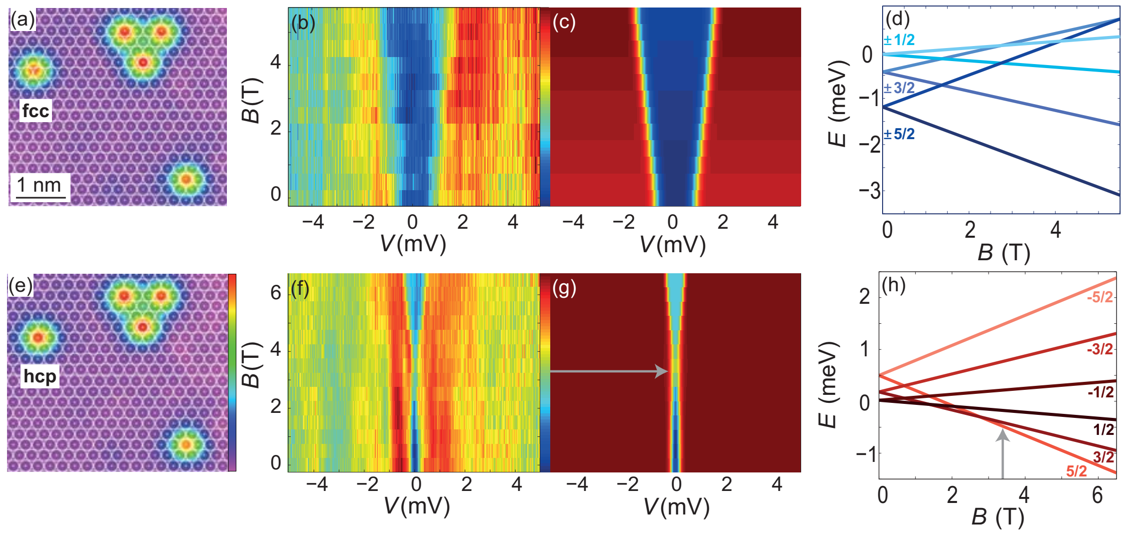

Figure 3.2: Fe atoms on Pt(111): STM constant-current images (a) before and (e) after manipulating the top left Fe adatom from an fcc to an hcp hollow site on Pt(111). The center of the drawn white atomic lattice corresponds to one of two possible hollow sites. ($V_S = 6$ mV, $I_t = 500$ pA, $T = 0.3$ K; manipulation parameters: $V_S = 2$ mV, $I_t = 50$ nA). The colorscale represents $\Delta z = 0.12$ nm. Magnetic field dependence of the measured ISTS intensity for (b) fcc (f) hcp (stabilization: $V_S = 6$ mV, $I_t = 3$ nA, $V_{\mathrm{mod}} = 40\ \mu$V, $T = 0.3$ K) and the simulated ISTS intensity based on the effective spin Hamiltonian assuming: (c) $D_{\mathrm{fcc}} = -0.19$ meV, $J_{\mathrm{fcc}} = 5/2$, $g_{\mathrm{fcc}} = 2.4$, $u_{\mathrm{fcc}} = 2.3$, $T_{\mathrm{eff}}^{\mathrm{fcc}} = 2$ K (g) $D_{\mathrm{hcp}} = 0.08$ meV, $J_{\mathrm{hcp}} = 5/2$, $g_{\mathrm{hcp}} = 2$, $u_{\mathrm{hcp}} = 2.3$, $T_{\mathrm{eff}}^{\mathrm{hcp}} = 0.8$ K. Level diagrams for (d) fcc and (h) hcp. The eigenvalues M_J of $\hat{J}_z$ are indicated by numbers [4].

Fe atoms on Ag(111)

If the Fe atoms are adsorbed on a Ag(111) surface, ISTS reveals a magnetization excitation with a lifetime of about 400 fsec which again decreases linearly upon application of a magnetic field [Fig. 3.1(e)]. Astoundingly, we find that the g-factor, which characterizes the shift in energy of the excitation in a magnetic field, is $g \approx 3.1$ in this system, instead of the regular value of 2. This very large g-shift can be understood when considering the complete electronic structure of both the Ag(111) surface state and the Fe atom, as shown by the *ab initio* calculations of the magnetic susceptibility [2].

Co and Fe atoms on Pt(111)

For Co atoms on Pt(111), a broad distribution of magnetic moments has been revealed by single atom magnetization curves. By measuring magnetization curves of atoms in different distances of surrounding magnetic objects, like other adatoms or ferromagnetic islands, this effect has been explained by (i) the long-range RKKY exchange interaction and (ii) inhomogeneities in the substrate electronic structure [3].

For single Fe atoms adsorbed on Pt(111) [4], we have demonstrated, that the amplitude and sign of the magnetic anisotropy energy can be influenced using STM based atomic manipulation to modify the adatom binding site (Fig. 3.2). Since the magnitude of the measured anisotropy is remarkably small, up to an order of magnitude smaller than previously reported, electron-hole excitations are weak and thus the spin-excitation exhibits long lived precessional lifetimes compared to the values found for the same adatom on noble metal surfaces. Interestingly, the adsorption site dependent change in the anisotropy can be ascribed to the contribution of a cloud of more than 60 polarized platinum atoms beneath the Fe atom, which can quench the total anisotropy or even change its sign, dependent on the adsorption site.

The results of this section show, that the itinerant electrons of the substrate play an important role in all kinds of magnetic properties of adatoms, whose local d-orbitals strongly hybridize with the $s-p$ electron states of the substrate.

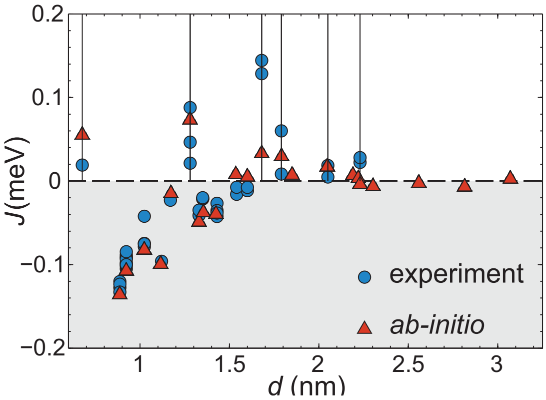

Figure 3.3: Distance dependency of the RKKY interaction in pairs of Fe adatoms on Cu(111). Measured (blue circles) and KKR-calculated (red triangles, renormalized by a factor of 1/2) exchange energy J_{ij} in pairs of Fe atoms on Cu(111) as a function of separation. [5]

3.2.2 Artificial nanostructures from dilute spins with tailored RKKY couplings

A. A. Khajetoorians, J. Wiebe, B. Chilian, S. Lounis, S. Blügel, and R. Wiesendanger

A bottom-up approach to study adatom nanomagnets with a full control over each constituent atom and their mutual couplings has been developed [5]. The distance dependency of the RKKY interaction in pairs of magnetic Fe adatoms on Cu(111) was deduced measuring magnetization curves of each atom in pairs as described in Sec. 3.2.1 and compared against *ab-initio* calculations (Fig. 3.3). Strong magnetic anisotropy allowed the incorporation of these pairwise interactions into an Ising model to tailor nanomagnets. A plethora of different nanomagnets ranging from even and odd numbered chains to building blocks of different spin-frustrated lattices have been built using tip-induced atom manipulation (Fig. 3.4). The magnetic ground states of these nanomagnets have then been studied in real space as a function of an external magnetic field by means of single-atom magnetometry using SPSTS. The building blocks of the spin-frustrated lattices show stepwise lifting of multiple degenerate ground states. To reproduce small trends in the magnetization curves of the chains, the correct next-nearest neighbour interactions from an *ab-initio* calculation of the full nanomagnet, which slightly differ from the corresponding pairwise interactions, had to be taken into account. In the low-magnetic field regime there are deviations from the calculations, which hint towards new effects not accounted for in our theory.

3.2.3 All-spin-based information processing using adatoms

A. A. Khajetoorians, J. Wiebe, B. Chilian, and R. Wiesendanger

An ultimate goal of spintronic research is the realization of concepts for atomic-scale all-spin–based devices. We combined bottom-up atomic fabrication with spin-resolved scanning tunneling microscopy to realize a model system for logical operations that uses atomic spins of adatoms adsorbed on a nonmagnetic metallic surface and their mutual RKKY interaction in order to transmit and process information (Fig. 3.5). The atoms have two different states, 0 or 1, depending on the orientation of their magnetization (down or up, respectively). They are constructed to form anti-ferromagnetically RKKY-coupled chains that transmit the information of the state of small ferromagnetic islands ("input islands") to the gate region. The gate region, which comprises two "input atoms" from each chain and an "output atom", forms the core where the logic operation is performed. The states of the inputs and the resultant state of the output atom are read out by the magnetic tip of a STM, i.e., in the tunneling magnetoresistance device geometry. Although the STM is used to construct and characterize the device, the tunneling current is not essential for performing the given logic operation.

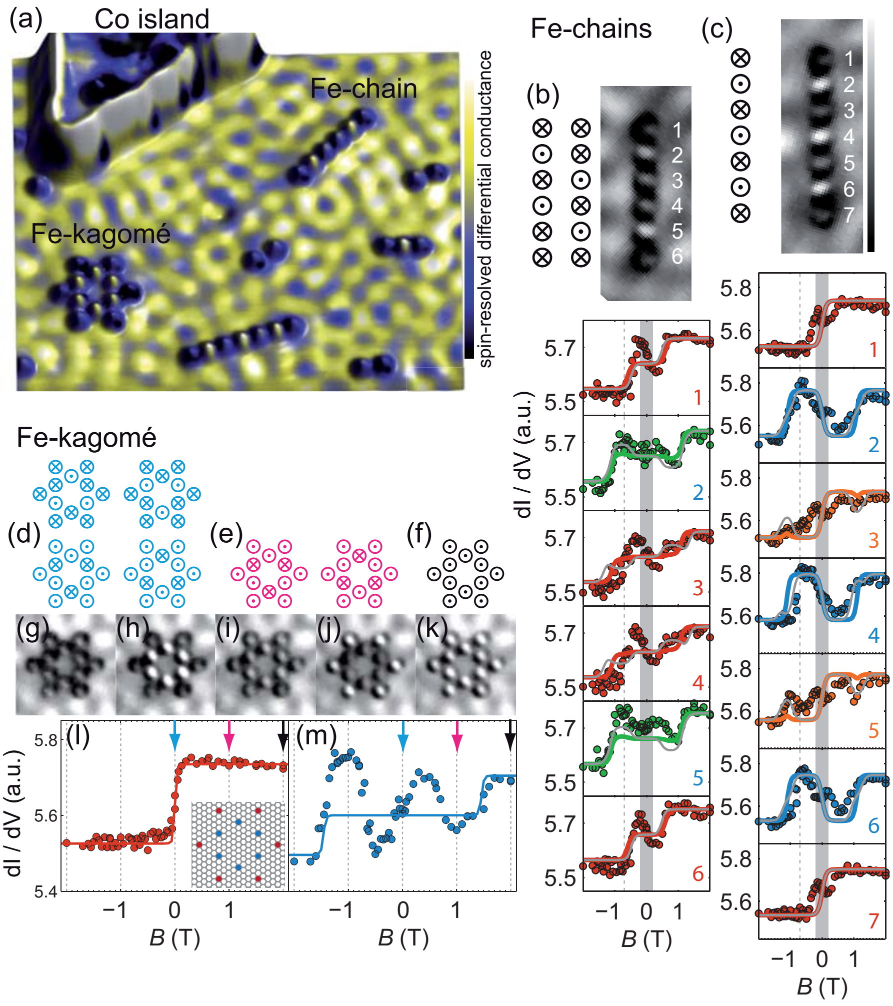

Figure 3.4: (a) SPSTS image of different manipulated nanomagnets consisting of RKKY coupled Fe atoms on Cu(111) (hillocks). (b,c) Top panels: magnetization states from an Ising model (left, partly degenerate) and SPSTS images (right) of chains of anti-ferromagnetically coupled Fe atoms with a length of six (b) and seven (c) atoms. Bottom panels: circles show magnetization curves measured on each atom of the chains. The magnetic images have been taken at B indicated by the dashed vertical line. (d) to (f), degenerate magnetization states from Ising model for an array of 12 anti-ferromagnetically coupled atoms at B as indicated by the arrows in (l,m); (g) to (k), SPSTS images of a Kagome of Fe atoms recorded at B as indicated by the dashed lines in (l,m); (l,m): magnetization curves measured on the Kagome atoms (circles). Thick coloured and thin gray lines in the magnetization plots show magnetization curves as calculated from different Ising models. The gray shaded areas indicate the B range, where the experimental magnetization curve deviates from the Ising models. [5]

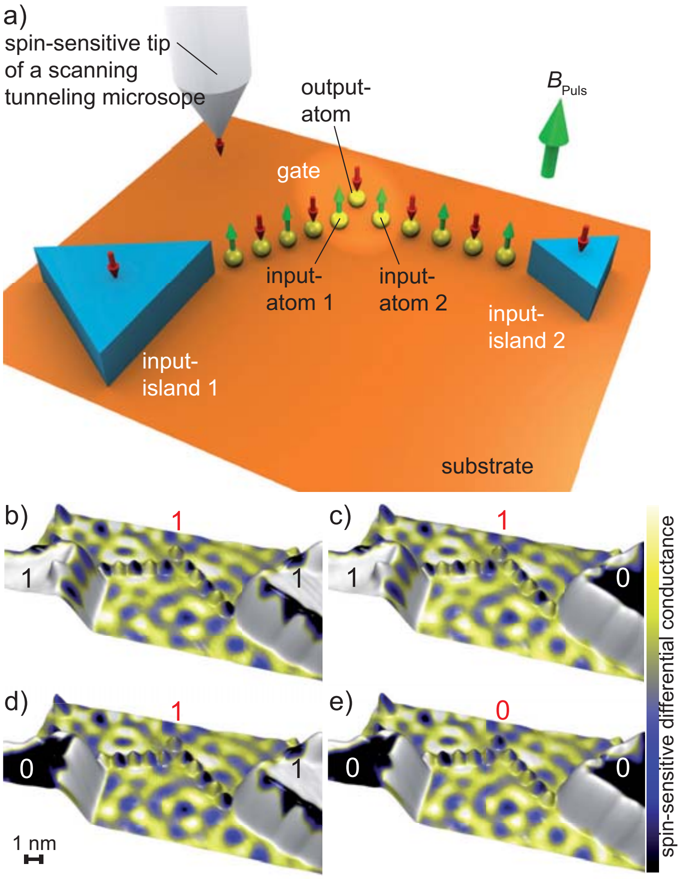

Figure 3.5: (a) Device concept: Two chains of anti-ferromagnetically coupled magnetic atoms (yellow spheres) on a nonmagnetic metallic substrate, are exchange-coupled to two “input islands” (1, 2) of different size, consisting of patches of ferromagnetic layers. The “input atom” (1, 2) of each spin lead and the final “output atom” form a magnetically frustrated triplet with an anti-ferromagnetic coupling which constitutes the logic gate. The field pulse $\vec{B}_{\text{pulse}}$ is used to switch the inputs. The magnetic tip of an STM is used to construct and characterize the device. (b) to (e) Side view 3D topographs colored with simultaneously measured SPSTS image of the constructed OR gate for all four possible input permutations. By applying out-of-plane magnetic field pulses of different strength and direction, each input island can be controllably switched and the two spin leads transmit the information to their end atoms. The output atom in the gate triplet reflects the logical operation of the inputs according to the numbers reflecting the truth table. [6]

The states of the inputs can be switched independently by external magnetic field pulses. Based on an all-spin concept, this model device is principally nonvolatile and functions without the flow of electrons, promising an inherently large energy efficiency.

References

[1] A. A. Khajetoorians, S. Lounis, B. Chilian, A. T. Costa, L. Zhou, D. L. Mills, J.Wiebe, and R.Wiesendanger, Itinerant Nature of Atom-Magnetization Excitation by Tunneling Electrons, Phys. Rev. Lett. **106**, 037205 (2011).

[2] B. Chilian, A. A. Khajetoorians, S. Lounis, A. T. Costa, D. L. Mills, J. Wiebe, and R. Wiesendanger, Anomalously large g factor of single atoms adsorbed on a metal substrate, Phys. Rev. B **84**, 212401 (2011).

[3] J. Wiebe, L. Zhou, and R. Wiesendanger, Atomic magnetism revealed by spin-resolved scanning tunnelling spectroscopy, J. Phys. D: Appl. Phys. **44**, 464009 (2011).

[4] A. A. Khajetoorians, T. Schlenk, B. Schweflinghaus, M. dos Santos Dias, M. Steinbrecher, M. Bouhassoune, S. Lounis, J. Wiebe, and R. Wiesendanger, Spin Excitations of Individual Fe Atoms on Pt(111): Impact of the Site-Dependent Giant Substrate Polarization, Phys. Rev. Lett. **111**, 157204 (2013).

[5] A. A. Khajetoorians, J. Wiebe, B. Chilian, S. Lounis, S. Blügel, and R. Wiesendanger, Atom-by-atom engineering and magnetometry of tailored nanomagnets, Nature Physics **8**, 497 (2012).

[6] A. A. Khajetoorians, J. Wiebe, B. Chilian, and R. Wiesendanger, Realizing All-Spin–Based Logic Operations Atom by Atom, Science **332**, 1062 (2011).

3.3 Complex spin textures

K. von Bergmann, A. Kubetzka, and R. Wiesendanger

On the micrometer scale complex magnetic domain patterns typically arise from a minimization of the magnetostatic energy. This interaction plays only a minor role in atomic layers and nanostructures due to the small amount of magnetic material. In these systems, the substrate surface and the accompanied symmetry breaking becomes important, and complex, non-collinear magnetic order can arise from the so-called Dzyaloshinskii-Moriya (DM) interaction, which favors a canting between adjacent spins. In addition to the uniaxial spin spirals found previously, recently also two-dimensionally modulated magnetic states were observed. Spin-polarized scanning tunneling microscopy (SP-STM) with its high lateral resolution in combination with spin sensitivity is the ideal tool to investigate and locally manipulate such novel atomic-scale spin textures.

3.3.1 Non-collinear magnetic ground states

K. von Bergmann, M. Menzel, S. Heinze, Y. Mokrousov, R. Wieser, J.E. Bickel, D. Serrate, Y. Yoshida, S. Schröder, P. Ferriani, J. Brede, E.Y. Vedmedenko, G. Bihlmayer, S. Blügel, A. Kubetzka, and R. Wiesendanger

Nanoskyrmion lattice in the Fe monolayer on Ir(111)

SP-STM measurements with an in-plane magnetized tip on all possible rotational domains of the two-dimensional magnetic state of the Fe monolayer (ML) on Ir(111) revealed a topologically protected non-collinear ground state [1]. Density functional theory (DFT) calculations in combination with simulations within an extended Heisenberg model were able to unravel the origin of this exotic state: the competition between magnetic exchange interaction and DM interaction sets the period, the DM interaction imposes the rotational sense, while the higher order term of the four-spin interaction couples the magnetic moments to form a two-dimensional spin texture.

Spin spiral in bi-atomic Fe chains on Ir(001)

The magnetic ground state of bi-atomic Fe chains on the reconstructed Ir(001) surface is a spin spiral with three atom periodicity [2]. Again DFT revealed as origin for the angle of 120° between adjacent magnetic moments the competition of magnetic exchange and DM interactions. The magnetic superstructure of the Fe chains cannot be observed at 8 K without external magnetic field due to thermal switching, as revealed by Monte-Carlo (MC) simulations. Only in an external magnetic field the net magnetic moment of a finite chain has a preferential direction which induces an asymmetry in the switching lifetimes, resulting in a time-averaged magnetic signal. Such an Fe chain can also be stabilized by other means: when a ferromagnetic Co

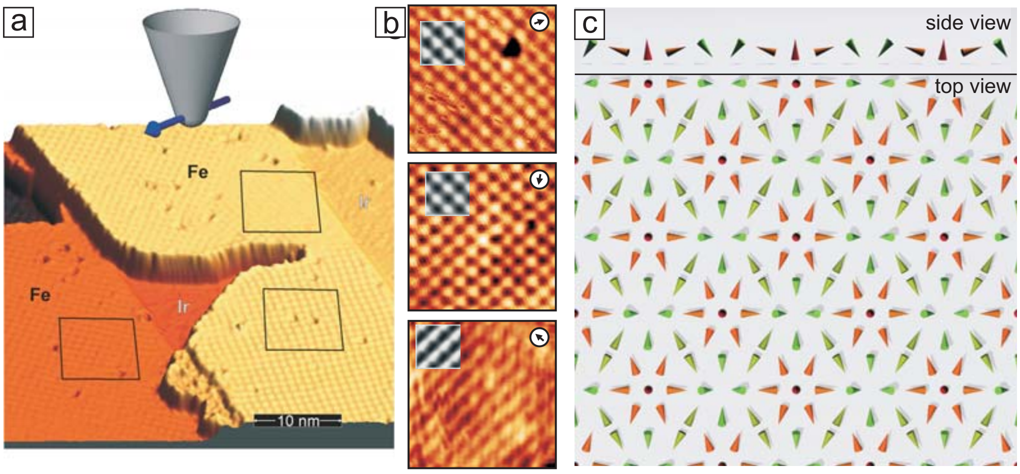

Figure 3.6: The system of one monolayer Fe on Ir(111). (a),(b) SP-STM measurements of all possible rotational magnetic domains imaged with an in-plane sensitive tip. (c) Sketch of the derived commensurate magnetic structure: the nanoskyrmion lattice is nearly square with a periodicity of about 1 nm.

chain is attached to one end of the Fe chain it suppresses the thermal fluctuations due to direct magnetic exchange and the magnetic periodicity is detected with SP-STM also without external magnetic field. The same is true when a Co chain is located in the adjacent trench of the Ir reconstruction, suggesting that there is significant substrate-mediated coupling.

Conical spin spiral in the Mn double-layer on W(110)

While in the Mn monolayer the angle between adjacent moments is ≈ 170°, SP-STM measurements on the Mn double-layer (DL) show a commensurate two-atom periodicity along the $[1\bar{1}0]$ direction [3]. However, there is a rotation of magnetic moments on a cone, leading to an additional periodicity in the [001] direction in SP-STM measurements. The driving force for this truly three-dimensional magnetic state was identified using DFT calculations as an interplay of magnetic exchange, DM, and the typically neglected four-spin interaction.

Tunneling anisotropic magnetoresistance

Interestingly, also with a spin-averaging tip, e.g. W, one can study non-collinear states [4]. Due to a different mixing of the orbitals for in-plane versus out-of-plane magnetized atoms they have a slightly different density of states, which is detectable in the tunnel current as the tunneling anisotropic magnetoresistance (TAMR) effect. Typically such TAMR images show twice the magnetic periodicity. While it is a great advantage that the magnetic tip preparation can be omitted and that there is no stray field from the tip some aspects of the magnetic properties remain hidden, such as the

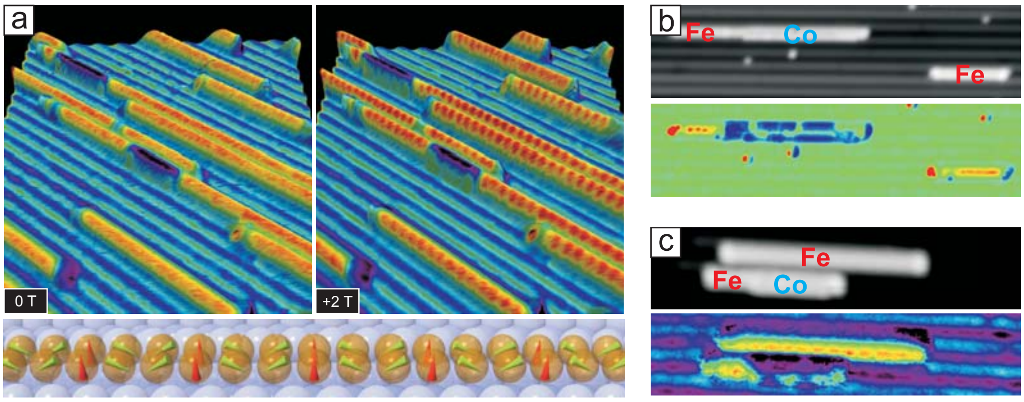

Figure 3.7: Bi-atomic chains on Ir(001). (a) SP-STM measurements at $T = 8\,\mathrm{K}$ (topography color-coded with $\mathrm{d}I/\mathrm{d}U$ signal) of Fe chains without external magnetic field and at $B = +2\,\mathrm{T}$; in magnetic field the three-atom magnetic periodicity of the spin spiral is visible, see sketch below. (b,c) SP-STM measurements (gray-scale topography, color-scale $\mathrm{d}I/\mathrm{d}U$ map) of isolated Fe chain and mixed CoFe chain at $B = 0\,\mathrm{T}$: (b) the ferromagnetic Co blocks the thermal fluctuation of the attached Fe part, (c) the magnetic orientation of the Fe chain is stabilized via substrate-mediated interactions with the Co chain grown in the adjacent trough.

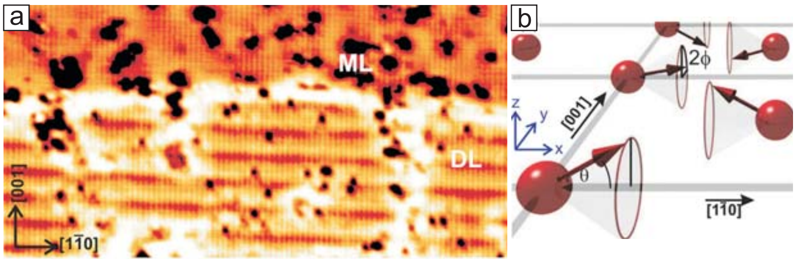

Figure 3.8: Conical spin spiral of the Mn-DL on W(110). (a) SP-STM image of ML and DL connected at a buried W step edge. The DL shows a two-atom magnetic periodicity along [1$\bar{1}$0] and a larger modulation along [001]. (b) Model of the conical magnetic state.

absolute magnetization direction or the rotational sense of a system.

3.3.2 Spin friction in atom manipulation imaging mode

B. Wolter, Y. Yoshida, S.-W. Hla, K. von Bergmann, A. Kubetzka, and R. Wiesendanger

Atom manipulation is a widespread technique to build artificial, well-defined atomic structures. Furthermore, an adatom trapped below the STM tip during scanning, can also be used as a local probe for surface potentials and forces. When a magnetic adatom is moved by a magnetic tip on a magnetic surface, competing magnetic interactions can severely influence the path of the manipulated atom, giving rise to enhanced magnetic contrast in this imaging mode. This is demonstrated for Co adatoms on the spin spiral state of the Mn-ML on W(110). Comparing experimental SP-STM images to MC simulations the underlying energy dissipation processes can be identified. It is found that the spin plays a significant role in frictional phenomena when the adatom jumps between magnetically non-equivalent adsorption sites [5].

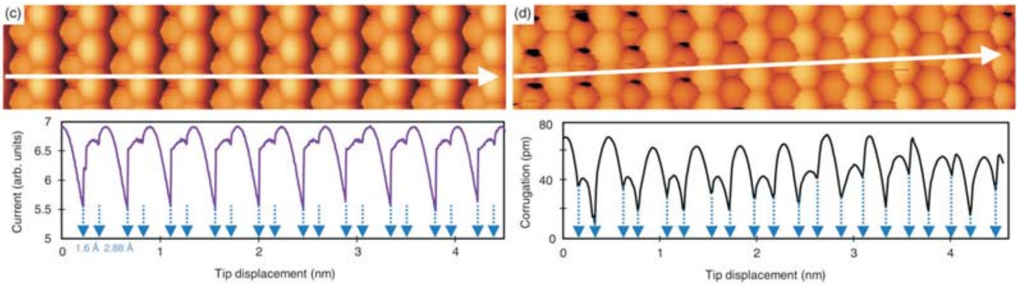

Figure 3.9: Occurrence of spin friction during manipulation of a magnetic adatom. MC simulation (left) and experimental SP-STM image of the Mn-ML on W(110) with a Co atom trapped in the tunnel junction; the blue arrows in the line profiles (bottom) highlight the deviation of the jump positions of the adatom from the equidistant atomic periodicity.

3.3.3 Tuning magnetic states with non-magnetic adlayers

L.V. Dzemiantsova, N. Romming, C. Hanneken, J.E. Bickel, M. Hortamani, B. Wolter, M. Karolak, F. Lofink, B. Sachs, S. Hankemeyer, T.O. Wehling, R. Frömter, F. Meier, J. Brede, M. Menzel, K. von Bergmann, A. Kubetzka, H.P. Oepen, A.I. Lichtenstein, and R. Wiesendanger

It is well-known that the choice of substrate plays a major role for the magnetic properties of adsorbed atomic layers. Completely different magnetic ground states have been found in the past for e.g. ultrathin Fe layers on different substrates, where the element, the symmetry, or the lattice constant is varied. To only slightly tune magnetic properties an alternative and much more practical way is to cover a specific magnetic system with one layer of non-magnetic material.

Graphene on Ni(111)

Adlayers can also be used as protective layers or spin filters. Graphene for instance, prepared on a single crystal Ni(111) surface, passivates the Ni surface efficiently, while it still allows surface sensitive techniques like SP-STM and scanning electron microscopy with polarization analysis (SEMPA) to image the magnetic domain structure below [6]. Furthermore, DFT calculations show that the graphene layer quenches a spin-polarized surface state, thereby acting as a spin filter, while the carbon atoms themselves remain virtually non-magnetic.

Pd layers on the system of the Co-ML on Ir(111)

The system of the Co-ML on Ir(111) is ferromagnetic with out-of-plane anisotropy. It exhibits an exceptionally high coercivity of $> 4\,\mathrm{T}$ and requires an external magnetic field $> 5.25\,\mathrm{T}$ to saturate [7]. When this system is covered with Pd it maintains it's ferromagnetic state. Density functional theory reveals that the Pd gets significantly polarized in the ML and the DL $(0.2 - 0.4\,\mu_\mathrm{B})$. SP-STM experiments with single Co adatoms show that they couple ferromagnetically to the Co/Ir(111) not only through a ML but also through a DL of Pd spacer [8].

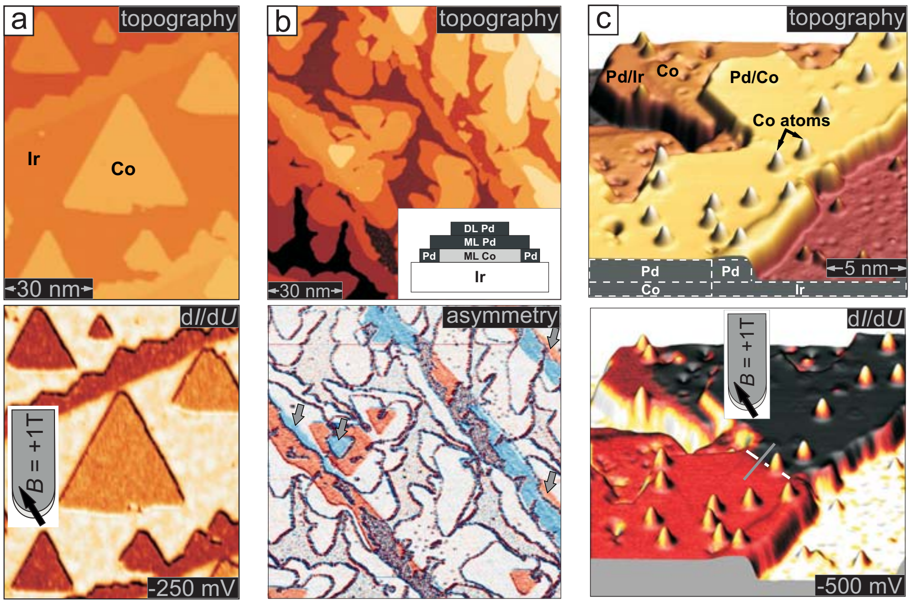

Figure 3.10: (a) SP-STM images (topography and spin-resolved $\mathrm{d}I/\mathrm{d}U$ signal) of out-of-plane ferromagnetic Co monolayer islands on Ir(111). (b) SP-STM measurements of Pd on Co/Ir(111): the map of magnetic asymmetry (bottom) reveals a spin-polarization for the ML as well as the DL Pd on Co/Ir(111); red and blue indicate areas with positive and negative magnetic asymmetry, respectively. (c) Co atoms on a PdCo bilayer with magnetic domain wall: a ferromagnetic coupling between the Co adatoms and the Co layer through the layer is observed.

Pd monolayer on the nanoskyrmion lattice

When Pd is deposited onto the nanoskyrmion lattice of the Fe-ML on Ir(111) this leads to a significant change of the magnetic ground state: The PdFe bilayer exhibits a spin spiral ground state with an approximately seven times larger period than the two-dimensional ground state of the uncovered Fe/Ir(111). In an external magnetic field transitions to other magnetic phases can be observed: at intermediate fields a hexagonal skyrmion lattice is induced which saturates to a ferromagnetic state at even higher magnetic fields. This is the first example of an interface-driven magnetic field induced skyrmion lattice [9].

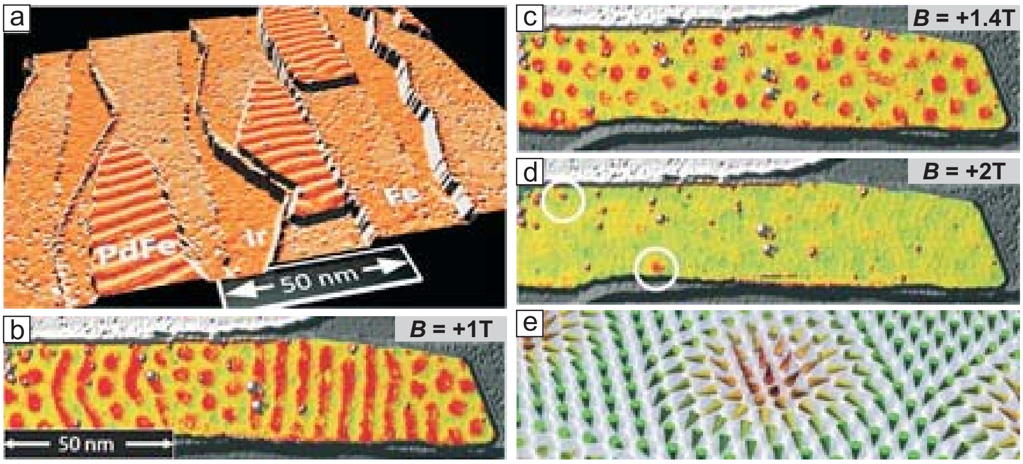

Figure 3.11: SP-STM measurements of the system of the PdFe bilayer on Ir(111) in dependence on an external magnetic field at $T = 8\,\mathrm{K}$. (a) $B = 0\,\mathrm{T}$: spin spiral state, (b) $B = 1\,\mathrm{T}$: coexistence of spin spiral and skyrmions, (c) $B = 1.4\,\mathrm{T}$: hexagonal skyrmion lattice, (d) $B = 2\,\mathrm{T}$: ferromagnetic phase. (e) Sketch of the magnetic skyrmion lattice phase.

3.3.4 Writing and deleting single magnetic skyrmions

N. Romming, C. Hanneken, M. Menzel, J. E. Bickel, B. Wolter, K. von Bergmann, A. Kubetzka, and R. Wiesendanger

At low temperature the system of the PdFe bilayer can be trapped in metastable states. Then isolated skyrmions, pinned at defects, can be locally addressed and created or annihilated. A systematic study of the switching behavior reveals that spin transfer torque can be utilized for a directional switching [9].

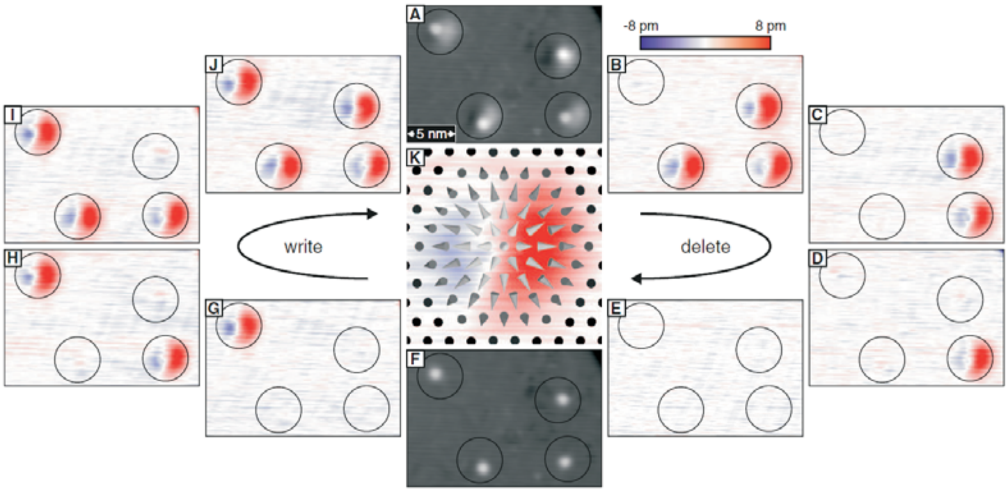

Figure 3.12: SP-STM measurements of a group of isolated skyrmions in the system of the PdFe bilayer on Ir(111) at $T = 4\,\mathrm{K}$, $B = 3.25\,\mathrm{T}$. Constant-current images (gray-scale) with (A) and without (F) skyrmions pinned at the four defects. The difference images (color-scale, with respect to (F)) show how the skyrmions can be deleted and written independently. The central image depicts the magnetization direction within a skyrmion.

References

[1] S. Heinze, K. von Bergmann, M. Menzel, J. Brede, A. Kubetzka, R. Wiesendanger, G. Bihlmayer, and S. Blügel, Spontaneous atomic-scale magnetic skyrmion lattice in two dimensions, Nature Physics **7**, 713 (2011).

[2] M. Menzel, Y. Mokrousov, R. Wieser, J.E. Bickel, E. Vedmedenko, S. Blügel, S. Heinze, K. von Bergmann, A. Kubetzka, and R. Wiesendanger, Information Transfer by Vector Spin Chirality in Finite Magnetic Chains, Phys. Rev. Lett. **108**, 197204 (2012).

[3] Y. Yoshida, S. Schröder, P. Ferriani, D. Serrate, A. Kubetzka, K. von Bergmann, S. Heinze, and R. Wiesendanger, Conical spin-spiral state in an ultra-thin film driven by higher-order spin interactions, Phys. Rev. Lett. **108**, 087205 (2012).

[4] K. von Bergmann, M. Menzel, D. Serrate, Y. Yoshida, S. Schröder, P. Ferriani, A. Kubetzka, R. Wiesendanger, and S. Heinze, Tunneling anisotropic magnetoresistance on the atomic scale, Phys. Rev. B **86**, 134422 (2012).

[5] B. Wolter, Y. Yoshida, A. Kubetzka, S.-W. Hla, K. von Bergmann, and R. Wiesendanger, Spin Friction Observed on the Atomic Scale, Phys. Rev. Lett. **109**, 116102 (2012).

[6] L.V. Dzemiantsova, M. Karolak, F. Lofink, A. Kubetzka, B. Sachs, K. von Bergmann, S. Hankemeier, T.O. Wehling, R. Frömter, H.P. Oepen, A.I. Lichtenstein, and R. Wiesendanger, Multiscale magnetic study of Ni(111) and graphene on Ni(111), Phys. Rev. B **84**, 205431 (2011).

[7] J. E. Bickel, F. Meier, J. Brede, A. Kubetzka, K. von Bergmann, and R. Wiesendanger, Magnetic properties of monolayer Co islands on Ir(111) probed by spin-resolved scanning tunneling microscopy, Phys. Rev. B **84**, 054454 (2011).

[8] L. V. Dzemiantsova, M. Hortamani, C. Hanneken, A. Kubetzka, K. von Bergmann, and R. Wiesendanger, Magnetic coupling of single Co adatoms to a Co underlayer through a Pd spacer of variable thickness, Phys. Rev. B **86**, 094427 (2012).

[9] N. Romming, C. Hanneken, M. Menzel, J. E. Bickel, B. Wolter, K. von Bergmann, A. Kubetzka, and R. Wiesendanger, Writing and Deleting Single Magnetic Skyrmions, Science **341**, 6146 (2013).

3.4 Magnetization dynamics and current-induced magnetization switching studied by SP-STM

S. Krause and R. Wiesendanger

Using SP-STM we were able to experimentally separate and quantify the contributions of Joule heating and spin-transfer torque for current-induced magnetization switching of nanomagnets across a vacuum barrier. Here, a quasi-classical macrospin model can be applied to describe the dynamics.

The energy of the electrons that are injected into a nanomagnet also plays a crucial role for the inelastic interactions involved in current-induced magnetization switching. In a detailed SP-STM study the impacts of low energy tunneling and high-energy field-emitted electrons have been compared, and similarities as well as significant differences in the relaxation processes have been elaborated in terms of phonon, magnon and Stoner mode excitations. We observed a drastic influence of the field-emission current onto the switching behavior of an individual nanomagnet, even at tip-sample distances of several nanometers.

The local electric field that is present between a biased STM tip and an atomic-scale magnet has been shown to significantly couple to the magnet, resulting in an effective magnetic anisotropy the direction of which depends on the sign of the electric field. Using solely the magnetoelectric coupling at a vanishing current we drastically modified the thermally driven magnetization switching behavior of individual nanomagnets.

At very low temperatures of 300 mK we fabricated smallest clusters by atomic manipulation using SP-STM. We demonstrated that a cluster consisting of only five iron atoms on a Cu(111) surface already exhibits a significant hysteresis. A collaborative study involving theoretical support from the University of Hamburg, University of Bremen and the Research Center in Jülich elaborated a detailed theoretical model to understand and describe the experimentally observed magnetization dynamics in terms of state-resolved lifetimes. It turned out that the magnetism of a five-atom iron cluster and its magnetization dynamics is dominated by quantum effects, resulting in unexpected high intrinsic magnetic state lifetimes.

3.4.1 Joule heating and spin-transfer torque investigated on the atomic scale using a spin-polarized scanning tunneling microscope

S. Krause, G. Herzog, A. Schlenhoff, A. Sonntag, and R. Wiesendanger

Re-orienting the magnetization of a nanostructure by injecting a spin-polarized current is in the focus of ongoing research because of its relevance for future spintronic and magnetic memory devices. A magnetic torque exerted by a spin-polarized current can cause the magnetization to flip, as proposed theoretically [1, 2] and demonstrated experimentally, for example, in lithographically fabricated magneto-tunnel junctions (MTJs) [3–5]. Recent experiments using spin-polarized scanning tunneling microscopy (SP-STM) demonstrated that this current-induced magnetization switching (CIMS), driven by Joule heating, spin-transfer torque and Oersted field, is possible even when vacuum serves as the tunnel barrier [6–8]. In contrast to lithographically fabricated MTJs, the ultimate lateral resolution of SP-STM allows for a very local observation and manipulation of atomic-scale magnets. The details of the driving microscopic processes for CIMS are still to be discovered, and one important prerequisite on this way is the possibility to separate and quantify the Joule heating and spin-transfer torque on the atomic scale.

We specially utilize a superparamagnetic Fe/W(110) nanoisland to explore CIMS with SP-STM. By simultaneously observing and manipulating its switching behavior with a spin-polarized tunnel current, we separate and quantitatively determine the individual contributions of Joule heating and spin-transfer torque, with the nanoisland serving as a combined local thermometer and spin-torque analyzer. Comparing our results to experiments performed on nanopillar MTJs reveals a very high spin-transfer torque efficiency for SP-STM MTJs.

As has been shown theoretically [9,10] and verified experimentally [11], the intrinsic switching behavior of a superparamagnetic particle with uniaxial anisotropy can be described by the so-called macrospin model, as illustrated in Fig. 3.13(a). Here, the particle magnetization has to overcome an energy barrier E_b to reverse its orientation. All magnetic moments inside the particle rotate coherently, thereby behaving like one giant spin, and E_b is given by the total magnetic anisotropy of the particle. The mean lifetime $\bar{\tau}$ between two consecutive switching events as a function of temperature T is then given by

$$\bar{\tau} = \frac{1}{f_0} \exp\left(\frac{E_\mathrm{b}}{k_\mathrm{B}T}\right), \tag{3.1}$$

with f_0 being the attempt frequency and k_B the Boltzmann constant. The two possible magnetization orientations are labeled state **0** and state **1**, respectively. Temperature-dependent SP-STM studies on individual Fe/W(110) nanoislands revealed that the magnetization reversal is realized by a nucleation and propagation of a domain wall

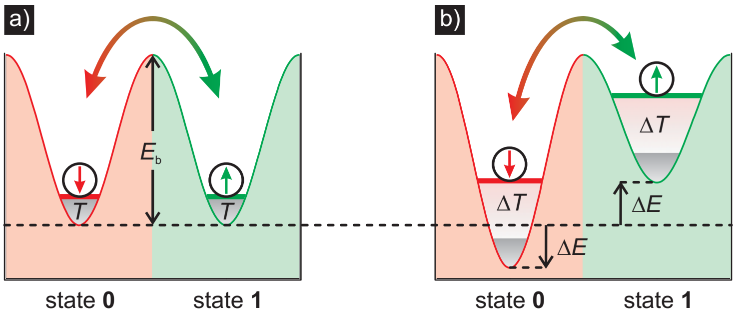

Figure 3.13: (**a**) Energy landscape schematics of a magnet with uniaxial anisotropy. Due to thermal agitation at temperature T, the magnetization may overcome the effective activation barrier E_b between the two states **0** and **1**. (**b**) Influence of a high spin-polarized current: Joule heating effectively increases T by ΔT, and spin-torque modifies E_b by $\pm\Delta E$, thereby lifting the state degeneracy and favoring switching from state **1** to state **0**.

rather than by a coherent rotation [12]. However, the macrospin ansatz has been shown to be adequate to describe the switching behavior as long as E_b is interpreted as the effective activation energy barrier for magnetization reversal [12].

CIMS experiments using SP-STM demonstrated that the intrinsic thermal switching behavior of a Fe/W(110) nanoisland is modified when passed by a high spin-polarized tunnel current I [6]: The temperature is effectively increased by ΔT due to Joule heating [13], and the activation energy barrier E_b is modified by $\pm\Delta E$ due to spin-transfer torque [14], the latter leading to an asymmetry of the state lifetimes. The situation is illustrated schematically in Fig. 3.13(b). There are first experimental indications for additional contributions to CIMS, like dissipation of a pure spin current [15] and thermal spin-transfer torque [16, 17]. In this paper all interactions resulting in an effective temperature rise are summarized by the term Joule heating, and all contributions leading to an asymmetry of the switching behavior are called spin-transfer torque for the sake of clarity. Oersted field contributions are found to be negligible as long as I is injected at a high symmetry point of the magnet [6]. To account for Joule heating and spin-transfer torque, we expand Eq. 3.1 to

$$\bar{\tau}_{0,1}(I) = \frac{1}{f_0} \exp\left(\frac{E_\mathrm{b} \pm \Delta E(I)}{k_\mathrm{B}[T + \Delta T(I)]} \right), \tag{3.2}$$

where $\bar{\tau}_0(I)$ and $\bar{\tau}_1(I)$ are the I-dependent mean lifetimes of state **0** and state **1**, respectively.

In order to quantify $\Delta T(I)$ and $\Delta E(I)$, the switching behavior of an individual nanoisland has been investigated using SP-STM at elevated I. The experiments were performed in an ultrahigh vacuum system that is equipped with a homebuilt spin-polarized scanning tunneling microscope for variable temperatures. Within our experimental setup, the entire microscope including the tip is cooled to minimize the thermal drift between tip and sample. To exclude any unwanted dipolar tip-sample interaction, antiferromagnetic Cr coated W tips were used which are sensitive to the in-plane component of the sample magnetization [18,19]. A W(110) single crystal serves as substrate for our experiments. Its preparation is described in detail in Ref. [20]. Evaporating 0.14 atomic layers of iron onto the substrate held at room temperature leads to the formation of pseudomorphically grown monolayer nanoislands consisting of about 30–150 atoms [12]. At a temperature of 50.6 K, these nanoislands are found to switch their magnetization frequently due to thermal agitation [12].

The differential conductance dI/dU between tip and sample is measured adding a small ac modulation voltage ($U_{\mathrm{mod}} = 40\,\mathrm{mV}$, $f_{\mathrm{mod}} = 4.333\,\mathrm{kHz}$) to the sample bias and detecting the resulting modulation of I by lock-in technique. Here, the spin-dependent contribution to the dI/dU signal scales with the cosine of the angle between the magnetization directions of the tip and sample [19]. Hence, positioning the tip stationary above a sample and measuring dI/dU as a function of time t allows for recording the temporal evolution of the sample magnetization.

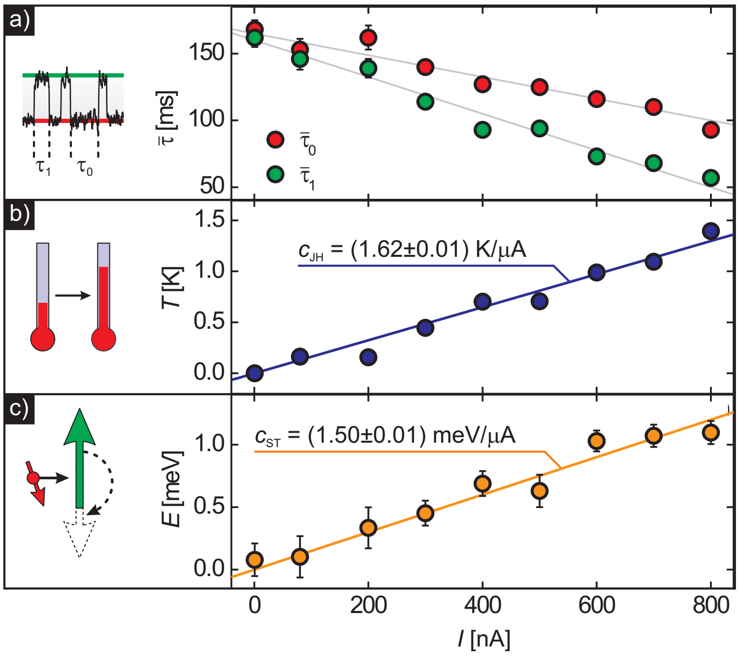

Figure 3.14: Tunnel current dependence of the (**a**) mean lifetimes $\bar{\tau}_0$ and $\bar{\tau}_1$ (gray lines are guides for the eye), (**b**) effective island temperature increase ΔT and (**c**) energy barrier modification ΔE. Error bars indicate SD. Linear fittings yield the coefficients c_{JH} and c_{ST}. $U = -200\,\mathrm{mV}$, $T = 50.6\,\mathrm{K}$.

The dI/d$U(t)$ signal recorded above an individual Fe/W(110) nanoisland exhibits a telegraphic noise, reflecting the magnetization switching between two configurations with respect to the stable tip magnetization. As a convention, a low (high) signal is attributed to the nanoisland being in the magnetic state **0** (**1**). To extract the state-dependent mean lifetimes $\bar{\tau}_0$ and $\bar{\tau}_1$ from the telegraphic signal, every state lifetime τ_0

and τ_1 between two consecutive switching events has been determined. Traces with at least 1500 switching events have been evaluated for sake of a good statistics. Fitting the respective histograms of τ_0 and τ_1 with an exponential decay results in the mean lifetimes $\bar{\tau}_0$ and $\bar{\tau}_1$. To determine the current-dependent mean lifetimes, $\bar{\tau}_0$ and $\bar{\tau}_1$ have been evaluated for various values of I between 2 nA and 800 nA at a fixed bias voltage of $U = -200\,\text{mV}$. The results are plotted in Fig. 3.14(a). As has been shown before, an overall tendency of decreasing lifetime and increasing state lifetime asymmetry towards high I is clearly visible [6].

Combining Eqs. 3.1 and 3.2 allows for the determination of the temperature rise $\Delta T(I)$ due to Joule heating and the energy splitting $\Delta E(I)$ due to spin-transfer torque:

$$\Delta T(I) = \left(\frac{1}{T} + \frac{k_\text{B}}{2E_\text{b}} \ln \frac{\bar{\tau}_0(I)\bar{\tau}_1(I)}{\bar{\tau}^2}\right)^{-1} - T, \tag{3.3}$$

$$\Delta E(I) = \frac{k_\text{B}\,[T + \Delta T(I)]}{2} \ln \frac{\bar{\tau}_0(I)}{\bar{\tau}_1(I)}, \tag{3.4}$$

where $\bar{\tau}$ is the intrinsic mean lifetime determined at $I = 2\,\text{nA}$. To deduce E_b, the mean lifetimes of the intrinsic thermal switching behavior have been determined at two different temperatures and low I, resulting in $E_\text{b} = (133 \pm 4)\,\text{meV}$.

The results for $\Delta T_\text{JH}(I)$ are plotted in Fig. 3.14(b). Obviously, the temperature rises linearly as a function of I. This is consistent with an experimental study of heat generation between an STM tip and a metallic sample, demonstrating that the Joule heat dissipated in the sample scales linearly with I at constant bias voltage U [13]. Fitting the data with $\Delta T(I) = c_\text{JH} I$ yields $c_\text{JH} = (1.62 \pm 0.01)\,\text{K}/\mu\text{A}$, where c_JH is introduced as the differential heating coefficient of the MTJ. Consequently, the thermal energy of the nanoisland is increased by up to 3% of $k_\text{B}T$. Due to the Arrhenius-like switching behavior, this tiny temperature increase already considerably reduces the mean lifetimes by a factor of two.

It has been shown experimentally that the thermal conductivity of a nanocontact is drastically reduced with respect to its bulk value due to phonon confinement [21]. Since Fe/W(110) nanoislands are strongly confined vertically as well as laterally, we expect a very local heat dissipation within the nanoisland due to phonon generation by the tunneling electrons, with the temperature of the substrate remaining almost unaffected. Likewise, variations of the temperature within the nanoisland are assumed to be negligible, although the spot of tunnel current injection is confined to a cross-sectional area given by the typical SP-STM lateral resolution of 5 Å [22].

Many experiments addressing Joule heating were performed on lithographically fabricated nanopillar MTJs. Here, a typical temperature increase of about $2\,\text{K}/(\text{mW}\mu\text{m}^{-2})$ is deduced on μm size junctions [23]. However, the layered nature of these devices strongly hinders a direct investigation of the local Joule heating inside an MTJ. For example, imperfections may create so-called hot spots where the local current density and therefore also the local temperature rise may increase by up to 13 times the average value [23]. Our SP-STM experiments allow for a very local and quantitative investigation of Joule heating on the atomic scale on well-defined structures. The Fe nanoisland has a base area of about $5.5\,\mathrm{nm}^2$, resulting in a temperature increase of $44\,\mathrm{K}/(\mathrm{mW}\mu\mathrm{m}^{-2})$. This value is in accordance with STM experiments performed on Co/Cu(111) nanoislands, where the temperature increase has been roughly estimated to be 30–$300\,\mathrm{K}/(\mathrm{mW}\mu\mathrm{m}^{-2})$ [24].

In Fig. 3.14(c), the results for the spin-transfer torque contribution $\Delta E(I)$ are plotted. As for $\Delta T(I)$, a linear scaling behavior with I is observed. This finding is in accordance with theoretical studies on the thermally assisted magnetization reversal in the presence of a spin-transfer torque [14]. Fitting the data with $\Delta E = c_{\mathrm{ST}} I$ results in $c_{\mathrm{ST}} = (1.50 \pm 0.01)\,\mathrm{meV}/\mu\mathrm{A}$, with c_{ST} being introduced as the differential modification of E_{b}.

To compare the spin-transfer torque in our SP-STM experiments to that in nanopillar MTJs, we calculate the so-called torkance [25]

$$\frac{d\Gamma}{dU}(I) = \frac{d\Gamma}{dI}\frac{dI}{dU}(I) = \frac{\hbar}{2e}\eta\frac{dI}{dU}(I). \tag{3.5}$$

Here, η is the tunnel current spin-polarization. It can be determined from the MTJ work function ϕ and the tip-sample distance variation Δz between parallel and antiparallel configuration of tip and sample magnetization at closed feedback loop [26]. From $I(z)$ spectroscopy experiments we deduce $\phi = 3.12\,\mathrm{eV}$, resulting in $\eta = 0.07$.

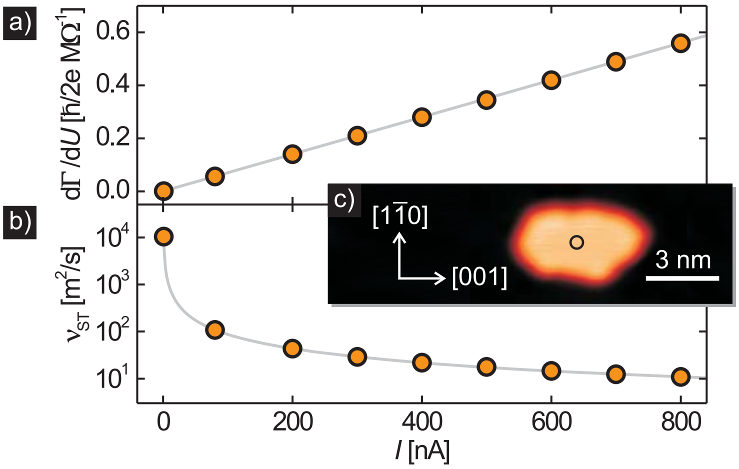

Figure 3.15: Experimentally determined tunnel current dependence of the (**a**) torkance $d\Gamma/dU$ and (**b**) spin-transfer torque viscosity ν_{ST}. Gray lines are guides to the eye. (**c**) Topography map of the nanoisland. The point of current injection is marked by a circle.

The experimental results for the torkance are shown in Fig. 3.15(a). In contrast to CIMS experiments performed on nanopillar devices at low bias [5], the torkance is not constant. This is reasonable, since in our experiments high tunnel currents are realized by reducing the distance between the SP-STM tip and the nanoisland, thereby increasing the tunnel conductivity. We find $dI/dU(I) = 0.01\,\mu\mathrm{S}/\mathrm{nA}\cdot I$, resulting in

$d\Gamma/dU(800\,\mathrm{nA}) = 5.6 \times 10^{-4}\hbar/(2e)\,\mathrm{k\Omega}^{-1}$ for the maximum tunnel current of $I = 800\,\mathrm{nA}$. This value is by four orders of magnitude lower than in experiments performed on lithographically fabricated MTJs, yielding $d\Gamma/dU \approx 0.1\hbar/(2e)\,\mathrm{k\Omega}^{-1}$ [5]. However, the magnetic moment that has to be switched in an atomic-scale nanoisland is much lower than in a nanopillar structure. From the topography map shown in Fig. 3.15(c), we estimate the nanoisland consisting of about 78 atoms. Given a magnetic moment of 2.79 Bohr magneton per Fe atom [27], this results in a total magnetic moment of $m = 2 \times 10^{-21}\,\mathrm{A/m^2}$. The nanopillar MTJ of Ref. [5] has a total magnetic moment of $m = 1 \times 10^{-17}\,\mathrm{A/m^2}$. To provide a measure of the switching efficiency, we relate the torkance to the magnetic moment by defining the spin-transfer torque viscosity ν_{ST}:

$$\nu_{\mathrm{ST}}(I) := m \cdot \left(\frac{d\Gamma}{dU}(I)\right)^{-1}. \tag{3.6}$$

Here, a low viscosity implies a high impact of the spin-transfer torque onto m. As can be seen from Fig. 3.15(b), $\nu_{\mathrm{ST}} \approx 10^4\,\mathrm{m^2/s}$ at low I. With increasing I, the spin-transfer torque viscosity drops by about three orders of magnitude, indicating a dramatic increase of the switching efficiency. At $I = 800\,\mathrm{nA}$, $v_{\mathrm{ST}} = 11\,\mathrm{m^2/s}$. For the nanopillar MTJ of Ref. [5], $v_{\mathrm{ST}} = 217\,\mathrm{m^2/s}$. Consequently, the spin-transer torque impact onto m within our SP-STM experiments is by a factor of 20 higher than in experiments performed on typical nanopillar MTJs. For a fictious spin-polarization of $\eta = 1$, the spin-transfer torque viscosity will drop down by another order of magnitude, with $v_{\mathrm{ST}} \leq 1\,\mathrm{m^2/s}$ for $I = 800\,\mathrm{nA}$.

As discussed before, in contrast to experiments on nanopillar MTJs where the current is generally considered to be homogeneously distributed, the area of spin-polarized tunnel current injection in our studies is confined to a spot diameter of 5 Å [22], resulting in a local current density of up to $4 \times 10^8\,\mathrm{A/cm^2}$. Hence, only a fractional part of the nanoisland will be directly affected by the spin-polarized tunnel current. For smaller nanoislands with sizes being comparable to that of the current injection spot, we expect a further decrease of ν_{ST}, since then the whole nanomagnet is affected by the spin-transfer torque.

In summary, we performed an experimental study on an individual Fe/W(110) nanoisland using SP-STM to quantitatively determine the contributions of Joule heating and spin-transfer torque as a function of the spin-polarized tunnel current. A detailed lifetime analysis reveals that both the effective temperature rise as well as the modification of the effective activation energy barrier scale linearly with the tunnel current. Comparing the temperature increase and the spin-transfer torque to that in lithographically fabricated MTJs in terms of torkance and spin-transfer torque viscosity, we find a very high switching efficiency in our SP-STM experiments. The presented concept of investigating the current-dependent switching behavior of a single superparamagnetic nanoisland by means of SP-STM opens the perspective for a variety of new experiments. For example, the influence of single impurities on the switching efficiency are not accessible in experiments using nanopillar MTJs. Our studies allow for a detailed investigation of Joule heat generation and spin-transfer torque switching on the atomic scale, thereby providing new insight into the details of CIMS.

References

[1] J. C. Slonczewski, J. Magn. Magn. Mater. **159**, L1 (1996).

[2] L. Berger, Phys. Rev. B **54**, 9353 (1996).

[3] Y. Huai, F. Albert, P. Nguyen, M. Pakala, and T. Valet, Appl. Phys. Lett. **84**, 3118 (2004).

[4] G. D. Fuchs,N. C. Emley, I. N. Krivorotov, P. M. Braganca, E. M. Ryan, S. I. Kiselev, J. C. Sankey, D. C. Ralph, R. A. Buhrman, and J. A. Katine, Appl. Phys. Lett. **85**, 1205 (2004).

[5] J. C. Sankey, Y.-T. Cui, J. Z. Sun, J. C. Slonczewski, R. A. Buhrman, and D. C. Ralph, Nature Phys. **4**, 67 (2008).

[6] S. Krause, L. Berbil-Bautista, G. Herzog, M. Bode, and R. Wiesendanger, Science **317**, 1537 (2007).

[7] G. Herzog, S. Krause, and R. Wiesendanger, Appl. Phys. Lett. **96**, 102505 (2010).

[8] S. Loth, M. Etzkorn, C. P. Lutz, D. M. Eigler, and A. J. Heinrich, Science **329**, 1628 (2010).

[9] M. L. Néel, Ann. Géophys. **5**, 99 (1949).

[10] W. F. Brown, Phys. Rev. **130**, 1677 (1963).

[11] W. Wernsdorfer, E. B. Orozco, K. Hasselbach, A. Benoit, B. Barbara, N. Demoncy, A. Loiseau, H. Pascard, and D. Mailly, Phys. Rev. Lett. **78**, 1791 (1997).

[12] S. Krause, G. Herzog, T. Stapelfeldt, L. Berbil-Bautista, M. Bode, E. Y. Vedmedenko, and R. Wiesendanger, Phys. Rev. Lett. **103**, 127202 (2009).

[13] I. Bat'ko and M. Bat'ková, Eur. Phys. J. Appl. Phys. **31**, 191 (2005).

[14] Z. Li and S. Zhang, Phys. Rev. B **69**, 134416 (2004).

[15] A. A. Tulapurkar and Y. Suzuki, Phys. Rev. B **83**, 012401 (2011).

[16] M. Hatami, G. E. W. Bauer, Q. Zhang, and P. J. Kelly, Phys. Rev. Lett. **99**, 066603 (2007).

[17] H. Yu, S. Granville, D. P. Yu, and J.-P. Ansermet, Phys. Rev. Lett. **104**, 146601 (2010).

[18] A. Kubetzka, M. Bode, O. Pietzsch, and R. Wiesendanger, Phys. Rev. Lett. **88**, 057201 (2002).

[19] A. Wachowiak, J. Wiebe, M. Bode, O. Pietzsch, M. Morgenstern, and R. Wiesendanger, Science **298**, 577 (2002).

[20] M. Bode, S. Krause, L. Berbil-Bautista, S. Heinze, and R. Wiesendanger, Surf. Sci. **601**, 3308 (2007).

[21] D. Li, Y. Wu, P. Kim, L. Shi, P. Yang, and A. Majumdar, Appl. Phys. Lett. **83**, 2934 (2003).

[22] J. Tersoff and D. R. Hamann, Phys. Rev. Lett. **50**, 1998 (1983).

[23] R. C. Sousa, I. L. Prejbeanu, D. Stanescu, B. Rodmacq, O. Redon, B. Dieny, J. Wang, and P. P. Freitas, J. Appl. Phys. **95**, 6783 (2004).

[24] N. Néel, J. Kröger, and R. Berndt, Appl. Phys. Lett. **95**, 203103 (2009).

[25] J. C. Slonczewski and J. Z. Sun, J. Magn. Magn. Mater. **310**, 169 (2007).

[26] R. Wiesendanger, H. J. Güntherodt, G. Güntherodt, R. J. Gambino, and R. Ruf, Phys. Rev. Lett. **65**, 247 (1990).

[27] J. Hauschild, H. J. Elmers, and U. Gradmann, Phys. Rev. B **57**, R677 (1998).

3.4.2 Individual atomic-scale magnets interacting with spin-polarized field-emitted electrons

A. Schlenhoff, S. Krause, A. Sonntag, and R. Wiesendanger

Nonequilibrium hot-electron spins interacting with magnetic solids are at heart of numerous spin-electronic applications [1–3]. For example, they govern spin-dependent transport through spin-valve systems and magneto-tunnel junctions, resulting in the phenomena of giant [4] and tunneling magnetoresistance [5]. Moreover, several spin-polarized electron spectroscopy and magnetic imaging techniques are based on the use of hot-electron spins [6–8]. Time-resolved two-photon photoemission has provided first insight into the interaction of hot electrons with an underlying spin system by exciting electrons into image-potential states (IPS) located above the surface in vacuo, thereby creating electron-hole pairs that subsequently recombine [9,10]. However, this technique fails for a study of individual nanomagnets due to its low lateral resolution. Moreover, it is not clear how an atomic-scale spin system is affected by pumping its IPS with spin-polarized hot electrons from an external source. A very local investigation of IPS is realized by scanning tunneling microscopy in the field emission mode [11–13]. Here, the electric field applied between tip and sample transforms the IPS into field-emission resonance (FER) states [14]. Using a magnetic tip to generate spin-polarized emission, the magnetic vortex structure of a bulk-like Fe surface has been imaged via its spin-split FER states [15]. The question arises whether magnetic structures ultimately being only one atomic layer in height can be imaged as well and how they will be affected by spin-polarized field emission. A detailed understanding of the interplay of hot-electron spins with e.g. phonons, spin waves or electrons in a magnetic solid is essential for a precise interpretation of many hot electron spin phenomena and characterization techniques, as well as for spintronic devices and data storage technologies.

Here we show that the FER states of magnets consisting of only about 50 iron atoms on a W(110) surface already exhibit a significant spin-splitting that allows for resonant imaging. We find that a spin-polarized field-emission current resonantly injected into these nanomagnets generates considerable Joule heating and spin-transfer torque, thereby severely affecting the thermally driven magnetization reversal. The switching frequency is increased due to phonon generation, and a lifetime asymmetry develops with increasing emission current, most likely driven by Stoner excitations. Our experiments demonstrate the capability of field-emitted electrons for magnetic observation and controlled manipulation on the atomic scale at nm distances: As we show, even magnetization reversal of quasistable nanomagnets can be triggered by spin-polarized field-emission.

In Fig. 3.16(a), the basic idea of resonantly injecting field-emitted spin-polarized electrons into a magnet is shown. A magnetic tip is approached at nanometer distance,

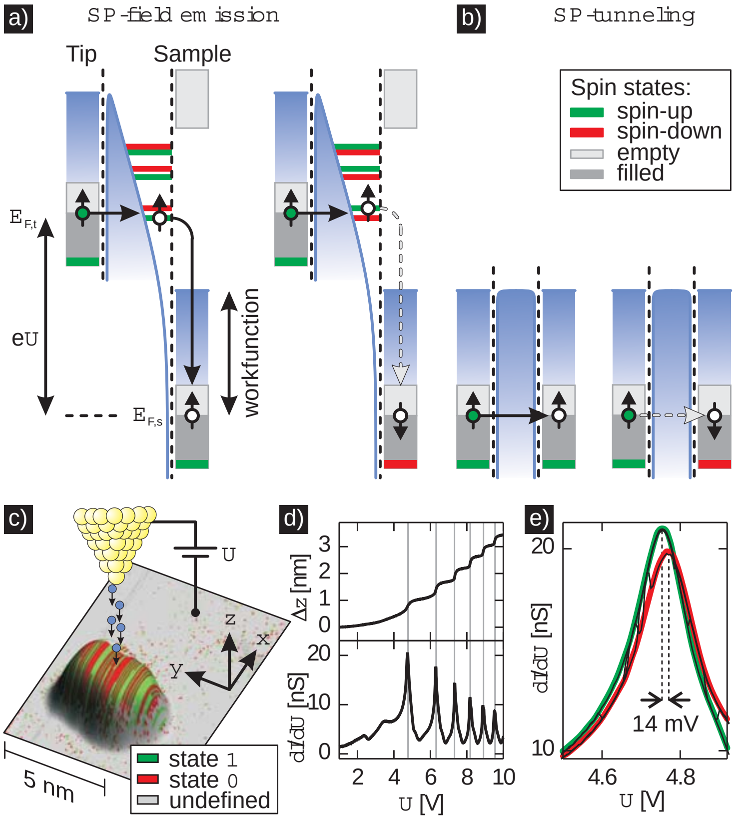

Figure 3.16: **Injecting spin-polarized field-emitted electrons into a nanomagnet** (**a**) Physical picture of resonantly injecting spin-polarized field-emitted electrons for parallel (left) or antiparallel (right) alignment of tip and sample magnetization. (**b**) Situation for conventional SP-STM. (**c**) Sketch of the experimental setup and topography of a Fe/W(110) nanomagnet, textured with a magnetic map. The nanomagnet frequently switches between two states (red and green). The fast scanning direction of the tip is along x. (**d**) $\Delta z(U)$ and $\mathrm{d}I/\mathrm{d}U$, revealing the first six field emission resonances. (**e**) First FER peak. It changes as the nanomagnet switches its magnetization. $I = 2\,\mathrm{nA}$, $T = 38.8\,\mathrm{K}$.

and an electric field is generated by applying a bias U. A series of unoccupied FER states evolves in the confinement given by the combined sample surface and vacuum potential [16, 17], and spin-polarized electrons may be injected resonantly from the tip into the region above the sample [18]. Subsequently, they penetrate into the sample by inelastically relaxing to its Fermi level $E_{\mathrm{F,s}}$. As the FER states are spin-split [19, 20], the overall emission conductance depends on the relative orientation between tip and sample magnetization, being high for the parallel configuration and low for the antiparallel one. In spin-polarized scanning field-emission microscopy (SP-SFEM), the tip moves above the surface at constant current I. Recording the site-dependent differential emission conductance allows for imaging the magnetization of a sample on a very local scale [15]. Using the same setup for spin-polarized scanning tunneling microscopy (SP-STM) allows for a comparative investigation of the sample with low-energy electrons tunneling directly from the tip into the sample, as shown schematically in Fig. 3.16(b).

Fe nanomagnets on a W(110) substrate are known to be monodomain particles with an uniaxial anisotropy lying in the surface plane. At a temperature of $T \approx 40\,\mathrm{K}$, they frequently invert the magnetic orientation due to thermal agitation [21]. By observing their switching behavior it has been demonstrated that these nanomagnets may serve as local thermometers and spin-transfer torque analyzers [22]. Hence, this sample system is well suited for a detailed investigation of the interaction between spin-polarized field-emitted electrons and atomic-scale magnets.

Our experiments were performed in an ultrahigh vacuum system equipped with a homebuilt SP-STM setup for variable temperatures. In order to minimize the thermal drift between tip and sample, the entire microscope including the tip is cooled. Antiferromagnetic Cr-coated W tips [23] and bulk Cr tips [24,25] were used being sensitive to the in-plane component of the sample magnetization. The differential conductance $\mathrm{d}I/\mathrm{d}U$ is measured by adding a small ac modulation voltage ($U_{\mathrm{mod}} = 40\,\mathrm{mV}$) to the sample bias and detecting the resulting modulation of the tunneling current I by a lock-in technique. The spatially resolved $\mathrm{d}I/\mathrm{d}U$ is recorded simultaneously with constant current topography images at closed feedback loop. These maps are correlated with the magnetization structure of the sample, since $\mathrm{d}I/\mathrm{d}U$ scales with the cosine of the enclosed angle between the tip and sample magnetization [26]. The preparation of the sample system is described in detail in Ref. [21].

In Fig. 3.16(c), an SP-STM magnetic map of an individual Fe nanomagnet on a clean W(110) substrate is shown. A stripe pattern is visible on the nanomagnet, reflecting its thermally induced magnetization switching between two states (**0** and **1**) when imaged line by line. In order to identify the FER states of the nanomagnet, the bias is ramped above its center between 1 and 10 V at a fixed current of 2 nA, thereby generating an electric field on the order of $10^9\,\mathrm{V/m}$. Recording both the tip-sample distance variation $\Delta z(U)$ and $\mathrm{d}I/\mathrm{d}U(U)$ reveals that the FER states give rise to a series of pronounced steps in Δz, and at each step a local maximum evolves in the $\mathrm{d}I/\mathrm{d}U$ channel [16,17], as can be seen in Fig. 3.16(d). For $U = 10\,\mathrm{V}$, the tip-sample distance – which is only several Å for $U = 1\,\mathrm{V}$ – is increased by more than 3 nm. Note that at this distance low bias tunneling experiments would be impossible since I decreases by about one order of magnitude per Å [26]. The first FER peak is shown in Fig. 3.16(e) in more detail. Several spectroscopy curves are taken, with each of them exhibiting sudden jumps. Plotting them on top of each other reveals that the jumps indicate switching events of the nanomagnet, with the FER peak slightly changing in terms of position and height. This finding indicates a significant overlap of two spin-split FER peaks that reflect the magnetization of the underlying nanomagnet. Consequently, for a fixed bias U both FER spin states are accessible for the respective spin-polarized field-emitted electrons. An effective splitting can be determined from the shifting of the peak position, resulting in about 14 meV, being comparable with previous studies on a bulk-like Fe particle [15]. Consequently, the FER state of atomic-scale magnets already exhibit a significant spin-splitting.

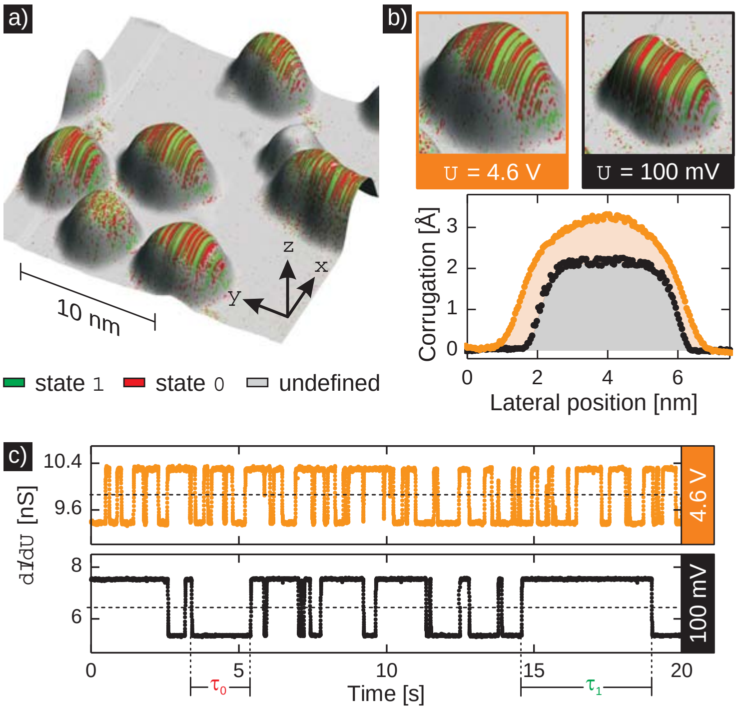

Figure 3.17: **Magnetic imaging using spin-polarized field emission** (**a**) SP-SFEM topography and magnetic map, recorded at $U = 4.6\,\mathrm{V}$. Characteristic stripe patterns evolve on the nanomagnets. The fast scanning direction is along x. (**b**) Zoom to one nanomagnet, imaged with spin-polarized field-emitted electrons (left) and conventional SP-STM (right). The topography line sections show an increase of apparent height and lateral dimension. $I = 2\,\mathrm{nA}$, $T = 38.8\,\mathrm{K}$. (**c**) Trace section of the magnetic telegraph noise recorded on the nanomagnet of b) using SP-SFEM (top) and SP-STM (bottom). $I = 2\,\mathrm{nA}$, $T = 39.4\,\mathrm{K}$.

By choosing U appropriately, the difference in the $\mathrm{d}I/\mathrm{d}U$ signal allows for magnetic imaging by SP-SFEM, as demonstrated in Fig. 3.17(a). An overview image is taken around the nanomagnet of Fig. 3.16(c) using spin-polarized field emission at $U = 4.6\,\mathrm{V}$. As can be seen from the magnetic map textured onto the topography, characteristic stripe patterns evolve on the nanomagnets, whereas the substrate shows no magnetic features. In Fig. 3.17(b), SP-SFEM and SP-STM images of the same nanomagnet are compared. The nanomagnet imaged by SP-SFEM is apparently enhanced in size, reflecting the smooth variation of the local electronic surface potential between the substrate and the nanomagnet.

Positioning the tip stationary above the nanomagnet and recording the magnetic $\mathrm{d}I/\mathrm{d}U$ signal as a function of time allows for the observation of its temporal magnetization evolution. In Fig. 3.17(c), two sections of the $\mathrm{d}I/\mathrm{d}U$ raw signal are shown, one recorded by SP-SFEM using field-emitted electrons, and one by conventional SP-STM using low-energy tunneling electrons. A characteristic telegraph noise is observed with both techniques. Although the tip-sample distance is considerably increased by about 1 nm in SP-SFEM, the differential conductance in field emission is enhanced compared to SP-STM. Moreover, Fig. 3.17(c) uncovers the switching frequency being clearly increased in SP-SFEM, indicating that field emission considerably affects the nanomagnet.

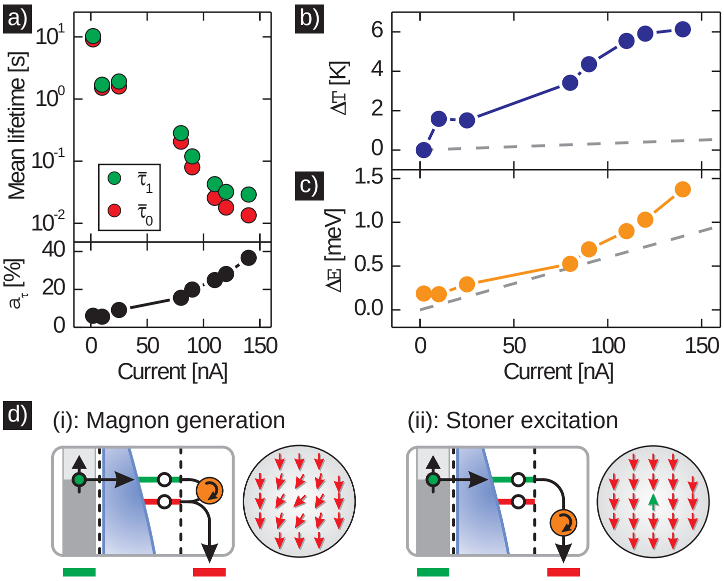

Figure 3.18: **Manipulation of the magnetic switching behavior using spin-polarized field-emitted electrons.** (**a**) Mean lifetimes as a function of current (top) and respective lifetime asymmetry (bottom). (**b**) Temperature increase $\Delta T(I)$ of the nanomagnet. (**c**) Modification $\Delta E(I)$ of E_b. For comparison, the results using low-energy tunneling electrons on the same nanomagnet are indicated by dashed lines. $U = 4.9\,..\,5.1\,\mathrm{V}$, $T = 35.4\,\mathrm{K}$. (**d**) Spin-flip of electrons: (i) within the FER spin states, generating magnons (ii) when relaxing from the FER spin state into the sample, resulting in Stoner excitations.

In order to get a more detailed understanding of the interaction of spin-polarized field-emitted electrons with magnets, we perform a current-dependent lifetime analysis based on the telegraphic signal on one particular nanomagnet between 2 nA and 140 nA. Increasing the current is realized by further approaching the tip to the sample. To compensate for the resulting Stark shift the bias voltage is slightly adjusted for a maximum magnetic contrast on the edge of the first FER peak at every current setpoint. Likewise in SP-STM experiments, the mean lifetimes $\bar{\tau}_0$ and $\bar{\tau}_1$ of the magnetic states **0** and **1** are determined [22]. The results of this analysis are shown in Fig. 3.18(a), revealing that the mean lifetime drops by about three orders of magnitude when increasing I from 2 nA to 140 nA. Obviously, this experimental observation indicates a considerable Joule heating by the field-emitted electrons. Additionally, an increasing lifetime asymmetry $a_\tau(I) = (\bar{\tau}_1 - \bar{\tau}_0)/(\bar{\tau}_1 + \bar{\tau}_0)$ of up to 40 % is observed with increasing current, meaning that one magnetic orientation of the nanomagnet is favored at the cost of the other. This purely magnetic feature is a direct experimental demonstration of spin-transfer torque generated by field emission. In analogy to investigations of the effects of spin-polarized tunnel currents on the switching behavior of nanomagnets [22], the mean lifetime $\bar{\tau}_{0/1}(I)$ affected by spin-polarized field emission is given by

$$\bar{\tau}_{0/1}(I) = \nu_0^{-1} \exp\left(\frac{E_\mathrm{b} \pm \Delta E(I)}{k_\mathrm{B}(T + \Delta T(I))}\right),$$

with ν_0 being the attempt frequency, E_b is the effective activation energy barrier for reversal and k_B is the Boltzmann constant. The temperature T of the nanomagnet is increased by $\Delta T(I)$ due to Joule heating, and spin-transfer torque modifies E_b by $\pm\Delta E(I)$, depending on the relative orientation of tip and sample magnetization. From $\bar{\tau}_{0/1}(I)$, ΔT and ΔE are elaborated for each setpoint of I. The results for $\Delta T(I)$ are plotted in Fig. 3.18(b). For comparison, an SP-STM analysis using low-energy tunneling electrons at $U = 200\,\mathrm{mV}$ with the same tip on the same nanomagnet has been performed. The temperature of the nanomagnet increases by up to 6 K when affected by a field emission current of $I = 140\,\mathrm{nA}$, which is a factor of ten higher than for tunneling electrons. However, in terms of the total power injection $P = UI$, the differential temperature increase dT/dP is only $9\,\mathrm{K}/\mu\mathrm{W}$ for SP-SFEM, but $17\,\mathrm{K}/\mu\mathrm{W}$ for SP-STM, indicating a less effective heating of the nanomagnet for field emission than for tunneling electrons. In contrast to low-energy tunneling electrons, an electron in a FER may relax in various ways: While electron-photon and electron-phonon coupling is weak, electron-electron interaction is the dominating mechanism [27–29], thereby generating hot electrons in the nanomagnet that finally will thermalize. Our experiments indicate that this thermalization takes place in the substrate rather than in the nanomagnet. Consequently, the overall phonon generation *within* the nanomagnet is weaker in SP-SFEM than in SP-STM.

In Fig. 3.18(c), the spin-transfer torque contribution $\Delta E(I)$ is shown. It scales linearly for tunneling electrons [22, 30], but exhibits an overproportionality for field emission, indicating an enhancement of the spin-transfer torque per electron with increasing I. To understand this finding, note that the microscopic processes of the observed spin-transfer torque in field emission will differ from those for tunneling electrons, the latter predominantly creating magnons [31]. A two-step process is expected for field-emitted spin-polarized electrons, first being injected into the spin-split FER and subsequently relaxing into the sample. In a simple model, assuming a spin polarization of one, the electron has to flip its spin in order to relax into the sample when tip and sample are in the antiparallel magnetic configuration. This is accomplished by interacting with the sample, either (i) by relaxing within the FER spin states, thereby generating low-energy spin waves (magnons) [10], or (ii) when relaxing from the FER state into the sample, resulting in higher-energetic single-site spin flips (Stoner excitations) [32], as shown in the schematics of Fig. 3.18(d). Both processes destabilize the sample magnetization and ultimately trigger reversal, resulting in a directed switching accompanied by a lifetime asymmetry. With increasing I the electric field pushes the FER states towards the surface, leading to an enhanced coupling of the FER to the magnet [14]. Consequently, we expect process (ii) to become more and more dominant. Since Stoner excitations have a much higher switching efficiency than low-energy magnons, we speculate that these excitations give rise to the observed increase of spin-transfer torque switching effiency with I. A detailed theory of spin-transfer torque generated by spin-polarized field emission via FER could provide deeper insight.

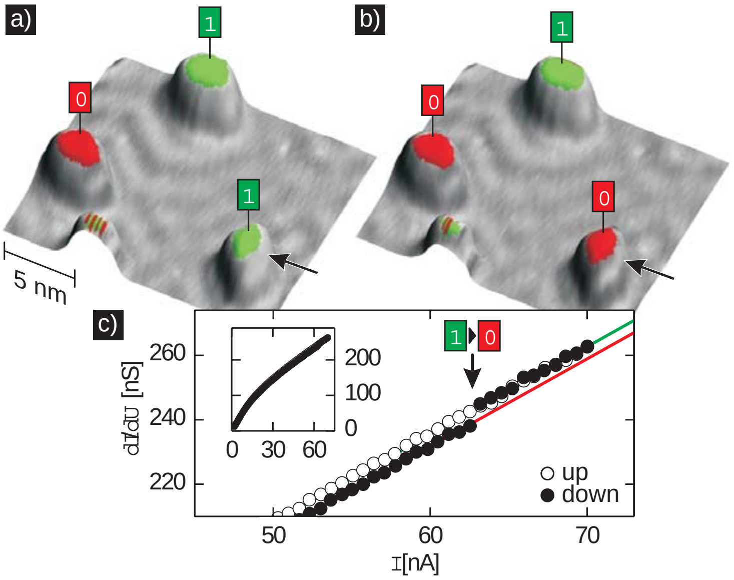

Figure 3.19: **Magnetization reversal triggered by field-emitted electrons.** SP-STM topography textured with the magnetic map of the sample (**a**) before and (**b**) after ramping a field-emission current on one individual nanomagnet (marked by arrow). $U = 0.1\,\mathrm{V}$, $I = 2\,\mathrm{nA}$. $T = 31.5\,\mathrm{K}$. (**c**) $\mathrm{d}I/\mathrm{d}U(I)$ signal while ramping I on the nanomagnet using field-emitted electrons. A jump is observed at $I = 63\,\mathrm{nA}$, indicating magnetization reversal. Red and green lines indicate the $\mathrm{d}I/\mathrm{d}U$ signal for state **0** and **1**, respectively. $U = 5\,\mathrm{V}$.

The high impact of field-emitted electrons onto the switching behavior of nanomagnets raises the question whether even magnetization reversal of otherwise thermally stable nanomagnets can be triggered. In Fig. 3.19(a), an SP-STM magnetic image of four nanomagnets is shown, with three of them exhibiting a stable magnetization. The tip is positioned above a nanomagnet being in the magnetic state **1**, and the spin-polarized field emission current is ramped up and down at moderate values between 2 and 70 nA while simultaneously recording the magnetic $\mathrm{d}I/\mathrm{d}U$ signal. As can be seen in Fig. 3.19(c), $\mathrm{d}I/\mathrm{d}U$ increases with I, reflecting the enhancement of conductance when decreasing the tip-sample distance. The $\mathrm{d}I/\mathrm{d}U$ downward curve initially fits the upward curve, but a sudden decrease of $\mathrm{d}I/\mathrm{d}U$ is observed at $I \approx 63\,\mathrm{nA}$, causing a deviation from the upward curve. This behavior indicates a switching event of the nanomagnet. A subsequently taken SP-STM image on the same area is shown in Fig. 3.19(b), revealing that the nanomagnet in fact has switched to the magnetic state **0**, whereas the surrounding remained unchanged. From a long-term observation with low-energy tunneling electrons the intrinsic lifetime is found to be on the order of an hour. Consequently, spin-polarized field emission severely decreases the state lifetime of the nanomagnet, ultimately resulting in the magnetization becoming unstable and switching its orientation. Repeating this experiment several times reveals that the nanomagnet is switched reliably at a threshold of about 60 nA. This value is tiny compared to experiments using low-energy tunneling electrons on the same sample system, where typical threshold currents in the μA range are found [33].

In summary we show that spin-polarized field emission can strongly affect magnets on the very local scale in terms of spin-transfer torque and Joule heating. Our studies provide insight into the microscopic processes involved in field-emitted hot-electron spins interacting with magnets, opening the pathway towards new scientific and technological applications based on magnetic imaging and manipulation using spin-polarized field emission.

References

[1] S. S. P. Parkin, X. Jiang, C. Kaiser, A. Panchula, K. Roche, and M. Samant, Proc. IEEE **91**, 661 (2003).

[2] R. Jansen, J. Phys. D: Appl. Phys. **36**, R289 (2003).

[3] S. A. Wolf, D. D. Awschalom, R. A. Buhrman, J. M. Daughton, S. von Molnár, M. L. Roukes, A. Y. Chtchelkanova, and D. M. Treger, Science **294**, 1488 (2001).

[4] M. N. Baibich, J. M. Broto, A. Fert, F. Nguyen Van Dau, F. Petroff, P. Etienne, G. Creuzet, A. Friederich, and J. Chazelas, Phys. Rev. Lett. **61**, 2472 (1988).

[5] J. S. Moodera, L. R. Kinder, T. M. Wong, and R. Meservey, Phys. Rev. Lett. **74**, 3273 (1995).

[6] M. Plihal, D. L. Mills, and J. Kirschner, Phys. Rev. Lett. **82**, 2579 (1999).

[7] H. Pinkvos, H. Poppa, E. Bauer, and J. Hurst, Ultramicrosc. **47**, 339 (1992).

[8] W. H. Rippard and R. A. Buhrman, Appl. Phys. Lett. **75**, 1001 (1999).

[9] A. B. Schmidt, M. Pickel, M. Wiemhöfer, M. Donath, and M. Weinelt, Phys. Rev. Lett. **95**, 107402 (2005).

[10] A. B. Schmidt, M. Pickel, M. Donath, P. Buczek, A. Ernst, V. P. Zhukov, P. M. Echenique, L. M. Sandratskii, E. V. Chulkov, and M. Weinelt, Phys. Rev. Lett. **105**, 197401 (2010).

[11] P. Wahl, M. A. Schneider, L. Diekhöner, R. Vogelgesang, and K. Kern, Phys. Rev. Lett. **91**, 106802 (2003).

[12] K. Schouteden and C. Van Haesendonck, Phys. Rev. Lett. **103**, 266805 (2009).

[13] K. Schouteden and C. Van Haesendonck, Phys. Rev. Lett. **108**, 076806 (2012).

[14] S. Crampin, Phys. Rev. Lett. **95**, 046801 (2005).

[15] A. Kubetzka, M. Bode, and R. Wiesendanger, Appl. Phys. Lett. **91**, 012508 (2007).

[16] G. Binnig, K. H. Frank, H. Fuchs, N. Garcia, B. Reihl, H. Rohrer, F. Salvan, and A. R. Williams, Phys. Rev. Lett. **55**, 991 (1985).

[17] R. S. Becker, J. A. Golovchenko, and B. S. Swartzentruber, Phys. Rev. Lett. **55**, 987 (1985).

[18] K. H. Gundlach, Solid State Electron. **9**, 949 (1966).

[19] M. Nekovee, S. Crampin, and J. E. Inglesfield, Phys. Rev. Lett. **70**, 3099 (1993).

[20] A. Hanuschkin, D. Wortmann, and S. Blügel, Phys. Rev. B **76**, 165417 (2007).

[21] S. Krause, G. Herzog, T. Stapelfeldt, L. Berbil-Bautista, M. Bode, E. Y. Vedmedenko, and R. Wiesendanger, Phys. Rev. Lett. **103**, 127202 (2009).

[22] S. Krause, G. Herzog, A. Schlenhoff, A. Sonntag, and R. Wiesendanger, Phys. Rev. Lett. **107**, 186601 (2011).

[23] A. Kubetzka, M. Bode, O. Pietzsch, and R. Wiesendanger, Phys. Rev. Lett. **88**, 057201 (2002).

[24] S. Li Bassi, C. S. Casari, D. Cattaneo, F. Donati, S. Foglio, M. Passoni, C. E. Bottani, P. Biagioni, A. Brambilla, M. Finazzi, *et al.*, Appl. Phys. Lett. **91**, 173120 (2007).

[25] A. Schlenhoff, S. Krause, G. Herzog, and R. Wiesendanger, Appl. Phys. Lett. **97**, 083104 (2010).

[26] R. Wiesendanger, Rev. Mod. Phys. **81**, 1495 (2009).

[27] J. H. Coombs, J. K. Gimzewski, B. Reihl, J. K. Sass, and R. R. Schlitter, J. Microsc. **152**, 325 (1988).

[28] R. Berndt, J. K. Gimzewski, and R. R. Schlitter, Ultramicrosc. **42-44**, 335 (1992).

[29] P. M. Echenique, R. Berndt, E. V. Chulkov, T. Fauster, A. Goldmann, and U. Höfer, Surf. Sci. Rep. **52**, 219 (2004).

[30] Z. Li and S. Zhang, Phys. Rev. B **69**, 134416 (2004).

[31] T. Balashov, A. F. Takács, W. Wulfhekel, and J. Kirschner, Phys. Rev. Lett. **97**, 187201 (2006).

[32] J. Hong and D. L. Mills, Phys. Rev. B **62**, 5589 (2000).

[33] G. Herzog, S. Krause, and R. Wiesendanger, Appl. Phys. Lett. **96**, 102505 (2010).

3.4.3 Current-driven spin dynamics of artificially constructed quantum magnets

A.A. Khajetoorians, B. Baxevanis, C. Hübner, T. Schlenk, S. Krause, T.O. Wehling, S. Lounis, A. Lichtenstein, D. Pfannkuche, J. Wiebe, and R. Wiesendanger

For magnetic storage technology [1], where magnets represent bits of information [2, 3], effective manipulation of the magnetization without a magnetic field is of crucial importance. All-electrical manipulation offers technological advantages, such as highly localized bit control free of moving parts and compatibility with standard semiconductor technology [4, 5]. Integral to current-induced switching is the spin-transfer torque [4–6] (STT) effect where angular momentum transfer from a flux of incident spin-polarized electrons can exert "torque" on the magnetization, causing it to switch in a preferential direction [7]. STT can efficiently reverse the magnetization of magnetic layers [8, 9], drive domain walls [10] and vortices, and can be combined with giant magneto resistance technology to generate high-frequency electrical oscillators [11, 12]. The ultimate goal of such spin-based technologies would be the total electrical-control of an atomic "bit." Factors complicating the achievement of this goal include the presence of a substrate, which can dramatically modify both the magnetic anisotropy and the moment at the single atom level, [13] and spin quantization, which can play an enhanced role in the magnetization dynamics, for example via quantum tunneling [14].

For small magnets that are sufficiently decoupled from an electron bath, such as molecular magnets [15], STT can be ascribed to asymmetric spin pumping induced by spin-polarized transport electrons which favorably excite particular spin states, via transfer of angular momentum, over or through an anisotropy barrier [16, 17]. A generalized Anderson model taking into account the coupling of the electron baths to the quantum spin adequately describes the dynamics of such isolated spins [16–19]. For small magnets that are directly adsorbed on a metallic substrate where the moment strongly couples to the substrate conduction electrons [20, 21], it is still questionable whether such a model is applicable, and what the exact role is of the substrate conduction electrons on the spin dynamics of the magnet [22].

Utilizing spin-polarized scanning tunneling microscopy (SP-STM), we demonstrate it is possible to characterize the real-time current-driven dynamics of tailored magnets comprised of a few direct-exchange coupled Fe atoms on a metallic copper single crystal surface. STM topographs of single Fe atoms on the surface and subsequent assembly of a five-atom Fe magnet by tip-induced atomic manipulation are shown in Figs. 3.20(A) and (B) [23, 24]. Density functional theory (DFT) [24] revealed two stable geometric configurations, the "pyramid" (Fig. 3.20(C)) and "flat" (Fig. 3.20(D)) configuration, of such five-atom Fe magnets on the copper surface. The total magnetic moment of each configuration, including orbital contributions, is $m_J \approx 15.2\mu_\mathrm{B}$ and $\approx 14.74\mu_\mathrm{B}$,

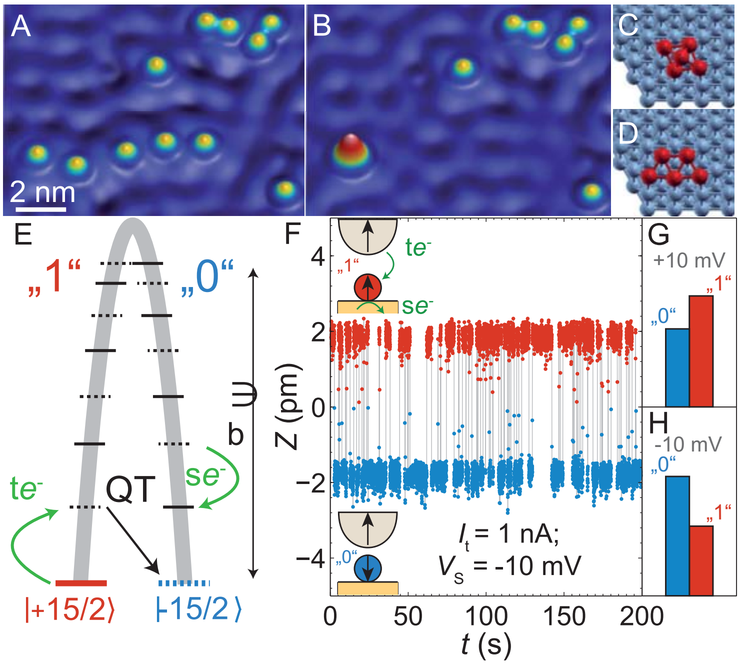

Figure 3.20: Constant-current STM images of single Fe atoms on the surface of Cu(111) (A) before and (B) after construction of a five-atom Fe magnet. V_s = -10mV, I_t = 0.6nA. (C and D) DFT calculations of the relaxed geometry of the two possible configurations (pyramid and flat respectively) of the five-atom Fe magnet (red spheres) on Cu(111) (blue spheres) constructed in (B). (E) Energy-dependent $|J_z\rangle$ states for a five-atom Fe magnet with total spin $J = 15/2$ and a magnetic anisotropy barrier of ϵ_b. The $\hat{J}_z$ states that have a finite overlap across the barrier are indicated by the same line (solid or dashed). The arrows indicate three of the many transitions mediated by non-equilibrium induced quantum tunneling (QT), as well as excitation and relaxation via tunneling electrons (te^-) and substrate electrons (se^-). (F) Spin-dependent telegraph signal in the tip height Z measured on a typical five-atom magnet where $\Delta Z \approx$ 4pm denotes switching between the two degenerate ground states “0” ($|\alpha_-\rangle$) and “1” ($|\alpha_+\rangle$) which are color-coded (blue/red) ($T = 0.3$K, $I_\mathrm{t} = 1$nA, $V_\mathrm{s} = -10$mV). (G and H) Voltage polarity-dependent histograms (y-scale from 0 to 1), at $B = 0$T, of the state-dependent lifetimes $\tau^\pm$ of $|\alpha_\pm\rangle$ illustrating favorability of the state “1”(“0”) for positive (negative) bias. The height of each bin represents the probability (%) of finding the labeled state at a given time.

respectively, which averages to $\approx 3\mu_\mathrm{B}$ per atom, close to the magnetic moment of a single Fe adatom ($\approx 3.5\mu_\mathrm{B}$) [20, 25]. The large total magnetic moment results from a strong ferromagnetic exchange coupling between the constituent Fe atoms to the total angular momentum [26]. We thus treat the magnet as a single total angular momentum, J [21], which is related to the total magnetic moment via $m_J = g\mu_B J$; we will refer to the total angular momentum as the spin for short. A considerable out-of-plane magnetic anisotropy [24] leads to a schematic level diagram of the spin states as shown in Fig. 3.20(E).

At modest current values using a magnetically coated tip which has out of plane spin-sensitivity [24], spin-based telegraph noise [27] can be read out on top of the assembled magnet in constant-current mode (Fig. 3.20(F)). It represents full reversal of the magnetization between two degenerate ground states, labeled $|\pm 15/2\rangle$ in Fig. 3.20(E), aligned parallel/antiparallel to the surface normal. We refer to these up/down states as "1" and "0". While all $\pm|J_\mathrm{z}|$ states contribute to the spin dynamics, the limited time resolution of our experiment allows us to resolve the signal from the magnet only in one of the two degenerate ground states, as they are the longest lived. Therefore, it is possible to extract the occupational lifetimes $\tau^{\pm}$ of the "1" and "0" states as well as the mean lifetime $\tau^* = (\tau^+ + \tau^-)/2$ from the measured spin noise, for a given tunneling current I_t, bias voltage V_s, out-of-plane magnetic field B, and temperature T [24]. The histogram of the two-state noise (Figs. 3.20(G)-(H)), at $B = 0$T, shows a considerable asymmetry in the state-resolved occupational lifetimes $\tau^{\pm}$, indicating a preferential state. This preferential state is reversed when the bias-polarity, and hence the spin-polarized current direction, is reversed. The polarity-dependent asymmetry in the state of the magnet, in the absence of a magnetic field, results from a considerable STT induced by the spin-polarized tunneling electrons.

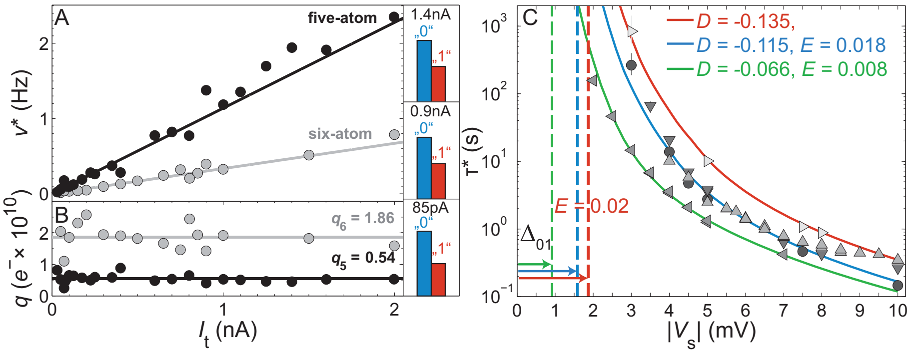

Figure 3.21: (A) Current-dependence of the mean switching frequency for five (black) and six (gray) atom Fe magnets (V_s = -10mV, T = 0.3K). Each data point represents an average value taken from 1-20 different magnets. All studied magnets of a particular size showed nearly identical values of ν^* at a given I_t. Solid lines: linear fits to the measured data. (B) Total number of tunneling electrons, $q = I_\mathrm{t} \times \tau^*$, extracted from (A), needed to switch a given magnet composed of the indicated number of atoms. Solid lines are fits to a constant q indicated in the figure. Right panels: Histograms (y-scale from 0 to 1) illustrating that the asymmetry in the two states "0" and "1" is independent of current (B = 0T). The height of each bin represents the probability (%) of finding the labeled state at a given time. (C) Bias voltage-dependence (V_s) of τ^* for selected five-atom magnets (symbols). Solid lines are model calculations for a quantum magnet having a spin of $J = 15/2$ and the indicated anisotropy values D and E in meV. The vertical dashed lines indicate the energy difference between the ground state and the first excited state Δ_{01} resulting from the model. (I_t = 3nA, T = 0.3K.)

The mean switching frequency ($\nu^* = 1/\tau^*$) has a linear dependence on I_t (Fig. 3.21(A)) indicating that the total number of tunneling electrons $q (= I_\mathrm{t} \times \tau^*)$

needed to reverse the magnetic state is independent of the current (Fig. 3.21(B)); for a five-atom magnet, $\approx 5 \times 10^9$ incident tunneling electrons are needed to reverse the magnetic state. Similar behavior is observed as the magnet size is increased from five to six atoms. The fact that q is independent of I_t is a hallmark of an inelastic spin excitation [17, 20, 21, 28, 29], where each tunneling electron has a fixed probability of exciting the spin eigenstates of the magnet [30]. Also the observed asymmetry between the state-dependent lifetimes ($\tau^\pm$) ($B = 0$), resulting from STT, is independent of the magnitude of I_t (Fig. 3.21(A) and (B), histograms). If Joule heating was important here, increasing I_t would reduce this asymmetry since heating would symmetrically reverse the magnetization, like seen for larger scale Fe islands [27]. Therefore, Joule heating can be ignored in the chosen range of both I_t and V_s in our experiment. This is most likely the result of the comparatively small bias voltage V_s utilized here which is too small to strongly couple the spin to phonons [31].

The dependence of the lifetime τ^* on the applied bias V_s shown in Fig. 3.21(C) for several selected five-atom magnets exhibits a stronger than exponential increase in τ^* as the energy of the tunneling electrons (eV_s) is lowered. Both current and voltage dependent studies of τ^* suggest that in the absence of current or for very small tunneling electron energy, these magnets remain stable for extremely long times. The exact current and energy dependence of τ^* depends intricately on the spin-dependent energy landscape of the magnet (Fig. 3.21(E)) which is determined by the magnetic anisotropy and the total spin of the system.

In order to quantify the dynamics and link the experimentally observed lifetimes to the magnetic properties of the system, we use the following quantum impurity model [24]. The spin eigenstates $|\alpha\rangle$ of the magnet in an out-of-plane magnetic field B are derived from a "giant spin" Hamiltonian $\hat{H}_\mathrm{spin} = g\mu_\mathrm{B}B\hat{J}_z + D\hat{J}_z^2 + E(\hat{J}_x^2 - \hat{J}_y^2)$ [15], where $\vec{\hat{J}} = \left(\hat{J}_x, \hat{J}_y, \hat{J}_z\right)$ is the vector spin operator of the magnet, g is the g-factor (assumed $g \approx 2$ [20]), and D and E are the axial and transverse magnetic anisotropy, respectively, which determine the preferential orientation of the spin. A master equation [24] characterizes the dynamics by considering all possible transition probabilities between the various spin eigenstates $|\alpha\rangle$ (Fig. 3.21(E)), induced by both sequential transitions over the anisotropy barrier (driven by spin-flip scattering of tunneling electrons (te^-) and substrate conduction electrons (se^-)), and by quantum tunneling (QT) through the anisotropy barrier.

Model calculations (Fig. 3.21(C)) show excellent agreement with the experimental data for magnetic anisotropy values of $D \approx$ -0.1meV and $E \approx$ 0.02meV, confirming the uniaxial out-of plane anisotropy with a weak in-plane anisotropy predicted by ab-initio methods [24]. Because E is small, $\hat{J}_z$ eigenstates are approximately the eigenstates of $\hat{H}_\mathrm{spin}$ (Fig. 3.21(E)). Interestingly, our model calculations show that $\tau^*(V)$ is very sensitive to small variations in the anisotropy as seen experimentally for different magnets. Moreover, as V_s is decreased, τ^* dramatically increases spanning three decades. This divergent behavior of τ^* is seen as the energy approaches the calculated first transition energy, Δ_{01} (Fig. 3.21(C), dashed lines), for a given magnet.

No switching was observed below $|V_s| < 2$mV for currents $I_t \leq 3$nA up to maximum observation times of 2 hours.

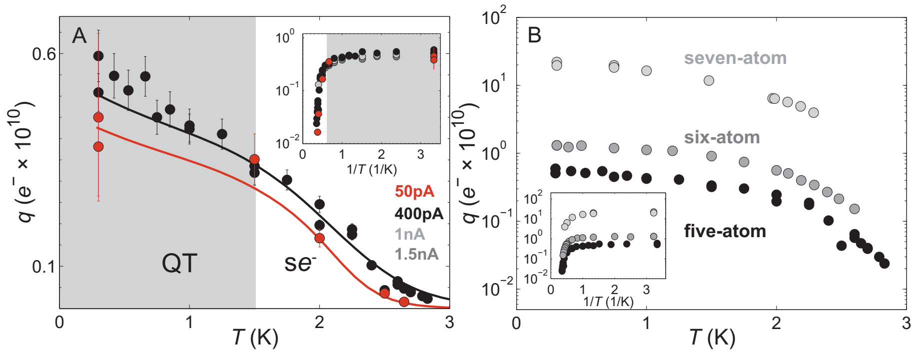

Figure 3.22: (A) Temperature dependence of the charge needed to reverse a five-atom magnet for various I_t as listed. Solid lines indicate the model calculations for a quantum magnet of spin $J = 15/2$ with the anisotropy values $D = -0.09$meV and $E = 0.02$meV. The indicated regions illustrate the temperature-range where QT and se^- driven transitions are important. (B) Magnet size dependency of $q(T)$ for five ($I_t = 0.4$nA), six ($I_t = 2.5$nA), and seven ($I_t = 26$nA) atom Fe magnets. (V_s = -10mV, B = 0T). (insets for A and B): q plotted logarithmically as a function of $1/T$.

To further investigate the role of QT and spin-flip scattering of (te^-) and (se^-) on the dynamics of the magnet, we vary the temperature. To remove the current dependency, the switching charge $q(T)$ is plotted rather than the lifetime in Fig. 3.22. The required charge q to switch a five-atom magnet decreases as the temperature increases reflecting the decrease of $\tau^*(T)$ (Fig. 3.22(A)). The slope is rather small for the low temperature range $T \leq 1.5$K, but q falls off more strongly for $T \geq 1.5$K, resulting in a shoulder in $q(T)$ at $T \approx 1.5$K. For $T \geq 2$K, an exponential tail indicates Arrhenius behavior, similar to what was observed for larger scale Fe islands [27]. The Arrhenius behavior for $T \geq 2$K is evident from the log plot in Fig. 3.22(A) (inset), whereas a plateau-like regime appears for $T \leq 1.5$K. Such plateaus have been attributed to QT of the magnetization through the anisotropy barrier [19]; our results however show a clear deviation from a constant transition rate in the low temperature regime indicating that QT alone cannot account for the observed temperature dependence of τ^*.

In order to link the temperature dependence of $q(T)$ to the different spin transition processes, we used the quantum impurity model with the D and E values extracted from the fits in Fig. 3.21(C), and fit the T dependence of q for different I_t [24] (solid lines in Fig. 3.22(A)), yielding good agreement with experiment. Upon closer inspection, the model reveals that this temperature dependence results from the following two spin transition mechanisms which contribute to the switching of the magnet in addition to te^- driven sequential transitions: (i) sequential transitions of the magnet induced by spin-flip scattering of thermally excited substrate electron-hole pairs generated by the broadening of the Fermi function. This process, which is analogous to "damping" [32], dominates at higher temperatures. (ii) Non-equilibrium QT resulting from transverse anisotropy ($E \neq 0$). Note that the equilibrium QT, which fully reverses the magnetic state from one ground state to the other, without any additional spin-flip processes [14], is blocked because for a half-integer spin the states across the barrier which have the same $|J_z|$ have zero overlap. However, in non-equilibrium, a two-step process where a te^- or se^- electron changes J_z can lead to QT because there is a finite overlap of states across the barrier for particular values of $\Delta J_z \neq 0$ since $E \neq 0$ (Fig. 3.20(E)). Note that the most significant QT channels responsible for reversal are closer to the top of the barrier, since the energy barrier is smaller for these states than for states near the bottom of the barrier. Therefore, QT processes are mainly preceded by sequential spin transitions which drive the system into higher excited states, resulting in a weak temperature dependence of the whole QT process. The temperature-dependent interplay between the two transition effects (i) and (ii) leads to a shoulder in $q(T)$; at higher temperature, the well known Arrhenius behavior is recovered. Moreover, the shape of the shoulder depends on the size of the transverse anisotropy E [24]. Thus, the shoulder serves as a delineation of the temperature range where QT plays a prominent role in the magnetization dynamics. Therefore, the underlying mechanism of how the magnetization is fully reversed can be understood within the quantum impurity model when accounting for both substrate conduction electrons and non-equilibrium induced QT.

We explored the effects of an external out-of-plane magnetic field B on the observed dynamics. With increasing B, the asymmetry in the spin noise increases, i.e. the lifetime τ^+ of one of the ground states $|\alpha_+\rangle$ becomes larger at the expense of the lifetime τ^- of the other ground state $|\alpha_-\rangle$ (Fig. 3.23(A) and (B)). This is a result of the Zeeman energy, $\epsilon_{\mathrm{Zeeman}} = g\mu_{\mathrm{B}} B \hat{J}_z$, favoring the ground state of the magnet which has a magnetization pointing parallel to B; τ^+ (τ^-) indeed shows a monotonic increase (decrease) with increasing B. Unexpectedly, the balance $\tau^+ = \tau^-$ occurs at a nonzero magnetic field, $|B_{\mathrm{STT}}| \approx 0.1\mathrm{T}$. The reason for this observed asymmetry, at $B = 0\mathrm{T}$, is a result of the spin-polarization of the tunneling current created by the magnetic tip. The spin-polarized current favors te^- sequential transitions over the barrier in one particular direction as opposed to the other [17], analogous to STT. As a proof of the STT effect, we reversed the direction of I_{t} by changing the bias polarity, resulting in the expected sign change of B_{STT} (Fig. 3.23(B)).

The observed asymmetry between the lifetimes $\tau^+(B)$ and $\tau^-(B)$ can be further quantified by the non-equilibrium magnetization $M(B) = (\tau^+(B) - \tau^-(B))/(\tau^+(B) + \tau^-(B))$ (Fig. 3.23(C)), which saturates toward ±1 at a comparatively large magnetic field $B > 0.5\mathrm{T}$ for the five-atom magnet. $M(B)$ calculated from the quantum impurity model assuming the anisotropy values extracted from the voltage-dependent τ^* (Fig. 3.21(C)) is in good agreement with experiment for both bias polarities. The spin-polarization of the tip, assumed to be about 10% in the calculation, accounts for the observed polarity-dependent STT effect, B_{STT}, of the non-equilibrium magnetization

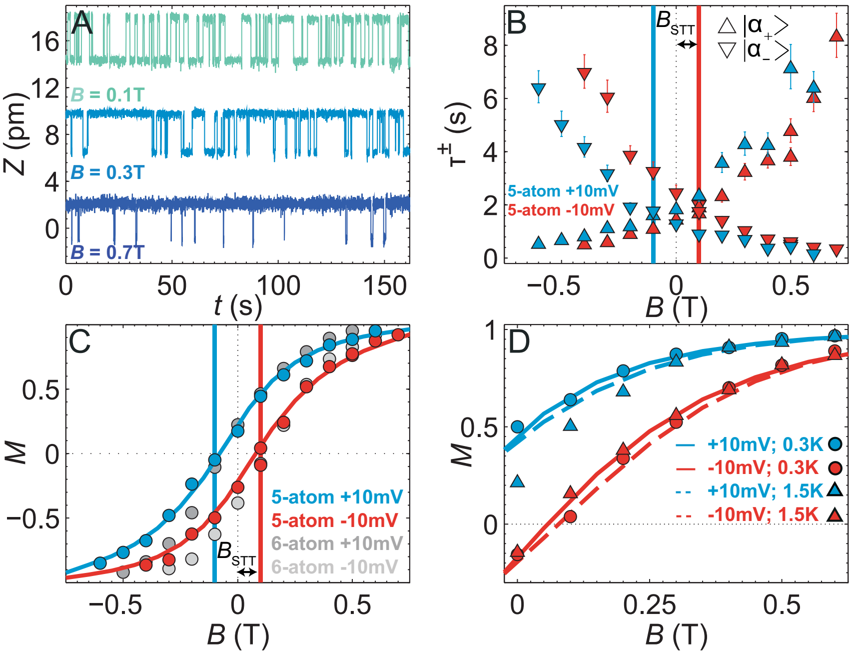

Figure 3.23: (A) Evolution of the spin-dependent telegraph-noise in increasing magnetic field for a five-atom magnet. ($V_\mathrm{s} = -10\mathrm{mV}$, $I_\mathrm{t} = 1\mathrm{nA}$, $T = 0.3\mathrm{K}$). (B) State-resolved lifetime ($\tau^{\pm}$) of a five atom magnet for negative and positive bias polarity in red and blue, respectively, at V_s as indicated. The vertical lines and arrow indicate the strength of the magnetic field, B_STT, needed to compensate the spin-transfer torque effect. (C) Non-equilibrium magnetization curve $M(B)$ of five and six atom magnets for negative and positive bias polarity, as indicated. (D) Temperature dependence of $M(B)$ for both positive and negative bias polarities. Solid and dashed lines in (C and D) indicate calculations from the quantum impurity model with a spin $J = 15/2$ using the anisotropy values $D = -0.09\mathrm{meV}$ and $E = 0.02\mathrm{meV}$ and assuming a tip spin polarization of 10%.

curve. The nonzero transverse anisotropy is responsible for the large magnetic field needed to saturate the magnetization as compared to the single Fe atom limit [20]. The presence of finite E in combination with a large spin (J) leads to a lineshape of $M(B)$ which is nearly independent of T for temperatures below the Arrhenius regime Fig. 3.23(D), in contrast to atoms which have no significant transverse anisotropy [13].

The observed STT behavior persists for larger magnets with the overall saturation field dropping as a result of the increased total spin as manifested by the sharper lineshape in $M(B)$ Fig. 3.23(C). As the size of the magnet increases, similar behavior is seen in $q(I_\mathrm{t})$ but the overall value of q needed to reverse the larger magnet increases (Fig. 3.21(A) and (B)). The general shape of $q(T)$ (Fig. 3.22(B)) persists for larger magnets, proving that the underlying mechanisms that govern the dynamics remain the same. Whereas D and E change as the size of the magnet increases, thus affecting $\tau^*(I_\mathrm{t}, V_\mathrm{s})$, the strong increase in q needed to switch the magnet, as the magnet gets larger, is most likely a consequence of the increased spin of the magnet. Increasing the spin results in an increased number of sequential transitions needed to reverse the magnetization requiring a higher total charge to reverse the magnetic state.

Although the relaxation of the magnets studied here is far from purely quantum, namely the quantum phase is destroyed, it is surprising that for such a strongly hybridized spin coupled to an electron bath, quantum effects are indeed necessary to fully describe the dynamics of the system. The strength of the STT studied here is determined solely by the total spin polarization of the tip independent of the total current [24]. This can be seen in the nearly constant asymmetry in Fig. 3.21(A) and (B), regardless of the mean switching frequency ν^* illustrating the quantum nature of STT in atomic scale magnets [16]. Our work brings to light fundamental processes which are of interest for future magnetic memory devices which are scaled to atomic dimensions.

References

[1] J. Åkerman, Science **308**, 508 (2005).

[2] M.N. Baibich, *et al.*, Phys. Rev. Lett. **61**, 2472 (1988).

[3] B. Dieny, *et al.*, Phys. Rev. B **43**, 1297 (1991).

[4] J. Slonczewski, J. Magn. Magn. Mater. **159**, L1 (1996).

[5] L. Berger, Phys. Rev. B **54**, 9353 (1996).

[6] D. Ralph and M. Stiles, J. Magn. Magn. Mater. **320**, 1190 (2008).

[7] A. Brataas, A. D. Kent, H. Ohno, *Nature Mat.* **11**, 372 (2012).

[8] M. Tsoi, *et al.*, Phys. Rev. Lett. **80**, 4281 (1998).

[9] E. B. Myers, D. C. Ralph, J. A. Katine, R. N. Louie, and R. A. Buhrman, Science **285**, 867 (1999).

[10] S. S. P. Parkin, M. Hayashi, L. Thomas, Science **320**, 190 (2008).

[11] M. Tsoi, *et al.*, Nature **406**, 46 (2000).

[12] S. I. Kiselev, *et al.*, Nature **425**, 380 (2003).

[13] F. Meier, L. Zhou, J. Wiebe, R. Wiesendanger, Science **320**, 82 (2008).

[14] W. Wernsdorfer, R. Sessoli, Science **284**, 133 (1999).

[15] D. Gatteschi, R. Sessoli, Molecular nanomagnets (Oxford Uni. Press, Oxford, ed. 1, 2006)

[16] F. Delgado, J. J. Palacios, J. Fernández-Rossier, Phys. Rev. Lett. **104**, 026601 (2010).

[17] S. Loth, *et al.*, Nature Phys. **6**, 340 (2010).

[18] M. Misiorny, J. Barnaś, Phys. Rev. B **76**, 054448 (2007).

[19] S. Loth, S. Baumann, C. P. Lutz, D. M. Eigler, A. J. Heinrich, Science **335**, 196 (2012).

[20] A. A. Khajetoorians, *et al.*, Phys. Rev. Lett. **106**, 037205 (2011).

[21] T. Schuh, *et al.*, Phys. Rev. B **84**, 104401 (2011).

[22] D. L. Mills, P. Lederer, Phys. Rev. **160**, 590-599 (1967).

[23] D. M. Eigler, E. K. Schweizer, Nature **344**, 524 (1990).

[24] Materials and methods are available as supporting material on Science Online.

[25] A. A. Khajetoorians, *et al.*, Nature Phys. **8**, 497 (2012).

[26] A. Bergman, L. Nordström, A. Burlamaqui Klautau, S. Frota-Pessôa, O. Eriksson, Phys. Rev. B **75**, 224425 (2007).

[27] S. Krause, L. Berbil-Bautista, G. Herzog, M. Bode, R. Wiesendanger, Science **317**, 1537 (2007).

[28] C. F. Hirjibehedin, C. P. Lutz, A. J. Heinrich, Science **312**, 1021 (2006).

[29] J. Fransson, Nano. Lett. **9**, 2414 (2009).

[30] N. Lorente, J.-P. Gauyacq, Phys. Rev. Lett. **103**, 176601 (2009).

[31] H. Gawronski, M. Mehlhorn, K. Morgenstern, Science **319**, 930 (2008).

[32] T. Gilbert, IEEE T. Magn. **40**, 3443 (2004).

3.4.4 Electric-field-induced magnetic anisotropy in a nanomagnet investigated on the atomic scale

A. Sonntag, J. Hermenau, A. Schlenhoff, J. Friedlein, S. Krause, and R. Wiesendanger

Manipulating magnetic properties with an electric field is in the focus of ongoing extensive research in the field of spintronics [1–9]. Especially, tuning the magnetic anisotropy by an electric field is a promising candidate to solve the fundamental dilemma in data storage applications: Whereas a large anisotropy is needed to stabilize a magnetic bit against thermal agitation, a low anisotropy is desired during magnetization reversal when writing information. An electric field can maximize or momentarily decrease the magnetic anisotropy [10–12], thereby stabilizing a magnetic bit for long-term storage or facilitating magnetization reversal when writing information. As virtually no current is needed for this electric-field based scheme, such devices could benefit from smaller power consumption compared to conventional magnetic field or spin-transfer torque based devices.

Experiments on semiconductors [1, 2, 5], multiferroic materials [3, 6] or metals [4, 7, 13, 14] demonstrated that an electric field can modify the magnetic properties via magnetoelectric coupling. Here, metallic systems have received considerable attention due to the potential easy integration into spintronic devices. However, in metals the electric field is screened by free electrons and thus cannot penetrate the bulk. Therefore electric-field induced modifications of the magnetic properties can only be expected at the surface and in thin-film systems. To our knowledge all studies to date were performed on layered extended thin films where the electric field is applied across an insulating layer of electrolyte or dielectric material [4, 7, 13, 14]. The preparation of these systems is challenging, since imperfections like local inhomogeneities and defects can complicate the correct interpretation of the experiments. In our studies using spin-polarized scanning tunneling microscopy (SP-STM) we realize a well-defined, atomically sharp magnet-to-vacuum interface and address single, defect-free magnets on the atomic scale for electric field induced manipulation of their magnetic properties.

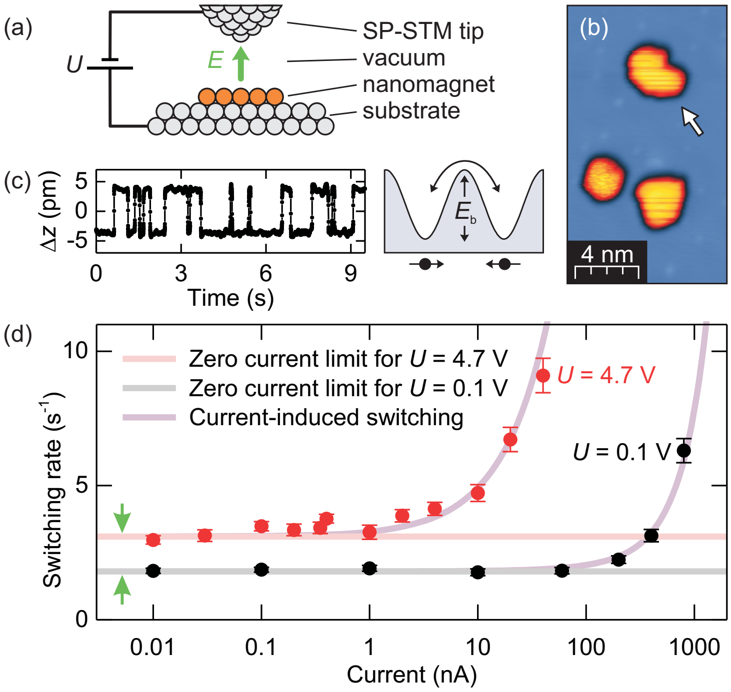

Figure 3.24: (**a**) Scheme of the experimental setup. (**b**) Spin-polarized STM topography taken at $U = -100\,\mathrm{mV}$, $I = 2\,\mathrm{nA}$, $T = 45\,\mathrm{K}$. (**c**) Telegraph signal observed when the tip is positioned above the island marked in (b) and scheme for thermal magnetization reversal. (**d**) Switching rate of the island as a function of tunnel current for two different bias voltages (lines are guides to the eye).

Fig. 3.24(a) illustrates our experimental approach: A ferromagnetic nanoisland consisting of only a few atoms is placed on a metallic substrate, and an electric field is applied by approaching a biased scanning probe tip. In this setup the magnetoelectric coupling is maximized by reducing the thickness of the nanomagnet to a single atomic layer.

Our experiments were performed under ultra-high vacuum conditions with a pressure below $1 \cdot 10^{-8}\,\mathrm{Pa}$ using a home-built variable temperature SP-STM. In the microscope, both the tip and the sample are cooled by a continuous flow He cryostat. Tungsten and molybdenum substrates were prepared by annealing in oxygen atmosphere and subsequent high temperature flashes [15].

Depositing iron onto these substrates leads to the pseudomorphic formation of atomic-scale monolayer nanoislands that are found to be ferromagnetic at cryogenic temperatures. When prepared on W(110) they exhibit an in-plane uniaxial magnetic anisotropy with the easy axis of magnetization lying in the $[1\bar{1}0]$ direction [16, 17]. In contrast, when prepared on Mo(110), the easy axis is pointing out of the surface plane [18].

Figure 3.24(b) shows an SP-STM topography map of three Fe nanomagnets on a W(110) substrate, taken with an in-plane sensitive bulk Cr tip. The nanomagnets consist of about 100 to 150 atoms and frequently switch their magnetic orientation due to thermal agitation at the given temperature of 45 K. In SP-STM, the tunnel current I is proportional to the projection of the magnetization of the tip onto the magnetization of the sample. As the measurements are performed in constant current mode the distance between tip and sample z has to be adjusted whenever the nanomagnet reverses its magnetization. Therefore a telegraphic noise pattern emerges in z, as can be seen in Fig. 3.24(c). Consequently, the magnetic orientation of the nanomagnet can be recorded in real time, and the switching rate ν can be derived.

As has been shown before, ν can be described by a Néel-Brown law [18–22]:

$$\nu = \nu_0 \exp\left(-\frac{E_\mathrm{b}}{k_\mathrm{B}T}\right). \tag{3.7}$$

Here, $k_\mathrm{B}T$ is the thermal energy, E_b the energy barrier that has to be overcome during magnetization reversal and ν_0 the attempt frequency.

The switching rate of an individual island was analyzed as a function of tunnel current I for two different bias voltages U, as can be seen in Fig. 3.24(d). More than 1000 switching events were recorded and evaluated for every data point. In agreement with previous studies, Joule heating strongly increases the switching rate when large currents are applied [23–25]. For low currents of $I \leq 1\,\mathrm{nA}$ we observe a constant switching rate as Joule heating is negligible in this regime. Although we expect to find the intrinsic switching rate for a vanishing tunnel current, irrespective of the bias voltage, the zero current limit of the switching rate at $U = 0.1\,\mathrm{V}$ clearly deviates from that at $U = 4.7\,\mathrm{V}$. This indicates that an additional, current independent effect modifies the switching behavior of the nanomagnet.

In Fig. 3.25(a), the telegraphic noise on another Fe/W(110) nanomagnet is shown for three different bias voltages at a very low tunnel current of 100 pA. Compared to the time trace recorded at 50 mV, the switching rate is again increased for a high positive bias voltage. Surprisingly the switching rate seems to be decreased when a high negative bias voltage is applied. The switching rate as a function of bias voltage is shown in Fig. 3.25(b). A clear trend from low switching rate at negative bias to high switching rate at positive bias is visible, ν being tunable by a factor of almost four between -5 and +5 V. The effect is volatile meaning that as soon as the bias voltage is reduced to almost zero, the switching rate of the island takes the intrinsic value.

The question arises how a change of the bias voltage can induce a change in the switching behavior of the nanomagnet. When changing U the tip-to-sample distance has to be adjusted in order to keep the tunnel current constant. However, when changing the bias voltage by two orders of magnitude the distance is only varied by

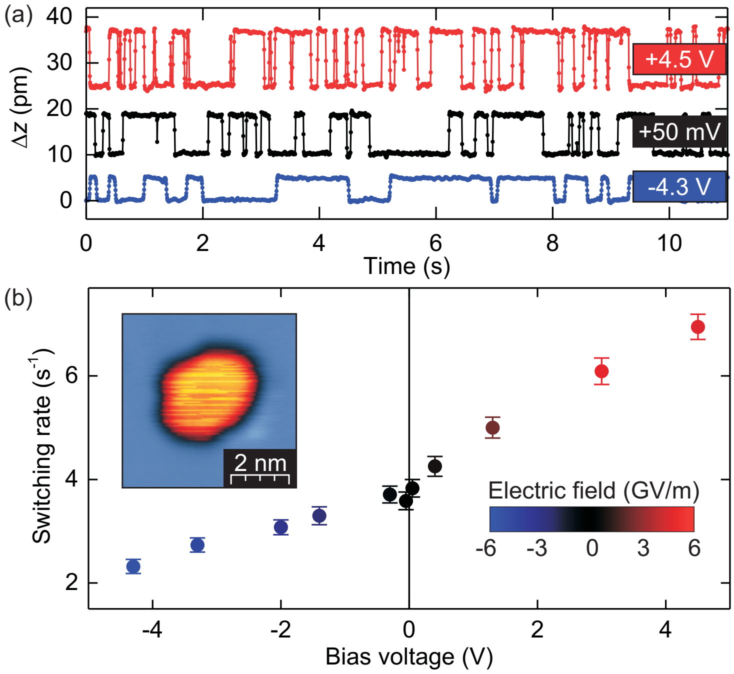

Figure 3.25: (**a**) Time traces recorded at different bias voltages. Curves were offset for clarity. (**b**) Switching rate as a function of applied bias voltage. Data points are color coded with the electric field between tip and sample. All measurements were performed at $I = 100\,\text{pA}$, $T = 45\,\text{K}$. The inset shows the topography of the investigated island.

a factor of 3. Consequently, the electric field increases significantly with increasing bias voltage. Therefore we attribute the observed modification of ν with U to the coupling of the nanomagnet to the electric field E. Values of E are derived from $z(U)$ measurements, resulting in a maximum of $E = \pm 6\,\text{GV/m}$ at $U = \pm 5\,\text{V}$. The electric field is used as a color coding in Fig. 3.25(b), indicating the direct relation between switching rate and the electric field strength.

In a simple picture the electric field causes a charge redistribution at the surface of the nanomagnet. Positive fields lead to a depletion and negative fields to an accumulation of electrons. This in turn leads to a shift of the Fermi level and a modification of the occupation of the 3d bands which are responsible for magnetism [7]. Recently, a generalized perturbation approach showed that a positive electric field can induce out-of-plane magnetic anisotropy due to Rashba spin-orbit coupling [26]. A more detailed understanding of the coupling mechanism can be achieved by first principle calculations. These have been performed for example on free standing Fe films [10] or Fe/MgO and MgO/Fe/MgO structures [27], revealing that the strength, sign and polarity symmetry of the effect can vary strongly from system to system.

In our experiment the electric field obviously modifies the energy barrier that has to be overcome during magnetization reversal. For $E < 0$ the switching rate is decreased,

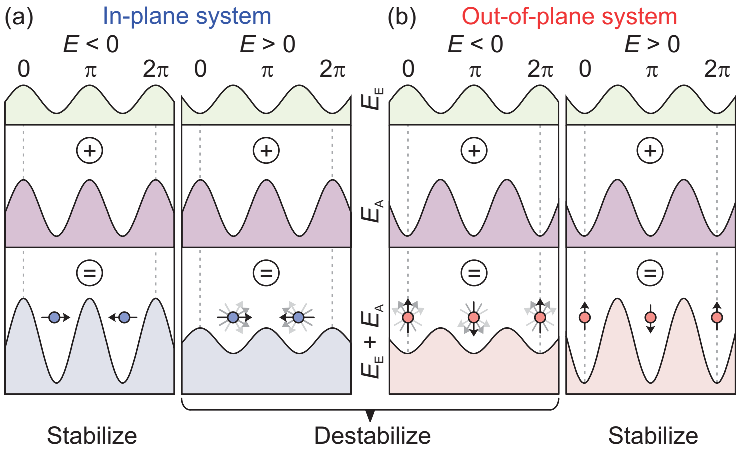

Figure 3.26: Schematics of the anisotropy energy as a function of the polar angle θ of a magnetic system under the influence of an electric field. The top row shows the energy contribution from the electric field E_E, the second row the undisturbed system E_A, and the third row the effective energy given by the sum of E_E and E_A. The electric field either favors in-plane ($E < 0$) or out-of-plane ($E > 0$) orientation of the magnetization. While the coupling mechanism is exactly the same for the in-plane (**a**) and out-of-plane system (**b**), the impact on the switching behavior is reversed: e.g. for $E < 0$ the in-plane system is stabilized, whereas the out-of-plane system is destabilized.

indicating an increase of the energy barrier (see Eq. 3.7). Likewise the switching rate is increased for $E > 0$, corresponding to a decrease of E_b. We attribute the change of E_b to magnetic anisotropy induced by the electric field. In a simple model it superimposes the intrinsic anisotropy, as illustrated in Fig. 3.26(a). For $E < 0$, the magnetoelectric coupling favors in-plane magnetization, whereas for $E > 0$ an out-of-plane magnetization is preferred. This results in a stabilization or destabilization of the in-plane Fe/W(110) nanomagnet against thermal agitation, respectively.

Depositing the same iron nanomagnets onto a Mo(110) substrate results in a system with an easy axis of magnetization pointing out of the surface plane [18]. Since the lattice constant, chemical properties and thus the electronic structure of molybdenum are similar compared to tungsten, it is reasonable to assume that the mechanism of magneto-electric coupling is the same on Fe/W(110) and Fe/Mo(110). However, an inversion of the electric field induced modification of the switching behavior is expected when changing between the two systems: the out-of-plane system is destabilized for $E < 0$ and stabilized for $E > 0$, as illustrated in Fig. 3.26(b).

Results of SP-STM experiments to validate this phenomenological model are shown in Fig. 3.27. The same tip could be used for the out-of-plane system since bulk Cr tips are known to be sensitive to both in-plane and out-of-plane magnetization [28]. The inset in Fig. 3.27 shows the topography of a Fe/Mo(110) nanomagnet that reverses its magnetization at an intrinsic switching rate of $8\,\mathrm{s}^{-1}$ due to thermal agitation. Just like in the case of the in-plane system we measured the switching rate as a function of U at

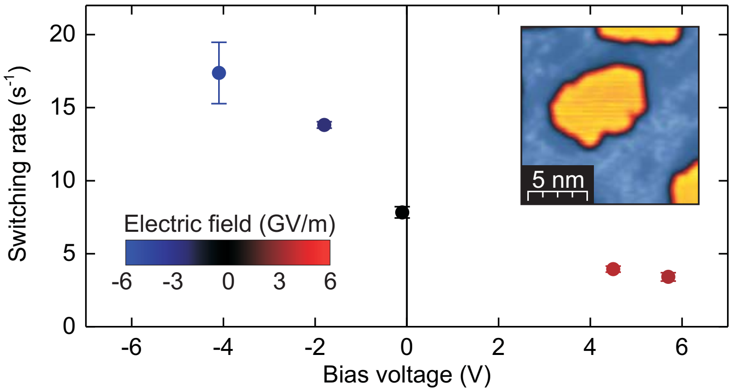

Figure 3.27: Switching rate as a function of applied bias voltage for the Fe/Mo(110) nanomagnet. Data points are color coded with the electric field strength. $I = 100\,\text{pA}$, $T = 26.5\,\text{K}$. The inset shows the topography of the island.

low I. The switching rate could be adjusted to be between 3 and $17\,\text{s}^{-1}$ by changing the bias voltage. We find a higher switching rate for $E < 0$ and a lower rate for $E > 0$. This is in contrast to the results on the in-plane Fe/W(110) nanomagnets and thereby in perfect agreement with our expectations. Hence we conclude that the coupling mechanism is analogous in this system and that the electric field indeed induces an additional magnetic anisotropy in the nanomagnet.

To quantify the strength of the magnetoelectric coupling we modify the energy barrier with an E-field dependent contribution: $E_\text{b} \to E_\text{b} + \Delta E_\text{b}(E)$. The energy barrier variation $\Delta E_\text{b}(E)$ can then be calculated from Eq. 3.7:

$$\Delta E_\text{b}(E) = k_\text{B} T \ln\left(\frac{\nu_\text{int}}{\nu(E)}\right), \tag{3.8}$$

where ν_int is the intrinsic switching rate at vanishing bias voltage.

A comparison of ΔE_b on Fe/W(110) and Fe/Mo(110) is shown in Fig. 3.28. We find energy barrier variations of up to $\Delta E_\text{b} = \pm 2\,\text{meV}$. This is a small change, compared to the intrinsic energy barrier of $E_\text{b} = 60\,\text{meV}$ for Fe/Mo(110) and $E_\text{b} = 125\,\text{meV}$ for Fe/W(110). Nevertheless the electric field significantly alters the switching behavior, as ν depends exponentially on ΔE_b. The strength of the effect is comparable to spin-transfer-torque (STT) at elevated tunneling currents observed on the same sample system ($\Delta E_\text{b,STT} = 1.5\,\text{meV}$ at $1000\,\text{nA}$) [24, 25]. Note that the STT generates a directed switching but does not change the magnetic anisotropy.

The out-of-plane Fe/Mo(110) islands switch their magnetization via a coherent rotation [18]. In this case $E_\text{b} = K \cdot V$ with the magnetic anisotropy K and the volume of the island V. We can calculate the change of the magnetic anisotropy $\Delta K(E)$ as a function of electric field:

$$\Delta K(E) = \Delta E_\text{b}(E)/V. \tag{3.9}$$

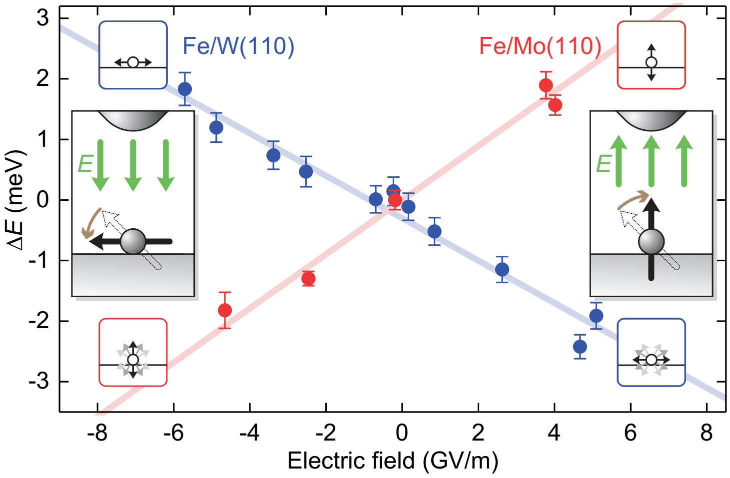

Figure 3.28: Electric field dependent energy barrier variation for an in-plane (Fe/W(110)) and an out-of plane (Fe/Mo(110)) system. Negative electric fields favor in-plane, positive electric fields out-of plane orientation of the magnetization.

Using this relation we find that the variation of anisotropy mounts up to 68 kJ/m^3. The intrinsic anisotropy was determined to be $K = 1100\,\mathrm{kJ/m^3}$ [18]. Consequently the anisotropy can be changed by 6% in our experiments. Conventionally the anisotropy variation is attributed to a change of the surface anisotropy ΔK_s, resulting in a change of $14\,\mu\mathrm{J/m^2}$.

To compare this value with studies on different systems we refer to an electric field of 1 GV/m. For this field we obtain $\Delta K_\mathrm{s} = 1.6\,\mu\mathrm{J/m^2}$. Significantly higher values ranging from 33 up to $93\,\mu\mathrm{J/m^2}$ have been reported in the literature [7, 13, 14]. However all of these experiments rely on the use of a dielectric material as an insulating barrier between the electrode and the magnetic film. This significantly increases the charge accumulation at the surface of the magnetic film compared to the case of a vacuum barrier [11]. Since the electron accumulation is the origin of the anisotropy change this explains the lower change of magnetic anisotropy in our experiments. To take the dielectric into account, it is reasonable to evaluate the strength of the effect in terms of a change of anisotropy per accumulated surface charge density $\sigma = \epsilon_0 \epsilon_\mathrm{r} E$. Here ϵ_0 is the electric constant and ϵ_r is the relative permittivity of the insulating layer. Referring to a surface charge density of $8.85\,\mathrm{mC/m^2}$ (which is the surface charge density at 1 GV/m in the case of a vacuum barrier), the published results project to values between 3.4 and $9.5\,\mu\mathrm{J/m^2}$ leading to a reasonable agreement with our finding of $1.6\,\mu\mathrm{J/m^2}$.

Our approach to investigate magnetoelectric coupling benefits from atomically well-defined interfaces. In thin film geometry interface roughness will create spots with a locally enhanced electric field and thus an inhomogeneous anisotropy. Additionally the interface composition and intermixing will play a crucial role for magnetoelectric coupling. It has been shown theoretically, that the magnetoelectric coupling is weak for an ideal MgO/Fe interface but can be strongly increased by the formation of an interfacial FeO layer [29]. In our experiments an ideal, atomically sharp surface to vacuum interface is realized.

In summary, we have investigated the influence of an electric field on the magnetic properties of magnets on the atomic scale using a spin-polarized scanning tunneling microscope. Using this setup we demonstrate magnetoelectric coupling across a vacuum barrier. We find that the electric field induces an uniaxial magnetic anisotropy energy, that favors in-plane magnetization for $E < 0$ and out-of-plane magnetization for $E > 0$. Consequently, negative (positive) electric fields stabilize (destabilize) in-plane magnets, whereas out-of-plane magnets are destabilized (stabilized). We have compared our results to investigations on extended thin films. Considering differences of the sample geometry, i.e. the usage of a dielectric material, we find a similar change of anisotropy in our measurements.

Our experimental technique permits to investigate the coupling between electric fields and magnetic properties down to the single atom level. The precisely defined interfaces will enable quantitative comparison with ab-initio theory and a better understanding of the underlying physical principles.

References

[1] H. Ohno, D. Chiba, F. Matsukura, T. Omiya, E. Abe, T. Dietl, Y. Ohno, and K. Ohtani, Nature **408**, 944 (2000).

[2] D. Chiba, M. Yamanouchi, F. Matsukura, and H. Ohno, Science **301**, 943 (2003).

[3] W. Eerenstein, N. D. Mathur, and J. F. Scott, Nature **442**, 759 (2006).

[4] M. Weisheit, S. Fähler, A. Marty, Y. Souche, C. Poinsignon, and D. Givord, Science **315**, 349 (2007).

[5] D. Chiba, M. Sawicki, Y. Nishitani, Y. Nakatani, F. Matsukura, and H. Ohno, Nature **455**, 515 (2008).

[6] Y.-H. Chu, L. W. Martin, M. B. Holcomb, M. Gajek, S.-J. Han, Q. He, N. Balke, C.-H. Yang, D. Lee, W. Hu, *et al.*, Nat. Mater. **7**, 478 (2008).

[7] T. Maruyama, Y. Shiota, T. Nozaki, K. Ohta, N. Toda, M. Mizuguchi, A. A. Tulapurkar, T. Shinjo, M. Shiraishi, S. Mizukami, *et al.*, Nat. Nanotechnol. **4**, 158 (2009).

[8] L. Gerhard, T. K. Yamada, T. Balashov, A. F. Takács, R. J. H. Wesselink, M. Däne, M. Fechner, S. Ostanin, A. Ernst, I. Mertig, *et al.*, Nat. Nanotechnol. **5**, 792 (2010).

[9] H. K. D. Kim, L. T. Schelhas, S. Keller, J. L. Hockel, S. H. Tolbert, and G. P. Carman, Nano Lett. **13**, 884 (2013).

[10] K. Nakamura, R. Shimabukuro, Y. Fujiwara, T. Akiyama, T. Ito, and A. J. Freeman, Phys. Rev. Lett. **102**, 187201 (2009).

[11] M. Tsujikawa and T. Oda, Phys. Rev. Lett. **102**, 247203 (2009).

[12] C.-G. Duan, J. P. Velev, R. F. Sabirianov, Z. Zhu, J. Chu, S. S. Jaswal, and E. Y. Tsymbal, Phys. Rev. Lett. **101**, 137201 (2008).

[13] M. Endo, S. Kanai, S. Ikeda, F. Matsukura, and H. Ohno, Appl. Phys. Lett. **96**, 212503 (2010).

[14] T. Nozaki, Y. Shiota, M. Shiraishi, T. Shinjo, and Y. Suzuki, Appl. Phys. Lett. **96** 022506 (2010).

[15] M. Bode, S. Krause, L. Berbil-Bautista, S. Heinze, and R. Wiesendanger, Surf. Sci. **601**, 3308 (2007).

[16] U. Gradmann, G. Liu, H. J. Elmers, and M. Przybylski, Hyperfine Interact. **57**, 1845 (1990).

[17] H. J. Elmers, J. Hauschild, H. Höche, U. Gradmann, H. Bethge, D. Heuer, and U. Köhler, Phys. Rev. Lett. **73**, 898 (1994).

[18] M. Bode, O. Pietzsch, A. Kubetzka, and R. Wiesendanger, Phys. Rev. Lett. **92**, 067201 (2004).

[19] M. L. Néel, Ann. Géophys. **5**, 99 (1949).

[20] W. F. Brown, Phys. Rev. **130**, 1677 (1963).

[21] W. Wernsdorfer, E. B. Orozco, K. Hasselbach, A. Benoit, B. Barbara, N. Demoncy, A. Loiseau, H. Pascard, and D. Mailly, Phys. Rev. Lett. **78**, 1791 (1997).

[22] S. Krause, G. Herzog, T. Stapelfeldt, L. Berbil-Bautista, M. Bode, E. Y. Vedmedenko, and R. Wiesendanger, Phys. Rev. Lett. **103**, 127202 (2009).

[23] A. Schlenhoff, S. Krause, A. Sonntag, and R. Wiesendanger, Phys. Rev. Lett. **109**, 097602 (2012).

[24] S. Krause, G. Herzog, A. Schlenhoff, A. Sonntag, and R. Wiesendanger, Phys. Rev. Lett. **107**, 186601 (2011).

[25] S. Krause, L. Berbil-Bautista, G. Herzog, M. Bode, and R. Wiesendanger, Science **317**, 1537 (2007).

[26] L. Xu and S. Zhang, J. Appl. Phys. **111**, 07C501 (2012).

[27] R. Shimabukuro, K. Nakamura, T. Akiyama, and T. Ito, Physica E **42**, 1014 (2010).

[28] A. Schlenhoff, S. Krause, G. Herzog, and R. Wiesendanger, Appl. Phys. Lett. **97** (2010).

[29] K. Nakamura, T. Akiyama, T. Ito, M. Weinert, and A. J. Freeman, Phys. Rev. B **81**, 220409 (2010).

3.5 Magnetic Exchange Force Microscopy

A. Schwarz and R. Wiesendanger

Magnetic exchange force microscopy (MExFM) is a spin sensitive atomic force microscopy (AFM) based technique. After we demonstrated its feasibility in 2007 on the antiferromagnetic bulk insulator NiO(001) [1], we could make a lot of progress in understanding the underlying physics by investigating the antiferromagnetic Fe monolayer on W(001) [2]. In the past three years we were able to quantitatively measure the distance dependence of the magnetic exchange interaction, cf. Sect. 3.5.1 [3], by inventing the magnetic exchange force spectroscopy (MExFS), and could show that it is possible to utilize the magnetic exchange interaction to switch the magnetization, cf. Sect. 3.5.2 [4]. Moreover, we could identify spin-dependent adhesion hysteresis as mechanism of magnetic dissipation often observed in MExFM and MExFS data, cf. Sect. 3.5.3 [5].

All three studies were performed with a homebuilt low temperature (8 K) atomic force microscope operated in ultra-high vacuum (UHV) located in Lab016 [3] using the frequency modulation (FM) technique in the non-contact (NC) regime. In this mode of operation the tip at the free end of a flexible cantilever with a spring constant c_z self-oscillates with constant amplitude A_0 at its eigenfrequency f_0. Typical values for c_z, A_0 and f_0 are 150 N/m, 3 nm and 180 kHz, respectively. Magnetic tips were prepared by coating commercially available oxidized Si cantilevers *in situ* with a few nanometers of Cr or Fe. Forces between tip and sample shift the unperturbed eigenfrequency f_0 of the cantilever to its actual frequency f by $\Delta f = f - f_0$. Scanning the tip line by line across the (x, y) sample surface while the frequency shift Δf is kept constant provides a $z(x, y)$ map of constant tip-sample interaction, i.e., the topography. In atomically resolved images the topography reflects variations in the magnitude of the short-ranged chemical and magnetic exchange forces between the foremost tip atom and the surface atom underneath. Distance dependent spectroscopy data, i.e., $\Delta f(z)$-curves, which can be converted into force curves $F(z)$ as well as interaction energy curves $E(z)$, are recorded at predefined (x, y) positions with the z-feedback switched off. In addition, the excitation amplitude a_{exc} required to keep the oscillation amplitude A constant is recorded simultaneously. It can be converted into the dissipation signal, i.e., the dissipated energy per oscillation cycle, $E_{\mathrm{D}} = \pi c_z A_0^2 Q^{-1}(a_{\mathrm{exc}}/a_{\mathrm{exc},0} - 1)$ with Q being the quality factor of the cantilever, which is related to the intrinsic energy dissipation, and $a_{\mathrm{exc},0}$ is the excitation amplitude without extrinsic dissipation. In atomically resolved data E_{D} is usually interpreted in terms of reversible but hysteretic atomic reconfigurations at the tip apex during approach and retraction of each oscillation cycle.

3.5.1 Magnetic Exchange Force Spectroscopy

R. Schmidt, A. Schwarz, and R. Wiesendanger

Properties of magnetic materials are governed by the magnetic exchange interaction between individual atomic magnetic moments (spins). A concept often used to describe the interaction between two spins $\mathbf{S_1}$ and $\mathbf{S_2}$ is the Heisenberg model, i.e., $H = -J\mathbf{S_1}\mathbf{S_2}$, where J is the exchange constant. Its sign determines, whether a parallel (ferromagnetic) or antiparallel (antiferromagnetic) alignment between the atomic magnetic moments is preferred. In solids a variety of very different coupling mechanisms are observed, e.g., direct exchange, superexchange or double exchange across non-magnetic bridging atoms as well as indirect coupling between localized spins in itinerant metals via polarization of the conduction electrons. In the latter case, an oscillatory Ruderman-Kittel-Kasuya-Yoshida (RKKY) behavior is expected, where the sign of J changes with distance. A change of sign can also occur, if only direct exchange between overlapping d-orbitals in transition metals is considered as in the Bethe-Slater curve or discussed by Moriya [7] based on the Alexander-Anderson model [8].

Experimentally, it is rather difficult to measure the distance dependence of the magnetic exchange interaction between two magnetic atoms. Recently, the oscillatory RKKY-type magnetic exchange interaction between pairs of individual Co adatoms has been measured employing scanning tunneling microscopy (STM) on Cu(111) and evaluating the Kondo resonance [9] and on Pt(111) by analyzing magnetization curves recorded with spin-polarized STM (SP-STM) [10]. In both cases the magnetic coupling is mediated via conduction electrons of the non-magnetic substrate.

Here we demonstrate that MExFS allows for a quantitative determination of the distance-dependent magnetic exchange interaction across a vacuum gap, which has so far only been considered theoretically utilizing density functional theory (DFT) [2, 11–14]. Experiments were performed with Cr coated tips on the antiferromagnetic Fe monolayer on W(001) and compared to first-principles calculations performed for different Fe- and Cr-terminated cluster tip models. Best agreement between theory and experiment was actually obtained for a Fe-terminated tip, indicating that surface material was transferred to the tip apex during *on-the-fly* sharpening. The DFT calculation reveal that antiferromagnetic coupling is always favored at short distances ($<$ 370 pm) and that the magnitude is on the order of 100 meV, in good agreement with experimental data.

Clean W(001) was prepared in situ by heating the single crystal for about 30 minutes at 1600 K in an oxygen atmosphere ($p_{O_2} = 1 \times 10^{-6}$ mbar) and finally flashing it at 2200 K for 10 s. Thereafter, about 1.3 atomic layers of Fe were deposited onto the substrate, which was finally postannealed to about 600 K. This procedure resulted in a closed antiferromagnetic Fe monolayer with out-of-plane anisotropy and second layer ferromagnetic Fe islands on top of it [15]. Magnetic tips were obtained by coating silicon tips with Cr. Often such as-prepared tips are not atomically sharp and do not exhibit magnetic sensitivity immediately. Thus, slight tip modifications are intention-

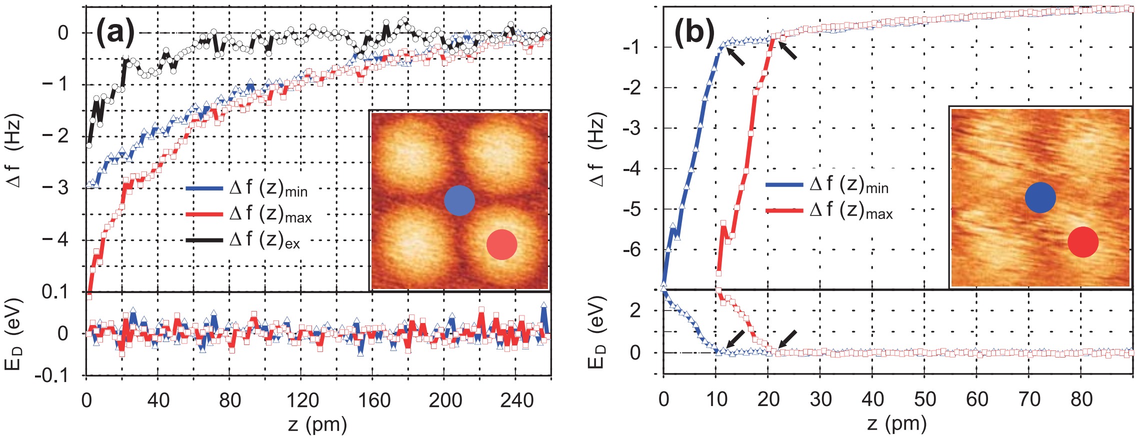

Figure 3.29: Two spectroscopy data sets each showing two individual $\Delta f(z)$-curves recorded with a non-dissipative stable **(a)** and dissipative unstable **(b)** tip on Fe atoms with opposite spins at locations marked in the corresponding MExFM image displayed in the insets. Only for the non-dissipative stable tip in **(a)** $\Delta f_{\text{ex}}(z)$ (black curve) and thus the magnetic exchange interaction $E_{\text{ex}}(z)$, cf. Fig. 3.30, can be obtained by subtracting both curves from each other.

ally induced, e.g., by scanning at closer and closer tip-sample distances, until the tip shows the characteristic antiferromagnetic c(2×2) pattern on the Fe monolayer, which proves magnetic sensitivity [2]. During this procedure, Fe might have been picked up. Thus, the initially Cr-coated tip could be Fe terminated afterwards. With such a magnetically sensitive tip 3D $\Delta f(x, y, z)$ data sets were recorded, as described in Ref. [5]. Based on such a 3D data set individual $\Delta f(z)$-curves on surface atoms with oppositely oriented spins can be unambiguously identified. They are displayed in Fig. 3.29 for two different experiments performed with a non-dissipative (a) and a dissipative (b) tip , respectively (see lower curves, in which E_{D} is plotted relative to the intrinsic dissipation). The insets show the atomically spin-resolved images recorded with the corresponding tips and the positions, where the $\Delta f(z)$-curves have been recorded. No absolute z-scale can be extracted from experimental data, thus we arbitrarily set $z = 0$ pm at the closest tip-sample distance.

With the stable tip the two $\Delta f(z)$-curves shown in Fig. 3.29(a) are indistinguishable at larger distances, but split smoothly into two branches at smaller distances. Both $\Delta f(z)$-curves represent the total tip-sample interaction. Since all non-magnetic contributions, e.g., the long-range van der Waals interaction and the short-range chemical interaction, are identical on both atomic sites of opposite spin orientation, the frequency shift $\Delta f_{\text{ex}}(z)$ representing the magnetic exchange interaction can be extracted simply by subtracting the curves from each other, i.e., $\Delta f_{\text{ex}}(z) = \Delta f_{\text{max}}(z) - \Delta f_{\text{min}}(z)$ (black circles). Note that the relative spin orientation is not known *a priori*, but choosing the sign definition $\Delta f_{\text{ex}}(z) = \Delta f_{\text{max}}(z) - \Delta f_{\text{min}}(z)$ is justified by comparison with theory (see below). For further quantitative comparison with theory, $\Delta f_{\text{ex}}(z)$ can be converted into the magnetic exchange energy $E_{\text{ex}}(z)$ (cf. Fig. 3.30). This whole procedure to determine $E_{\mathrm{ex}}(z)$ is called magnetic exchange force spectroscopy (MExFS).

In Fig. 3.29(b) both curves exhibit a sudden steep decrease of the $\Delta f(z)$-curve at z-positions separated by about 12 pm. At exactly the same positions the dissipation increases drastically to about 3 eV/cycle at the smallest separation. Such a large dissipation is usually associated with adhesion hysteresis [17–19], i.e., reversible reconfigurations of atoms at the tip apex, which occur at different tip-sample distances during approach and retrace of an oscillation cycle. Noteworthy, calculations revealed that the magnetic exchange interactions contribute to relaxation effects [13] and it is hence likely that they contribute to dissipative reconfigurations as well, which are then spin dependent (cf., Sect. 3.5.3). Since the tip apex structure is different before and after the onset of dissipation, $\Delta f_{\mathrm{ex}}(z)$, and hence $E_{\mathrm{ex}}(z)$, cannot be extracted by subtracting both curves form each other. Nonetheless, the tip is magnetically sensitive as demonstrated by the MExFM image displayed in the inset. The MExFM image presented in Fig. 3.29(b) is noisier than in (a), cf. insets, which also indicates that the tip apex used to record the data in (b) is less stable. Indeed, evaluating six 3D-MExFS data sets and more than 20 MExFM images shows that the features in the spectroscopy curves and image data as found in Fig. 3.29 are characteristic for non-dissipative (stable) and dissipative (unstable) tips.

In order to interpret the experimentally obtained $E_{\mathrm{ex}}(z)$-curves, we have performed DFT based first-principles calculations within the generalized gradient approximation (GGA) [20] to the exchange-correlation potential. We apply the full-potential linearized augmented plane wave method as implemented in the WIEN2K [21] code. The energy cut-off for the plane wave representation in the interstitial region is $E_{\mathrm{max}}^{\mathrm{wf}} = 13$ Ry and a $(3 \times 3 \times 1)$ Monkhorst-Pack grid was used for the Brillouin zone integration. The coupled system of tip and sample was calculated in a supercell geometry as described in Ref. [13]. The Fe monolayer on W(001) was modeled by a symmetric slab with five W layers and one Fe layer on each side. Four different pyramidal three layer tips consisting of 14 atoms were considered (see sketches in Fig. 3.30): (i) a Cr-base with an Fe termination, (ii) a pure Fe tip, (iii) a pure Cr tip, and (iv) an Fe-base with a Cr termination. These choices reflect possible tip configurations, which could occur after the deliberately induced collision between the Cr-coated tips and the Fe monolayer described above. Note that adjacent Cr layers as well as adjacent Fe and Cr layers are coupled antiferromagnetically, while coupling in the pure Fe tip is ferromagnetic. Tip and surface were relaxed independently before considering the coupled system. The tip was then approached to the surface along a trajectory of discrete points. For every distance we carried out a DFT calculation including structural relaxations of the tip atoms and the Fe monolayer and uppermost W layer. As in the experimental situation the separation z in the coupled system is defined as the distance between the tip apex atom and the Fe surface atom before considering relaxations. For none of the tip models hysteretic reconfigurations of the atomic structure can be observed. Thus, our tip models reflect stable non-dissipative tips.

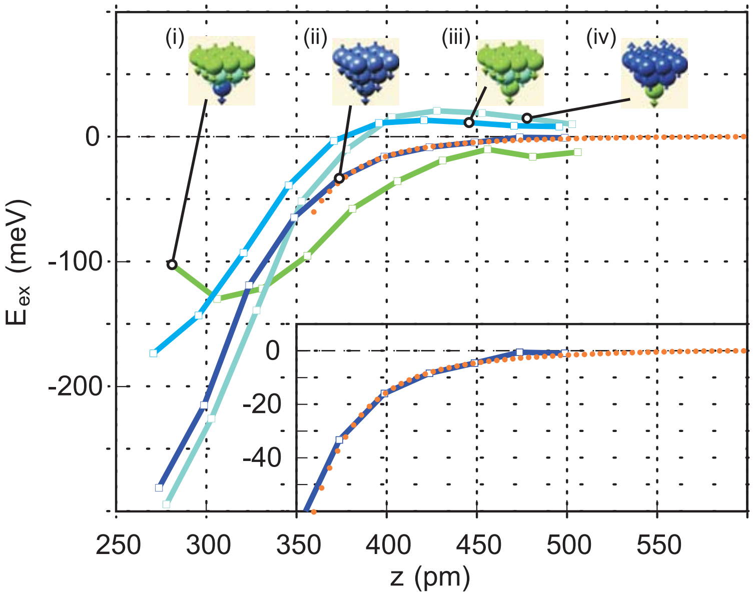

Figure 3.30: Comparison between theoretical and experimental $E_{\mathrm{ex}}(z)$-curves. $E_{\mathrm{ex}}(z)$ with the Fe-ML on W(001) was calculated using DFT for four different tips. Chemical composition (blue: Fe; green/cyan: Cr) and spin structure are indicated for each curve. $E_{\mathrm{ex}} > 0$ ($E_{\mathrm{ex}} < 0$) indicates a ferromagnetic (antiferromagnetic) coupling. $E_{\mathrm{ex}}(z)$ obtained with the non-dissipative tip, cf. Fig. 3.29(a) is plotted as well (orange curve). It fits very well with the theoretical result for a pure Fe tip apex (see inset).

For every tip we considered a parallel (p) and an antiparallel (ap) alignment of the magnetic moments of the tip apex atom and the surface atom underneath. Relaxations on the order of 10 pm were observed for all tips, but no reconfigurations or instabilities. The magnetic exchange energy $E_{\mathrm{ex}}(z)$ is obtained by subtracting the total energies in the ap- and p- alignment, i.e., $E_{\mathrm{ex}}(z) = E_{\mathrm{ap}}(z) - E_{\mathrm{p}}(z)$. $E_{\mathrm{ex}}(z) > 0$ (< 0) indicates ferromagnetic (antiferromagnetic) coupling. This approach is equivalent to subtracting the experimental data obtained on minima and maxima as performed for the stable non-dissipative tip. Due to reconfigurations at the tip apex, a direct comparison of the data recorded with dissipative tips is not possible. Note that the tips used for the calculations are much smaller than real tips and long-range interactions are not accounted for. However, after subtraction all non-magnetic contributions to the total tip-sample interaction, including the long-range van der Waals interaction, cancel out.

The calculated $E_{\mathrm{ex}}(z)$-curves are displayed in Fig. 3.30. At small tip-sample distances E_{ex} is negative indicating the favorable antiferromagnetic exchange interaction in accordance with the simple Bethe-Slater picture of direct exchange. This finding justifies the sign definition of $\Delta f_{\mathrm{ex}}(z)$ used for the experimental data. The magnitude at a distance of 300-350 pm, is antiferromagnetic and on the order of 100 meV. Interestingly, only Cr-terminated tips show a characteristic change of sign at large distances due to a transition from a direct to an indirect exchange mechanism [14].

For direct comparison between theoretical predictions and experimental data, $E_{\mathrm{ex}}(z)$ obtained with the non-dissipative stable tip is displayed in Fig. 3.30 as well. Since no sign change is observed in the experimental data, we can infer that the tip is Fe-terminated (only Cr-terminated tips exhibit a sign change), most probably because the Cr-coated tip picks up surface Fe atoms during our tip-preparation procedure. In the experiment, the absolute z-position is not known. Therefore, we shifted the experimental curve in z-direction with respect to the theoretical curves. Best agreement between theory and experiment is found for the pure Fe tip apex, for which magnitude as well as the distance dependence of the magnetic exchange energy fits very well as visible in the inset.

The exemplary result shown here demonstrates that our method enables us to quantitatively measure the magnetic exchange interaction across a vacuum gap. Both, distance dependence and magnitude can be accurately measured using stable and hence non-dissipative tips. Unsuitable tips can be identified by analyzing the dissipation signal. Our experimental procedure can be universally applied to any combination of similar or dissimilar atomic species to measure the distance dependence of the magnetic exchange interaction across a vacuum gap with atomic resolution, even on insulating tip-sample systems. Moreover, our experiments suggest that the magnetic exchange interaction can be utilized to switch the magnetic state of atoms, clusters or molecules in a controlled fashion by placing a magnetic tip in an MExFM (or SP-STM) set-up lower than about 0.5 nm above the specimen. That magnetic switching is indeed possible is demonstrated in the following section 3.5.2.

3.5.2 Magnetic switching induced by the magnetic exchange interaction

R. Schmidt, A. Schwarz, and R. Wiesendanger

Changing an external magnetic field is the common way to control the magnetization direction of a specimen and used, e.g., in magnetic hard discs for data recording [22]. Similarly, the magnetization direction of magnetic nanodots can be switched with the help of the local stray field emanating from a ferromagnetic tip in a magnetic force microscopy (MFM) set-up [23]. The opposite, i.e., switching of the tip magnetization direction, has been observed as well [24]. More recently, spin transfer torque has been established to switch the magnetization direction of a free magnetic layer with respect to a fixed magnetic layer by a spin-polarized tunneling current in a planar spin-valve or magnetic tunnel junction geometry [25, 26]. On an even smaller length scale it has been demonstrated that the spin-polarized tunneling current across a vacuum gap in a SP-STM set up, can be employed to selectively reverse the magnetization direction of individual magnetic nanoislands [27].

Here, we also use a local probe technique in a tip-sample geometry, but instead of a spin-polarized tunneling current, as in SP-STM, or a long-range magnetostatic stray

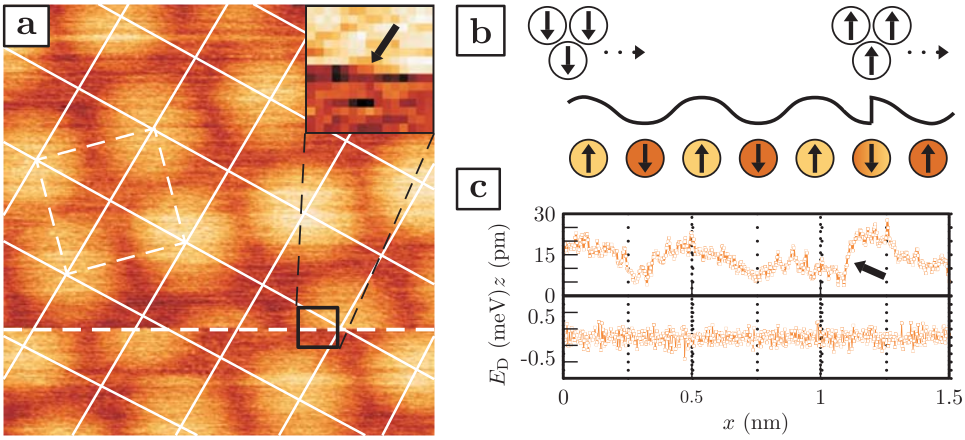

Figure 3.31: **(a)** $(1.5 \times 1.5)\,\mathrm{nm}^2$ MExFM image of the Fe monolayer on W(001). The grid marks the position of Fe atoms. Minima and maxima correspond to surface atoms with parallel (p-site) and antiparallel (ap-site) spins with respect to the magnetic tip, respectively. On the dashed line the switching event (see inset), visible as a contrast reversal, took place. **(b)** Sketch of the contrast reversal after a sudden switching of the magnetization direction at the tip apex. **(c)** Scan line with the switching event (dashed line in the image) and the simultaneously recorded dissipation signal.

field, as in MFM, we utilize the distance dependence of the short-ranged magnetic exchange interaction in an MExFM configuration. We find that while imaging the antiferromagnetic Fe monolayer on W(001) some tip apices behave like superparamagnetic clusters with uniaxial anisotropy. Their switching rate can be controlled via the distance dependence of the magnetic exchange interaction as well as by an external magnetic field. By measuring lifetimes, we could determine the energy barrier between both possible states and study the influence of an externally applied magnetic field. In the present investigation it is the tip apex that exhibits properties of a superparamagnetic cluster. However, we envisage that MExFM and MExFS are appropriate tools to characterize magnetization dynamics of small magnetic particles or even atoms that are prepared in a more controlled fashion on substrates similar to previous investigations performed with SP-STM. Note the advantages of a force based technique compared to a tunneling current based detection scheme in this context: spin torque and Joule heating effects are absent and it can be applied to non-conducting sample systems.

Figure 3.31(a) shows an image scanned from bottom to top with a magnetically sensitive tip. The overlaid grid shows the position of Fe atoms, i.e., the $p(1 \times 1)$ chemical surface unit cell. Since only every second Fe atom is imaged as maximum, the image contrast represents the antiferromagnetic $c(2{\times}2)$ spin structure (see dashed square). In the surface area marked by the frame, a switching event occurred (see inset), whereby the minima appear as maxima and vice versa. The scan line with the switching event is displayed in (b) together with a sketch that explains the contrast reversal. Note that the spins at the tip apex are reversed and this reversal is detected

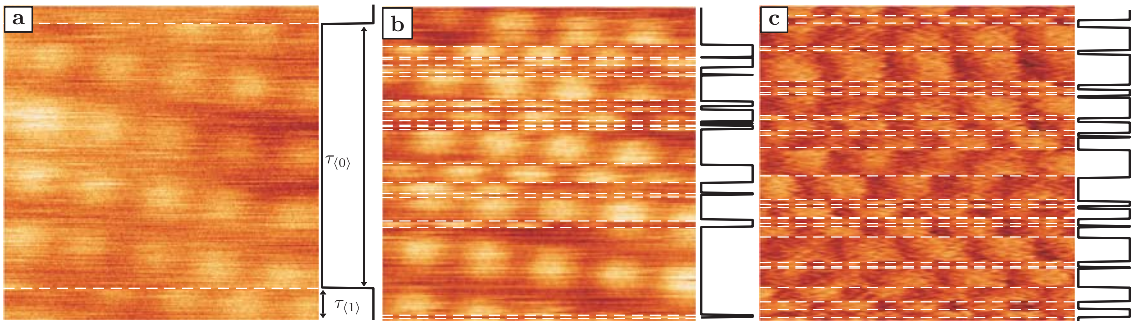

Figure 3.32: **(a)**-**(c)** $(2 \times 2)\,\mathrm{nm}^2$ MExFM images demonstrating distance and magnetic field dependence of the switching. **(a)** and **(b)** were recorded in $B = 4.5$ T with the same tip, but in **(b)** the tip was 40 pm closer to the surface. Clearly, the number of switching events increased drastically. The two lifetimes $\tau_{\langle 0\rangle}$ and $\tau_{\langle 1\rangle}$ are unequal. **(c)** was recorded with another tip and in $B = 0$ T. The two lifetimes $\tau_{\langle 0\rangle}$ and $\tau_{\langle 1\rangle}$ are also unequal, but the difference is significantly smaller than in **(b)** with $B \neq 0$.

via their interaction with the unchanged surface spins. From the featureless dissipation signal in (c) and the absence of any z-offset due to a tip that becomes either longer or shorter, and since the registry between the overlaid grid and positions of maxima and minima, respectively, remains perfect after the switching event, we can infer that the magnetization reversal is not accompanied by any structural change at the tip apex. That structural and magnetic switching events at the tip apex can occur simultaneously and can be identified has been discussed in the previous section 3.5.2 [3]. Such tips are not considered here, because data recorded with them cannot be evaluated quantitatively with the simple model proposed in the following.

According to theoretical calculations, maxima and minima in MExFM images denote Fe atoms aligned antiparallel (ap-site) and parallel (p-site) with respect to the tip magnetic moment, respectively [2]. Thus, in Fig. 3.31(a) the tip expectedly switches from a p- to the energetically preferred ap-configuration (the switching occurs on a minimum, which becomes a maximum). The transition is not as sharp as sketched in Fig. 3.31(b), but takes about 5 ms (5 data points). However, this is not the real switching time, which is several orders of magnitude faster, but related to the much slower response time of the z-feedback during data acquisition. Since the magnetic corrugation before and after the switching event is identical (≈ 14 pm), we can infer that the magnetization direction of the tip rotated by 180°.

Figure 3.32 summarizes our experimental findings regarding the distance and magnetic field dependence of the switching behavior. In all three images (a), (b) and (c) the tips did not exhibit site- or spin-dependent dissipation and can thus be regarded as structurally stable. The corresponding tip states, denoted as $\langle 0\rangle$ and $\langle 1\rangle$, respectively, are plotted to the right. Since the scan speed is known, the duration, in which the tip state remains unchanged, i.e., its lifetime, can be determined. Images (a) and (b) were acquired with the same tip in an external magnetic field ($B = 4.5\,\mathrm{T}$ applied perpendicular to the surface), but at different Δf set-points, i.e., -25 Hz and -29 Hz, respectively. As a result, (b) was recorded at a 40 pm smaller tip-sample separation than (a). The strong increase of the number of switching events demonstrates that the switching probability can be influenced via the tip-surface separation. For the relatively large number of switching events in the images (b) and (c), the mean lifetimes $\tau_{\langle 0 \rangle}$ and $\tau_{\langle 1 \rangle}$ can be determined (for (a) no reasonable analysis is possible). For (b) we find different lifetimes, i.e., $\tau_{\langle 0 \rangle} = (45 \pm 17)$ s and $\tau_{\langle 1 \rangle} = (15 \pm 4)$ s, respectively. Image (c), which has been recorded with another tip and in zero field, also exhibits different lifetimes, but with $\tau_{\langle 0 \rangle} = (27 \pm 5)$ s significantly closer to $\tau_{\langle 1 \rangle} = (17 \pm 3)$ s than for $B = 4.5$ T. As in Fig. 3.31, all switching events in Fig. 3.32 were initiated on a minimum, which then became a maximum, meaning that the tip magnetization always changed from a p- into an ap-configuration.

Our experimental observations can be explained assuming a nanotip at the apex of the macroscopic tip pyramid that behaves like a superparamagnetic cluster with uniaxial anisotropy: The energy landscape of such a superparamagnetic cluster is depicted in Fig. 3.33 (a) and (b): In zero field the two states of magnetization are separated by a single symmetric barrier E_{b}. According to the Néel-Brown law $\tau = 1/\nu_0 \cdot \exp\left(-E_{\mathrm{b}}/k_{\mathrm{B}}T\right)$ [28, 29] the lifetime τ depends exponentially on the relation between E_{b} and thermal energy $k_{\mathrm{B}}T$ on the attempt frequency ν_0. In the presence of an external magnetic field ($B \neq 0$) the energy minimum for the magnetization direction parallel (antiparallel) to B is lowered (elevated) by the Zeeman energy E_{Z}. As a result, the energy barrier becomes asymmetric and the lifetimes of the magnetization state parallel to B is different, i.e., larger, than the magnetization state antiparallel to B.

In the presence of a magnetic exchange force, the model has to be modified. Figure 3.33(c) explains the increased switching rate visible in the image data in Fig. 3.32(a) and (b). Treating the tip apex as a superparamagnetic cluster, its magnetization direction, and thus the spin of the foremost tip apex atom, can either point upwards or downwards (black arrows in the sketch). In whatever direction the spin at the tip apex actually points, during scanning it periodically changes its relative orientation with respect to the antiferromagnetic surface from ap- to p-configuration. As mentioned above, the ap-configuration is energetically favored. Therefore, the energy barrier E_{b} becomes asymmetric at close tip-sample separations. The difference between the energy barriers form ap- to p-configuration and vice versa, i.e., $E_{\mathrm{ap/a}}$ and $E_{\mathrm{p/ap}}$, respectively, is the magnetic exchange energy E_{ex}. This immediately explains, why switching events during topography imaging are initiated on minima, which represent p-configurations between tip and sample spin. Note the different effect of the Zeeman energy due to an external magnetic field and the exchange energy: the former does affect both states symmetrically, cf. 3.33 (b), while the exchange energy does not. Since E_{ex} is distance dependent and increases at smaller separations, it is obvious that the difference between $E_{\mathrm{p/ap}}$ and $E_{\mathrm{ap/p}}$ is distance dependent as well and thus becomes larger for smaller tip-sample distances. Additionally, the increased switching rate demonstrates that the energy barrier $E_{\mathrm{p/ap}}$ is actually lowered as sketched in Fig.

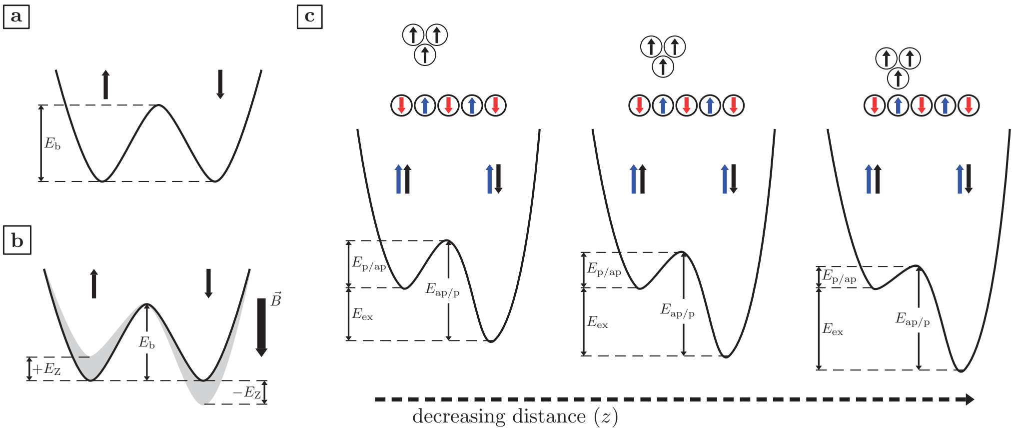

Figure 3.33: **(a)** depicts the two states of a magnetic particle with uniaxial anisotropy without external magnetic field. In **(b)** the shaded area represents the relative shift of the two states due to the Zeeman energy in an external magnetic field. **(c)** shows the influence of the distance dependent magnetic exchange energy between tip and surface on the two states. The decreased barrier height between p- and ap-configuration explains the experimentally observed increased switching rate after decreasing the tip-sample separation; cf. Fig. 3.32 **(a)** and **(b)**.

3.33 (c).

To understand the two different lifetimes found in Fig. 3.32(b) the presence of the magnetic exchange interaction plus an external magnetic field has to be considered. All four possible initial configurations between tip apex and sample spins are shown in Fig. 3.34. Since the corresponding energy barriers are all different, four different lifetimes exist. However, only two of them, i.e., the transitions from the p- into the ap-configuration, actually show up (left- and rightmost sketches in Fig. 3.34), because the energy barrier in the opposite direction is larger by E_ex, which is on the order of 10 meV [3]. Thus, both lifetimes $\tau_{\langle 0\rangle}$ and $\tau_{\langle 1\rangle}$ correspond to transitions from the p- into the ap-configuration, but for the longer one, i.e., $\tau_{\langle 0\rangle}$, the tip apex magnetization is parallel to the external magnetic field. Note that E_ex is much larger than E_Z which, for Fe and $B = 5$ T, amounts to only about 0.1 meV per atom.

Since the image displayed in Fig. 3.32(c) was recorded in zero field, the lifetimes for the two states $\langle 0\rangle$ and $\langle 1\rangle$ should be equal. As before, they both correspond to transitions from the p- into the ap-configuration, but now no magnetization direction at the tip apex is preferred. Indeed, the difference between both lifetimes is smaller, but still significant. We could imagine two possible explanations for this observation: Firstly, the self stray field emanating from the thin film surface covering the whole macroscopic tip pyramid can act in the same way on the tip apex as an external magnetic field. Note that due to uncompensated spins at surfaces even an antiferromagnetic Cr coating can exhibit a small self stray field. Secondly, a zero field anisotropy could be induced by the geometric structure at the tip apex (it certainly will not possess

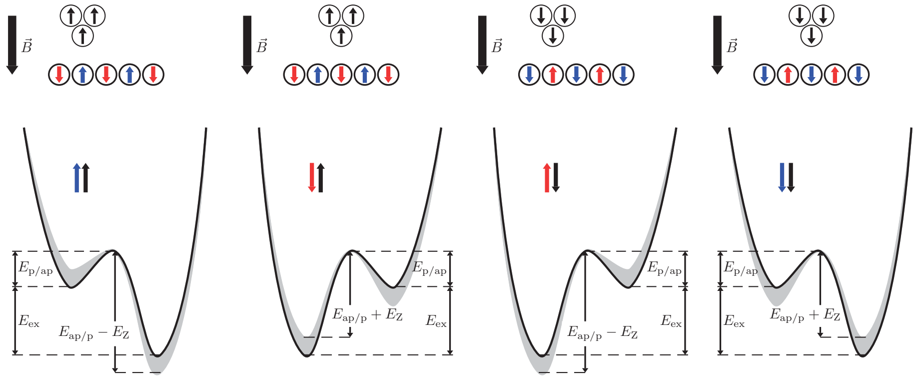

Figure 3.34: Combined effect of an external magnetic field and the magnetic exchange energy between tip and sample on the energy landscape. Note that the magnetic exchange energy is much larger than the Zeeman energy. Since the ap-configuration is energetically favored, only p to ap switching events are observed. Due to the Zeeman energy, the state with the tip apex magnetization parallel to the external magnetic field is preferred.

spherical symmetry), which affects the local magnetocrystalline anisotropy energy [30].

Applying the Néel-Brown law, the energy barrier $E_{\mathrm{b}} = E_{\mathrm{p/ap}}$ can be estimated. For the attempt frequency ν_0 we use the Larmor frequency, which is on the order of 1 GHz for Cr and Fe. The available thermal energy $k_{\mathrm{B}}T$ (T = 8.1 K) is about 0.7 meV. For Fig. 3.32(b) ($B = 4.5$ T) the corresponding barrier heights $E_{\mathrm{p/ap}}$ are 16.3 meV ($\tau_{\langle 0\rangle}$) and 17.1 meV ($\tau_{\langle 1\rangle}$), respectively. The larger lifetime (higher energy barrier) can be assigned to a tip apex with a magnetization direction parallel to the magnetic field. The difference of 0.8 meV ($E_{\mathrm{Z}} = \pm 0.4$ meV) corresponds to an effective Zeeman energy E_{Z} felt by the tip apex. In zero field, cf. Fig. 3.32(c), the corresponding energy barriers are 16.4 meV ($\tau_{\langle 0\rangle}$) and 16.8 meV ($\tau_{\langle 1\rangle}$), respectively. In this case the difference of 0.4 meV could be attributed to a residual self stray field from the Cr covered tip due to uncompensated spins, as mentioned above. Note that different tips were used, hence the exact magnitude of the self stray field in Fig. 3.32(b) and (c) can be different. Since $E_{\mathrm{ap/p}} = E_{\mathrm{p/ap}} + E_{\mathrm{ex}}$ and E_{ex} is on the order of 10 meV the corresponding lifetime is on the order of one year for $E_{\mathrm{ap/p}} = 26.4$ meV at 8.1 K, which justifies the presumption that all switching events are p to ap reversals.

Additionally, our experimental data allows us to roughly estimate the number of atoms in the nanotip that participate in the magnetization switching. The magnitude of the Zeeman energy of $E_{\mathrm{Z}} = \pm 0.4$ meV indicates that the nanotip in Fig. 3.32 (b) consists of a few atoms only, because, as already mentioned above, at 5 T the Zeeman energy is on the order of 0.1 meV per Fe atom. Another estimation is possible via the barrier height, which is determined by the magnetocrystalline anisotropy energy (MAE). Compared to typical values found in bulk samples, the MAE per atom is significantly larger on surfaces as well as within small clusters, i.e., typically on the order of 1 meV per atom or more [31]. Thus, an energy barrier of about 17 meV would indicate a nanotip made of 10-20 atoms. This number is in agreement with our nanotip model, which behaves like a superparamagnetic cluster. Indeed, the formation of nanotips on top of macroscopic tip pyramids are commonly assumed to explain atomic resolution imaging in atomic force microscopy [32]. However, it is not obvious how such a nanotip can be magnetically independent from the rest of the tip, a prerequisite to observe superparamagnetic behavior. We believe that the nanotip is actually not fully decoupled and that the remaining magnetic coupling, e.g., across a grain boundary, to the rest of the tip is responsible for the energy barrier. In fact, most magnetic tips (about 80%) do not exhibit superparamagnetic behavior, indicating such a strong coupling that they never switch.

Our finding demonstrates that MExFM (and MExFS) can be applied to study magnetization reversal processes with atomic resolution by modifying the energy barrier between different magnetic states in a controllable fashion utilizing the distance dependence of the magnetic exchange interaction. Future systematic studies can be envisaged to investigate the magnetization dynamics on small islands, molecules or even single atoms. Moreover, with this force microscopy based scanning probe method such sample systems can be prepared and studied on insulating substrates. Noteworthy, the magnetic exchange force can also become relevant in STM studies, e.g., if conductance measurements through a single adatom on a surface are performed with a magnetic tip in the contact or near contact regime [33].

3.5.3 Spin-dependent magnetic dissipation

Q. Zhu, E. Vedemedenko, A. Schwarz, and R. Wiesendanger

Magnetic excitations can provide important, new and exciting insights into atomic scale magnetism as the analysis of inelastic tunneling processes with STM or SP-STM have demonstrated [34,35]. The dissipative MExFM signal is to some extent analogous (and at the same time complementary) to the inelastic tunneling current. Thus, it could be applied to detect and study spin excitations or magnons on insulating sample systems like NiO(001), which can only be investigated with MExFM and MExFS. In the following we will analyze possible mechanisms that can lead to a spin-dependent dissipation signal.

While possible atomic scale dissipative mechanisms for non-magnetic tip-sample systems have been discussed intensively in the literature [36], only two publications address atomic scale magnetic dissipation, i.e., spin-excitations via friction following Landau-Lifshitz-Gilbert dynamics [37] and spin-phonon coupling within the Caldeira-Leggett model [38]. Spin excitation is a straightforward mechanism for a dissipation signal of magnetic origin. However, this mechanism is not very efficient due to the large mismatch between the oscillation frequency of the cantilever (100 kHz regime) and typical spin excitation resonances (GHz regime). Note that analogously, phonon excitations cannot be responsible for the experimentally observed magnitude of the

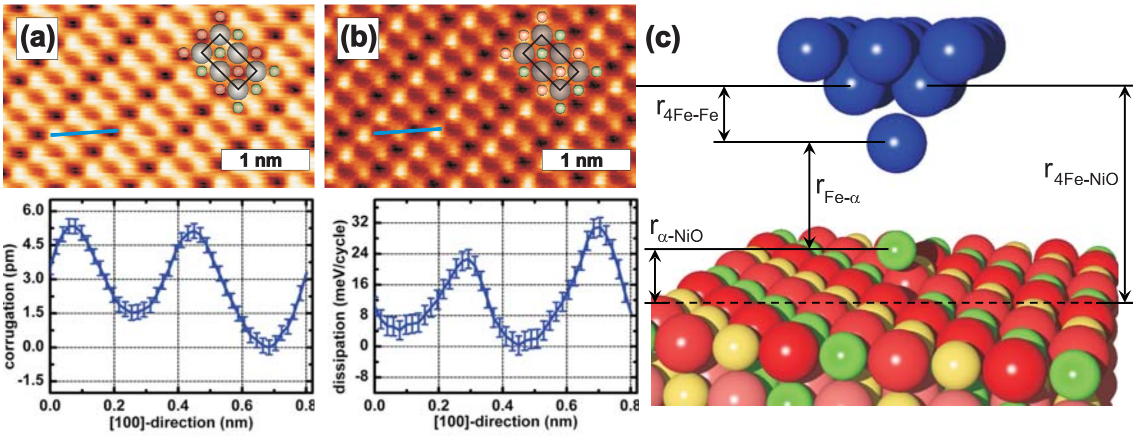

Figure 3.35: Atomically resolved MExFM topography image **(a)** and simultaneously recorded dissipation image **(b)**. The ball model shows the chemical and magnetic structure of the surface. Line sections along the [100]-direction of the unit cell visualize the magnitude of the spin-dependent contrast. **(c)** Tip-sample geometry and definition of distances used in the simulations. Green/yellow balls denote "up" and "down" Ni atoms respectively, while red balls correspond to the oxygen atoms.

dissipation contrast found between chemically different species in atomically resolved AFM images [39]. Instead, site-dependent *adhesion hysteresis* [40] appeared to be the dominating mechanism for non-magnetic dissipation: Due to strong chemical interactions at small tip-sample distances, reversible but hysteretic reconfigurations of atoms during approach and retraction of each oscillation cycle dissipate energy.

Here, we analyze magnetic dissipation data obtained with an Fe coated tip on the antiferromagnetic insulator NiO(001) and provide simulations using Monte-Carlo minimization techniques. We demonstrate that the magnetic dissipation is complementary to the *normal* non-magnetic adhesion hysteresis: For a magnetic tip-sample system the magnetic exchange interaction contributes to the total interaction. As a result, the hysteretic reconfiguration at the tip apex, and hence the energy dissipation involved in this process, depends on the relative orientation between the interacting spins. Based on our calculations, we are able to qualitatively and quantitatively explain the experimentally observed dissipation contrast on chemically equivalent Ni and on O surface atoms by such spin-dependent adhesion hysteresis mechanism.

Figure 3.35 displays atomically resolved spin-dependent unit cell averaged experimental data obtained with an Fe-tip on NiO(001) [1]. The spin carrying d-electrons localized at the Ni atoms are coupled ferromagnetically along ⟨110⟩-directions and antiferromagnetically between {111}-planes by superexchange via the O atoms. Hence, a row-wise antiferromagnetic order emerges at the (001) surface. The topography image (a) obtained with an Fe coated tip reproduces the chemical arrangement of atoms at the (001) surface due to the presence of chemical interactions as well as the row-wise antiferromagnetic order due to the presence of the magnetic exchange interaction. Since anions on ionic surfaces generally interact stronger with metal tips than cations [1], O sites are imaged as maxima and Ni sites as minima. This assignment is consistent with the row-wise magnetic contrast visible on minima, which reflect the spin carrying Ni cations. The ball model depicts the positions of the O (red) and Ni sites (yellow and green to indicate opposite spin orientations). The simultaneously recorded dissipation image (b) also exhibits a row-wise contrast on Ni atoms with opposite spin orientation. Peculiarly, there seems to be an additional but weaker contrast between rows of O atoms with Ni atoms of opposite spin orientations in the layer below, which is absent in the topography signal.

The line sections in (c) and (d) along the [110]-direction visualize the magnitudes of the site- and spin-dependent topography and dissipation signals, respectively. The spin dependent contrast between Ni atoms with opposite spin orientations is about 1.5 pm and thus much smaller than the chemical contrast between Ni and O atoms. No difference is visible between O atoms. In the dissipation signal the contrast is inverted, i.e., more energy is dissipated above the Ni atoms than above the O atoms. The magnetic dissipation on Ni atoms, i.e., the energy difference between Ni atoms with opposite spin orientations, is about 13.3 meV/cycle. For O atoms with oppositely oriented spins at the Ni atoms below them the magnetic dissipation is about 6.2 meV/cycle.

To investigate the origin of the large spin-dependent dissipation on Ni and O surface sites, we model the coupled tip-sample systems including all magnetic and non-magnetic interactions between tip and sample on an atomistic level. The geometry of the system under investigation is defined in Fig.3.35(c). As model for the Fe tip we used a pyramidal 14 atom cluster of bcc(001) stacking with parameters taken from Ref. [13]. For the sake of simplicity only vertical equilibrium motions of the tip with $\partial r/\partial t \rightarrow 0$ have been permitted. The tip-sample distance $r_{\mathrm{4Fe-NiO}}$ has been defined as the distance between the second layer of the pyramidal cluster consisting of four Fe atoms and the unperturbed surface of NiO. The foremost Fe atom of the tip was free to relax. The rocksalt structure of the NiO crystal has been represented by a slab with dimensions $8 \times 8 \times 8$ interatomic distances a. According to the theoretical [12] as well as experimental studies [42–44] the relaxation of a bulk terminated, clean NiO(001) surface layer is smaller than 3% of an ideal interlayer distance while the relaxation of deeper layers is negligible. Therefore, we assume a bulk terminated NiO(001) structure with vertical structural relaxation of the surface atomic layer only. The distances between (i) the foremost Fe-atom and the studied atom $r_{\mathrm{Fe}-\alpha}$, (ii) the studied atom and the unperturbed surface $r_{\alpha-\mathrm{NiO}}$ and (iii) the studied atom and the rest of the tip $r_{\mathrm{4Fe}-\alpha}$, have been analyzed as a function of the tip-sample distance $r_{\mathrm{4Fe-NiO}}$, respectively. The studied atom α is either Ni$\uparrow$, Ni$\downarrow$, O$\uparrow$ or O$\downarrow$, where the arrows at the O atoms refer to the spin orientations of the Ni atoms in the layer underneath.

All structural relaxations have been performed in the framework of the standard Monte-Carlo (MC) technique [45, 46] or by steepest-descent energy minimization including generalized Buckingham potentials and magnetic exchange. Since the employed model allows for movements along the vertical axis only, these two methods give identical results at zero temperature [47]. The Hamiltonian of the coupled tip-sample system can be expressed by

$$\mathcal{H} = \sum_{i<j} V_{ij}(r) + J_{ij}(r) \sum_{i<j} \vec{S}_i \vec{S}_j, \tag{3.10}$$

where the summation includes all considered interatomic interactions with the corresponding distance dependent potential $V(r)$, and the exchange parameter $J(r)$. In the simulations all interactions within the NiO slab and the Fe tip as well as between all tip and sample atoms were considered. The coefficients in Eq. 3.10 have been taken from *ab-initio* calculations or experiments [48]. No parameters were fitted to match the experimental data.

First, the NiO crystal has been relaxed without the Fe tip. The relaxed NiO surface showed an outwards expansion of Ni and inwards contraction of O atoms, respectively (rumpling). This result is in good agreement with molecular dynamics calculations [49] and experiments [44]. For the calculations including magnetic tip we considered an unperturbed initial configuration of the Fe tip. However, the foremost tip atoms were able to relax during the simulation. A starting distance $r_{4\mathrm{Fe-NiO}} = 6.2$ Å was chosen to insure an initially well separated tip-sample system. In the next step $r_{4\mathrm{Fe-NiO}}$ was decreased stepwise. For each tip position the system was relaxed during n_0 initial steps plus N additional MC steps until convergence was reached. At each MC step the positions of the foremost Fe atom as well as of each of the 24 surface atoms have been sampled within a step width of $\pm 10^{-2} ... 10^{-4}$ Å and accepted or rejected according to the Metropolis probability or the steepest descent procedure. For the sake of simplicity we did not allow for spin flips in this set of simulations; i.e., the magnetization of Fe atoms was always "upwards".

The effective chemical potential energy for atomistic simulations on NiO includes pairwise ionic as well as Buckingham-type potentials of general form [48]

$$V_{\mathrm{NiO}} = \frac{q_i q_j}{r} + A \cdot e^{-r/\rho} - \frac{C}{r^6}, \tag{3.11}$$

with ρ extension of the occupied spin orbitals, q ionic charges, and parameters A and C. The parameter set for NiO is by no means unique. The coefficients A and C have been generated variationally to best-fit experimental data for bulk NiO [48]. In our computations, the interaction cut-off length is taken as $r_{\mathrm{co}} \simeq 6a$. This corresponds to ≈ 520 bonds in NiO.

The superexchange interactions between {111}-planes in NiO have been recently mapped onto the Heisenberg Hamiltonian [50]. We have fitted these data by an RKKY-like expression

$$J_k(r) = \frac{c \cdot e^{-k_2 \cdot r} \cdot \sin(k_1 \cdot r + b)}{r^3} \tag{3.12}$$

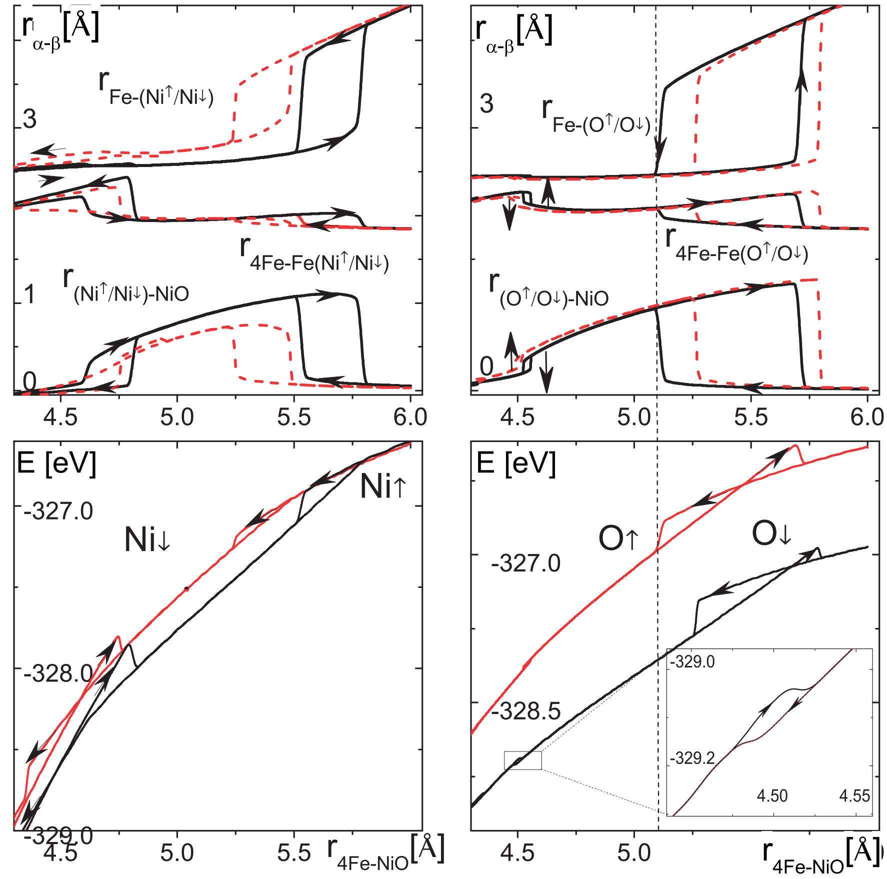

Figure 3.36: Calculated equilibrium interatomic distances (upper panels) and total energy E_t (lower panels) above Ni atoms (left) and O atoms (right), respectively, as a function of the tip-sample distance $r_{4Fe-NiO}$. Solid (black) and dashed (red) lines correspond to "spin up" (parallel) and "spin down" (antiparallel) orientations with respect to the Fe tip atom. All curves in the upper panels exhibit hysteresis (arrows indicate approach and retrace cycles), which result in the site- and spin-dependent energy dissipation visible in the lower panels.

where k_1 and k_2 correspond to the Fermi wave-vectors of majority and minority states, while c and b are parameters. The best fit for $J_1(r)$ has been obtained with $c = 30.85$ meV/Å^3, $b = 10.87$, $k_1 = -3.0720$ Å^{-1}, and $k_2 = 0.68410$ Å^{-1}, while for $J_2(r)$ with $a = -7390$ meV/Å^3, $b = 9.139$, $k_1 = -0.05006$ Å^{-1}, and $k_2 = 0.00269$ Å^{-1}. A similar scheme has been used for calculations of the iron tip. The effective Morse potential reads

$$V_{\mathrm{Fe}} = D[e^{-2\alpha(r-r_0)} - 2e^{-\alpha(r-r_0)}] \tag{3.13}$$

with $D = 0.4174$ eV, $r_0 = 2.845$ Å, and $\alpha = 1.3885$ Å^{-1} being experimentally determined parameters [51]. The ferromagnetic exchange interaction $J_{\mathrm{Fe}}(r)$ calculated in [52] has been fitted by Eq. 3.12 with $a = -0.4132$ meV/Å^3, $b = 1.355$, $k_1 = 1.284$ Å^{-1}, and $k_2 = 0.1513$ Å^{-1}.

To minimize the tip-sample interaction energy we have adapted the data from published first-principle calculations [12]: The total force curves have been integrated to obtain the distance dependent potentials, and recursively separated to obtain the pairwise interactions between the apex Fe atom of the tip with its surface counterparts. These potentials include all chemical as well as magnetic contributions and are of the form

$$V(r_{Fe-\alpha}) = -r_{\mathrm{Fe}-\alpha}(\frac{r_{\mathrm{Fe}-\alpha}}{d})^{-2n}(\frac{A}{1-2n} - \frac{B(r_{\mathrm{Fe}-\alpha}/d)^n}{1-n}) \tag{3.14}$$

with α corresponding to Ni↑, Ni↓, O↑, or O↓, and fitting parameters A, B, n. The potential $V(r_{Fe-\alpha})$ describes ≈ 340 bonds between all considered Fe and NiO atoms.

Our calculations show that due to the mutual interaction between tip and sample atoms the potential landscapes of the interacting atoms exhibit more than one minimum. At certain distances the energy barrier between two minima vanished and the atom jumped abruptly towards its new position. This can directly be seen in the distance dependent equilibrium interatomic separations at zero temperature plotted in the upper panel of Fig. 3.36. On all sites the foremost Fe tip atom as well as the surface atom directly underneath exhibits the above mentioned abrupt positional changes. The distances at which these jumps occur are site- and spin-dependent. Moreover, they are hysteretic, i.e., different during approach and retract cycles.

To quantify the dissipated energy due to the observed hysteresis we have calculated the total energy of the system E_{t} for all four different sites on NiO(001), including all magnetic and non-magnetic contributions for all considered bonds, as a function of $r_{\mathrm{4Fe-NiO}}$ (see lower panel of Fig. 3.36). At several $r_{\mathrm{4Fe-NiO}}$ values, jumps in atomic distances appear and E_{t} abruptly decreases, i.e., energy is released. Therefore, the energy curves are also hysteretic and exhibit a distinctive distance dependence.

The sum of all jumps is the total energy released in the system (ΔE_{t}) during one oscillation cycle. This energy is equivalent to the area of the force curve $-\partial E(r_{\mathrm{4Fe-NiO}})/\partial r_{\mathrm{4Fe-NiO}}$ typically regarded as a measure for the energy dissipation. Note that for our highly symmetric tip multiple distinct hysteresis loops are present

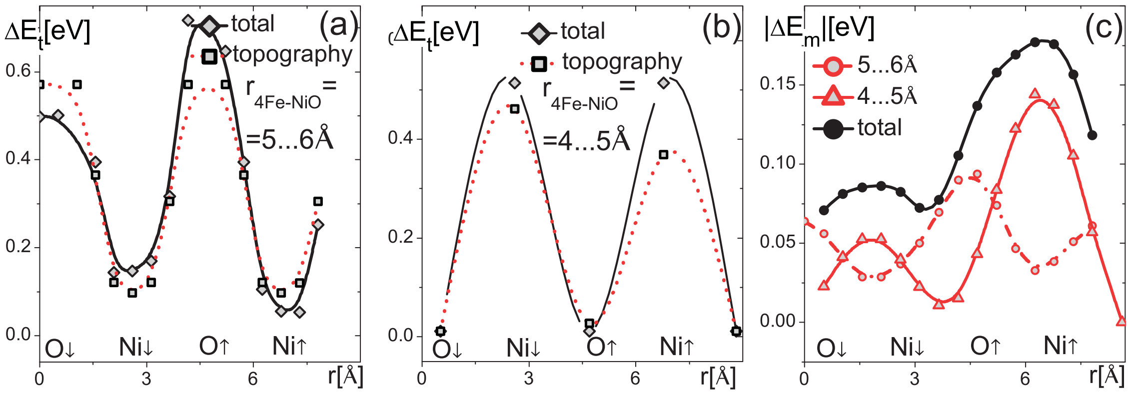

Figure 3.37: Total and non-magnetic energy along the [001] direction of NiO(001) for $r_{4\mathrm{Fe-NiO}}$ = 5...6 Å **(a)** and $r_{4\mathrm{Fe-NiO}}$ = 4...5 Å **(b)**. In (c) the difference between total and non-magnetic contribution, i.e., the magnetic dissipation, is shown for $r_{4\mathrm{Fe-NiO}}$ = 5...6 Å (triangles), $r_{4\mathrm{Fe-NiO}}$ = 4...5 Å (hollow circles). Additionally, the sum of both curves is plotted (black solid circles).

in all curves of Fig. 3.36. More realistic complex tip geometries would probably result in a continuous distance dependence. The energy loops are different not only for different chemical elements but also for ↑ and ↓ orientations of moments, meaning that even without any spin flips a dissipative magnetic contrast exists on Fe as well as on O atoms. The part of the energy dissipated due to the adhesion hysteresis may then excite versatile flip processes in NiO as well as in the Fe tip. Note that the magnetic dissipation is only one part of the total dissipated energy ΔE_{t}. The purely magnetic contribution can be extracted via subtraction of all non-magnetic contributions.

In Fig. 3.37 the site dependence along the [001]-direction of the total and the non-magnetic part of the dissipated energy is displayed for two distance regimes, i.e., $r_{4\mathrm{Fe-NiO}}$ = 5...6 Å (a) and $r_{4\mathrm{Fe-NiO}}$ = 4...5 Å (b), respectively. Each point corresponds to the sum of all jumps shown in Fig. 3.36 in the respective distance regime. F Interestingly, in our simulation the site of largest dissipation depends on the tip-sample distance $r_{4\mathrm{Fe-NiO}}$. This is already evident in Fig. 3.36, where jumps in energy for Ni atoms are larger than those for O atoms at $r_{4\mathrm{Fe-NiO}}$ = 4...5 Å, while the opposite is true at $r_{4\mathrm{Fe-NiO}}$ = 5...6 Å. Furthermore, magnitude and sign of the dissipated energy depends on the distance regime through which the tip oscillates and therefore depends on the oscillations amplitude A_0.

To obtain the spin-dependent dissipation, the non-magnetic contribution is subtracted from the total dissipation. For small amplitudes, e.g., $A_0 = 1$ Å, the contrast is inverted, if the distance regime is changed from $r_{4\mathrm{Fe-NiO}}$ = 5...6 Å to $r_{4\mathrm{Fe-NiO}}$ = 4...5 Å. Thus, the experimentally observed contrast can depend on A_0. Note that such small amplitudes are experimentally accessible and actually often used nowadays in q-plus tuning fork set-ups [53]. Since the experimental data presented in Fig. 3.35 are recorded with $A_0 = 6.65$ nm, the sum of both distance regimes, i.e., the black curve in (c) is displayed as well. The range of about 100 meV between minimum and maximum, is close to the experimental value. Note that for distances larger than 6 Å no further jumps occur. Therefore, for sufficiently large amplitudes the contrast only depends on the tip-sample distance at the lower turnaround point, but not on A_0.

As for the experimental data, the calculated dissipated energy ΔE_t in all three curves of Fig. 3.36 is different on the four chemically and magnetically distinctive sites, i.e., Ni↑, Ni↓, O↑ and O↓, respectively. Moreover, the sign of the contrast in Fig. 3.36 coincides with the calculated contrast for the sum. Considering that the atomic configuration of model tip and real tip are probably quite different, the order of magnitude (tens of meV) for the calculated spin-dependent dissipation contrast is in reasonable good agreement with the experimental data.

Our simulations show that the NiO(001)/Fe-tip system exhibit a strikingly complex site-, distance-, and spin-dependent adhesion hysteresis for small tip-sample separation, which can explain magnitude and sign of the experimentally observed energy dissipation. Since we did not allow for spin flips in our model, such spin flips are not a prerequisite for magnetic dissipativion to occur as proposed in the Caldeira-Leggett model [38]. However, the released energy may subsequently excite versatile spin-flips either in the tip or in the sample.

References

[1] U. Kaiser and A. Schwarz and R. Wiesendanger, Nature **446**, 522 (2007).

[2] R. Schmidt *et al.*, Nano Lett. **490**, 211 (2009).

[3] R. Schmidt *et al.*, Phys. Rev. Lett. **106**, 257202 (2011).

[4] R. Schmidt, A. Schwarz, and R. Wiesendanger, Phys. Rev. B **86**, 174402 (2012).

[5] E. Y. Vedmedenko *et al.*, Phys. Rev. B **85**, 174410 (2012).

[6] M. Liebmann *et al.*, Rev. Sci. Instrum. **73**, 3508 (2002).

[7] T. Moriya, Solid State Comm. **2**, 239 (1964).

[8] S. Alexander und P.W. Anderson, Phys. Rev. **133**, A1594 (1964).

[9] P. Wahl *et al.*, Phys. Rev. Lett. **98**, 056601 (2007).

[10] L. Zhou *et al.*, Nature Phys. **6**, 187 (2010).

[11] A. S. Foster and A. L. Shluger, Surf. Sci. **490**, 211 (2001).

[12] H. Momida and T. Oguchi, Surf. Sci. **590**, 42 (2005).

[13] C. Lazo, V. Caciuc, H. Hölscher, and S. Heinze, Phys. Rev. B **78**, 214416 (2008).

[14] K. Tao *et al.*, Phys. Rev. Lett. **103**, 057202 (2009).

[15] A. Kubetzka *et al.*, Phys. Rev. Lett. **94**, 087204 (2005).

[16] H. Hölscher *et al.*, Appl. Phys. Lett. **81**, 4428 (2002).

[17] N. Sasaki and M. Tsukada, Jpn. J. of Appl. Phys. **39**, L1334 (2000).

[18] T. Trevethan and L. Kantorovich, Nanotechnology **15**, S34 (2004).

[19] S. A. Ghasemi *et al.*, Phys. Rev. Lett. **100**, 236106 (2008).

[20] J. P. Perdew, K. Burke and M. Ernzerhof, Phys. Rev. Lett. **77**, 3865 (1996).

[21] K. Schwarz, P. Blaha, and G. K. H. Madsen, Comput. Phys. Commun. **147**, 71 (2002).

[22] D. A. Thompson and J. S. Best, IBM J. Res. Dev. **44**, 311 (2000).

[23] G. A. Gibson and S. Schultz, J. Appl. Phys. **73**, 4516 (1993).

[24] P. Grütter *et al.*, J. Appl. Phys. **69**, 5883 (1991).

[25] D. C. Ralph, M. D. Stiles, J. Mag. Mag. Mat. **320**, 1190 (2008).

[26] G. A. Prinz, Science **282**, 1660 (1998).

[27] S. Krause, *et al.*, Science **317**, 1537 (2007).

[28] L. Néel, Ann. Géophys. **5**, 99 (1949).

[29] W. F. Brown, Phys. Rev. **130**, 1677 (1963).

[30] G. M. Pastor, J. Dorantes-Davila, S. Pick, and H. Dreyssé, Phys. Rev. Lett. **75**, 326 (1995).

[31] G. Bihlmayer, in *Reduced Dimensions II: Magnetic Anisotropy*, edited by S. Blügel, Magnetism goes Nano (Jülich, 2005).

[32] M. Guggisberg*et al.*, Phys. Rev. B **61**, 11151 (2000).

[33] J. Bork *et al.*, Nat. Phys. **7**, 901 (2011).

[34] S. Loth *et al.*, Science **329**, 1628 (2010).

[35] A. A. Khajetoorians *et al.*, Nature **467**, 1084 (2010).

[36] S. Morita, R. Wiesendanger, and E. Meyer (Eds.), Noncontact Atomic Force Microscopy, Springer Verlag (2002).

[37] M. P. Magiera *et al.*, Euro. Phys. Lett. **87**, 26002 (2009).

[38] F. Pellegrini *et al.*, Phys. Rev. Lett. **105**, 146103 (2010).

[39] M. Gauthier and M. Tsukada, Phys. Rev. B **60**, 11716 (1999).

[40] N. Sasaki and M. Tsukada, Japn. J. Appl. Phys. **39**, L1334 (2000).

[41] G. Teobaldi *et al.*, Phys. Rev. Lett. **106**, 216102 (2011).

[42] C. G. Kinniburgh, J. A. Walker, Surf. Sci. **63**, 274 (1977).

[43] M. R. Welton-Cook, M. Prutton, J. Phys. C: Solid State, Phys. **13**, 3993 (1980).

[44] T. Okazawa, Y. Nakagawa and Y. Kido, Phys. Rev. B **69**, 125412 (2004).

[45] E. E. Zhurkin, M. Hou, J. Phys.: Condens. Matter **12**, 6735 (2000).

[46] A. A. Dzhurakhalov, M. Hou, Phys. Rev. B **76**, 045429 (2007).

[47] M. C. Payne *et al.*, Rev. Mod. Phys. **64**, 1045 (1992).

[48] C. X. Guo *et al.*, J. Am. Chem. Phys. **84**, 2677 (2001).

[49] T. E. Karakasidis, D. G. Papageorgius and G. A. Evangelakis, Appl. Surf. Sci. **162**, 223 (2000).

[50] G. Fischer *et al.*, Phys. Rev. B. **80**, 014408 (2009).

[51] L. A. Girifalco and V. G. Weizer, Phys. Rev. **114**, 687 (1959).

[52] I. Turek, V. Drchal, J. Pajda, J. Kudrnovsky, and P. Bruno, Phys. Rev. B **64**, 174402 (2001).

[53] F. J. Giessibl, Rev. Mod. Phys. **75** 1287 (2003).

3.6 Theory and simulation

E. Y. Vedmedenko

In the three-year period between 2011 and 2013 the efforts of the theory group have been devoted to the three main topics:
- temperature dependent properties and stability of small classical and quantum systems at finite observation times;
- theoretical proposal for the manipulation of magnetic domain walls using the tip of a spin-polarized scanning tunneling microscope;
- theoretical proposal for the spin manipulation using the tip of an atomic force microscope.

The work on the first topic permitted us to understand several essential issues like critical temperatures for incomplete statistical averaging corresponding to a finite observation time, the time dependence of magnetization switching, the stability of non-collinear nanostructures, and to elaborate new calculation techniques. This knowledge has been used to propose new concepts for the experimental manipulation of magnetic domain walls and single atoms. While several findings already allowed explaining experimental results, other are still waiting for their experimental realization. In the following the three scientific directions and corresponding publications are reviewed.

3.6.1 Critical properties at finite temperatures and dynamics of classical and quantum magnetic nanosystems

T. Stapelfeldt, K. Them, N. Mikuszeit, R. Wieser, and E. Y. Vedmedenko

The theory of collective magnetic order is usually concerned with infinite or semi-infinite systems [1]. Real magnetic samples, however, have a finite size, and magnetic properties are measured during a finite observation period. This gives rise to many interesting questions as a matter of principle. For magnetic nanoparticles and atomic clusters it also has profound physical consequences. The recent advances in controlling and measuring magnetic properties of nanoparticles [2] as well as applications for magnetic data storage technology rely on the fact that information, i.e. the magnetic state of a finite, small area representing a single bit, is stable over a finite observation time. To transfer information one tries to use also some novel types of magnetic ordering, for example, spin spirals. The stability of those non-collinear configurations are also extremely important and are the subject of ongoing scientific discussion.

We tried to shed light on two issues: What is the critical temperature of magnetic nanoobjects and how can it be measured? What is the life-time of quantum spins of magnetic adatoms on semiconducting and metallic substrates perturbed by the tip of a spin-polarized scanning tunneling microscope (SP-STM)? The related study of stability of non-collinear Dzyloshinski-Moriya spirals [3] has been performed in a close collaboration with experiment and has been discussed in Chapter 3.3.

Crossover temperatures of finite magnets at finite observation times

The Curie temperature of a ferromagnetic sample is a typical concept that must be reconsidered for nanosized objects. From the experimental point of view, this is a well defined quantity which can be measured, e.g. as a function of the size L of the nanoparticle. From the theoretical point of view, there is no Curie temperature as there is no phase transition in a system with a finite number of degrees of freedom. Magnetic susceptibilities as well as the specific heat stay finite in the entire temperature regime. Nevertheless, they show enhancements at $T = T_{\mathrm{C}}(L)$, which defines a "Curie temperature" up to some residual arbitrariness. Usually, one finds $T_{\mathrm{C}}(L) < T_{\mathrm{C}}(\infty)$ for open boundaries.

Below $T_{\mathrm{C}}(L)$, the magnetic state of the system is not stable temporally. This gives rise to superparamagnetic (SPM) behavior for temperatures $T_{\mathrm{b}}(L) < T < T_{\mathrm{C}}(L)$, which is neglected in finite-size-scaling. It is rather the blocking temperature $T_{\mathrm{b}}(L)$ than $T_{\mathrm{C}}(L)$ that is relevant for storage technology since it characterizes the crossover from the stable ferromagnetic (FM) state at low T to the SPM state where the system "switches" between different energy minima determined by magnetic anisotropies. The relative position of $T_{\mathrm{b}}(L)$ with respect to $T_{\mathrm{C}}(L)$ is not well understood. Experimentally, both quantities are usually defined via the peak in the temperature-dependent susceptibility, i.e. one and the same physical phenomenon, namely an increase of fluctuations is used for the determination of the lower as well as of the upper limit of the SPM temperature range. Furthermore, the theoretical modelling is often inconsistent: If the transition from a paramagnetic (PM) to an ordered ferromagnetic state is addressed, the nanosystem is described within models of interacting *microscopic* (atomic) spins. On the other hand, investigations on superparamagnets refer to a *macrospin* representing the magnetic state of the nanoparticle as a whole. While it is plausible to assume a simple macrospin model to be valid below the Curie temperature, a microscopic and systematic theoretical underpinning is highly desirable. The topic is complicated by the fact that $T_{\mathrm{b}}(L)$ cannot be considered as a pure property of the system – it must be seen as a relative value, which depends on the observation time τ. For $\tau \to \infty$, there is no blocking of the magnetization because of quantum tunneling and thermal excitations, and hence $T_{\mathrm{b}}(L) \to 0$. For $\tau \to 0$ (referring to e.g. laser-probe methods), $T_{\mathrm{b}}(L) \to T_{\mathrm{C}}(L)$ while for intermediate τ (like in spin-polarized scanning tunneling microscopy) $0 < T_{\mathrm{b}}(L) < T_{\mathrm{C}}(L)$.

The discussion shows that existing theoretical studies based on a microscopic spin model [6] have to be refined when dealing with the superparamagnetic regime. In our recent publication [9] we show that the latter can nicely be achieved by a Monte-Carlo (MC) approach, where with an increasing number of MC steps per temperature, the blocking temperature $T_{\mathrm{b}}(L)$ decreases. Furthermore, a simple but reliable *effective* theory is utterly needed to cover the phenomenology of magnetic nanoparticles. Here we define a two-point order-parameter correlation function $G(r)$, which explicitly takes account of the finite system size. It turns out that the model $G(r)$ is exceptionally effective in describing the numerical data for the entire temperature range. Motivated by this finding, unambiguous definitions of $T_\mathrm{C}(L)$ and $T_\mathrm{b}(L)$ can be given, and moreover, a new method to determine critical temperatures for infinite systems is proposed. For low temperatures, however, the exponential trend persists only at small r for corner atoms along the edges of the array only. For the following we define a two-point correlation function, which is independent of the direction and depends on the distance r only and which furthermore directly refers to X-ray- or neutron-scattering experiments:

$$\widetilde{G}(r) = G(r) - M^2 = \frac{1}{n(r)} \sum_{\substack{i<j \\ |r_i - r_j| = r}} \langle S_i S_j \rangle - M^2 \,. \tag{3.15}$$

Here, the sum in the first term runs over all $n(r)$ pairs separated by the distance r. The second term involves the magnetization $M = |\sum_i \langle S_i \rangle|/N$ with N being the number of sites.

We have calculated the above-defined correlation function $\widetilde{G}(r)$ for different classical spin models on lattices with a finite number of sites L. Especially interesting results have been obtained for two-dimensional lattices of Ising or Heisenberg spins. Data for a 5×5 Ising system are shown in Fig. 3.38(b). The correlations with respect to a central and to a corner atom of a 20×20 2D Ising square array are shown in Fig. 3.38(c) and (d), respectively. Analyzing the data of Fig. 3.38(b) in detail we identify three specific temperatures: (i) For any finite T, the magnetization is $M = 0$, while for $T_1 = 0$ the magnetization jumps to $M = 1$. This explains the corresponding jump of $\widetilde{G}(r)$ seen in Fig. 3.38(a) and (b); (ii) at the temperature T_2 ($1.7J$ in fig. 3.38(b)) the curvature of $\widetilde{G}(r)$ and $G(\boldsymbol{r})$ changes its sign; and (iii) at the temperature $T_3 = 2.3J$ the trend of $\widetilde{G}(r)$ changes from algebraic convex to exponential.

The first characteristic temperature T_1 is evidently equivalent to $T_\mathrm{b}(L)$. The mostly remarkable feature is the change in the curvature of $\widetilde{G}(r)$ from concave to convex at some temperature which cannot be expected from previously published results.

To identify the physical meaning of T_2 and T_3, a model function $G(r)$ has been constructed.

$$G(r) = G(r, T) \approx B(T) e^{-r/\varepsilon(T)} + y(T) \,, \tag{3.16}$$

The form of $G(r)$ is reminiscent of the OZ theory. Note, however, Eq. (3.16) refers to a finite system and that it applies to all distances r up to the system boundary. In particular, there are no constraints on the sign of the r-independent constants $\varepsilon(T)$, $B(T)$ and $y(T)$.

Using this model $G(r)$, the numerically exact expectation values for the 1D, 2D and 3D finite Ising systems (Fig. 3.38) can be used to fit the unknowns $\varepsilon(T)$, $B(T)$ and $y(T)$. It turns out that the quality of the fit is exceptionally good, see lines in (a) and (b). It excellently describes the data in the entire temperature range. From this fit (see details in [9]) we interpret T_3 as the Curie temperature of the infinite system: $T_3 \approx T_\mathrm{C}(\infty)$, and the temperature $T_2 = T_\mathrm{C}(L)$ corresponding to the change in the

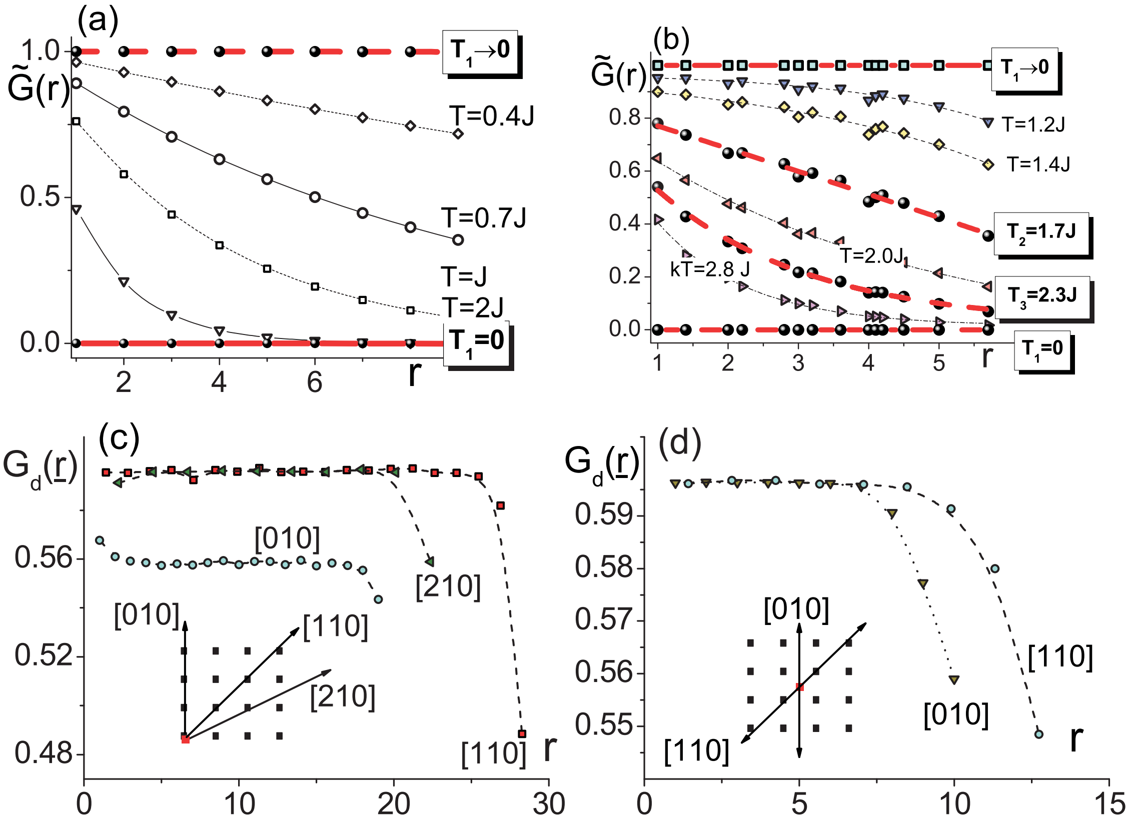

Figure 3.38: Two-point correlation functions $\widetilde{G}(r)$ (symbols) calculated for an open Ising chain consisting of 10 atomic sites (a) and for an open 5×5 Ising square lattice (b). Correlation functions $G(r)$ starting from an edge (c) and from the central (d) atom obtained from MC simulations for an open 20×20 Ising square lattice at $T = 0.5J \ll T_{\mathrm{C}}(\infty)$. The lines in (a) and (b) are fits of the numerical data by the model correlation function given in Eq. (3.16). Three thick lines correspond to three critical temperatures: the blocking temperature $T_{\mathrm{b}}(L)$, the reduced Curie temperature of a finite sample $T_{\mathrm{C}}(L)$, and the Curie temperature of an infinite sample $T_{\mathrm{C}}(\infty)$.

curvature of $\widetilde{G}(r)$ gives the reduced Curie temperature of a finite magnet. Thus, our method yields a good estimate of $T_\mathrm{C}(\infty)$, $T_\mathrm{C}(L)$ and $T_\mathrm{b}(L)$ from a single calculation without finite-size scaling. Our analysis shows that $T_\mathrm{C}(L)$ as well as $T_\mathrm{b}(L)$ satisfy the finite-size scaling law $(T_\mathrm{C}(\infty) - T(L))/T_\mathrm{C}(\infty) = (L/L_0)^{-1/\nu}$ [10].

In conclusion, motivated by an effective Landau free-energy functional, a simple analytical form for the two-point magnetic correlation function is suggested for magnetic nanoparticles and shown to excellently fit numerically exact Ising, Heisenberg and Monte-Carlo data of finite anisotropic spin models. A complex phenomenology governed by different temperature scales emerges and is traced back to the enhancement of fluctuations at the system's boundary and to an incomplete statistical average corresponding to a finite observation time. Unambiguous definitions of crossover temperatures for finite systems and an effective method to estimate the critical temperature of corresponding infinite systems are given. Precise definitions for the Curie and the blocking (crossover) temperatures of a finite system can be given, and a new method to estimate $T_C(\infty)$ is suggested – based on a quantity $G(r)$, which is related to the experimentally accessible magnetic structure factor $S(\mathbf{q})$. Our results can thus be expected to be highly relevant for (theoretical and experimental) studies of $S(\mathbf{q})$ of nanoarrays and for direct investigations of $G(r)$ of individual particles.

Finite temperature dynamics of magnetic quantum systems: Applications to spin-polarized scanning tunneling microscopy

Spin sensitive studies of individual magnetic adatoms and atomic ensembles on surfaces with spin-polarized scanning tunneling microscopy (SP-STM) have raised the necessity of a quantum-mechanical description of the spin dynamics evoked by SP-STM experiments. Magnetization curves obtained in experiments are typically described using the expectation values of observables using a time independent, i.e. kinematic, Gibbs ensemble average. However, an SP-STM measurement is a time-average of the orientation of a spin component selected by the given spin orientation of the probe tip. Therefore, the dynamics of the magnetization in the sample under study remains unknown within the experimental time resolution. It would be helpful to compensate this lack of knowledge with theoretical investigations.

In a recent publication [11] we calculate the real time non-equilibrium dynamics of small quantum spin systems at finite temperatures. The mathematical framework originates from the C^*-approach to quantum statistical mechanics and is applied to samples investigated by means of spin-polarized scanning tunneling microscopy. The numerical scheme is shown in Fig. 3.39.

The SP-STM set-up is approximated by (in general) two different Hamiltonians in our approach. There is a Hamiltonian H for the free system and, if a measurement is started, we get an additional hermitian operator P for the interaction between the tip and the sample. Hence, if the tip is moved towards the surface, the system switches from H to $H + P$ because of the sudden emergence of tunneling electrons causing the interaction between the tip and the sample.

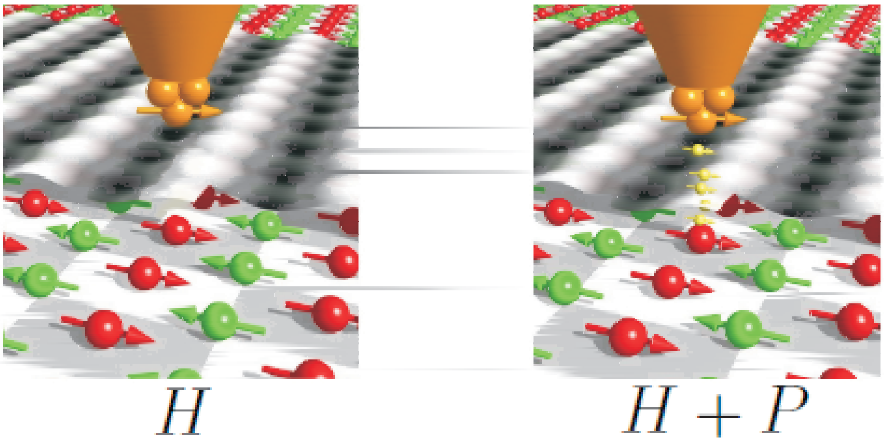

Figure 3.39: H describes the free system and $H + P$ describes the perturbed system, i.e. the system with interaction between the tip and the sample.

The STM-tip can be used to prepare a system with desired expectation values. For the corresponding state a perturbed Kubo-Martin-Schwinger description $\omega^{\beta P}$ has been used. Quantum fluctuations around thermal equilibrium were analyzed and calculated using the density matrix formalism $\omega^{\beta}(\tau_t^P(S_z))$. The evaluation of expectation values of $\omega^{\beta}(\tau_t^P(S_z))$ have been performed using the exact diagonalization technique for a given Hamiltonian of a system under investigation. It is demonstrated that the calculated time averaged expectation values agree with the time averaged experimental data for magnetization curves. After this check up the proposed method was used to investigate the dynamics of a sample for shorter times than the resolution time of the experimental setup; i.e., on time scales which are not accessible for an STM.

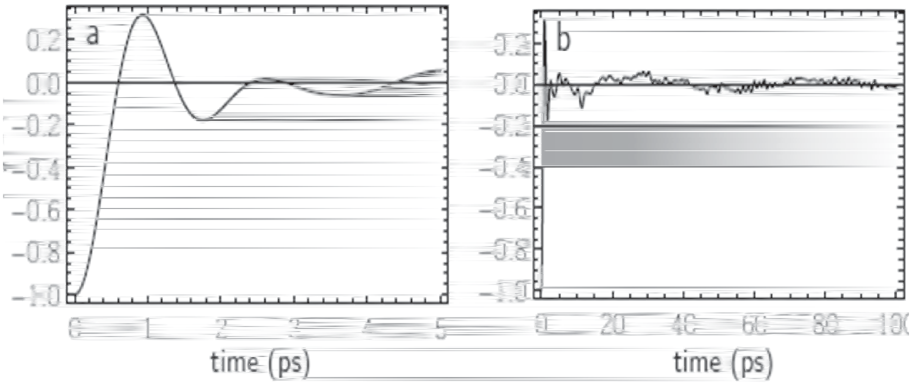

Figure 3.40: Return to equilibrium for the spin component S_y of an iron atom on an indium antimonide surface for short and long times at $T = 4.2$ K. (a): The experimentally estimated life time of 800 fs is in good agreement with the calculated relaxation process. (b): After the relaxation is done the expectation value remains near thermal equilibrium $\omega^{\beta}(S_y) = 0$.

Predictions for relaxation times (using $\omega^{\beta P}(\tau_t(S_z)))$ of single spins on metallic and semiconductor surfaces were made and compared with experimental data obtained for Fe adatoms on InSb and Co adatoms on Pt(111).

It is a priori not clear, whether the described small finite quantum system is able to approach its equilibrium. Fig. 3.40 shows our results for the short- and long-time dynamics of a single Fe adatom on an InSb substrate coupled to bath electrons. From this data one can see that taking into account $n = 8$ substrate electrons acting as a heat bath are sufficient, for a single adatom at zero magnetic field, to reach thermal equilibrium, when a perturbed Kubo-Martin-Schwinger state is used as initial configuration. After a characteristic time t_0 the expectation value $\langle S^\alpha \rangle_2(t)$ relaxes and fluctuates around its thermal equilibrium value, i.e.,

$$\omega^{\beta P}(\tau_t(S_z)) \longrightarrow\approx \omega^{\beta}(S_z) = \frac{Tr\left(e^{-\beta H} S_z\right)}{Tr\left(e^{-\beta H}\right)}. \tag{3.17}$$

The amplitude and the form of fluctuations are temperature dependent. To make sure that we get realistic relaxation times, we compared our calculations with the lifetime of an Fe adatom on InSb estimated in recent SP-STM experiments [12, 13]. The experimental estimation of the lifetime $t_{l.t.}$ of the excited state was done by the formula $t_{l.t.} = \frac{\hbar}{2\Delta E}$, where ΔE is the energy difference between the states, obtained from inelastic SP-STM. According to our calculations the relaxation can be approximated with an exponential function, which is decaying on the time-scale of nanoseconds and, hence, is in agreement with experimental results.

Apart from estimations of the time-scale of the spin relaxation the temperature dependence of the quantum fluctuations in adatom systems has been investigated. It is demonstrated that the lifetime of saturated states for single adatoms increases with increasing anisotropy barrier and decreasing temperature. Additionally, it has been demonstrated that even a weak perturbation due to tunneling electrons initiates a quantum tunneling in otherwise diagonal systems. The expectation value of magnetization at $B_z = 0$ remains nearly zero.

3.6.2 Control of ferro- and antiferromagnetic domain walls with spin currents

T. Stapelfeldt, R. Wieser, and E. Y. Vedmedenko

Recent exciting developments towards new storage and logic devices are based on the current- and field-driven motion of magnetic domain walls (DWs) [14, 15]. To read or write a bit of information, a DW has to be moved towards the reading or writing device. However, neither external fields nor currents allow us to address each DW individually. A spin-polarized current moves neighboring DWs in the same direction, while a magnetic field moves them in opposite directions. In previous investigations, the individual manipulation of a DW has been achieved by the stray field emanating from a tip of a magnetic force microscope (MFM) [4]. The best resolution of the MFM experiments is of the order of 20 nm. The goal of our investigations was to give a comprehensive theoretical concept for the manipulation of narrow DWs of 2 nm width in nanowires of monolayer thickness, which is about one order of magnitude smaller than for walls in soft magnetic materials. Special attention has been paid to the elaboration of the multiscale schemes which were able to give a reliable description of the domain wall movements [5].

The influence of an SP-STM tip on a DW has been studied by means of the atomistic spin dynamics as well as by Monte-Carlo (MC) simulations. Several magnetization geometries and time regimes have been analyzed. Our investigations have shown that this setup might be suitable for manipulation of ferromagnetic [6] as well as antiferromagnetic [7] domain walls. The theoretically proposed setup is depicted in Fig. 3.41

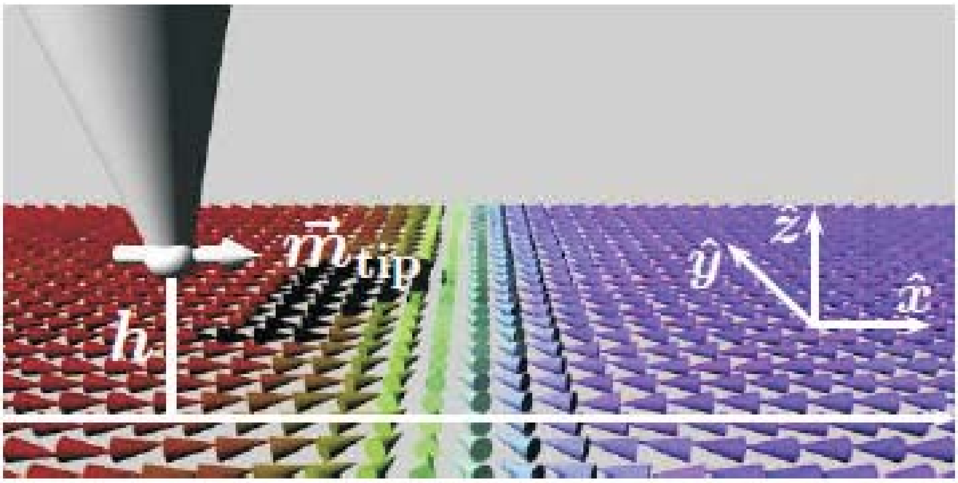

Figure 3.41: Scheme of the initial spin configuration of the sample. A DW elongated in y-direction separates two domains. The spins in the domains point along the easy-axis with blue ($-x$) and red colored cones ($+x$). A tip with a magnetization $\vec{m}_{\text{tip}}$ and distance h from the sample moves towards the DW on the indicated track (white dashed line).

An example is given by a ferromagnetic monolayer stripe of dimensions up to $L_{\text{x}} \times L_{\text{y}} = 40\ a \times 70\ a$ (15 nm × 26 nm (sc(001) or bcc(110) stacking) with the lattice constant a. Each site is occupied by a classical Heisenberg moment $\vec{S}_i = (S_i{}^x, S_i{}^y, S_i{}^z)$ of unit length $\vec{\mu}_i/\mu_s$. The magnetic properties are given by the following Hamiltonian:

$$\mathcal{H} = -J \sum_{\langle ij \rangle} \vec{S}_i \vec{S}_j - D_x \sum_i (S_i^x)^2 + D_z \sum_i (S_i^z)^2, \tag{3.18}$$

where $J > 0$ denotes the ferromagnetic exchange coupling between nearest neighbors, $D_x > 0$ is an easy-axis and $D_z > 0$ a hard-axis anisotropy, respectively. Hence, the rotation of magnetization is confined to the xy-plane. The dipolar coupling of such an ultrathin in-plane system is small and has been neglected. Material parameters in the range typical for recently studied experimental systems like Fe/W(110) or Co/Pt(111) monolayers ($J = 10...13$ meV, $D_x = 0...5$ meV and $D_z = 0...2.5$ meV) have been used in the calculations.

For the spin dynamics calculations the motion of DWs has been described by the generalized Landau-Lifshitz-Gilbert equation at zero temperature

$$\begin{aligned}\frac{\partial \vec{S}_i}{\partial t} = & - \frac{\gamma}{(1+\alpha^2)\,\mu_S} \vec{S}_i \times \left[\vec{H}_i + \alpha \left(\vec{S}_i \times \vec{H}_i \right) \right] \\ & + \mathcal{C} \vec{S}_i \times \vec{\mathcal{T}}_i + \mathcal{D} \vec{S}_i \times \left(\vec{S}_i \times \vec{\mathcal{T}}_i \right) \ , \end{aligned} \tag{3.19}$$

with the gyromagnetic ratio γ, the Gilbert damping $\alpha = 0.025$, the internal field $\vec{H}_i = -\partial \mathcal{H} / \partial \vec{S}_i$, and the spin current $\vec{\mathcal{T}}_i$. The last two terms are the contributions (precession and relaxation) of the spin torque. The influence of the electric current is described similar to the case of a spin valve $\mathcal{C} = 0$ and $\mathcal{D} = 1$. In the MC scheme the *sd*-model has been used to account for the spin torque of tunneling electrons:

$$\mathcal{H}_{\mathcal{T}} = -g \sum_i \vec{\mathcal{T}}_i \cdot \vec{S}_i, \tag{3.20}$$

where g is the coupling constant. In the following we set g to unity, so that the whole information on the spin-polarized current is given by $\vec{\mathcal{T}}_i$.

In the low-bias regime the local strength and the orientation of the tunneling current can be successfully described by the Tersoff-Hamann model:

$$\vec{\mathcal{T}}_i = -I_0 \cdot \mathrm{e}^{-2\kappa \sqrt{(x_i - x_{\mathrm{tip}})^2 + (y_i - y_{\mathrm{tip}})^2 + h^2}} \cdot P \cdot \vec{m}_{\mathrm{tip}}, \tag{3.21}$$

with the polarization P of the tip-magnetization $\vec{m}_{\mathrm{tip}}$ (a unit vector in the direction of the tip-magnetization), the inverse decay length of the wave-function in vacuum κ, the time dependent tip and atom positions $\vec{r}_{\mathrm{tip}} = (x_{\mathrm{tip}}, y_{\mathrm{tip}}, h, t)$, $\vec{r}_i = (x_i, y_i, 0, t)$, and the current density I_0. In the spin dynamics simulation we set $I_0 = 1.0 \cdot 10^7 \frac{\mu_S}{\gamma t J}$, however, the MC procedure does not allow for the direct time evaluation, therefore we chose a current density sufficiently high for domain wall manipulation. κ contains the work-function ϕ of the tip material and is set to 4.5 eV, in the range of magnetic materials used in experiments (e.g. Fe or Cr). For the chosen sample and tip parameters we assume the spin torque acting on the magnetic moments to be large compared to Oersted-fields and Joule-heating, which have been neglected in our simulations. The simulations have been performed for three principal geometries: **I** $\vec{m}_{\mathrm{tip}} || \pm x$; **II** $\vec{m}_{\mathrm{tip}} || \pm y$, and **III** $\vec{m}_{\mathrm{tip}} || \pm z$. An initial tip-wall configuration is shown in Fig. 3.41. During the simulation the tip is moved at a constant height $h \; || + z$ along the stripe (in $+x$-direction) with a constant velocity v_{tip}. All our calculations correspond to the experimental constant-height mode with a spin current sufficiently high to influence the magnetization of a DW. The time dependence of the DW displacement Δx_{DW} for

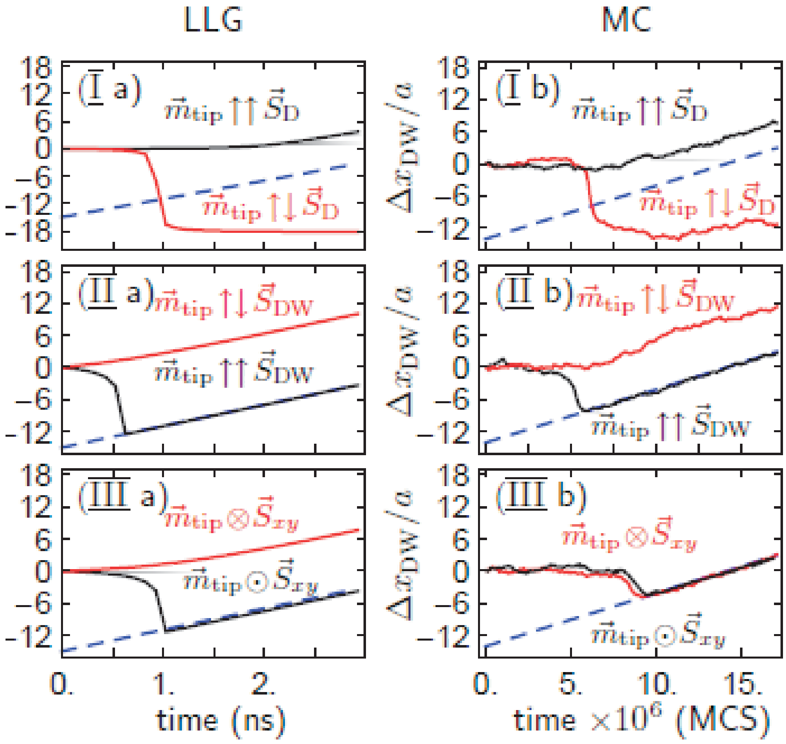

Figure 3.42: Domain wall displacement $\Delta x_{\rm DW}$ of a ferromagnetic stripe versus time. Results for MC simulations in the left column (MC) and for spin dynamics (LLG) in the right column. The tip moves with constant velocity marked by the dashed line. (a) and (b) for a tip magnetization parallel and antiparallel to the starting domain ($\vec{m}_{\rm tip}|| \pm x$). (c) and (d) parallel and antiparallel to the DW orientation ($\vec{m}_{\rm tip}|| \pm y$). (e) and (f) in- and out-of-plane ($\vec{m}_{\rm tip}|| \pm z$), according to a stripe in the xy-plane.

the three scenarios is plotted in Fig. 3.42. The black/gray solid curves correspond to the parallel/antiparallel orientation of the tip to a corresponding axis while the dashed line represents the tip displacement.

As one can see from Fig. 3.42 for ferromagnetic domain walls, almost all studied geometries are suited for DW manipulation as the black and gray lines corresponding to the displacement of the walls follow the dashed line representing the motion of the tip. One can also see that both simulation methods give identical results with one exception revealed, for $\vec{m}_{\mathrm{tip}} \otimes \vec{S}_{\mathrm{d}}$. This effect is a result of the different simulation models and disappears in the regime of strong currents, when neglecting the hard-axis anisotropy, and also in the regime of strong damping. The detailed analysis given in [6–8] has demonstrated that there are at least three different modes suitable for DW manipulation, but the investigation of costs and benefits reveals the $\vec{m}_{\mathrm{tip}} \uparrow\uparrow \vec{\mathrm{S}}_{\mathrm{DW}}$ as the optimal one. In order to manipulate the antiferromagnetic domain walls the tip polarization $\vec{m}_{\mathrm{tip}}$ has to be perpendicular to the magnetization inside the domains and domain wall. The direction of the domain wall motion is identical for $\vec{m}_{\mathrm{tip}}|| \pm z$. To change the direction of the domain wall motion one has to change the orientation of the tip polarization [7].

The theoretical time and distance dependence of the conductivity G shows characteristic features for each studied geometry and can be used in future experiments for the identification of the corresponding manipulation modes.

3.6.3 Theoretical concepts of dynamical switching of single spins by a non-contact force microscope tip.

Q. Zhu, R. Wieser, and E. Y. Vedmedenko

Spin-sensitive studies of magnetic surfaces at the atomic scale are currently a very active field of research. Recently, magnetic exchange force microscopy (MExFM) experiments demonstrated that spin mapping with atomic resolution can also be achieved with an atomic force microscopy (AFM) based setup, which brings several advantages with respect to scanning tunneling microscopy and spectroscopy.

Until now the AFM-based experiments were utilized for magnetic imaging only. The scientific aim of our investigations is to develop a realistic theoretical concept of the atomic-scale spin-dependent dissipation observed in recent magnetic exchange force microscopy experiments and to propose a theoretical concept for the manipulation of individual spins or domain walls with the tip in non-contact MExFM experiments. We regard our work as a guide for future experiments.

Because the theoretical investigation of magnetic dissipation has been done in a close cooperation with the experiment, this study [16] is discussed in Chapter 3.5.3. Below, the study of the dynamical switching of a single spin by exchange forces [17] is reviewed.

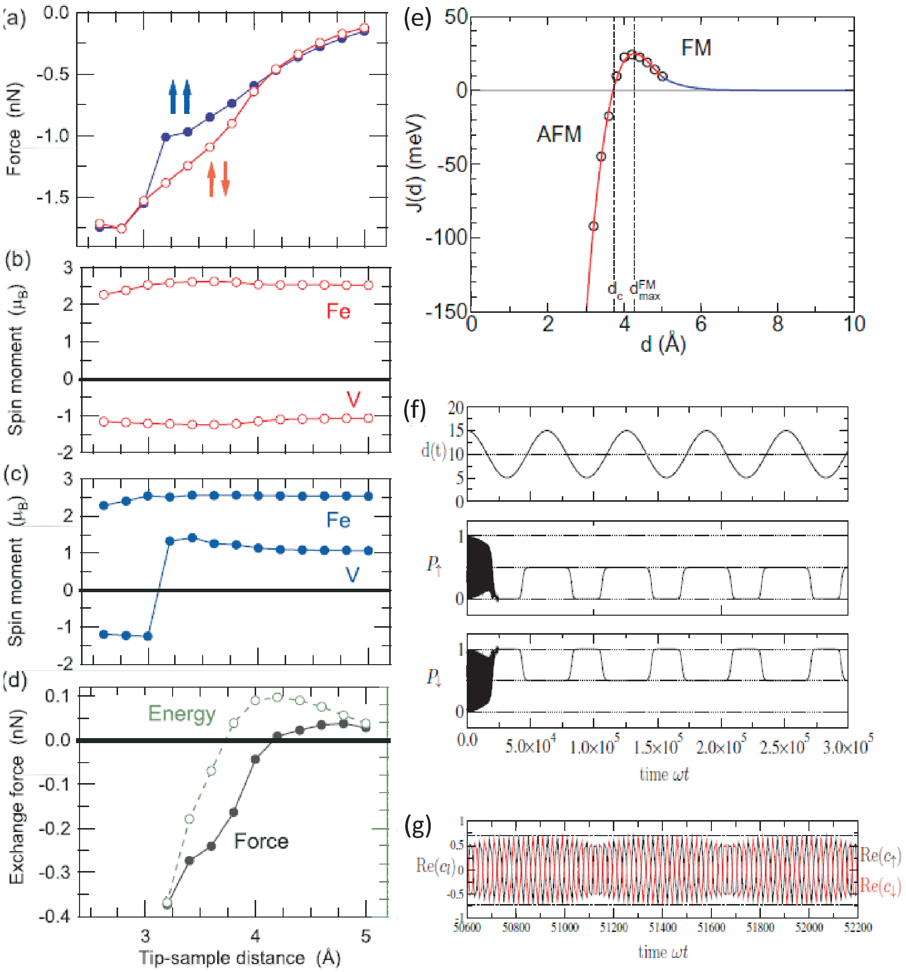

Figure 3.43: (a) Calculated z-component of the force between a vanadium-benzene molecule and a Fe tip in the ferro- (FM) and antiferromagnetic (AFM) starting configuration. The magnetic moments of the Fe apex and vanadium atoms for (b) an AFM and (c) a FM starting configuration. During the electronic self-consistency cycle, for each tip-molecule separation distance the magnetic moments of the tip-molecule system were allowed to relax. Therefore, in (c) the direction of the magnetic moment of V atoms switches when approached by the tip. (d) Exchange force and energy defined as the difference between the forces/energies in the AFM and FM configuration. Note that for a molecule-tip distance $d>3.8$ Å, a FM configuration is the ground-state while below this distance an AFM one is energetically more stable. Starting with a separation distance $d=3.0$ Å, a starting AFM configuration also relaxes to a FM one. (e) Distance dependence of the exchange constant J, which becomes negative (antiferromagnetic) below d_c and has a maximum in the ferromagnetic regime ($J > 0$) at $d_{\mathrm{max}}^{\mathrm{FM}}$.

In the quest for smaller magnetic data storage devices, single magnetic atoms or molecular magnets on surfaces have recently come into the focus of experimental research as they constitute the ultimate limit of a single bit. The experimental challenge is to position the atoms or molecules controllably on a surface, to stabilize the magnetization against thermal fluctuations, to read the magnetic state and to switch between states. The first issue has been tackled with the aid of different experimental techniques such as atom manipulation with the tip of a scanning probe microscope or by self-organization. While the reading of the magnetic state of a single atom or molecule has recently been demonstrated both for single magnetic atoms and molecules, no system has been identified that allows one to manipulate a single magnetic moment in a controlled manner so far. In this work, we use a combination of first-principles calculations and spin dynamics simulations to explore the feasibility of switching the spin of a single magnetic molecule due to the exchange forces with a magnetic tip in the dynamic mode of a MExFM.

We have chosen a simple model system for our study which consists of an Fe tip composed of five atoms and magnetic half-sandwich vanadium-, niobium- and tantalum-benzene molecules. This class of transition-metal-benzene molecules has been theoretically investigated and can be synthesized experimentally [18]. For simplicity, the influence of the substrate on the molecule was neglected and the direct interaction between the tip and the molecule has been investigated.

The first-principles density functional theory (DFT) calculations of the magnetic exchange forces between tip and molecule have been performed with the Vienna *ab initio* simulation package (VASP) by V. Cacius, C. Lazo, and H. Hölscher. The calculated forces for the Fe tip/V-benzene system in a ferro- (FM) and antiferromagnetic (AFM) alignment between Fe and V magnetic moments are displayed in Fig. 3.43(a). One can notice a significant difference between the forces calculated in the two configurations amounting to about 0.5 nN in a tip-molecule separation range between 3.2 and 3.5 Å. However, at a separation of 3 Å the two curves suddenly become identical. This surprising disappearance of the exchange force, which is the difference between the forces in the two alignments, for small tip-molecule distances, can be understood by looking at the magnetic moments of the Fe apex and V atoms. While the Fe and V moments in the AFM state, Fig. 3.43(b), remain nearly constant upon approaching the tip, there is a sudden jump in the FM state, Fig. 3.43(c), to an AFM alignment. This effect is due to the strong exchange interaction with the Fe tip which makes the ferromagnetic alignment unstable and it converges into the AFM solution in the DFT calculation.

It follows from the first-principles calculations that one might experimentally detect and even switch the magnetic state of a magnetic molecule depending on the distance between tip and molecule (see Fig. 3.43(e)). While the exchange energies are large enough to overcome the magneto-crystalline anisotropy barrier, the question how a switching process can be observed in a dynamic MExFM experiment needs to be addressed by spin dynamics simulations.

The dynamical response of the TM-benzene molecule, in the following V-benzene, disturbed by a magnetic tip have been studied in the framework of the quantum mechanical Heisenberg model [17]. The corresponding Hamiltonian reads:

$$\hat{\mathcal{H}} \;=\; -J\left(d\right)\mathbf{S}_{\mathrm{t}}\cdot\hat{\mathbf{S}}_{\mathrm{s}} - D_s^x\left(\hat{S}_{\mathrm{s}}^x\right)^2 - D_s^y\left(\hat{S}_{\mathrm{s}}^y\right)^2 - D_s^z\left(\hat{S}_{\mathrm{s}}^z\right)^2 \ . \tag{3.22}$$

The first term describes the exchange interaction between tip and sample coming from the *ab initio* calculations described before. Due to the tip oscillation in the MExFM experiment the exchange interaction is time dependent: $d = d(t) \Rightarrow J(d) = J(t)$. The oscillation of the tip-sample distance is given by:

$$d(t) = d_0 + A\cos\left(\omega t\right) \ . \tag{3.23}$$

Here we assume a neutral position of the tip d_0 at 10Å above the molecule. The oscillation amplitude A is assumed to be 5Å resp. 6.5Å and $\omega = 2\pi f$, the oscillation frequency of the cantilever of the exchange force microscope, corresponds to time scales much larger than the relaxtion times of the spin dynamics.

A stable tip polarization with a magnetization direction given by the classical spin vector $\mathbf{S}_{\mathrm{t}}$ has been assumed. Therefore, the exchange interaction acts as a time dependent external field: $\hat{\mathcal{H}}_J = -\mathbf{h}(t)\cdot\hat{\mathbf{S}}_{\mathrm{s}}$, with $\mathbf{h}(t) = J\left(d\right)\mathbf{S}_{\mathrm{t}}$. The last three terms in Eq. (3.22) are uniaxial anisotropies in x-, y- and z-direction. In the following, we take the z-axis as quantization axis and assume that this axis is an easy axis with $D_s^z = 0.05$meV. For the x- and y-axis we assume that $D_s^x = 0$ and $D_s^y = 0$ or, in the later cases $D_s^x = 0.01$meV and $D_s^y = 0.06$meV. After Landau and Zener, quantum tunneling can be found in the latter case due to the additional off-diagonal elements in the Hamilton Matrix. In the former case quantum tunneling is prohibited. We will show that in both cases interesting physics occurs.

The underlying equation of motion is the time dependent Schrödinger equation (TDSE) with an additional relaxation term:

$$i\hbar\frac{\partial}{\partial t}\left|\psi\right\rangle = \hat{\mathcal{H}}\left|\psi\right\rangle - i\lambda(\hat{\mathcal{H}} - \langle\hat{\mathcal{H}}\rangle)\left|\psi\right\rangle \ . \tag{3.24}$$

While the left hand side and the first term on the right hand side form the well known TDSE, the second term on the right hand side is an additional relaxation similar to the classical Landau-Lifshitz damping with damping constant λ and $\langle\hat{\mathcal{H}}\rangle = \left\langle\psi\right|\hat{\mathcal{H}}\left|\psi\right\rangle$. $\left|\psi\right\rangle = \sum_l \psi_l \left|\psi_l\right\rangle$ is a linear combination of the eigenstates $\left|\psi_l\right\rangle$ of an orthonormal basis (see details in [17]).

Depending on the tip polarization and the strength of the anisotropies six possible scenarios of the dynamical behaviour have been identified. They are defined by the combination of quantum tunneling and relaxation, and depend on the geometry of the tip-sample potential. In Fig. 3.43(f-g) the third scenario is exemplified. This scenario appears if D_s^x and / or D_s^y are nonzero and the minimal tip-sample distance doesn't exceed a critical distance shown in Fig. 3.43(e)$d_{\min} > d_c$. In this specific case both states $|\uparrow\rangle$ and $|\downarrow\rangle$ are energetically degenerate. The periodic oscillation of $\langle \hat{S}_s^z \rangle$ between $+1$ and -1 (black area) is a direct consequence of a periodic tunneling between $|\uparrow\rangle$ and $|\downarrow\rangle$ at the zero field level crossing. With decreasing tip-sample distance d the degeneracy between $|\uparrow\rangle$ and $|\downarrow\rangle$ lifts up and $|\psi\rangle$ becomes $|\psi\rangle = a\,|\uparrow\rangle + b\,|\downarrow\rangle$ with arbitrary a and b. Due to the additional relaxation, $\langle \hat{S}_s^z \rangle$ follows the effective field generated by the exchange interaction and becomes -1. Back at $J(d) = 0$, $\langle \hat{S}_s^z \rangle$ becomes zero, corresponding to $|\psi\rangle = \frac{1}{\sqrt{2}}\,(|\uparrow\rangle + |\downarrow\rangle)$. This is a direct consequence of the interplay of quantum tunneling and relaxation. $|0\rangle$ plays an unimportant role caused by the fact that this state is higher in energy.

To reinforce these predictions Fig. 3.43(g) shows the probabilities $P_\uparrow = \langle \uparrow \mid \uparrow \rangle$ and $P_\downarrow = \langle \downarrow \mid \downarrow \rangle$ corresponding to the third scenario [Fig. 3.43a)]. The oscillation of $\langle \hat{S}_s^z \rangle$ at the beginning can be clearly seen as oscillations of the probabilities $P_\uparrow$ and $P_\downarrow$. A zoom in (not shown) shows that there is a phase shift of $\pi/2$ between the oscillation of $P_\uparrow$ and $P_\downarrow$ which means that $|\psi\rangle$ oscillates between the eigenstates $|\uparrow\rangle$ and $|\downarrow\rangle$. After the first oscillation cycle a periodic change between 0 and 0.5 for $P_\uparrow$ and 0.5 and 1 for $P_\downarrow$ can be seen corresponding to a periodic change of $\langle \hat{S}_s^z \rangle$ between 0 and -1. From this signal it is quite simple to make conclusions about $|\psi\rangle$, especially for $|\psi\rangle = |\uparrow\rangle$ or $|\psi\rangle = |\downarrow\rangle$. The states $|\psi\rangle_+ = \frac{1}{\sqrt{2}}\,(|\uparrow\rangle + |\downarrow\rangle)$ as well as $|\psi\rangle_- = \frac{1}{\sqrt{2}}\,(|\uparrow\rangle - |\downarrow\rangle)$ correspond to the probabilities $P_\uparrow = P_\downarrow = 0.5$. However, $|\psi\rangle_+$ leads to $\langle \hat{S}_s^z \rangle = 0$ and $|\psi\rangle_-$ leads to $\langle \hat{S}_s^z \rangle = 1$. Therefore, we can exclude $|\psi\rangle_-$ in our simulations.

In conclusion, we have demonstrated that the interaction between a magnetic tip and a single magnetic moment leads to a Bethe-Slater like curve of the exchange energy. Depending on the distance between tip and sample the interaction is either ferromagnetic or antiferromagnetic. We were able to show that the assumed conditions play an important role and discussed six different scenarios. As a consequence of the Bethe-Slater like exchange interaction the minimal tip position $d_{\min}$ has been defined. We saw that a system without the appearance of quantum tunneling shows a controlled switching of the molecule from an antiparallel spin alignment of tip and sample (molecule) to a parallel one if the minimal tip-sample distance $d_{\min}$ is bigger than the distance d_c where the ferromagnetic exchange becomes antiferromagnetic. If $d_{\min} < d_c$ the molecule switches back to the antiparallel spin alignment caused by the changing exchange interaction. The physics becomes more complicated if quantum tunneling plays a role.

References

[1] K. Binder, Applications of Monte Carlo Methods to Statistical Physics, Rep. Progr. Phys. **60**,487 (1997).

[2] S. Krause,G. Herzog, T. Stapelfeldt, L. Berbil-Bautista, M. Bode, E.Y. Vedmedenko, and R. Wiesendanger, Magnetization Reversal of Nanoscale Islands: How Size and Shape Affect the Arrhenius Prefactor, Phys. Rev. Lett. **103**, 127202 (2009).

[3] M.Menzel, Y. Mokrousov, R. Wieser, J. E. Bickel, E. Y. Vedmedenko, S. Blügel, S. Heinze, K. von Bergmann, A. Kubetzka, and Roland Wiesendanger, Information Transfer by Vector Spin Chirality in Finite Magnetic Chains, Phys. Rev. Lett. **108**, 197204 (2012).

[4] T. Yamaoka, K. Watanabe, Y. Shirakawabe, K. Chinone, E. Saitoh, and H. Miyajima, Observations of Single Magnetic Domain Wall in Nanomagnet by Magnetic Force Microscopy,Jpn. J. Appl. Phys. **45**, 2230 (2006).

[5] P. Weinberger, E.Y. Vedmedenko, R. Wieser and R. Wiesendanger, A multi-scale model of domain wall velocities based on ab initio parameters, Phil. Mag. **17**, 2248 (2011).

[6] T. Stapelfeldt, R. Wieser, E.Y. Vedmedenko and R. Wiesendanger, Domain Wall Manipulation with a Magnetic Tip, Phys. Rev. Lett. **107**, 027203 (2011).

[7] R. Wieser, E.Y. Vedmedenko and R. Wiesendanger, Indirect Control of Antiferromagnetic DomainWalls with Spin Current, Phys. Rev. Lett. **106**, 067204 (2011).

[8] R. Wieser, T. Stapelfeldt, E.Y. Vedmedenko and R. Wiesendanger, Manipulation of domain walls using a spin-polarized STM, Eur. Phys. Lett. **97**, 17009 (2012).

[9] E.Y. Vedmedenko, N. Mikuszeit, T. Stapelfeldt, R. Wieser, M. Potthoff, A. I. Lichtenstein, and R. Wiesendanger, Spin-spin correlations in ferromagnetic nanosystems, Eur. Phys. J. B **80**, 331 (2011).

[10] O. Iglesias and A. Labarta, Finite-Size and surface effects in maghemite nanoparticles: Monte Carlo simulations, Phys. Rev. B **63**, 184416, (2001).

[11] K. Them, T. Stapelfeldt, E. Y. Vedmedenko, R. Wiesendanger, Non-equilibrium finite temperature dynamics of magnetic quantum systems: Applications to spin-polarized scanning tunneling microscopy, New J. Phys. **15**, 013009, (2013).

[12] A. A. Khajetoorians, B. Chilian, J. Wiebe, S. Schuwalow, F. Lechermann, and R. Wiesendanger, Detecting excitation and magnetization of individual dopants in a semiconductor, Nature **467**, 1084 (2010).

[13] A. A. Khajetoorians, S. Lounis, B. Chilian, A. T. Costa, L. Zhou, D. L. Mills, J. Wiebe, and R. Wiesendanger, Itinerant Nature of Atom-Magnetization Excitation by Tunneling Electrons, Phys. Rev. Lett. **106**, 037205 (2011).

[14] S. S. P. Parkin, M. Hayashi, L. Thomas, Magnetic Domain-Wall Racetrack Memory, magazine **320**, 190 (2008).

[15] M. Klaui et al., Concepts for Domain Wall Motion in Nanoscale Ferromagnetic Elements due to Spin Torque and in Particular Oersted Fields, J. Magn. **14**, 53 (2009).

[16] E. Y. Vedmedenko, Q. Zhu, U. Kaiser, A. Schwarz, and R. Wiesendanger, Atomic-scale magnetic dissipation from spin-dependent adhesion hysteresis, Phys. Rev. B **85**, 174410 (2012).

[17] R. Wieser, V. Caciuc, C. Lazo, H. Hölscher, E Y Vedmedenko,and R Wiesendanger, A theoretical study of the dynamical switching of a single spin by exchange forces, New J. Phys. **15**, 013011 (2013).

[18] Y. Mokrousov, N. Atodiresei, G. Bihlmayer, S. Heinze and S. Blügel, The interplay of structure and spin–orbit strength in the magnetism of metal–benzene sandwiches: from single molecules to infinite wires, Nanotechnology **18**, 495402 (2012).

3.7 SP-STM on molecular and carbon based systems

J. Brede and R. Wiesendanger

This section focuses on the ongoing research on carbon and molecule based magnetism.

The very active research field of molecular electronics is founded upon the idea to put few or even single molecules between two electrodes and perform the basic operations of digital electronics - rectification, amplification and storage. Aviram and Ratner [1] were the first to propose in the mid 1970s that a molecule with a donor - spacer - acceptor characteristic would function as a diode when placed between two electrodes. When using molecules instead of silicon based semiconductors major benefits can be expected as essentially all electronic processes in nature occur in molecule based structures [2].

While the potential of molecule based devices is tremendous, so are the challenges which need to be overcome both experimentally and theoretically.

One experimental approach is to measure the conductance of molecules utilizing break junctions [3]. These experiments are very tedious as small changes in the device geometry may induce large changes in the measured conductance, making a quantitative interpretation of the results difficult and lead to a rather limited yield of successful devices per device prepared. The addition of a gate voltage lead to an extension of the device set-up into a three terminal one, making it possible to observe fascinating properties such as Coulomb blockade and Kondo effect in single molecule transistors [4]. More recently the spin states of molecules could be controlled mechanically [5] and the electronic read-out of nuclear spin states was realized [6].

Another experimental approach is utilized in the organic thin film community. Here, one particular device attracted a lot of attention: the organic spin valve.

In a spin valve two magnetic layers are separated by a non-magnetic spacer. Depending on the relative alignment of the magnetization direction of the two magnetic leads the device exhibits a different magneto resistance (MR). Organic semiconductors are a promising spacer material, because they show long spin relaxation times and substantial spin-diffusion lengths [7, 8] due to the weak spin-orbit interactions in the light elements of organic molecules (or graphene).

Interestingly organic spin valves often exhibit an inverse MR effect, *i.e.* when the two ferromagnetic leads are in anti-parallel alignment the resistance decreases compared to the case of parallel alignment. This inverse magneto-resistance effect has been experimentally verified for a variety of organic semiconductors [9] but its origin was discussed controversially [10].

More recently, it was demonstrated that organic semiconductors are also a promising material for applications in quantum computing. The population relaxation time (T_1) and phase memory time (T_2) in molecular thin-film semiconductors can compete with other materials such as nitrogen vacancies in diamond [11].

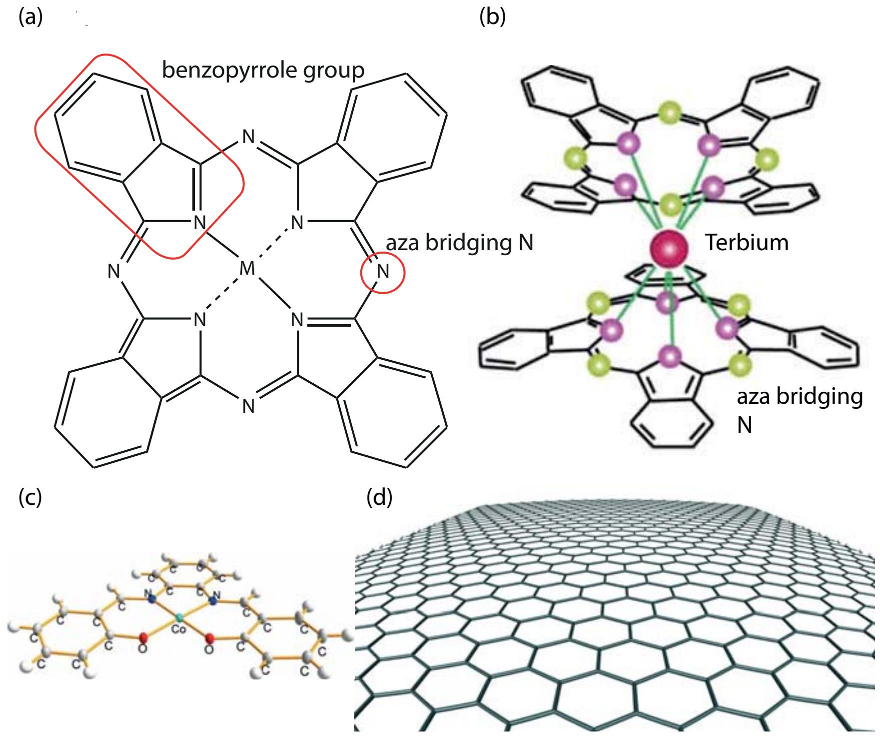

Figure 3.44: Schematic representation of the metal phthalocyanine (MPC) molecule (a) and the double decker bis(phthalocyaninato) Terbium(III) (TbPC2) molecule (b). The MPC (a) has a planar two-dimensional structure -4 benzopyrrole groups that are interconnected *via* aza bridging nitrogen atoms - and houses the metal atom in the central cavity. The TbPC2 consists of two PC rings that are vertically stacked to host a large Tb-ion at its center. A related molecule is the Schiff base complex also known as salophene (c). A single layer of Carbon atoms arranged in a hexagonal honeycomb lattice is known as graphene (d), chemically, it can be seen as an infinite aromatic π-system consisting of alternating carbon single and double bonds.

Despite the impressive progress in the field major challenges in the interpretation of the experimental findings remain. This is largely due to the lack of insight into the precise composition of the devices and their interfaces. Therefore, it is no surprise that a “call for spectroscopic studies” has been reaffirmed [12].

Already in the past, we were able to shed unprecedented light into the physics of the organic-ferromagnet interface [13,14]. In this research period we extended our work toward a better understanding of the physical and chemical processes determining the transport properties of molecule-ferromagnet interfaces by systematically studying the interaction of phthalocyanine molecules with different magnetic nano-structures. Our experimental findings are corroborated by state-of-the art first principles calculations [Prosenc (Hamburg), Atodiresei (Jülich), and Sanvito (Dublin)].

The phthalocyanine molecule (see Fig. 3.44 (a) for the chemical structure) is an aromatic macrocyclic compound that can host almost every metal atom in its central cavity. In particular, tailoring of the molecular spin-state can be systematically achieved by varying the central metal from, *e.g.*, Cu to Mn. More recently, another PC molecule attracted a lot of attention: bis(phthalocyaninato) Terbium(III) (see Fig. 3.44 (b) for the chemical structure of TbPC2). The double decker type TbPC2 molecule consist of a Terbium atom sandwiched between two PC ligands and shows an interesting spin system, consisting of the localized spin and orbital moment of the central Tb-ion (12/2) and a delocalized radical spin of 1/2 on the organic PC ligands. In a joint effort with the chemistry groups of Heck and Prosenc the salen molecule [depicted in (c)] was studied. Additionally, our research activity was extended to incorporate graphene (G). Chemically, graphene may be viewed as an extended aromatic π-system - similar to the organic macrocycle of the phthalocyanine molecule - it is made up of alternating carbon single and double bonds arranged in a honeycomb lattice.

The highlights of the research period include the formation of a molecular Kondo chain [58] the real-space imaging (and quantification) of the spatial distribution (and magnitude) of a spin-split molecular orbital [57], or the demonstration of atomic scale magnetism induced in graphene *via* intercalation of a transition metal [56].

In order to achieve this unprecedented insight into carbon based magnetism we established a novel reference system of cobalt islands grown on an Ir(111) [53] for our SP-STM measurements. The nanoscale Co-islands are expected to yield similar properties - without the experimental drawbacks - as the prototypical system of two atomic layer thick Co-islands grown on Cu(111) that were previously investigated in the group [15]. Before turning to the spin-resolved studies a view into the magnetism of multi-spin center molecules using spin-averaged techniques is given.

3.7.1 Molecular Kondo chain

A. DiLullo, S.-H. Chang, N. Baadji, K. Clark, J.-P. Klöckner, M.-H. Prosenc, S. Sanvito, G. Hoffmann, S.-W. Hla, and R. Wiesendanger

On-surface polymerization of Co-salophen molecules, that were synthesized in the group of Marc-Heinrich Prosenc, was utilized to generate multi-spin center molecules under UHV conditions on a Au(111) surface. These novel macro molecules were characterized using low temperature STM and the experimental observations corroborated with state-of-the art first principles calculations performed in the group of Stefano Sanvito.

The successful on-surface synthesis is a big step forward in the study of multi-spin-center macromolecules as they frequently disintegrate when thermally evaporated under UHV conditions [54].

The formation of the chain-like macromolecules was achieved *via* covalent linking of individual Co-Salophene molecules upon Br removal. To this end Co-Salophene molecules were first thermally evaporated under UHV conditions onto a Au(111) single

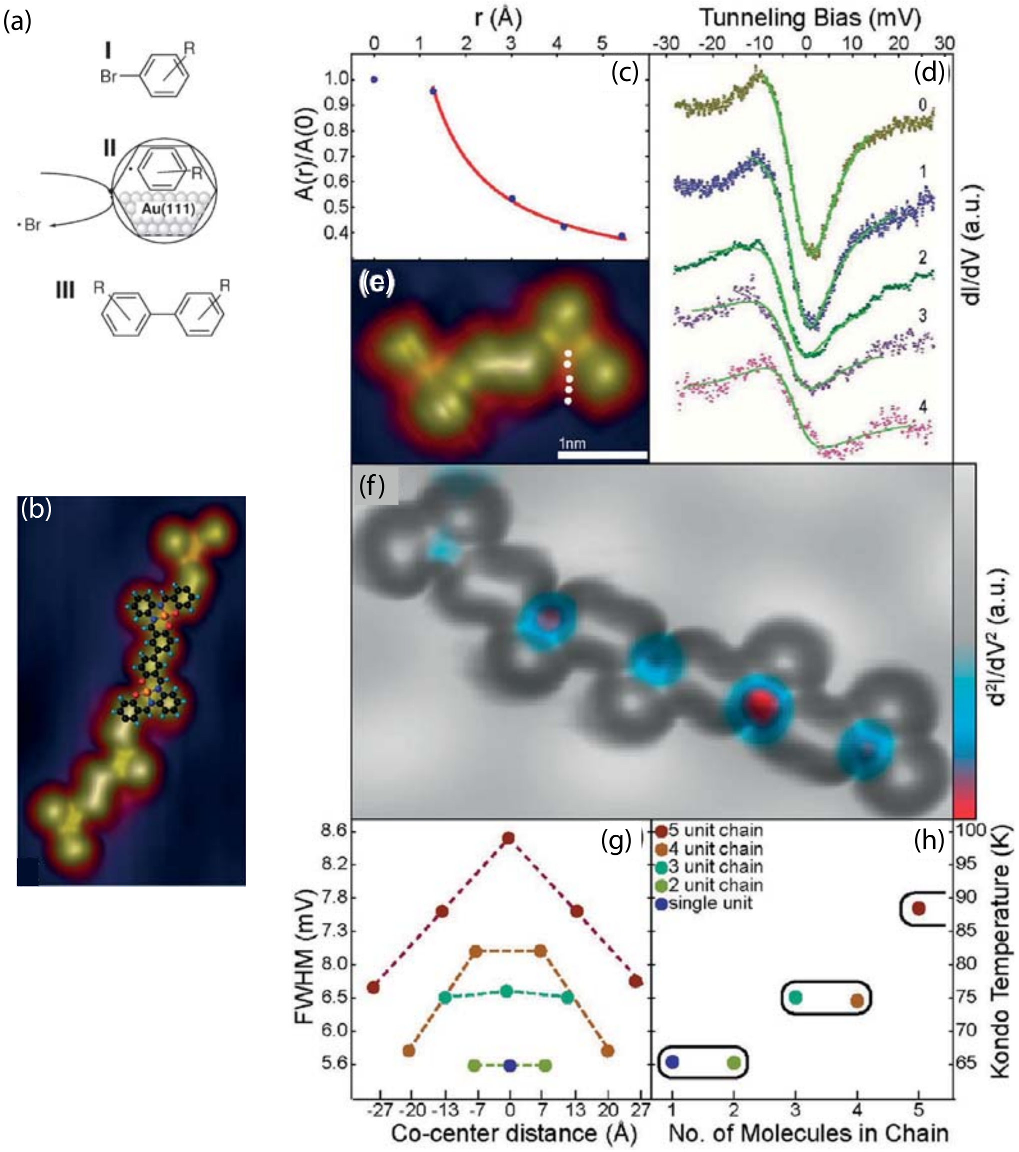

Figure 3.45: (a) Schematic depiction of the Ullmann reaction used to polymerize the individual Co-Salophene-Br into a multi-spin-center macro molecule. Topograph of the molecular Kondo chain with the molecular structure superimposed. Evaluating the Fano resonance arising from the Kondo effect on different macro-molecules (c)-(f). Dependence of the Kondo temperature on the molecular chain length showing a clear even/odd dependence (g) and (h).

crystal, next the sample temperature was raised to 400 K for 10 minutes. During this process, a thermally activated Au-catalyzed aryl-aryl coupling reaction (Fig. 3.45 (a)) is triggered. Upon polymerization molecular chains (Fig. 3.45 (b)) are found on the surface, where the central carbon ring is pointing either parallel or antiparallel to its neighbor. The molecular structure can be directly fit onto the STM images visualized by the overlay in (Fig. 3.45 (b)). DFT calculations reveal that each building block of the molecular chain has an unpaired electron on the central Co atom. The interaction of a localized magnetic impurity (here, the spin on the Co atom) and conduction electrons (here, supplied by the Au surface) may lead to the so-called Kondo effect which entails a fingerprint of magnetic interactions. In STM experiments the Kondo effect leads to a zero bias anomaly (ZBA) in the differential tunneling conductance, *i.e.*, a dip or a peak right at the Fermi Energy. The resulting spectral features - visible in STS (Fig. 3.45 (d)) - are fit by Fano line shapes using the relation:

$$\frac{dI}{dV} = a(r)\frac{q(r)^2 + 2q(r)\epsilon + 1}{1+\epsilon^2} + const, \epsilon = \frac{meV\Delta E}{k_B T_K},\ and\ A(r) = a(r)[1+q(r)^2] \quad (3.25)$$

Here, $q(r)$ is the asymmetry parameter, k_B the Boltzmann constant, ΔE the energy shift from E_F, and $A(r)$ is the Kondo amplitude. The energy width of the resonance quantifies the spin-electron interaction strength in terms of the Kondo temperature, T_K. To confirm that the spectral feature is indeed due to a Kondo resonance spectra along the path indicated Fig. 3.45 (e) were obtained. Plotting the Kondo amplitudes against the distance from the molecular Co site (Fig. 3.45 (c)) follows closely the $1/r$ behavior as expected for a Kondo system [55]. Further insight into the spatial extent of the Kondo resonance is gained by mapping the second derivative of the tunneling current d^2I/dV^2. In Fig. 3.45 (f) the second derivative map is overlaid onto a three-dimensional representation of the simultaneously acquired surface topography. As observed in Figure 3d, the Kondo active sites are localized at the Co atoms, and so we have created covalently bound chains (macromolecules) with multiple spin-interaction sites from basic molecular units. Interestingly, we find the Kondo resonance widths, and the corresponding T_K values are dependent on the number of basic blocks in the molecular chains for up to five unit chains (Fig. 3.45 (g) and (h)) that we can form in the current work. The significant change in $T_K$values is indicative for a magnetic interaction among the spin centers. The average T_K increases with increasing chain length and is also dependent on the even or odd number of molecular units within the chains. Such an even-odd asymmetry suggests an antiferromagnetic (AFM) coupling and, as in the ferromagnetic (FM) case, the total spin would linearly increase with the number of Co centers. Indeed, the interpretation of an AFM coupling between the Co centers *via* organic molecular linkers is further corroborated by first principles calculations.

In summary, the experimental observations demonstrate the first successful on-surface creation of multi-spin center macromolecules. DFT calculations and spectroscopic measurements reveal that the molecular spins are magnetically coupled and remain localized on the Co centers. More importantly, the basic units are linked via covalent bonding, which might maintain magnetic coupling for higher temperatures than dipolar and van der Waals interactions in conventionally self-assembled structures. Extending this approach with heteromolecular catalysis and design of multifunctional spin systems may enable bottom up engineering of molecular and hybrid-molecular structures for future applications in nanospintronics.

3.7.2 Magnetic properties of monolayer Co islands on Ir(111) probed by spin-resolved scanning tunneling microscopy

J. E. Bickel, F. Meier, J. Brede, A. Kubetzka, K. von Bergmann, and R. Wiesendanger

Material properties are intimately tied to both the amount of material present and the dimensionality of the structure. Thus it is important to understand how the fundamental properties of materials, such as the magnetic structure, change as small-scale structures become more commonly employed in devices. A significant reduction in device size was obtained in the field of magnetism by the discovery of giant magnetoresistance (GMR) [16,17], which revolutionized the design of magnetic storage devices. The GMR requires two magnetic thin films, one that is magnetically hard and does not change its orientation in an applied field. Thus, in order to continue this size reduction, it remains critical to develop magnetically hard ferromagnetic nanostructures.

Cobalt films and nanostructures on noble metals have attracted a lot of interest due to the experimentally measured and predicted high anisotropies and coercivities. Theoretically, Co monolayers and atoms on noble metal substrates such as Pt and Ir are predicted to have significant anisotropies and spin-orbit coupling [18,19]. Experimental studies of Co nanostructures on Pt show that both the magnitude and direction of the magnetic anisotropy depends critically on the detailed structure of the Co as nano-islands or wires [18,20]. However, little work has been devoted to examine nanostructures of Co on Ir experimentally.

The electronic structure of the Co islands is shown in Fig. 3.46c. These spin-averaged $\mathrm{d}I/\mathrm{d}U$ curves were taken with a W-tip on the single island shown in Fig. 3.46d-e. Figure 3.46 shows the topography image of the island and Fig. 3.46e shows a differential conductance ($\mathrm{d}I/\mathrm{d}U$) map which is taken as a constant voltage slice ($\mathrm{U} = -140$ mV) of a full STS field. Spin-averaged $\mathrm{d}I/\mathrm{d}U$ curves were taken at the points marked in Fig. 3.46e and averaged to obtain the curves in Fig. 3.46c. The Ir substrate is rather featureless with a step appearing at $U \approx -400$ mV, where $\mathrm{U} = 0$ mV is the Fermi energy ($\mathrm{E_F}$). This step, which is highlighted by the light blue arrow in 3.46c, is in agreement with previous measurements on Ir(111) [21]. In contrast to the Ir substrate, the Co islands have a large peak at $U = -260$ mV which is highlighted by the black arrow in 3.46c). A small shoulder, which is highlighted

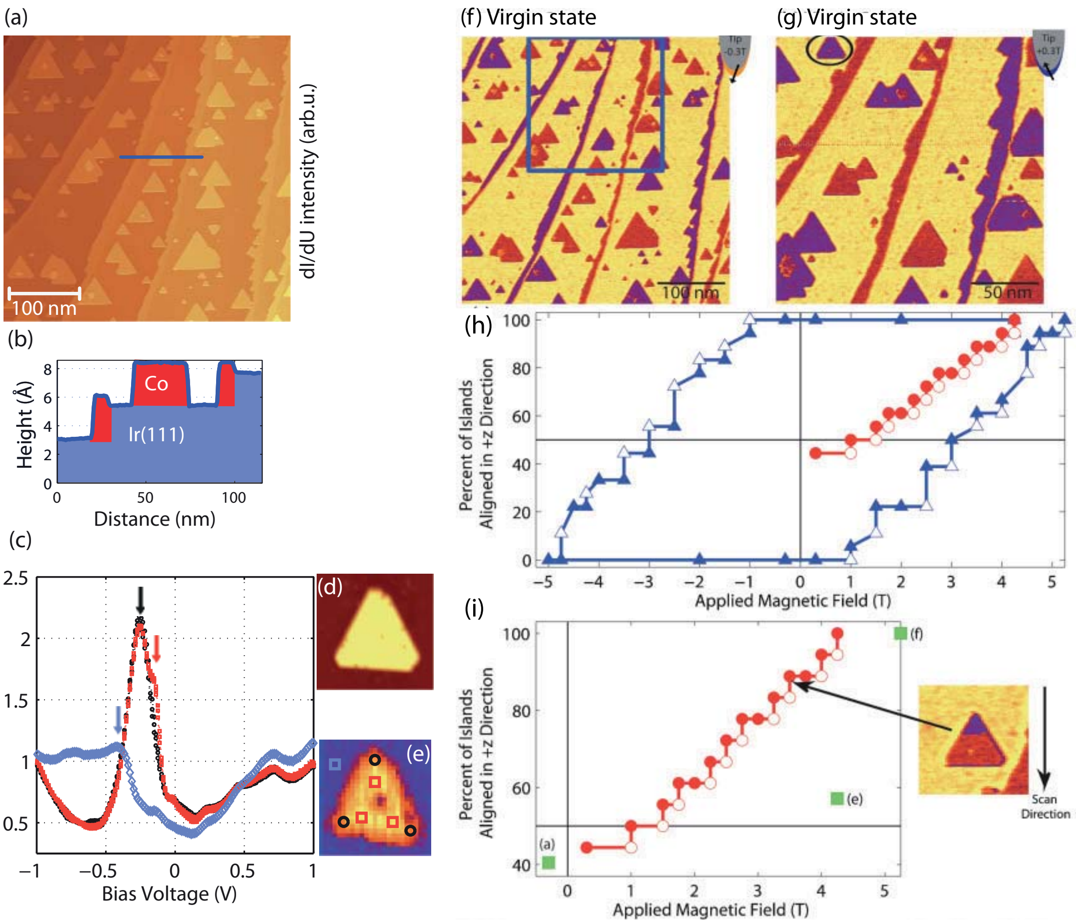

Figure 3.46: (a) STM topography image of Co islands and wires on Ir(111) and (b) corresponding height profile. (c) Spin-averaged $\mathrm{d}I/\mathrm{d}U$ curves of a typical Co/Ir(111) sample shown below in the topography image (d) and taken at the points marked in (e), a $\mathrm{d}I/\mathrm{d}U$ slice of the same island. Arrows highlight the features of (left to right) the Ir, Co, Co island center. All: W-tip. (a-b) $T = 6$K, $B = -300$ mT, $U_{bias} = -500$ mV, $I = 0.5$ nA. (c),(d),(e), $T = 13$K. (c) $U_{stab} = +1.0$ V, $I_{stab} = 1.5$ nA. (d) $I = 1.5$ nA, $U = -400$ mV. (e) $\mathrm{d}I/\mathrm{d}U$ slice taken at $U = -140$ mV. (f),(g),(j),(k) Spin-resolved $\mathrm{d}I/\mathrm{d}U$ images. Note: (g) is a zoomed area from image (f). (h),(i) Hysteresis curve taken from the area shown in (g). Inset of (i) is the island circled in (g). The hysteresis curves start from the virgin state (red circles) through a full magnetization demagnetization cycle (blue triangles). Open markers are the first image taken at applied field and closed markers are the final image taken at applied field. The green squares data points are calculated from area *outside* the scanned area marked in (f). All: Fe/W-tip, $T = 6$ K. (f),(g) $U_{bias} = -500$ mV, $I = 0.5$ nA.

by the red arrow in 3.46c, appears at $U \approx -150$ mV for STS spectra taken in the center of the island (red squares) that disappears for spectra taken at the edge of the island (black circles). This can be seen clearly in the dI/dU map in Fig. 3.46e taken at $U = -140$ mV. The black circles and red squares correspond to the markers in the STS curves and the dI/dU image highlights the edge of the island where the shoulder peak appears. (The depression at the center of the image is an impurity which can be seen on the topography image to the left.) A comparison of these spectra to combined experimental and theoretical studies of Co/Cu(111) [22], Co/Pt(111) [18], and Co/W(110) [23] indicates that this $U = -260$ mV peak is characteristic of Co nanostructures, and the origin of the peak is a d-like minority-spin state, although the energy shifts slightly on different substrates.

Upon establishing the electronic properties of the Co-islands we turn toward their magnetic properties and in particular their response to an external magnetic field applied. Initially, as seen in the spin-polarized dI/dU images in Fig. 3.46f-g and in the virgin state in the hysteresis curve in Fig. 3.46h, the surface has an almost equal distribution of islands aligned in the +z and -z directions, where the +z (-z) direction is defined as aligned parallel (anti-parallel) with the Fe/W tip. The area in Fig. 3.46g was scanned while the magnetic field was increased in successive small intervals, resulting in the hysteresis curve shown in 3.46h. There appears to be a slight size dependence with higher magnetic fields required to switch the smaller area islands, but this dependence is very small relative to the large scatter of area vs. switching field. Regardless, the islands show complete remanence as is seen by the 100% alignment when the applied field is reduced and inverted ($B = 0$ T), and a very large coercive field of $H_c \approx 3$ T is measured. This is a very high value relative to common coercivities such as $H_c \approx 1.5$ T for Co/Cu(111) [15] or $H_c \approx 0.25($ 2.0 T) for monolayer (and double-layer) Co islands on Pt(111) [18] which is in agreement with the high values obtained for the anisotropy of Co/Ir(111) relative to these other systems. A very large saturation field of $B = +5.25$ T was required to align all the islands in the +z direction.

In summary, we have examined Co islands grown on Ir(111). The Co grows pseudomorphically on the Ir(111) surface exhibiting a predominantly single stacking which is most likely FCC. The electronic structure of the islands exhibits a strongly spin-polarized peak at $U = -260$ mV. The spin-polarized contrast shows up clearly in spin-resolved dI/dU maps, demonstrating that the investigated islands are single domain ferromagnetic with the easy magnetization axis normal to the surface. The Co islands exhibit a very high coercivity of more than 3$-$4 T as extracted from the hysteresis loops. The saturation field required to align all islands in the easy-axis is $B = +5.25$ T. This high value for saturation combined with 100% remanence and high coercivity makes the islands magnetization direction very stable under applied magnetic fields of a few Tesla.

Thus, the Co-islands are an almost ideal “hard” magnet for studies of the spin-valve type, *i.e.* where one magnetization direction (here, the sample) is fixed and the other

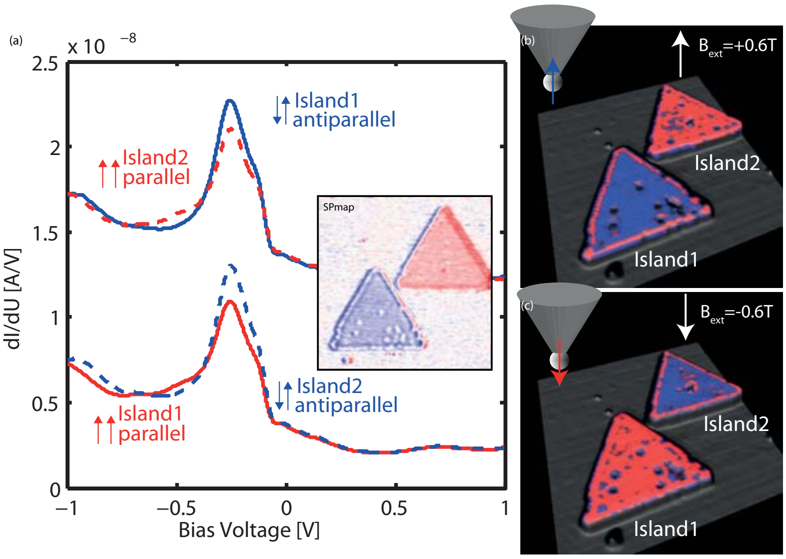

Figure 3.47: Illustration of an SP-STM type spin valve experiment. SP-STS (a) curves are recorded over the center of Island 1 (red, solid line) and Island 2 (blue, dashed line) with an external B-field of -0.6 T applied. Next the external magnetic field is reversed to +0.6 T - thus reversing the magnetization direction of the tip - and SP-STS curves are recorded again for Island 1 (blue, solid line) and Island 2 (red, dashed line), respectively. A pseudo three-dimensional visualization of the topography of the two islands, which is overlayed with the magnetic dI/dU maps for the two external magnetic fields applied, are given in (b) and (c). A map of the effective local spin polarization (SPmap) is shown in the inset of (a).$U_{bias} = -250$ mV, $I = 2$ nA.

(here, the Fe-coated W-tip) is controlled *via* the application of an external magnetic field. In this kind of experimental set-up it is possible to study the same Co-island (or molecule) under identical tunneling conditions which differ only in the relative alignments of tip and sample magnetization, thereby allowing to precisely determine the local effective spin polarization (SP) of the junction without having to rely on the comparison of sample areas which differ only in their magnetization direction. The experimentally obtained SP-map in the inset of Fig. 3.47 (a) clearly shows that the two triangular islands have a similar magnitude of the spin polarization but are of opposite sign, *i.e.*, one island appears “blue” while the other appears “red”, due to the islands’ opposite magnetization directions with respect to the tip. Furthermore, there is no SP (white area) around the islands due to the non-magneteic Ir(111) surface. Figures 3.47 (b) and (c) give pseudo three dimensional representations of the topography of two Co-islands superimposed by the magnetic dI/dU maps.

3.7.3 Spin-resolved characterization of single cobalt phthalocyanine molecules on a ferromagnetic Co support

J. Brede and R. Wiesendanger

In 2008 Iacovita *et al.* [24] reported the application of SP-STM to visualize the spin polarization of single CoPC molecules in contact with ferromagnetic Co islands grown on a Cu(111) crystal. The CoPC molecules showed a spin-polarized electronic resonance below the Fermi energy. By comparison with first principles calculations Iacovita *et al.* identified that the resonance arises due to a ferromagnetic coupling of the CoPC and the Co nanostructure. Two mechanisms were suggested to be responsible for the coupling: a direct exchange coupling of the Co-ion inside the PC macrocycle to the Co-atoms of the island underneath and a $\sim 90°$ superexchange mechanism of the Co-ion via the inner molecular N atoms to the Co-islands. Both favor a ferromagnetic coupling. It is interesting to note, that the images presented in the work by Iacovita *et al.* suggest that the CoPC molecules studied were in close proximity to one another. Recent work by Tsukahara *et al.* [25] indicated that FePCs on a Au(111) surface couple magnetically via RKKY interaction on a non-magnetic Au(111) surface when they are about one nanometer apart. Gopakumar *et al.* [26] showed that an ordered superstructure of FePCs on Ag(111) is partially electronically decoupled from the metal surface. Iacovita *et al.* did not address the spin dependence of the same molecule, but relied on the comparison of structurally and electronically identical molecules situated on oppositely magnetized domains. In our research we demonstrate how magnetic contrast in the spin-resolved SP-STM images is unambiguously established by the application of an external magnetic field and we proceed to record the spin dependence of a single CoPC molecule [59]. Note that in the experiment by Iacovita *et al.* the observed molecular spin polarization was attributed and observed experimentally close to the central Co-ion. In contrast, more recent SP-STM experiments, in which the molecular spin polarization was resolved on a sub-molecular scale, clearly demonstrate that the organic molecular ligand can carry spin information as well [13].

Individual CoPC molecules appear with a reduced C_S symmetry when deposited on-top of cobalt nanostructures grown on Ir(111). The reduced symmetry of the CoPC molecules in STM images indicates an adsorption geometry with the Co-ion of the CoPC situated in a hollow site of the underlying Co-nanostructure (see fig. 3.48 (a)). Spin-resolved STS taken above the Co-ion shows a spin-polarized resonance right below the Fermi energy. The molecular resonance is of the same spin-character as the surface-resonance of the Co-nanostructure which lies at slightly lower energies (see fig. 3.48 (b) and (c)). A similar behavior was previously reported by Iacovita *et al.* for CoPC molecules on Co/Cu(111). With the help of first-principles calculations they were able to show that the molecular resonance is a finger-print that arises due to a ferromagnetic coupling of the (reduced) molecular Co-ion to the underlying Co-nanostructure. Using the submolecular resolution capabilities and the method established previously [13,14],

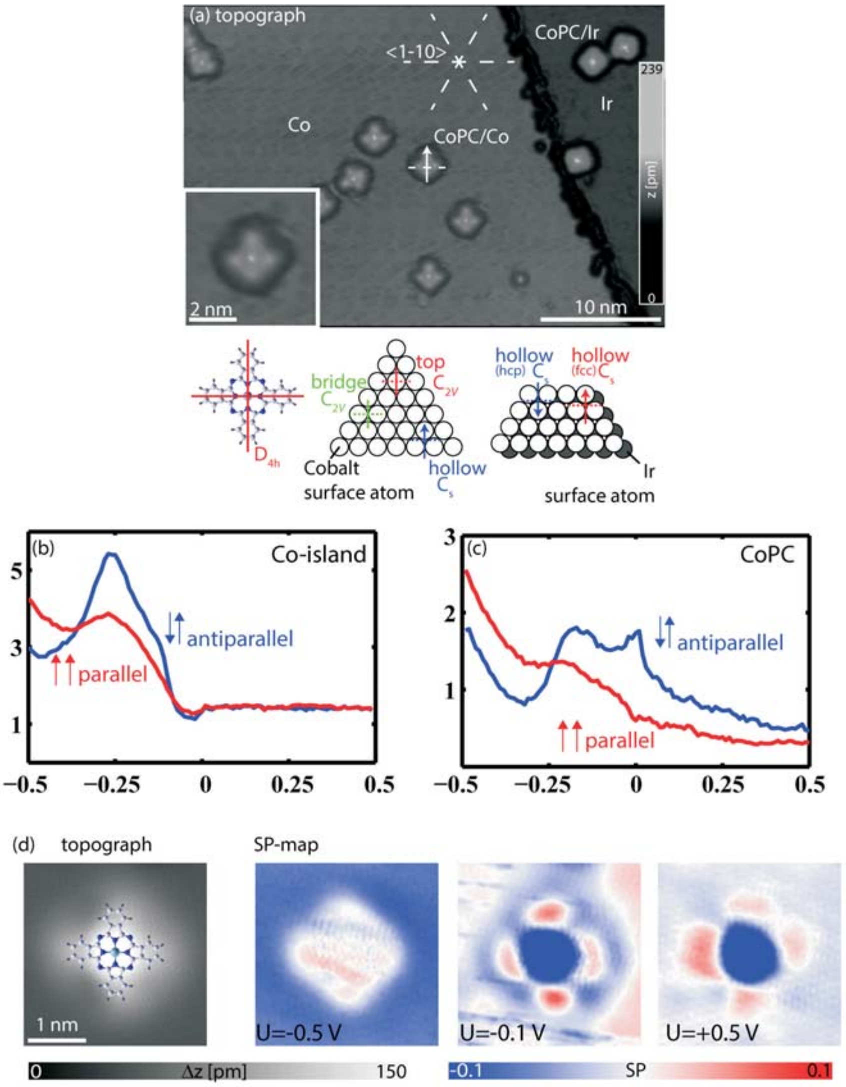

Figure 3.48: SP-STM and STS on CoPC molecules on Co on Ir(111). (a) A topograph of CoPC molecules adsorbed on top a Co-nanostructure (CoPC/Co) and directly on top the Ir(111) surface. A reduced C_S symmetry is apparent for CoPC/Co molecules and indicates that the molecular Co-ion is situated in a hollow site of the underlying atomic Co-lattice. SP-STS shows the characteristic minority resonance for the Co-island (b) and a similar resonance, shifted toward the Fermi energy above the Co-ion for CoPC/Co. Mapping the spin polarization of a single molecule (d) clearly shows the localization of the resonance above the Co-ion (blue), but also spin polarization of opposite sign above the organic ligand (red).

maps of the local effective spin polarization (SP-maps) were calculated (see fig. 3.48 (d)). Three properties of the SPmaps are noteworthy: an almost circular spin-down (blue) feature above the central Co-ion due to the ferromagnetic resonance explained above, spin-up (red) features above the outer benzopyrolle groups, and the spin-down polarization of the surrounding Co-nanostructure. The origin of the inversion of the spin-polarization above the organic ligand compared to the clean ferromagnetic surface was previously shown to arise due to the hybridization of the molecular π orbitals with the d states of the underlying ferromagnet [13, 14].

The work helped to establish several important aspects that are to be considered when designing future molecule based spintronic devices: a general effect arises on the organic backbone of the molecule, namely an inversion of the spin-polarization due to the formation of new $p - d$ molecule-ferromagnet hybrid states which are situated in an energy interval close to the Fermi energy and may change, *e.g.*, the sign of the magnoteresistance effect observed for the ferromagnet-molecule spin valves. Second, when the molecule itself carries a spin the precise adsorption geometry is of utter importance, in the present case the molecular spin of 1/2 situated for the free molecule on the Co-ion, can be either quenched or greatly reduced depending on the choice of the ferromagnetic support. Another aspect that should always be considered is the presence and spin-character of surface states in the ferromagnet below as molecular states will be pinned by such surface states with the appropriate spin-character. Lastly, tailoring the work function of the ferromagnet in appropriate ways may open up a route to purposely quench or induce magnetic moments in adsorbed molecules.

Equipped with a basic understanding of the PC-Co-nano-island interactions we proceeded to map the spin properties of TbPC2 molecules on the same surface. First, TbPC2s in direct contact with the Ir(111) surface were studied and a rare reversible chiral switch elucidated.

3.7.4 Reversible chiral switching of Bis(phthalocyaninato) Terbium(III) on a metal surface

Y.-S. Fu, J. Schwöbel, S.-W. Hla, A. Dilullo, G. Hoffmann, S. Klyatskaya, M. Ruben, and R. Wiesendanger

Molecular switches interconvert between bistable states and could function as potential storage bits for building molecule-based devices. Most molecular switches operate by changing conformation although other forms of operations like electron charging or bond formation were demonstrated recently. Chirality, on the other hand, is of fundamental importance in biological systems and also has technological significance for asymmetric heterogeneous catalysis. If one could control the chirality within a single molecule, its physical properties (e.g., photophysics) as well as functionalities (e.g., catalytic activities) could also be controlled. We demonstrate a molecular switch using bis(phthalocyaninato) terbium(III) (TbPC2) molecules adsorbed on Ir(111), where a

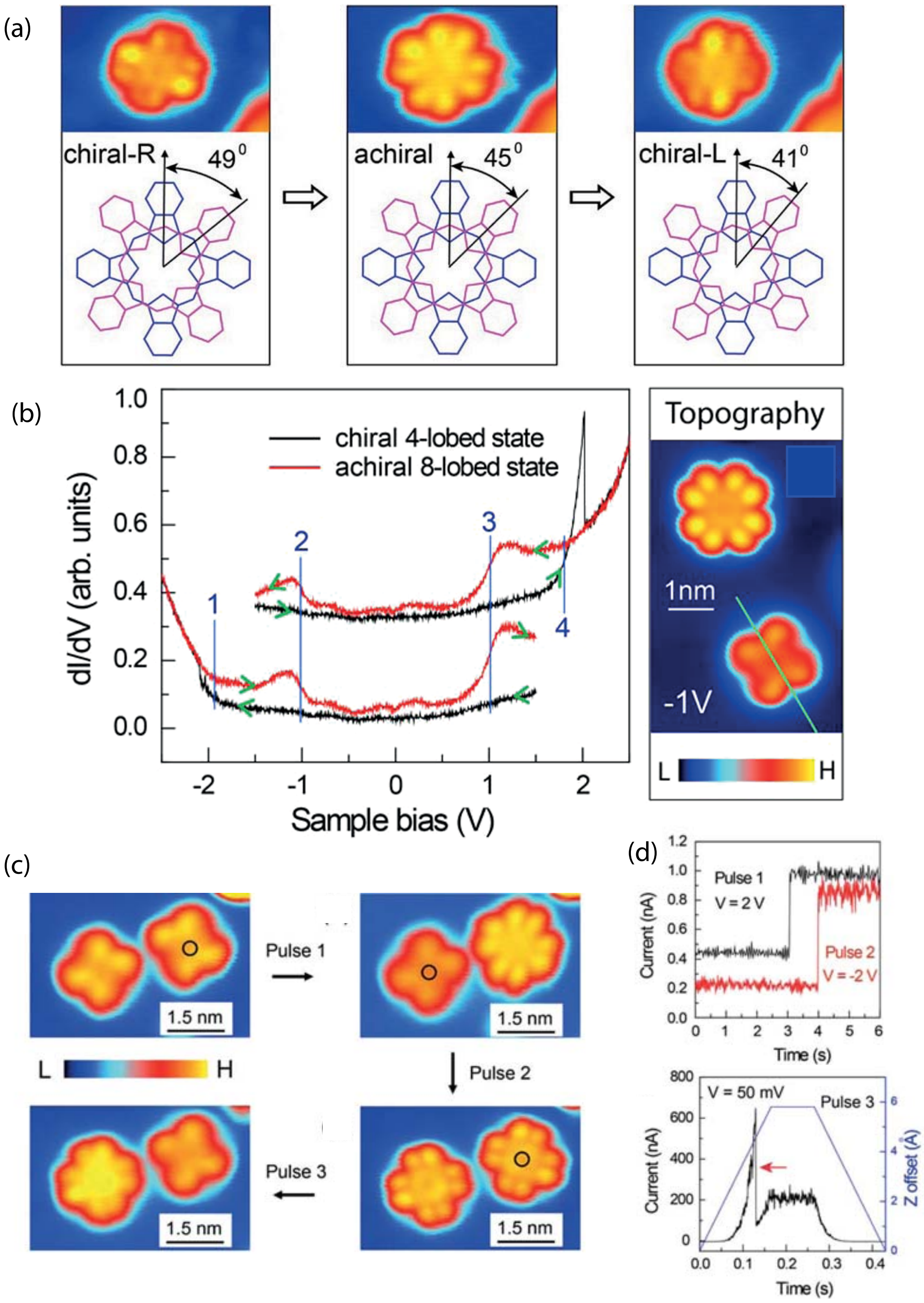

Figure 3.49: Reversible STM induced switching of TbPC2 molecules on Ir(111). TbPC2 can be switched between a chiral and an achiral state(a). The STS signature of the achiral and chiral state, respectively (b). A controlled manipulation sequence (c(demonstrating the interconversion between states *via* the manipulation protocols given in (d).

chirality change is explicitly manifested [60].

TbPC2 molecules show two different conformations when adsorbed on the bare Ir(111), which can be easily distinguished by local scanning tunneling spectroscopy. Interestingly, the conformations are distinguished in an achiral and a chiral one. The chiral and achiral molecules differ in the rotation of the upper PC ring with respect to the lower one: a rotation of 45^0 degrees for the achiral one and 41^0 (49^0) for the chiral one are determined, respectively (see Fig. 3.49). Injecting tunneling electrons into the highest occupied or lowest unoccupied molecular orbital triggers the switch of the chiral into the achiral conformation. A detailed analysis of the switching event suggests that the switching mechanism is based on inelastic tunneling of electrons, *i.e.* the energy of the electron is (partially) transferred to the molecule and subsequently relaxes *via* inelastic excitations. In the present case, the energy transfer must be large enough to overcome the energy barrier of an azimuthal rotation of the upper PC ring. Switching from the achiral into the chiral state proves more complex and requires a substantial flow or electrons (several 100nA) at low bias voltage (see Fig. 3.49). Therefore, it is likely that the switch is thermally activated as is corroborated by additional experiments; a deposition of TbPC2 at a sample held at low temperatures ($\sim$ 100K) yields only achiral molecules on the surface, subsequently warming the sample up to RT transfers all molecules into their chiral state.

Modifying the angle between upper and lower ring can be used to controllably quench the ligand spin. Therefore, the experiments demonstrate electric current control of the molecular spin state which can be envisioned for future spintronic applications. In the next section the spin-resolved properties of the TbPC2 SMM are presented.

3.7.5 Real-space observation of spin-split molecular orbitals of adsorbed single-molecule magnets

J. Schwöbel, Y.-S. Fu, J. Brede, A. Dilullo, G. Hoffmann, S. Klyatskaya, M. Ruben, and R. Wiesendanger

Single Molecule Magnets (SMMs) exhibit new properties such as electric control of molecular spin states [27], remarkably high blocking temperatures, hysteresis [28], quantum tunneling of magnetization [29, 30], and tunable coupling to magnetic substrates [31]. Recently, the realization of novel devices, such as multiple-field-effect nanotransistors [32] or supramolecular spin valves [33] was reported, demonstrating the potential of SMMs for technological applications, in particular spintronics [34] and quantum computing [35, 36]. Further progress in the field requires a detailed understanding of structural properties and magnetic interactions of an individual SMM in contact with a ferromagnetic electrode in an atomically well-defined environment. Here, bis(phthalocyaninato)terbium(III) (TbPC2) was chosen as a model-type system because of its high blocking temperature ($T_B \sim 30 - 50\,\mathrm{K}$) [37, 38], its comparably small size, and its high stability which allows for thermal deposition in ultra-high vacuum (UHV) environments.

The spin-averaged electronic structure of TbPC2 is investigated by point spectroscopy above the ligand. The spin-averaged differential tunneling conductance ($\mathrm{d}I/\mathrm{d}U$) (Fig. 3.50a) shows two pronounced peaks at $U = -0.9\,\mathrm{V}$ and $U = +1.3\,\mathrm{V}$. These features are attributed to the HOMO and the LUMO, respectively. The spatial distribution of these states is imaged in the respective topographs and shows an eight lobe structure for both HOMO and LUMO. This particular appearance is characteristic for π-orbitals of phthalocyanine molecules only weakly interacting with the surface [39]. The fact that we observe this eight lobe structure for the TbPC2 molecules as well indicates that we are imaging the molecular orbital contribution originating from the upper PC ring, which is only weakly electronically interacting with the Co support.

The appearance of an eight lobe structure is expected for both a neutral $[\mathrm{TbPC2}]^0$ (with the ligand spin still present) as well as for a negatively charged $[\mathrm{TbPc_2}]^-$ molecule (with the ligand spin quenched by the reduction with the additional electron) [40]. Therefore, spin-averaged measurements cannot distinguish between the charged and the neutral state of adsorbed TbPC2. Moreover, spin-averaged measurements cannot determine the spin state of the frontier orbitals. In order to address the spin character of these orbitals, SP-STM data is collected.

Measuring the energy dependence of the LUMO with a spin-polarized tip for parallel and antiparallel tip and sample magnetization directions shows that two states of opposite spin character are in the energy range spanned by the broad LUMO feature in the spin-averaged data. Figure 3.50 b) and c) summarizes the experimental findings: The point spectroscopy mode data (Fig. 3.50b) show that the broad feature with a maximum at $U = +1.3\,\mathrm{V}$, which we assigned to the LUMO in the spin-averaged measurements (see Fig. 3.50a), contains two spectroscopic features: the first feature at $U = +0.9\,\mathrm{V}$ is clearly visible only if tip and sample magnetizations are aligned antiparallel (in the following referred to as LUMO_{ap}), while the second feature at $U = +1.2\,\mathrm{V}$ is more pronounced if tip and sample magnetizations are aligned parallel (LUMO_p). The lower pannel of figure 3.50b depicts the difference of spin-resolved normalized differential tunneling conductance for antiparallel and parallel alignment, which is a measure of the spin polarization of LUMO_{ap} and LUMO_p. Clearly, LUMO_{ap} is of opposite spin character compared with LUMO_p. Their exact energetic positions are determined by fitting two Lorentzian functions. Note that the areas below the “antiparallel” and the “parallel” LUMO features are equal, indicating that the total spin polarization of the entire LUMO is zero. After determining the spin character of these states in point spectroscopy mode we have mapped the spatial distribution of both states in the spin-split LUMO. To do this we performed constant height mode measurements. In order to avoid any topographic effects in SP-STM data [41] the tip was stabilized above the non-magnetic Ir substrate, which results in the same tip-sample distance for both parallel and antiparallel alignment of the tip and the Co

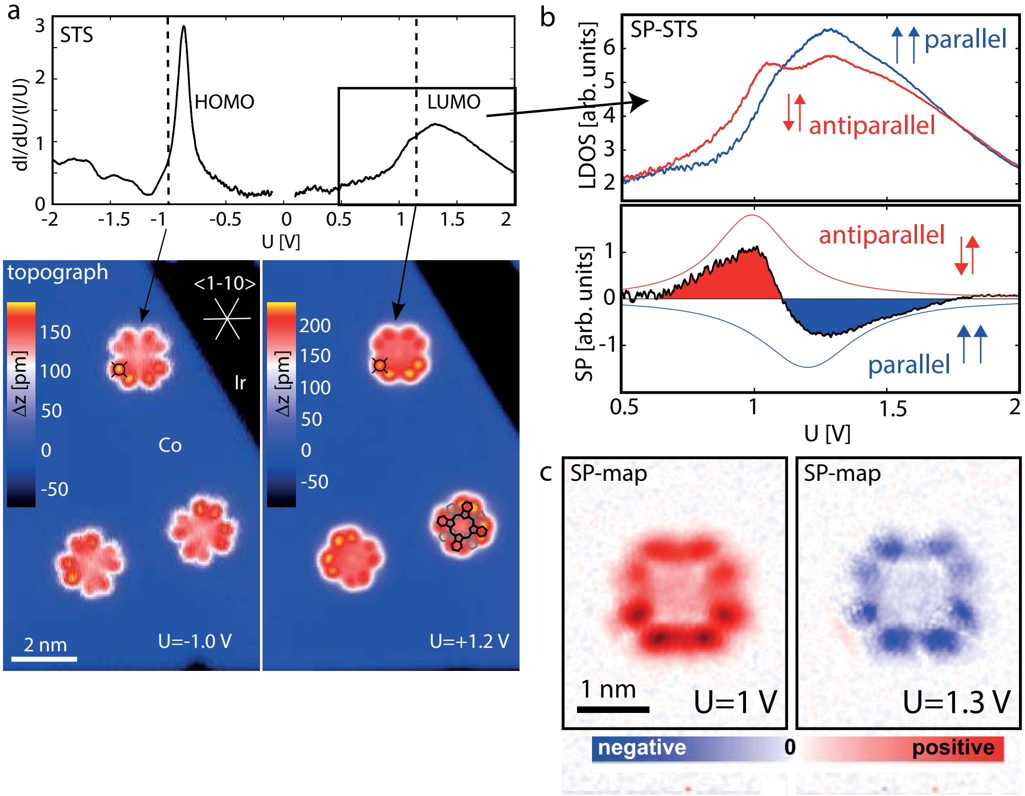

Figure 3.50: SP-STM and SP-STS of TbPC2 molecules on Co on Ir(111). Spin-averaged STS (a) clearly resolves the HOMO and LUMO of TbPC2 on Co/Ir. The corresponding spin-averaged STM topographs show a characteristic eight-lobe appearance of TbPC2 molecules: this appearance is characteristic for both HOMO and LUMO and originates from the upper PC ring ligand orbitals. Mapping the LUMO with a spin-polarized tip (b) reveals that the broad SP-STS feature corresponds not to one but two features (as is evident by the two peaks in the red curve). Calculating the spin-polarization (SP) shows that both features have equal weight but are in opposite spin channels. Mapping the SP (c) shows that both features have the same spatial distribution characteristic for the LUMO state but appear in opposite spin-channels.

island magnetization direction. The difference between the antiparallel and parallel case yields information about the spatial distribution of the molecular spin polarization (Fig. 3.50c): For $U = +1.0\,\mathrm{V}$, it is positive, and negative for $U = +1.3\,\mathrm{V}$, consistent with the point spectroscopy data. More importantly, both orbitals are clearly of eight lobe character. This proves that both features originate from the LUMO π-orbital. The fact that LUMO_{ap} and LUMO_p have an identical spatial distribution with opposite spin character allows us to unambiguously attribute the two spectral features in the different spin channels to the same molecular orbital, *i. e.* we spatially and energetically resolve the spin splitting of the LUMO. The magnitude of the spin splitting of the LUMO amounts to $\Delta E = eU^{LUMO_p} - eU^{LUMO_{ap}} = 210 \pm 20\,\mathrm{meV}$. As shown above, the total spin polarization of the LUMO is zero, thereby excluding the presence of a radical spin in the LUMO.

Interestingly, the spin-resolved data allows an unambiguous determination of the charge state of the TbPC2 molecule: the isolated TbPC2 molecule has an unpaired spin on the organic ligand as introduced above. This radical would show up in an SP-STM experiment as a spectroscopic feature for both bias polarity, i.e., below and above the Fermi-energy. A spin-dependent spatial mapping of these features would show the same molecular orbital but with opposite spin character, similar to the situation observed in our experiment, yet, the fact that we observe this behavior for the positive bias polarity only means that the orbital is completely empty and, therefore, the radical spin must be lost upon adsorption of the molecule. These central experimental observations are of crucial importance for device applications for this kind of SMM as the coupling of the Tb-ion to its surrounding is believed to be mediated by the ligand orbitals.

3.7.6 Atomic-scale magnetism of cobalt-intercalated graphene

R. Decker, J. Brede, N. Atodiresei, V. Caciuc, S. Blügel, and R. Wiesendanger

The electronic properties of graphene [42] depend critically on its environment and in particular on its substrate. Therefore, it is important to be able to precisely design and control the physical properties of the graphene-substrate interfaces. Inspired by the extensively studied graphite intercalation compounds [43,44], an emerging method to engineer technologically relevant hybrid organic-metal interfaces is to intercalate specific elements at the interface. So far, most efforts in that direction have been employed to use intercalants to reduce the graphene-substrate interaction in order to keep the unprecedented exotic properties of bare graphene intact [45], open a gap at the Dirac point [46], or induce superconductivity [47]. However, this approach has not yet been exploited to create an interstitial ferromagnetic layer and study its effects on the properties of graphene.

Being made of light atoms, the spin-orbit coupling in graphene is known to be very weak and the intrinsic magnetic properties of graphene are difficult to observe experimentally. Therefore, most studies concerning the magnetic properties of graphene have been focusing on its edges, defects, and impurities [48]. Experimentally, however, many features predicted by theory were not observed yet and the magnetic properties of graphene in general remain an almost unexplored and challenging research topic [49]. Since graphene is only one layer thick and is known to be an inert material, graphene-based ferromagnetic heterostructures are an ideal candidate for a new class of tunnel magnetoresistance (TMR) or giant magnetoresistance (GMR) devices. A detailed state-of-the-art experimental and theoretical description at the atomic scale of the topography as well as of the complex phenomena occurring at the hybrid graphene-ferromagnetic surface and interface represents the first necessary steps towards the development of graphene-based spintronics.

In this combined experimental and theoretical study, we gain a unique and detailed insight into the physical properties of the cobalt-intercalated graphene/Ir(111) system [56]. Using spin-polarized scanning tunneling microscopy (SP-STM) [50], we resolve simultaneously the morphology and the local magnetic properties of graphene on top of monolayer cobalt islands which were intercalated between the graphene and the Ir(111) substrate. State-of-the-art first principles calculations were performed to gain a thorough insight into the nature of the local bonding and the magnetic interactions present at the hybrid graphene-ferromagnet interface that lead to the experimentally observed topography and local spin polarization in this system.

SP-STM measurements were performed under UHV conditions ($p_{base} < 1.10^{-10} mbar$). All tip and sample preparations were done *in vacuo*. The Ir(111) substrate was prepared by repeated cycles of sputtering and annealing in O_2 atmosphere ($P_{O_2} = 10^{-7}\ mbar$) followed by a flash at ~ 1000°C . After the cobalt intercalation process (see below), samples were transferred in situ into a home-built SP-STM operated at ~ 6 K. Fe-coated (~ 50ML) tungsten tips were used to observe the magnetic structure of the sample. All data were acquired in the constant-current mode. Spin-polarized differential tunneling conductance maps were recorded using the lock-in technique, by detecting the ac tunneling current induced by a sinusoidal voltage added to the dc sample bias V_b, with the magnetic orientation of the tip aligned by applying an external magnetic field $|B| \geq 1$ T. Calculations were performed via DFT in the Generalized Gradient Approximation + Hubbard term (GGA+U), including van der Waals interactions.

The Ir(111) surface was partially covered by micron sized graphene patches obtained by a chemical vapor deposition as described in ref. [51]. Cobalt was deposited onto the graphene/Ir(111) sample, which was kept at or slightly above room temperature. The intercalation occurs by annealing the graphene + Co covered Ir(111) surface at ~ 200°C for several minutes. At the graphene-covered areas, this results in the formation of random sized but well-defined intercalation regions, mostly located at Ir(111) step edges.

These intercalation regions are characterized by a Moiré pattern with a high corrugation (~ 1.2 to 1.8Å, depending on the tunneling current and/or the bias voltage).

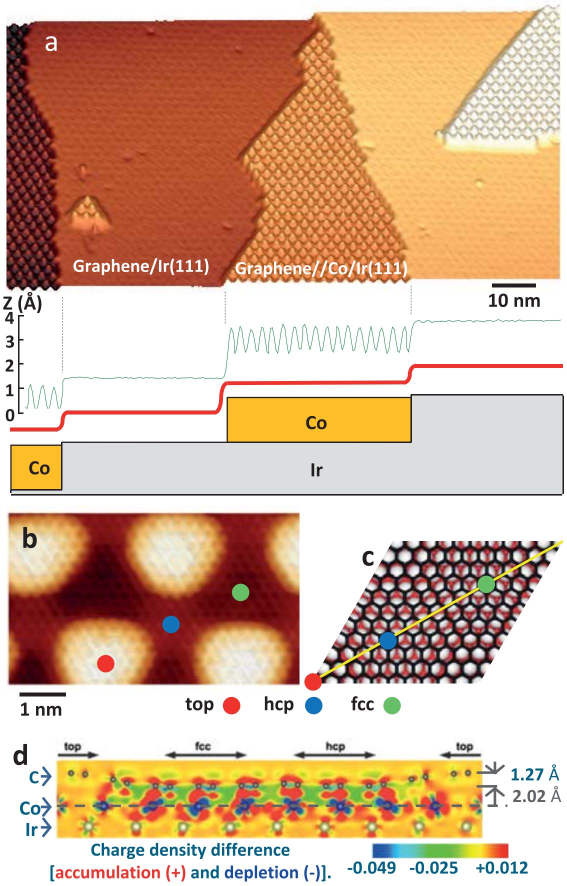

Figure 3.51: Structure of cobalt-intercalated graphene on Ir(111). a) Topography of the graphene/Ir(111) surface with four intercalation regions at typical locations (-0.7 V, 1 nA). The line profile taken at the bottom of the topograph illustrates the difference between the graphene/Ir(111) and the graphene/Co/Ir(111) Moiré corrugations. b) High resolution STM topograph (-0.1V, 4μA) with the graphene atomic lattice and the Moiré pattern at a cobalt intercalation region. c) Model of graphene/Co/Ir(111) (see text) showing the unit cell. black: graphene, white: cobalt, red: iridium atoms. d) Side view of the charge density difference plots of the graphene on Co/Ir(111) surface cut along the yellow plane in (c).

A typical STM image of the graphene/Ir(111) surface with intercalated cobalt areas is presented in Fig.1a. The line profile (green line) shown underneath Fig.1a clearly illustrates the striking difference of the graphene/Ir(111) and the graphene/Co/Ir(111) Moiré corrugations. A magnified view from a high resolution STM topograph in Fig.1b highlights the morphology at the atomic scale of the graphene/Co/Ir(111) heterostructure (see also the ball and stick model in Fig.1c). The lateral periodicity and orientation of this Moiré pattern is identical to the one of graphene/Ir(111), which demonstrates that the cobalt layer underneath graphene is pseudomorphic with the Ir(111) lattice. From the ground state geometry of the graphene/Co/Ir(111) sys-

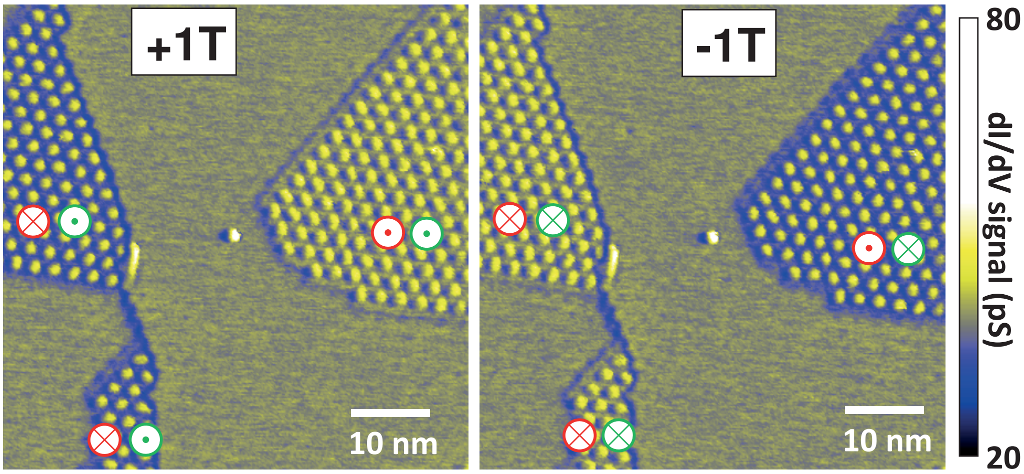

Figure 3.52: Out-of-plane magnetic maps of the intercalation regions. Spin-resolved dI/dV maps (-0.9V, 1nA) acquired with an applied out-of-plane magnetic field a) +1T, b) -1T. Green symbols: magnetic orientation of the SP-STM tip, red symbols: magnetic orientation of the intercalation regions.

tem obtained by means of density functional theory (DFT), we find that the highest and lowest C atoms above the Co layer are 3.29Å at the top position and 2.02Å at the hcp sites, respectively. Therefore, the theoretical atomic (geometrical) graphene corrugation is 1.27Å (Fig.1d) which is significantly larger than 0.41Å obtained for graphene/Ir(111) [52]. Note that in our STM experiments the measured corrugation is in the range of 1.2 - 1.8Å and comparable with the geometrical one. Therefore, the measured corrugation mainly reflects the corrugation within the Moiré pattern of the graphene layer itself on top of the atomically flat intercalated cobalt layer.

Detailed insights into the magnetic properties of the hybrid graphene/Co/Ir(111) system are revealed by our SP-STM experiments. Fig.2a and 2b present two maps of the spin resolved differential tunneling conductance (dI/dV-map) of the same area with an out-of-plane applied magnetic field of +1T and -1T, respectively. These magnetic fields are strong enough to align the magnetization direction of the Fe-coated tip but are too small to align the magnetization direction of the graphene/Co/Ir(111) heterostructures (see for example ref. [53]). For opposite field orientations we observe a contrast reversal for the intercalation regions in the spin-resolved dI/dV maps. The contrast reversal arises due to the tunneling magneto-resistance (TMR) effect and unambiguously establishes the spin sensitivity in the measurements. More precisely, the contrast is due to a difference between the majority and minority density of states (DOS) at this particular energy measured at the position of the tip. Therefore, primarily, the electronic states that have a long range decay into the vacuum give rise to the observed contrast. No spin contrast has been observed while applying an in-plane magnetic field, which clearly indicates a magnetic anisotropy of the heterostructure with an out-of-plane easy axis.

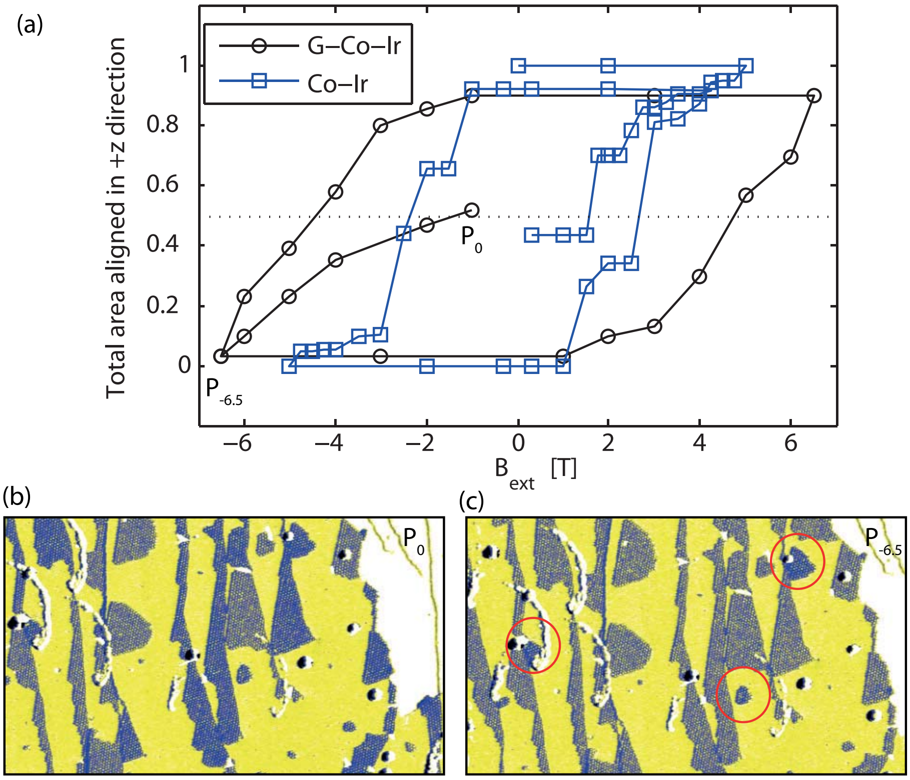

Figure 3.53: Coercivity of Co intercalated graphene. Hysteresis loop (black data points) obtained from large scale spin-resolved dI/dV maps presenting 33 intercalation regions (b) and (c). Light (dark) blue represent G-Co-Ir areas that are aligned parallel (antiparallel) with the tip. Yellow areas show G-Ir and white areas show the bare Ir surface. Each point represents the area of Co intercalated G that is aligned with the external magnetic field [a value of 1 (0) corresponds to 100 % of the intercalated area aligned in + z (-z) direction]. For direct comparison, th hysteresis loop obtained for Co on Ir (blue curve) is given as well. The increase in coercivity for G-Co-Ir compared to Co-Ir is apparent.

Our DFT calculations show that, due to a strong graphene-cobalt interaction at the fcc and hcp sites, a graphene unit cell acquires a total magnetic moment of $-1.36\mu_B$ (spin-down electrons) leading to an antiferromagnetic coupling to the Co layer beneath. At top sites, where the graphene-cobalt interaction is significantly weaker, the graphene has a much smaller total magnetic moment of $+0.14\mu_B$ (spin-up electrons) and couples ferromagnetically to the Co layer.

To characterize the response of the system to an external magnetic field and to get an estimate of the magnetic anisotropy energy, we performed a series of spin-polarized dI/dV measurements of large surface areas containing 33 intercalation regions of different sizes from ~ 40 nm^2 to ~ 2930 nm^2 and various shapes. Each subsequent map was acquired with a different out-of-plane magnetic field in the following order: 0 T → -6.5 T → +6.5 T → -6.5 T. The percentage of area among all intercalation regions which are aligned in the +z direction vs. the applied field is plotted in Fig.3 and shows a hysteresis loop. It indicates that even for an applied field as high as ± 6.5 T (our upper field limit), we are not able to align 100% of the intercalation regions. Therefore, the actual coercive field is in reality higher than the value of $\sim$ 4.5 T deduced from the loop and much higher than the one measured for Co/Ir(111) [51]. This clearly shows that the graphene/Co/Ir(111) heterostructures have a much higher magnetic anisotropy energy than cobalt islands on Ir(111).

In summary, by combining cutting-edge SP-STM experiments and state-of-art first principles calculations, we present a detailed characterization of the atomic structure and magnetic properties of the cobalt intercalated graphene/Ir(111) system. The graphene layer presents a magnetic Moiré pattern with a high corrugation on the underlying cobalt monolayer. The graphene/Co/Ir(111) heterostructures exhibit an out-of-plane magnetization direction and an extremely high coercivity of more than 4.5 T. The high coercivity, the extremely thin structure (1 AL of Co and 1 AL of C), and the chemical inertness of the graphene layer itself make these kind of heterostructures highly appealing for technological applications such as next generation read and write heads based on the TMR effect. Furthermore, our approach opens a new route towards the observation of the magnetic properties of graphene. Here, the graphene is incorporated in a well-defined geometry and has a complex magnetic structure, which leads to a variation of the local spin polarization on the atomic scale. Such a surface may in the future be exploited to energy selectively inject spin currents with different spin signs by choosing appropriate adsorption sites for spin active adsorbates such as single atoms, magnetic molecules, or metal clusters.

References

[1] A. Aviram and M. A. Ratner, Molecular rectifiers, Cemical Physics Letters **29**, 277-283 (1974).

[2] J. R. Heath and M. A. Ratner, Molecular Electronics, Physics Today **56**, 43-49 (2003).

[3] M. A. Reed, C. Zhou, C. J. Muller, T. P. Burgin, and J. M. Tour, Conductance of a Molecular Junction, Science **278**, 252-254 (1997).

[4] J. Park, A. N. Pasupathy, J. I. Goldsmith, C. Chang, Y. Yaish, J. R. Petta, M. Rinkoski, J. P. Sethna, H. D. Abruña, P. L. McEuen, and D. C. Ralph, Coulomb blockade and the Kondo effect in single-atom transistors, Nature **417**, 722-725 (2002).

[5] J. J. Parks, A. R. Champagne, T. A. Costi, W. W. Shum, A. N. Pasupathy, E. Neuscamman, S. Flores-Torres, P. S. Cornaglia, A. A. Aligia, C. A. Balseiro, G. K.-L. Chan, H. D. Abruña, and D. C. Ralph, Mechanical Control of Spin States in Spin-1 Molecules and the Underscreened Kondo Effect, Science **328** no. 5984, 1370-1373 (2010).

[6] R. Vincent, S. Klyatskaya, M. Ruben, W. Wernsdorfer, and F. Balestro, Electronic read-out of a single nuclear spin using a molecular spin transistor, Nature **488**, 357-360 (2012).

[7] C. B. Harris, R. L. Schlupp, and H. Schuch, Optically Detected Electron Spin Locking and Rotary Echo Trains in Molecular Excited States, Phys. Rev. Lett. **30**, 1019-1022 (1973).

[8] V. Dediu, M. Murgia, F. C. Matacotta, C. Taliani, and S. Barbanera, Room temperature spin polarized injection in organic semiconductor, Solid State Communications **122**, 181-184 (2002).

[9] V. A. Dediu, L. E. Hueso, I. Bergenti, and C. Taliani, Spin routes in organic semiconductors, Nature Materials **8**, 707-716 (2009).

[10] J. S. Jiang, J. E. Pearson, and S. D. Bader, Absence of spin transport in the organic semiconductor Alq$_3$, Phys. Rev. B **77**, 035303 (2008).

[11] M. Warner, S. Din, I. S. Tupitsyn, G. W. Morley, A. M. Stoneham, J. A. Gardener, Z. Wu, A. J. Fisher, S. Heutz,C. W. M. Kay, G. Aeppli, Potential for spin-based information processing in a thin-film molecular semiconductor, Nature **503**, 504-508 (2013).

[12] C. Boehme and J. M. Lupton, Challenges for organic spintronics, Nature Nanotechnology **8**, 612-615 (2013).

[13] J. Brede, N. Atodiresei, G. Hoffmann, S. Kuck, P. Lazić, V. Caciuc, Y. Morikawa, S. Blügel, and R. Wiesendanger, Spin- and Energy-Dependent Tunneling through a Single Molecule with Intramolecular Spatial Resolution, Phys. Rev. Lett. **105**, 047204 (2010).

[14] N. Atodiresei, J. Brede, P. Lazic, V. Caciuc, G. Hoffmann, R. Wiesendanger, and S. Blügel, Design of the Local Spin-polarization at the Organic-Ferromagnetic Interface, Phys. Rev. Lett. **105**, 066601 (2010).

[15] O. Pietzsch, A. Kubetzka, M. Bode, and R. Wiesendanger, Spin-polarized scanning tunneling spectroscopy of nano-scale cobalt islands on Cu(111), Phys. Rev. Lett. **92**, 57202 (2004).

[16] G. Binasch, P. Grünberg, F. Saurenbach, and W. Zinn, Enhanced magnetoresistance in layered magnetic structures with antiferromagnetic interlayer exchange, Phys. Rev. B **39**, 4828-4830 (1989) .

[17] M. N. Baibich, J. M. Broto, A. Fert, F. Nguyen Van Dau, and F. Petroff, Giant Magnetoresistance of (001)Fe/(001)Cr Magnetic Superlattices, Phys. Rev. Lett. **61**, 2472-2475 (1988) .

[18] F. Meier, K. von Bergmann, P. Ferriani, J. Wiebe, M. Bode, K. Hashimoto, S. Heinze, and R. Wiesendanger, F. Meier, K. von Bergmann, P. Ferriani, J. Wiebe, M. Bode, K. Hashimoto, S. Heinze, and R. Wiesendanger, Phys. Rev. B **74**, 195411 (2006).

[19] A. B. Shick and A. Lichtenstein, Orbital moment of a single Co atom on a Pt(111) surface - a view, from correlated band theory, Journal of Physics: Condensed Matter **20**, 015002 (2008).

[20] P. Gambardella, S. Rusponi, M. Veronese, S. S. Dhesi, C. Grazioli, A. Dallmeyer, I. Cabria, R. Zeller, P. H. Dederichs, K. Kern, C. Carbone, and H. Brune, Giant Magnetic Anisotropy of Single Cobalt Atoms and Nanoparticles, Science **300**, 1130-1133 (2003).

[21] F. Marczinowski, K. von Bergmann, M. Bode, and R. Wiesendanger, Growth of Cr on Ir(111) studied by scanning tunneling microscopy, Surf. Sci. **600**, 1034 (2006).

[22] O. Pietzsch, S. Okatov, A. Kubetzka, M. Bode, S. Heinze, A. Lichtenstein, and R. Wiesendanger, Spin-Resolved Electronic Structure of Nanoscale Cobalt Islands on Cu(111), Phys. Rev. Lett. **96**, 237203 (2006).

[23] J. Wiebe, L. Sacharow, A. Wachowiak, G. Bihlmayer, S. Heinze, S. Blügel, M. Morgenstern, and R. Wiesendanger, Scanning tunneling spectroscopy on cobalt(0001): spectroscopic signature of stacking faults and dislocation lines, Phys. Rev. B **70**, 35404 (2004).

[24] C. Iacovita, M. V. Rastei, B. W. Heinrich, T. Brumme, J. Kortus, L. Limot, and J. P. Bucher, Visualizing the Spin of Individual Cobalt-Phthalocyanine Molecules, Phys. Rev. Lett. **101**, 116602 (2008).

[25] N. Tsukahara, S. Shiraki, S. Itou, N. Ohta, N. Takagi, and M. Kawai, Evolution of Kondo Resonance from a Single Impurity Molecule to the Two-Dimensional Lattice, Phys. Rev. Lett. **106**, 187201-4 (2011).

[26] T. G. Gopakumar, T. Brumme, J. Kröger, C. Toher, G. Cuniberti, and R. Berndt, Coverage-Driven Electronic Decoupling of Fe-Phthalocyanine from a Ag(111) Substrate, The Journal of Physical Chemistry C **115**, 12173-12179 (2011).

[27] T. Komeda, H. Isshiki, J. Liu, Y.-F. Zhang, N. Lorente, K. Katoh, B. K. Breedlove, and M. Yamashita, Observation and electric current control of a local spin in a single-molecule magnet, Nature Communications **2**, 217 (2011).

[28] M. Mannini, F. Pineider, P. Sainctavit, C. Danieli, E. Otero, C. Sciancalepore, A. M. Talarico, M.-A. Arrio, A. Cornia, D. Gatteschi, and R. Sessoli, Magnetic memory of a single-molecule quantum magnet wired to a gold surface, Nature Materials **8**, 194-197 (2009).

[29] R. Sessoli, D. Gatteschi, A. Caneschi, and M. A. Novak, Magnetic bistability in a metal-ion cluster, Nature 365, 141-143 (1993).

[30] N. Ishikawa, M. Sugita, and W. Wernsdorfer, Quantum Tunneling of Magnetization in Lanthanide Single-Molecule Magnets: Bis(phthalocyaninato)terbium and Bis(phthalocyaninato)dysprosium Anions, Angewandte Chemie International Edition **44**, 2931-2935 (2005).

[31] A. L. Rizzini, C. Krull, T. Balashov, J. J. Kavich, A. Mugarza, P. S. Miedema, P. K. Thakur, V. Sessi, S. Klyatskaya, M. Ruben, S. Stepanow, and P. Gambardella, Coupling Single Molecule Magnets to Ferromagnetic Substrates, Phys. Rev. Lett. **107**, 177205 (2011).

[32] A. Candini, S. Klyatskaya, M. Ruben, W. Wernsdorfer, and M. Affronte, Graphene Spintronic Devices with Molecular Nanomagnets, Nano Letters 11, 2634-2639 (2011).

[33] M. Urdampilleta, S. Klyatskaya, J.-P. Cleuziou, M. Ruben, and W. Wernsdorfer, Supramolecular spin valves, Nat Mater **10**, 502-506 (2011).

[34] L. Bogani and W. Wernsdorfer, Molecular spintronics using single-molecule magnets, Nature Materials **7**, 179-186 (2008).

[35] M. N. Leuenberger and D. Loss, Quantum computing in molecular magnets, Nature **410**, 789-793 (2001).

[36] A. Dei and D. Gatteschi, Molecular (Nano) Magnets as Test Grounds of Quantum Mechanics, Angew. Chem. Int. Ed. 50, 11852-11858 (2011).

[37] N. Ishikawa, M. Sugita, T. Ishikawa, S. Koshihara, and Y. Kaizu, Lanthanide Double-Decker Complexes Functioning as Magnets at the Single-Molecular Level, Journal of the American Chemical Society **125**, 8694-8695 (2003).

[38] F. Branzoli, P. Carretta, M. Filibian, G. Zoppellaro, M. J. Graf, J. R. Galan-Mascaros, O. Fuhr, S. Brink, and M. Ruben, Spin Dynamics in the Negatively Charged Terbium (III) Bis-phthalocyaninato Complex, J. Am. Chem. Soc. **131** (12), 4387-4396 (2009).

[39] G. V. Nazin, S. W. Wu, and W. Ho, Tunneling rates in electron transport through double-barrier molecular junctions in a scanning tunneling microscope, Proc. Natl. Acad. Sci. U. S. A. **102**, 8832-8837 (2005).

[40] L. Vitali, S. Fabris, A. M. Conte, S. Brink, M. Ruben, S. Baroni, and K. Kern, Electronic Structure of Surface-supported Bis(phthalocyaninato) terbium(III) Single Molecular Magnets, Nano Lett. **8**, 3364-3368 (2008).

[41] A. Kubetzka, O. Pietzsch, M. Bode, and R. Wiesendanger, Determining the spin-polarization of surfaces by spin-polarized scanning tunneling spectroscopy, Appl. Phys. A **76**, 873 (2003).

[42] K. S. Novoselov, A. K. Geim, S. V. Morozov, D. Jiang, Y. Zhang, S. V. Dubonos, I. V. Grigorieva, and A. A. Firsov, Electric Field Effect in Atomically Thin Carbon Films **306**, 666-669 (2004).

[43] H. Zabel, and S. A. Sólin, Graphite Intercalation Compounds, SPRINGER VERLAG (1990).

[44] T. E. Weller, M. Ellerby, S. S. Saxena, R. P. Smith, and N. T. Skipper, Superconductivity in the intercalated graphite compounds C6Yb and C6Ca, Nat. Phys. **1**, 39-41 (2005).

[45] M. Gao, Y. Pan, L. Huang, H. Hu, L. Z. Zhang, H. M. Guo, S. X. Du, and H.-J. Gao, Epitaxial growth and structural property of graphene on Pt(111), Appl. Phys. Lett. **98**, 033101 (2011).

[46] C. Enderlein, Y. S. Kim, A. Bostwick, E. Rotenberg, and K. Horn, The formation of an energy gap in graphene on ruthenium by controlling the interface, New Journal of Physics **12**, 033014 (2010).

[47] G. Profeta, M. Calandra, and F. Mauri, Phonon-mediated superconductivity in graphene by lithium deposition, Nat. Phys. **8**, 131-134 (2012).

[48] O. V. Yazyev, Emergence of magnetism in graphene materials and nanostructures, Reports on Progress in Physics **73**, 056501 (2010).

[49] L. V. Dzemiantsova, M. Karolak, F. Lofink, A. Kubetzka, B. Sachs, K. von Bergmann, S. Hankemeier, T.O. Wehling, R. Frömter, H.P. Oepen, A.I. Lichtenstein, and R. Wiesendanger, Multiscale magnetic study of Ni(111) and graphene on Ni(111), Phys. Rev. B **84**, 205431 (2011).

[50] R. Wiesendanger, Spin Mapping at the Nanoscale and Atomic Scale, Rev. Mod. Phys. **81**, 1495 (2009).

[51] A. T. N'Diaye, S. Bleikamp, P. J. Feibelman, and T. Michely, Two-Dimensional Ir Cluster Lattice on a Graphene Moiré on Ir(111), Phys. Rev. Lett. **97**, 215501 (2006).

[52] C Busse, P. Lazić, R. Djemour, J. Coraux, T. Gerber, N. Atodiresei, V. Caciuc, R. Brako, A. T. N'Diaye, S. Blügel, J. Zegenhagen, and T. Michely, Graphene on Ir(111): Physisorption with Chemical Modulation, Phys. Rev. Lett. 107, 036101 (2011).

[53] J. E. Bickel, F. Meier, J. Brede, A. Kubetzka, K. von Bergmann, and R. Wiesendanger, Magnetic properties of monolayer Co islands on Ir(111) probed by spin-resolved scanning tunneling microscopy, Phys. Rev. B **84**, 054454 (2011).

[54] S. Sanvito, Molecular spintronics, Chem. Soc. Rev. **40**, 3336-3355 (2011).

[55] N. Knorr, M. A. Schneider, L. Diekhöner, P. Wahl, and K. Kern, Kondo Effect of Single Co Adatoms on Cu Surfaces, Phys. Rev. Lett. **88**, 096804 (2002).

[56] R. Decker, J. Brede, N. Atodiresei, V. Caciuc, S. Blügel, and R. Wiesendanger, Atomic-scale magnetism of cobalt-intercalated graphene, Phys. Rev. B **87**, 041403 (2013).

[57] J. Schwöbel, Y. Fu, J. Brede, A. Dilullo, G. Hoffmann, S. Klyatskaya, M. Ruben, and R. Wiesendanger, Real-space observation of spin-split molecular orbitals of adsorbed single-molecule magnets, Nature Communications **3**, 953 (2012).

[58] A. DiLullo, S.-H. Chang, N. Baadji, K. Clark, J.-P. Klöckner, M.-H. Prosenc, S. Sanvito, R. Wiesendanger, G. Hoffmann, and S.-W. Hla, Molecular Kondo Chain, Nano Lett. **12**, 3174-3179 (2012).

[59] J. Brede and R. Wiesendanger, Spin-resolved characterization of single cobalt phthalocyanine molecules on a ferromagnetic support, Phys. Rev. B **86**, 184423 (2012).

[60] Y. Fu, J. Schwöbel, S.-W. Hla, A. Dilullo, G. Hoffmann, S. Klyatskaya, M. Ruben, and R. Wiesendanger, Reversible chiral switching of Bis(phthalocyaninato) Terbium(III) on a metal surface, Nano Lett. **12**, 3931 (2012).

3.8 Atomic Force Microscopy on insulators

A. Schwarz and R. Wiesendanger

Only atomic force microscopy (AFM) is able to study fully insulating surfaces and species adsorbed on them with atomic resolution. In the past three years we could demonstrate that the Smoluchowski effect leads to the formation of an electrostatic dipole moment at the apex of metallic AFM tips, which allows us to identify the sublattice imaged as protrusion on binary ionic surfaces, cf. Sect. 3.8.1 [1] and to determine the exact adsorption geometry of molecules deposited on such surfaces, cf. Sect. 3.8.2 [2].

Both studies were performed with a homebuilt low temperature (8 K) atomic force microscope operated in ultrahigh vacuum (UHV) [3] using the frequency modulation (FM) technique in the non-contact (NC) regime. In this mode of operation the tip located at the free end of a flexible cantilever with a spring constant c_z self-oscillates with constant amplitude A_0 at its eigenfrequency f_0. Typical values for c_z, A_0 and f_0 are 150 N/m, 3 nm and 180 kHz, respectively. Metallic tips were produced by coating commercially available oxidized Si cantilevers *in situ* with a few nanometers of Cr or Ti. In the presence of tip-sample forces the eigenfrequency f_0 is shifted to its actual cantilever frequency f by $\Delta f = f - f_0$. Scanning the tip line by line across the (x, y) sample surface while Δf is kept constant provides a $z(x, y)$ map of constant tip-sample interaction, i.e., the topography. In atomically resolved images the topography reflects variations in the magnitude of the short-ranged forces between the foremost tip atom and the surface atom underneath. Distance dependent spectroscopy data, i.e., $\Delta f(z)$-curves that can be converted into force curves $F(z)$, are recorded at predefined (x, y) positions with the z-feedback switched off.

3.8.1 Chemical identification of oppositely charged ions on polar surfaces

K. Lämmle, A. Schwarz, and R. Wiesendanger

To investigate the feasibility of chemical identification on ionic surfaces utilizing metallic tips we studied the (001) surface of bulk insulating NaCl single crystals, because this surface contains anions and cations in its surface layer. It turns out that due to the Smoluchowski effect metallic tip apices generally exhibit a permanent electrostatic dipole moment, which will always point with its positive end towards the surface. Therefore, metallic tips interact stronger with the negatively charged anions, allowing for an unambiguous identification of oppositely charged ions on polar surfaces.

Clean NaCl(001) was prepared by *in-situ* cleavage and subsequent heating. Single Co-Salen molecules were deposited to serve as marker molecules, because their adsorption site is well known [4]. 3D spectroscopy data were recorded and evaluated

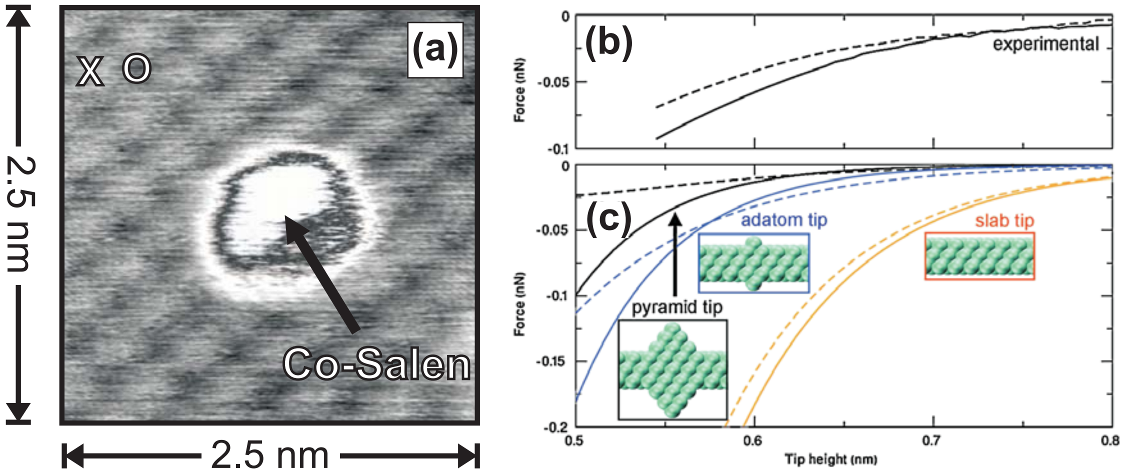

Figure 3.54: **(a)** Atomically resolved NaCl(001) imaged together with a single Co-Salen marker molecule using a metallic Cr-coated tip. Protrusions correspond to Cl-sites. X and O indicate the location of the two experimental spectroscopy curves shown as solid and dotted line, respectively, in **(b)**. Simulated force curves for each of the three tip models (see insets: blunt, single adatom and three layer pyramid, respectively) above Cl and Na ions are shown in **(c)**.

quantitatively similar to procedures described by us earlier [5]. All measurements were performed with metal-coated tips. Density functional theory (DFT) based calculations employing the plane augmented VASP code [6] and the PBE exchange correlation functional [7] were conducted in the group of A. L. Shluger at the University College London.

Based on the position of the Co-Salen marker molecule, which adsorbs with its central Co-atom on top of Cl-sites [4], protrusions in Fig. 3.54(a) represent the Cl sublattice. Two exemplary force curves recorded with a Cr-coated tip above a protrusion (Cl) and depression (Na), respectively, are shown in Fig. 1(b). Note that no absolute z-scale can be obtained from experimental spectroscopy curves alone. However, the presence of a marker molecule provides an estimate of the lower limit of absolute tip-sample separation. In the presented data set, the distance of closest approach was chosen to obtain the best resolution of the surface ions in the vicinity of the molecule, but without altering the original position of the molecule.

DFT calculations [4] have demonstrated that the Co-Salen molecule adsorbs in a planar configuration at ≈ 0.38 nm above the surface plane. Additional calculations demonstrate that the short-range interaction between the Cr tip apex and the Co-Salen enters the repulsive regime at a separation of about 0.15 nm. Assuming that closer approach would lead to strong deformation or displacement of the molecule, we estimate that the minimum tip-surface separation required to avoid manipulating the molecule is ≈ 0.53 nm.

For calculations the tip base is represented by a 5×7 slab of the Cr(110) surface, 3 atomic layers deep, with the central layer of atoms frozen in the bulk positions and with all other atoms free to relax. This Cr slab is slightly stretched/compressed to match the periodicity of the NaCl slab (2.019×2.019 nm^2). This does not significantly affect the electronic structure, and only changes the work function of the Cr slab by ≈ 0.05 eV. We consider three different tip models based on the Cr slab, cf. insets of Fig. 3.54(c): (i) the slab alone (slab tip); (ii) the slab with a single protruding adatom (adatom tip); and (iii) the slab with a three layer pyramidal protrusion terminating with a single atom (pyramid tip). Both protrusions are replicated on both sides of the Cr slab, and symmetrically relaxed. For both prodruding tips we observe the formation of a surface dipole due to the Smoluchowski effect [8] caused by the incomplete screening of the positive ion cores, because the spatial variation of the charge density is limited by the Fermi wavelength of the conduction electrons. The calculated dipole moments for the adsorbed atom (1.23 D/step atom) and the pyramid tip (1.98 D/step atom) broadly agree with the results of previous studies on extended steps at metal surfaces (0.16 - 1 D/step atom [9,10]) and increase with decreasing the coordination of surface atoms [11]. Noteworthy, this fundamental property of metal surfaces is difficult to describe within continuum approximations to the tip polarization [12] and remained unaccounted for in some recent models of Kelvin probe force microscopy [13].

For each of the three tip models, the apex atom (or, in the case of the slab tip, an atom in the surface layer) is placed directly above either a Na or a Cl ion at various initial tip heights. The tip height is defined as the distance between the topmost Na (Cl) ion and the apex atom of the initially relaxed tip. The positions of all free atoms in the system are then fully relaxed. For tip-surface distances smaller than 0.6 nm, the short-range chemical interaction above the Cl ion is more attractive than above the Na ion. A marked energy change at a height of about 0.4 nm is due to the jump of the surface Cl ion by about 0.15 nm towards the tip apex. The displaced Cl ion remains charged and as the tip is retracted away from the surface, it returns back into the surface plane.

For each tip model and lateral position, the total energy as a function of the tip height was fitted to a Morse function, which was differentiated to obtain the force as a function of the tip height; cf. Fig. 3.54(c). The tip-surface force decreases with increasing the tip sharpness, since the blunter the tip, the more Cr atoms are closer to the surface for a given tip height, which is defined by the lowest atom. It is also apparent that the sharper the tip, the larger the difference between the forces on the tip above a Cl ion and a Na ion. For the flat slab tip, there is no significant difference between the two lateral configurations, which is to be expected. The other two tip models, in spite of some quantitative differences in the behavior of the force-distance curves, demonstrate reasonable agreement with the experiment in the relevant distance range of 0.5-0.6 nm. Due to their idealized structure, none of the tips gives perfect quantitative agreement with the experiment in the whole distance range, however, there is a good agreement with the measured difference between the forces above Cl and Na ions at the closest approach, which is 0.032 nN. For the adatom tip, this difference would correspond to a tip height of 0.53 nm whereas for the pyramid tip to a tip height of 0.55 nm. These results are consistent with the independent estimate of the distance of closest approach on the basis of the adsorption height of the Co-Salen molecule and the minimum tip height at which the tip-molecule interaction is likely to induce manipulation (≈ 0.53 nm).

At closer tip-surface separations of ≈ 0.3 nm, the calculations show a significant charge transfer to the tip, which is more pronounced when the tip is above a Cl ion. This chemical interaction due to a hybridization of the Cl $3p$ and Cr $3d$ electronic states decays rapidly as the tip moves away from the surface. Above ≈ 0.4 nm, there is negligible charge transfer and the tip-surface interaction and the image contrast is primarily due to the electrostatic interaction of the *dipole moment* of the tip apex with the surface ions. The orientation of the tip dipole (its positive pole is pointing to the surface) favors the interaction with the negative surface Cl ion and is enhanced by the additional polarization of the tip and the surface caused by the interaction, in agreement with Ref. [10].

Our simulations for our model system show that the electrostatic interaction between surface ions and the permanent dipole in the Cr tip apex dominates the short-range component of the total tip-sample interaction on NaCl(001) for separations larger than 0.4 nm, where tip instabilities are absent. At the same time this kind of short-range electrostatic interaction is strong enough to allow for atomic resolution in the distance regime up to 0.6 nm. These findings can be generalized: Since the Smoluchowski effect is universally observed on corrugated metal surfaces and in nanoclusters [14], an electric dipole will always be present at a metallic tip apex. Moreover, it will always point with its positive pole into the vacuum region, i.e., towards the sample surface. As a result, on negatively charged anions the tip-sample interaction will be more attractive than on positively charged cations. Thus, the former appear as protrusions and the latter as depressions in constant Δf images on polar surfaces and thus allow for an unambiguous atom identification.

3.8.2 Accurate determination of the adsorption geometry of Co-Salen on NiO(001)

J. Grenz, K. Lämmle, A. Schwarz, and R. Wiesendanger

Here we apply the chemical identification capabilities of AFM described above, cf., Sect. 3.8.1, to investigate the adsorption geometry of Co-Salen deposited on NiO(001) and compare these results with a previous study on NaCl(001) [4]. We find that on NiO(001) Co-Salen adsorbs with its central Co atom above the anions, i.e., the O sites, and is aligned ±4° away from <110>-directions. On NaCl(001) Co-Salen also adsorbs with its central Co atom above the anions, i.e., the Cl sites, but it can be either aligned ±5° away from <110>- or <100>-directions. These finding are in agreement with Density Functional Theory (DFT) based calculations performed in the group of A. L. Shluger at the University College London.

Understanding the geometric parameters and mechanisms of adsorption and diffusion of organic molecules at insulating surfaces in general is central to catalysis, molecular electronics, molecular sensors and molecular magnets. It is also a necessary step in elucidating the mechanisms of formation and structure of molecular assemblies at surfaces. To date, most experimental studies on individual molecules at surfaces have been performed on conducting and in most cases metallic substrates using Scanning Tunneling Microscopy (STM) [15]. Although AFM has been successfully employed to investigate organic thin films on insulating substrates, systematic high-resolution studies of individual molecules, well-separated on a surface are still rare. One reason is that organic molecules usually bind weakly to insulating surfaces and are therefore often mobile at room temperature. Moreover, interaction with the tip can change their position and configuration during imaging at short tip-surface separations. However, many existing and future applications require exploring the properties of molecules on electrically insulating surfaces like oxides, which exhibit a wide range of interesting magnetic, optical, and electronic properties [16]. Studying individual molecules with atomic resolution on such surfaces requires the application of AFM.

In order to determine the exact adsorption site accurately from an experimental image of an individual molecule, atomic resolution together with chemical identification of the substrate must be obtained simultaneously. Recently, pentacene and other relatively large molecules have been studied using NC-AFM on patches of ultrathin NaCl layers deposited on Cu(111) [17]. In this setup, tunneling was still possible and suitable tips could be prepared on the bare metallic substrate in the STM mode. Certain atomic or molecular species were transferred from the surface to the tip apex using standard procedures to improve imaging. Such well-controllable procedures still do not exist for pure AFM measurements on bulk-insulating surfaces.

Co-Salen is known for its ability to reversibly coordinate molecular oxygen [18] and is used in numerous applications in material chemistry and transition metal catalysis [19]. The (001) surface of NiO is a well-defined charge neutral easy cleavage plane. Since the surface exhibits a row-wise antiferromagnetic order, it is a very interesting substrate to study paramagnetic metal-organic complexes like Co-Salen utilizing magnetic exchange force microscopy (MExFM) [20, 21]. Although NiO has the same crystal structure as NaCl and is an ionic surface as well, it turns out that adsorption, bonding and growth are very different in these two systems.

NiO(001) substrates were prepared by *in-situ* cleavage of single crystals in UHV and subsequent annealing at about 500°C to remove residual charges. Thereafter, low-density molecule deposition onto the cold substrate (about 27 K) took place directly in the low-temperature microscope kept in a cryogenic environment with a miniaturized crucible loaded temporarily into the cantilever stage [22]. To unambiguously identify the atomic species in the substrate, the oxidized tips of Si cantilevers were coated *in-situ* with a few nanometers of Cr. To determine the contact potential difference (CPD)

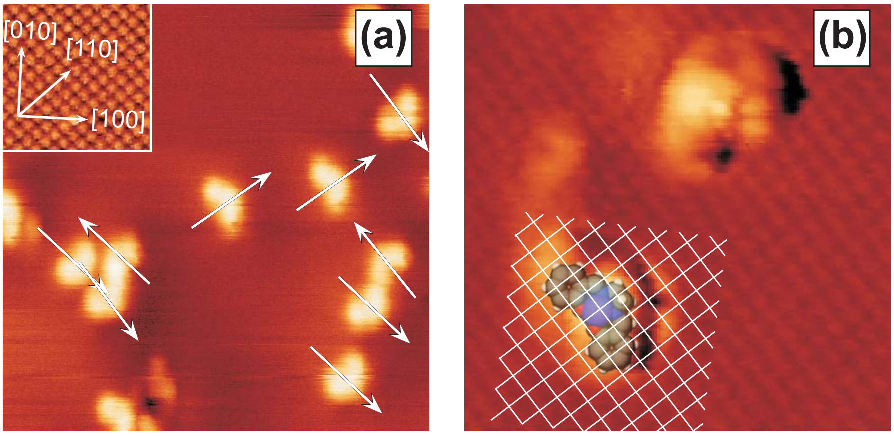

Figure 3.55: **(a)** (16 × 16) nm^2 AFM image of individual molecules adsorbed on NiO(001). The arrows mark the orientations of the symmetry axis of the molecule, which is oriented ±4° away form the <110> substrate directions determined from atomically resolved images as shown in the inset. **(b)** (5.5 × 5.5) nm^2 high-resolution AFM image showing two Co-Salen molecules along with the atomically resolved substrate. The grid indicates the positions of bright spots in relation to the half-transparent ball model fit to one Co-Salen molecule demonstrating that the molecule adsorbs with its central Co atom on top of bright spots on the surface, i.e., at O sites.

between tip and sample, we recorded $\Delta f(U_{\mathrm{bias}})$-curves and applied the voltage U_{CPD} measured at the apex of the parabola to minimize the average long-range electrostatic interaction. These curves were also used to characterize the metal coated tips [1].

DFT based simulations were performed using the CP2K code and the mixed Gaussian and plane waves basis set [23]. These include geometry minimization and diffusion and rotational barrier calculations. The density of states of NiO(001) was also examined in the presence and absence of the Co-Salen molecule. To describe the interactions between Co-Salen and NiO(001) the B3LYP [24, 25] hybrid functional was selected. Using B3LYP we obtained a reasonable band gap of 3.6 eV compared to the experimental value of 4.3 eV [26]. The expense of using a hybrid functional combined with a need to minimize basis set superposition error (BSSE) by using an extensive basis set was mitigated by employing the auxiliary density matrix method [27]. The auxiliary density matrix method employs an auxiliary basis set to greatly improve the efficiency of calculating Hartree-Fock exchange when using hybrid functionals. We employed an auxiliary basis set to calculate the electron repulsion integrals consisting of three uncontracted Gaussians for each angular momentum channel. Basis sets for all elements except Ni and Co were taken from the standard CP2K distribution (pFIT3 [27]).

The NiO (001) surface was simulated as a 3-layer slab consisting of 288 atoms. The surface size was selected to avoid interactions between Co-Salen molecules in the 2D periodic simulation by increasing the cell size until the adsorption energy converged.

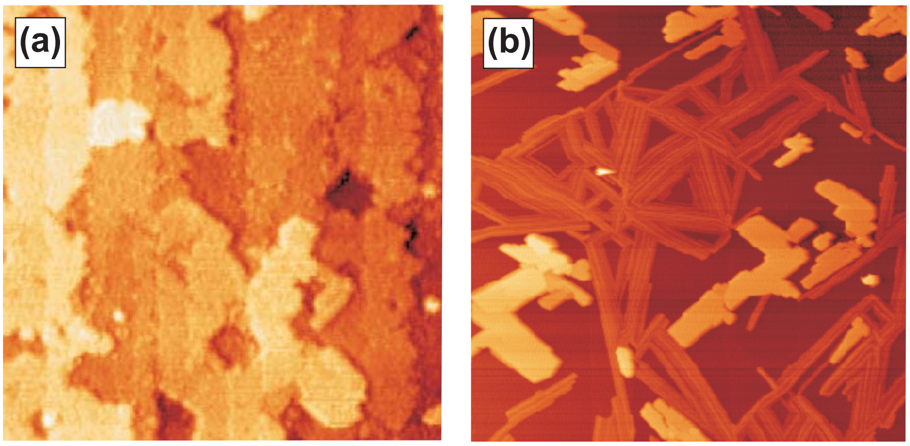

Figure 3.56: **(a)** (200×200) nm^2 AFM image after deposition of several monolayers of Co-Salen molecules on NiO(001) at room temperature showing layer-by-layer step-flow growth. **(b)** $(2 \times 2)\mu$m^2 AFM image after deposition of several monolayers of Co-Salen molecules on NaCl(001) at room temperature exhibiting a biomodal island growth composed of compact nanocrystallites and long nanowires.

The plane wave cutoff was selected to be 400 Ry by increasing it until the adsorption energy of the system converged. A semi-empirical correction was employed to account for long range dispersion interactions [28]. In addition to examining the NiO(001), Co-Salen on NaCl(001) was treated with the same approach to ensure comparability with prior data.

Figure 3.55(a) presents a typical overview image of the NiO(001) surface after molecular deposition. The banana-shaped objects can be identified as flat lying Co-Salen molecules. They can be straightforwardly distinguished from contaminations by their characteristic shape and apparent height (typically about 100-200 pm). Note that the apparent height depends on both the mesoscopic tip radius and the tip-sample distance. The orientations of the molecules appeared to be random, but a systematic analysis of the images revealed eight clearly distinguishable orientations relative to the underlying lattice. Using atomically resolved NC-AFM data on the bare substrate as a reference (see inset), we found that the primary axes of all the molecules are rotated either clockwise or anticlockwise by about 4° away from the $<110>$ directions of the substrate, as shown in Fig. 3.55(a). Using a sample of N=133 evaluated molecules we found that 80 molecules (60%) were rotated clockwise while 53 (40%) were rotated anticlockwise with respect to the $<110>$ directions. Peculiarly, on NaCl(001), which possesses the same symmetry, a total of 16 orientations along two different principal crystallographic substrate directions ($<110>$ and $<100>$) with a deviation angle of 5° were found with a significant preference for orientations along the $<110>$ directions [4].

An image containing two isolated Co-Salen molecules on the atomically resolved NiO(001) substrate is shown in Fig. 3.55(b). The data set was recorded using a metallic Cr coated tip to facilitate chemical identification on the surface [1]. The measured apparent height, length, and width of the molecule are about 180 pm, 1.8 nm and 1.0 nm, respectively. Taking the convolution with the tip into consideration, the measured dimensions fit very well to the expected values of 200 pm, 1.3 nm and 0.6 nm. A half-transparent ball model has been superimposed above the lower molecule in the AFM image. The overlaid grid indicates the positions of the protrusions, which can be seen to be located above the central Co atom of the molecule. Combined with theoretical modeling these results allow us to identify the protrusions as O sites on NiO and thus unambiguously determine the adsorption geometry and orientations of Co-Salen.

Occasionally, we were able to observe single Co-Salen molecules moving during the scan process on NiO(001). These motions were always seen to be a stepwise displacement from one adsorption site to a neighboring one along the $<110>$ directions. On the NaCl(001) surface we observed such tip-induced stepwise displacements much more often, indicating a lower molecular diffusion barrier. Moreover, on NaCl(001) such displacements were not only observed along the $<110>$ directions, but along the $<100>$ directions as well. Interestingly, the observed displacement directions coincide with the preferred adsorption orientations of Co-Salen on the respective substrates.

We note that, although the single molecule adsorption site seems to be similar on both surfaces, growth modes of thin films are very different. When relatively large amounts of molecules are deposited and subsequently imaged at room temperature, a layer-by-layer step flow growth is observed on NiO(001), as can be seen in Fig. 3.56(a). In contrast, the deposition of Co-Salen on NaCl(001) prepared in the same way exhibits island growth as displayed in Fig. 3.56(b) [29]. Layer-by-layer growth indicates that the molecule-substrate interaction is stronger than the interaction between individual molecules, while island growth indicates stronger interaction between individual molecules in comparison to the molecule-substrate interaction.

To determine the adsorption geometry on NiO(001), the Co-Salen molecule was initially positioned above the surface in a variety of configurations with the plane of the molecular board parallel to the surface. All atoms in the Co-Salen molecule and the first two layers of NiO were allowed to relax. In the lowest energy configuration the molecule is orientated in the $<110>$ directions with the Co atom directly above a surface O ion and the two molecular O atoms above Ni surface ions. In contrast to results on NaCl(001), no extra energy minimum was found near the $<100>$ directions. The shorter lattice parameter of NiO results in molecular O atoms approaching surface O atoms when the molecule rotates towards $<100>$ orientations. As a result, the local minima near the $<100>$ directions are destabilized, resulting in only 8 stable energy configurations on NiO(001) compared to 16 on NaCl(001).

On NiO(001) the Co-Salen molecule is distorted as the Co complex is pulled towards the surface and the weakly bound aromatic portions of the molecule move to compensate. In comparison to the NaCl system, the deformation energy of the molecule is greater by 0.12 eV, while the deformation of the surface costs 0.09 eV less. The Co atom to surface plane separation is 2.5 Å on NiO(001) compared to 3.0 Å on NaCl(001) with

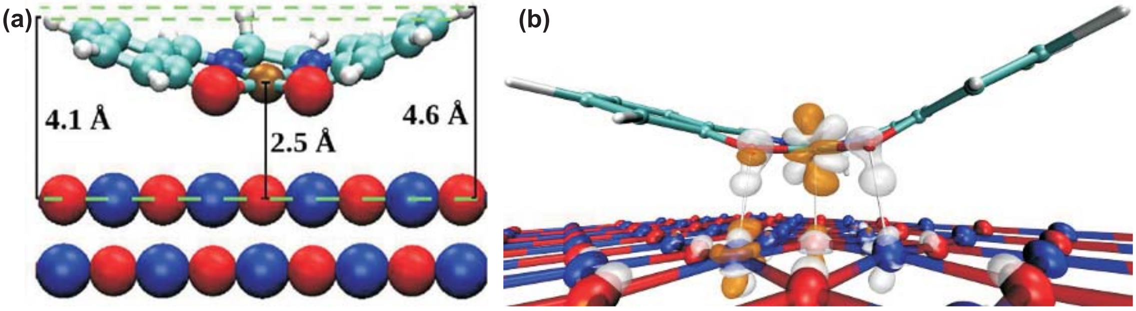

Figure 3.57: **(a)** A schematic drawing of the Co-Salen molecule adsorbed onto NiO(001). The asymmetry of the Co-Salen molecule results in a difference in height between the two aromatic rings on either side of the structure. **(b)** The difference in charge density induced by Co-Salen interacting with the NiO(001) surface is shown. Three regions of interaction are visible with positive isosurfaces represented in silver and negative isosurfaces represented in gold. The Co atom on the molecule interacts with O on the surface while O atoms on the molecule interact with the Ni atoms on the surface.

the aromatic portions of the molecule residing at comparable heights in both systems. These results indicate that Co center interacts stronger with the NiO(001) surface than with the NaCl(001) surface. In addition, the Co-Salen molecule is chiral due to its asymmetrical C_2H_4 bridge. This leads to a height difference between the hydrogen atom at each tip of both aromatic rings to the surface plane of 0.5 Å as shown in Fig. 3.57(a). The AFM images of single molecules appear indeed asymmetrical, however this might be also a result of the interaction with a somewhat asymmtric tip rather than a direct observation of the chirality of Co-Salen.

The commensurability of the Co-Salen molecule with the NiO(001) surface enhances the electrostatic interaction with a predicted adsorption energy of 1.33 eV compared to only 0.60 eV on NaCl(001). The charge density difference plot shown in Fig. 3.57(b) indicates three regions of strong local interaction with the surface. The Co atom interacts with the surface O ion, while the molecular O atoms interact with the surface Ni atoms, strengthening the bond beyond the physisorption observed previously on NaCl(001). The additional long-range dispersion contribution to the adsorption energy is estimated to be 0.66 eV.

The molecule-surface interaction can be further characterized by analyzing the work function of the system. Averaging the electrostatic potential of the system in planes parallel to the surface indicates a 0.40 eV difference in vacuum level or shift in work function due to the adsorption of Co-Salen. On the computed clean surfaces and in the NaCl system however, this change is an order of magnitude smaller (0.04 eV), indicating much smaller charge transfer or molecule polarization. This change in the work function corresponds to a 4.4 D vertical dipole moment in the adsorbed system. The total dipole moment of the system is composed of a 2.4 D contribution from the distortion of the molecule, a 0.3 D contribution from the distortion of the surface, and

1.7 D due to electronic polarization in the adsorbed system. For comparison, the gas phase molecule itself possesses a dipole of 6.0 D along the symmetry axis, which would lie parallel to the surface plane when adsorbed onto NiO(001) or NaCl(001).

A Bader analysis for the NiO(001) substrate shows net charge transfer below 0.02 e. Examining the charge density difference between the adsorbed and isolated systems, it is clear that rather than electron transfer, we observe the formation of covalent bonds between the three metal-electronegative ions. These interactions also cause the molecule to deform, further driving the polarization. The Co-Salen molecule possesses a 6 D dipole moment along the symmetry axis, which results in local attractive interactions when they approach each other on the surface. However, when adsorbed on NiO(001) it also exhibits a 4.4 D vertical dipole that arrives from both ionic and electronic relaxation as previously discussed. This vertical component decreases the interaction between Co-Salen molecules when they are confined to the surface resulting in the observed difference between Co-Salen behavior on NiO(001) and NaCl(001) as for the latter the interaction is purely electrostatic with no transfer of charge or polarization.

The barriers for rotation and translation of Co-Salen on NiO(100) have been computed in order to study diffusion and manipulation. On NaCl(001), the lattice constant is so large that the O atoms of the molecule do not come close to the surface Cl atoms in the process of rotation. On the NiO surface the repulsion between the O atoms of the molecule and the surface destabilizes the local minimum in the <100> direction resulting in only half the number of orientations compared to NaCl(001). This also leads to a relatively large energy barrier for rotation of the molecule of 0.8 eV.

The calculated barrier for diffusion from one adsorption site to the next of Co-Salen on NiO(100) is 0.6 eV, with a minimum energy pathway corresponding to translation of the molecule in the <110> directions. These results indicate that Co-Salen is most likely to move along the <110> directions when manipulated. This is in agreement with observed tip-induced motions. On NaCl(001) the minimal barrier of diffusion has been estimated to be only 0.4 eV, in agreement with the observations that Co-Salen is more easily displaced by the scanning tip than on NiO(001).

Combining experimental images obtained with metallic tips and DFT calculations allowed us to accurately determine adsorption site and adsorption geometry of Co-Salen on NiO(001). Moreover, the theoretical calculations elucidate the different contributions to the total adsorption energy and explain the different number of observed orientations as well as the preferred diffusion pathway and thin film growth mode on the structurally similar ionic surfaces NiO(001) and NaCl(001), respectively.

References

[1] G. Teobaldi *et al.*, Phys. Rev. Lett. **106**, 216102 (2011).

[2] A. Schwarz *et al.*, J. Phys. Chem. C **117**, 1105 (2013).

[3] M. Liebmann *et al.*, Rev. Sci. Instrum. **73**, 3508 (2002).

[4] K. Lämmle *et al.*, Nano Lett. **10**, 2965 (2010).

[5] H. Hölscher *et al.*, Appl. Phys. Lett. **81**, 4428 (2002).

[6] G. Kresse and J. Furthmüller, Phys. Rev. B **54**, 11169 (1996).

[7] J. P. Perdew, K. Burke, and M. Ernzerhof, Phys. Rev. Lett. **77**, 3865 (1996).

[8] R. Smoluchowski, Phys. Rev. **60**, 661 (1941).

[9] J. F. Jia, K. Inoue, Y. Hasegawa, W. S. Yang, and T. Sakurai, Phys. Rev. B **58**, 1193 (1998).

[10] J. Y. Park *et al.*, Phys. Rev. Lett. **95**, 136802 (2005).

[11] K. Besocke, B. Krahl-Urban, and H. Wagner, Surf. Sci. **68**, 39 (1977).

[12] L. Nony, A. S. Foster, F. Bocquet, and C. Loppacher, Phys. Rev. Lett. **103**, 036802 (2009).

[13] F. Bocquet, L. Nony, C. Loppacher, and T. Glatzel, Phys. Rev. B **78**, 035410 (2008).

[14] H. Oka *et al.*, Science **327**, 843 (2010).

[15] S. W. Hla and K. H. Rieder, Annu. Rev. Phys. Chem. **54**, 307 (2003).

[16] U. Diebold, S.-C. Li, and M. Schmid, Annu. Rev. Phys. Chem. **61**, 129 (2010).

[17] L. Gross, Nature Chemistry **3**, 273 (2011).

[18] T. Tsumaki, Bull. Chem. Soc. Jap. **13**, 252 (1938).

[19] N. S. Vankatarananan, G. Kuppuraj and S. Rajagopal, Coord. Chem. Rev. **249**, 1249 (2005).

[20] U. Kaiser, A. Schwarz and R. Wiesendanger, Nature **446**, 522 (2007).

[21] R. Schmidt *et al.*, Nano Lett. **490**, 211 (2009).

[22] K. Lämmle, A. Schwarz and R. Wiesendanger, Rev. Sci. Instrum. **81**, 053902 (2010).

[23] G. Lippert, J. Hutter and M. Parrinello, M. Mol. Phys. **92**, 477 (1997).

[24] A. D. Becke, J. Chem. Phys. **98**, 5648 (1993).

[25] P. J. Stephens *et al.*, J. Phys. Chem. **98**, 11623 (1994).

[26] G. A. Sawatzky and J. W. Allen, Phys. Rev. Lett. **53**, 2339 (1984).

[27] M. Guidon, J. Hutter, and J. VandeVondele, J. Chem. Theory Comput. **6**, 2348 (2010).

[28] S. Grimme, J. Comput. Chem. **27**, 1787 (2006).

[29] S. Fremy *et al.*, Nanotechnology **20**, 405608 (2009).

3.9 STS and SP-STS applied to semiconductors

J. Wiebe and R. Wiesendanger

The low-gap materials InAs and InSb are ideally suited for a study of the local properties of interacting electron systems in semiconductors by STS: they have a low effective mass and a high g-factor which results in large Landau and spin splittings in a magnetic field. The cleavage plane (110) does not exhibit any surface states within the band gap and within the area of the parabolic conduction and valence band due to the relaxation of the surface atoms. This feature, which is not present on GaAs-surfaces, is the key allowing to modify the dimensionality of the electron system systematically. E.g., a two-dimensional electron system (2DES) is formed by deposition of a dilute density of adatoms (Cs, Rb, Fe, Co, Nb, ...), resulting from an accumulation layer induced by the charge transfer of the adsorbed atoms. In InSb, because of the very large g-factor, in a relatively weak, and thus experimentally accessible, magnetic field, the resulting Landau levels of the 2DES are fully spin polarized. The local electronic density states of such a 2DES is directly accessible to STS at subkelvin temperatures. Here we studied the properties of the quantum Hall phase transition of the adsorbate-induced 2DES of InSb in real space on the nanometer scale (Sec. 3.9.1). Moreover, we studied the interaction of magnetic dopants at the surface of InSb with the 2DES Landau Levels and with the electrons tunneling between tip and 2DES (Sec. 3.9.2).

3.9.1 Landau level wave functions studied by Fourier-transform scanning tunneling spectroscopy

J. Wiebe, K. Hashimoto, T. Champel, S. Florens, C. Sohrmann, Y. Hirayama, R. A. Römer, T. Inaoka, Y. Hirayama, and M. Morgenstern, and R. Wiesendanger

We studied the real-space local density of states of the 2DES of InSb(110) in a magnetic field, in particular within higher Landau levels, by STS (Fig. 3.58). By Fourier transforming the local density of states, we find a set of n radial minima at fixed momenta for the nth Landau levels. The momenta of the minima depend only on the inverse magnetic length. By comparison with analytical theory and numerical simulations, we attribute the minima to the nodes of the quantum cyclotron orbits, which decouple in a Fourier representation from the random guiding center motion due to disorder. Adequate Fourier filtering reveals the nodal structure in real space in some areas of the sample with relatively smooth potential disorder [1].

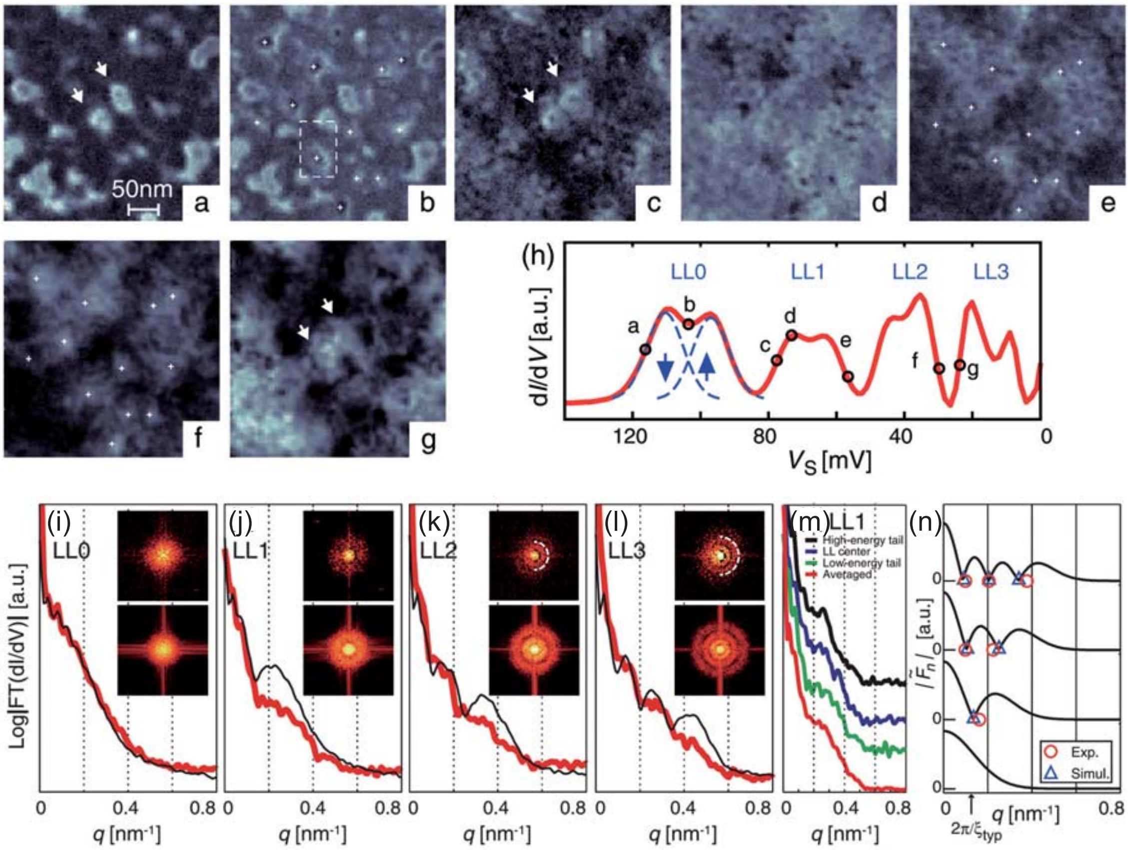

Figure 3.58: (a–g) Real-space LDOS taken at $B = 6$ T for the sample voltages V_s marked as circles in (h); measurements are done by lock-in technique with the modulation voltage $V_\mathrm{mod} = 1$ mV after stabilizing the tip at a current $I_\mathrm{stab} = 0.1$ nA and a sample voltage $V_\mathrm{stab} = 150$ mV. White arrows at the same positions in (a), (c), (g) mark localized states, which exhibit additional nodal structure in (c), (g). Crosses in (b), (e), and (f) mark states localized at potential hills; the dashed rectangle in (b) marks an area around a drift trajectory. (h) Spatially averaged dI/dV curve using the 1600 curves recorded in the area of $(350\ \mathrm{nm})^2$; dashed lines: Gaussian fits to the two spin levels of LL0. (i)–(l) Logarithmic absolute values of angular-averaged Fourier transformation (FT) of LDOS obtained in the tail of the Landau levels; thick red lines: experimental data taken from the LDOS of (a) (LL0), (c) (LL1), (f) (LL2), and (g) (LL3); thin black lines: FT of numerical simulations for an energy in the tail of the Landau band. Insets: FT-LDOS; upper panels: experiment with dashed half circles indicating q of simulated LDOS minima, lower panels: simulations. (m) Angular-averaged FT-LDOS of LL1 with (red curve) and without voltage averaging as derived from (e) (black), (d) (blue), and (c) (green). (n) Comparison of absolute FT structure factor (shifted vertically for clarity, black lines) and discrete mimima of the curves in (i)–(l); red circles: experiment; blue triangles: simulation [2].

3.9.2 Inelastic and spin-resolved scanning tunneling spectroscopy of magnetic adatoms and Landau Levels

B. Chilian, A. A. Khajetoorians, J. Wiebe, and R. Wiesendanger

The 2DES formed at the (110) surface of n-doped InSb by the charge transfer of deposited Fe atoms has one or two occupied sub-bands below the Fermi energy E_{F} [Fig. 3.59(a,b)]. In a magnetic field of 4.5 T, the spin splitting of the Landau levels of the electrons in the 2DES is well resolved. The Fe atoms act as localized atomic spins that may weakly couple to the 2DES. Interestingly, the spectra measured on top of the Fe atoms reveal an asymmetry of the spin-split Landau level peaks that was shown to reflect the adsorbate's magnetization as a function of magnetic field applied perpendicular to the surface. We investigated the dependence of the inelastic spin excitation contribution to STS recorded above the Fe adsorbates [Fig. 3.59(e,f)], on bulk doping, and tunnel junction resistance. To explain our observations, we showed how the inelastic contribution depends on the parameters describing the excitation mechanism and tunnel conditions in the framework of a well-established model [3]. We concluded that, in this particular system of an adsorbate that is strongly relaxed into the substrate, the tip-sample distance-dependent by-tunneling has to be taken into account in order to explain the observed variations in the inelastic tunnel spectra.

References

[1] K. Hashimoto, J. Wiebe, T. Inaoka, Y. Hirayama, R. Wiesendanger, and M. Morgenstern, Real-space mapping of a disordered two-dimensional electron system in the quantum Hall regime, J. Phys. C **334**, 012008 (2011).

[2] K. Hashimoto, T. Champel, S. Florens, C. Sohrmann, J. Wiebe, Y. Hirayama, R. A. Römer, R. Wiesendanger, and M. Morgenstern, Robust Nodal Structure of Landau Level Wave Functions Revealed by Fourier Transform Scanning Tunneling Spectroscopy, Phys. Rev. Lett. **109**, 116805 (2012).

[3] B. Chilian, A. A. Khajetoorians, J. Wiebe, and R. Wiesendanger, Experimental variation and theoretical analysis of the inelastic contribution to atomic spin excitation spectroscopy, Phys. Rev. B **82**, 195431 (2011).

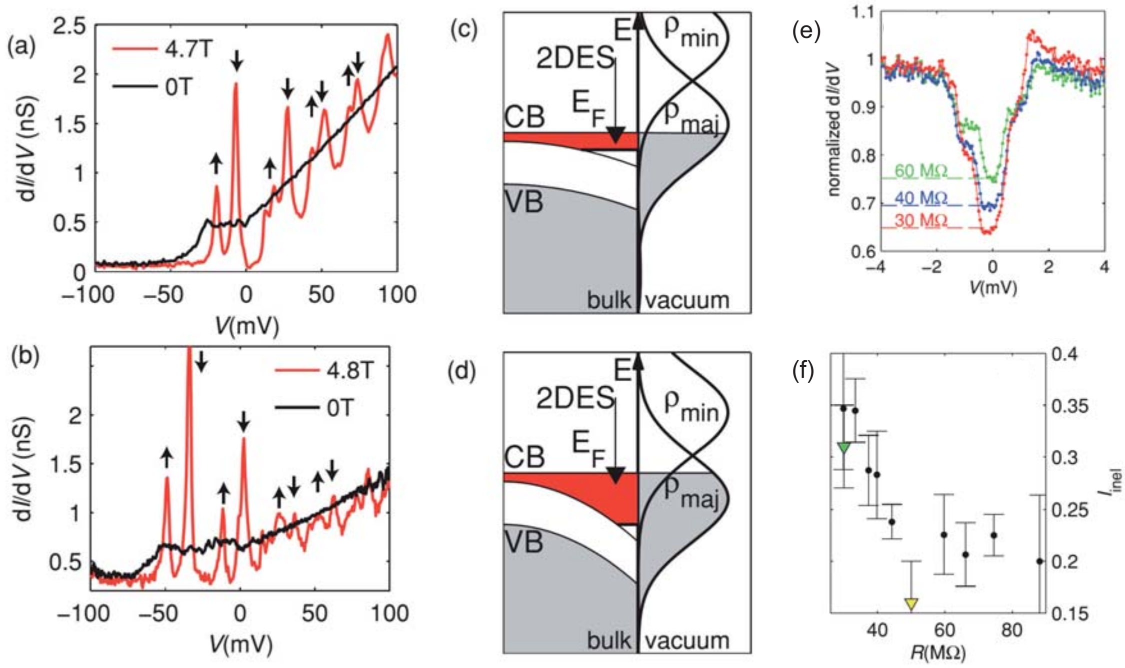

Figure 3.59: (a) Typical 2DES and Landau level spectra measured on the Fe adatoms for a high-doped sample, exhibiting weak band bending. The 2DES (black) and the Landau level (red) spectra were taken in zero magnetic field and in a magnetic field perpendicular to the surface, respectively, as indicated. (b) The same for a low-doped sample exhibiting strong band bending. The 2DES spectrum was multiplied by 3/4 to compensate for the different used stabilization parameters. The spin states of the spin-split Landau levels are indicated by arrows. (c,d) Schematic representation of the band bending for high and low doping. The conduction band (CB) and valence band (VB) edges are energetically lower at the surface (vertical line) than in the bulk, inducing a surface 2DES. An artificial distribution of the majority and minority vacuum LDOS of the Fe adsorbate is sketched. (e) ISTS spectra of an isolated Fe adsorbate on the higher-doped sample taken at different junction resistances. The spectra were normalized to align their flat tails at 1 and remove influences from the substrate LDOS. (f) Inelastic contribution to the ISTS spectra as a function of junction resistance. The black dots were extracted from a current-dependent measurement on the high-doped sample. The error bars represent a 95% confidence interval to the fit parameters. The green and yellow triangles represent the average measured on the higher- and lower-doped sample at the corresponding junction resistances and the error bar gives the standard deviation [3].

3.10 Topological insulators

J. Wiebe, A. A. Khajetoorians, and R. Wiesendanger

Topological insulators (TIs) are solids which are insulating in their bulk but metallic at the surface. The electronic states at the surface of a TI, the so called topological surface states (TSS) have a number of special electronic properties, e.g. that their existence is guaranteed by the electronic structure of the bulk and not by the particular configuration of the surface, and that the TSS electrons' direction of motion is rigidly coupled to their spin. A topologically guaranteed state can exist at the interface between a three-dimensional (3D) solid and vacuum, i.e. at the pristine surface of a material. In this case the state is a two-dimensional (2D) TSS. The first solid of this kind which has been experimentally realized was a BiSb alloy. Other Bi-based compounds (Bi_2Se_3, Bi_2Te_3 and others) soon followed, with several improved properties compared to the BiSb alloy.

While the existence of gapless TSSs is guaranteed in the presence of time-reversal symmetry, breaking this symmetry has been predicted to bring about unique new properties, such as the half-quantized surface Hall effect, the quantized anomalous Hall effect, the topological magnetoelectric effect, and the image magnetic monopole effect. For the experimental realization of such effects, time reversal symmetry can be broken by placing a magnetic material in close proximity to the surface. The strongest interaction with a magnetic material can be envisaged, when it is formed directly on the surface. Therefore, it is of key interest to study how magnetic and nonmagnetic atoms, which are adsorbed directly on top of the surface of a TI (magnetic adatoms), affect the TSS. This will depend crucially on a number of properties of the magnetic adatoms, i.e. their density, their magnetic moment and their magnetic anisotropy. Most previous investigations of perturbed TIs were done using nonlocal experimental techniques and without focusing on the specific properties of the dopants. Within this triannual research period, we started a systematic investigation of how the properties of adatoms affect the electronic band structure and the local electronic density of states of TIs, using a combination of local (STM/STS) and nonlocal (ARPES/XMCD) experimental techniques.

3.10.1 Novel topological insulator materials

A. Eich, A. A. Khajetoorians, J. Hagemeister, O. Pietzsch, J. Wiebe, S. V. Eremeev, G. Landolt, T. V. Menshchikova, B. Slomski, Y. M. Koroteev, Z. S. Aliev, M. B. Babanly, J. Henk, A. Ernst, L. Patthey, P. M. Echenique, S. S. Tsirkin, I. R. Amiraslanov, J. H. Dil, E. V. Chulkov, and R. Wiesendanger

A promising way to designing new TI materials with tunable surface electronic properties relies on the fact that pseudo-binary systems $A^{IV}B^{VI} - mA^{V}_{2}B^{VI}_{3}$

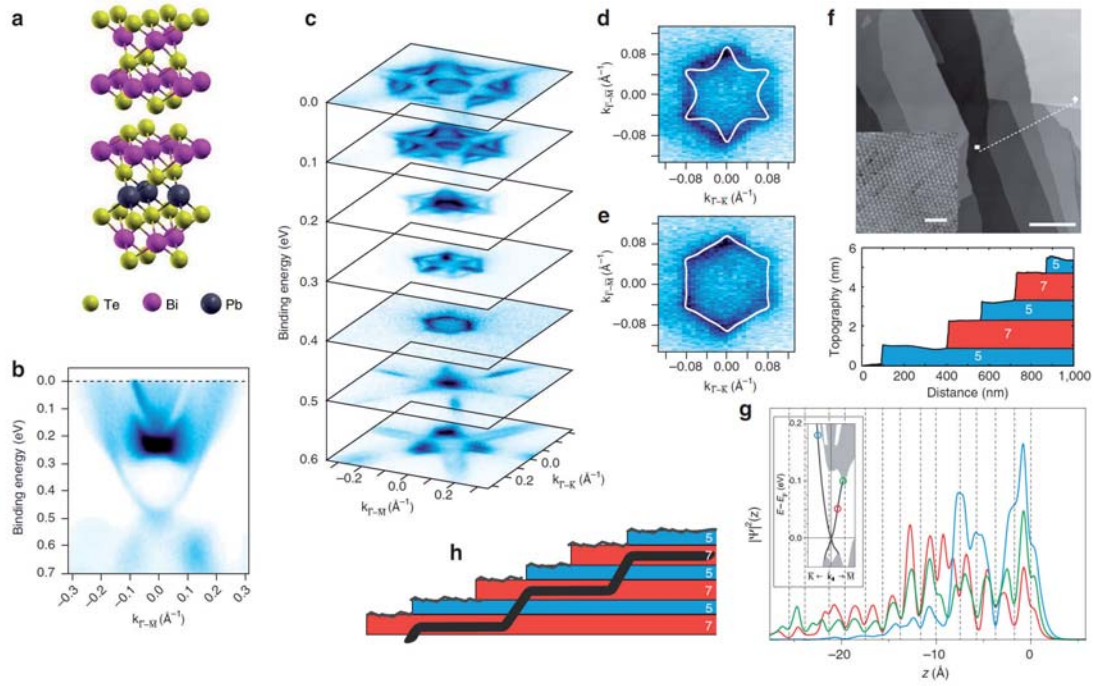

Figure 3.60: (a) Atomic structure of $PbBi_4Te_7$. (b) Spin-integrated band structure measured along the $\bar{M} - \bar{\Gamma} - \bar{M}$ direction. Measured iso-energy contours at $h \cdot \nu = 20$ eV (c) and comparison between measured and calculated iso-energy contours for the 7-layer (d) and 5-layer (e) surface terminations at 100 meV above the Dirac point. (f) STM topograph showing the mixture of both quintuple and septuple layer steps (bottom) along the dashed line ($V_{\text{bias}} = 0.5$ V, $I_{\text{t}} = 0.25$ nA). The white bar is 400 nm long. The inset shows an atomic resolution image on a typical quintuple layer ($V_{\text{bias}} = 0.5$ V, $I_{\text{t}} = 10.5$ nA). The white bar is 2 nm long. (g) Calculated energy-dependent charge density distribution, the vertical dashed lines indicate the position of the atom cores. (h) Proposed self-protecting behaviour of the topological state [1].

(A^{IV} = Ge,Sn,Pb; A^{VI} = Bi,Sb; A^{VI} = Te,Se) contain homologous series of ternary compounds. These include a wide variety of mixed-layer materials that have a more complex crystal structure than their parent Bi_2Te_3-type compounds. All these systems have tetradymite-like layered structures but with distinct many layered slabs stacked along the c-axis of the hexagonal unit cell. The bonding within the slabs is ionic-covalent, whereas the slabs are linked by weak van der Waals forces. In contrast to the parent compound Bi_2Te_3, the crystal structure, e.g., of $PbBi_4Te_7$, combines quintuple layer and septuple layer building blocks (Fig. 3.60). We showed [1] that most of the $A^{IV}B^{VI} - mA_2^VB_3^{VI}$ compounds are three-dimensional topological insulators. Peculiarities of the bulk spectrum of these materials give rise to a more complex surface band structure that depends on surface termination, which can be quintuple- or septuple-layer terminated. We predicted the existence of exotic buried topological surface states strongly protected against surface perturbations. A layer resolved spin mapping analysis of the topological states indicates layer variations in the spin-helicity and an oscillatory z spin component behaviour in the Dirac cone. We show that the spin localization varies with energy, allowing for control of the spin properties by varying the chemical potential. For $PbBi_4Te_7$, a detailed analysis of the band dispersion of the Dirac cone, as exemplified by the constant energy contours measured by ARPES, and the slightly convex energy dispersion, indicates that the photoemission signal primarily originates from a quintuple layer-terminated surface. On the other hand, the STM data clearly indicate that both surface terminations are present. Images show an alternating step height of 10Å and 14Å that corresponds to the predicted height of the quintuple and septuple layers of the $PbBi_4Te_7$ crystal, respectively [Fig. 3.60(f)]. This apparent contradiction between the ARPES and STM results might be resolved by considering the defect density at the surface and the fact that the topological state lies beneath the surface for energies well below the conduction band while on approaching the conduction band it shifts to the outermost quintuple block. The latter fact leads to further increase of the intensity and the linewidth of the Dirac cone at energies at (and above) the conduction band minimum with respect to the lower energies due to defect scattering. In the quintuple layer-terminated areas of the surface, the topological state is located for small $k_{||}$ in the septuple layer subsurface block, protecting this state against scattering at the surface. On the other hand, at the septuple layer-terminated surface areas defects might push the topological state down to the next subsurface septuple layer block, where it is no longer accessible by ARPES. This suggests the possibility to grow topological insulators with deep-lying, self-protecting and, thus, technologically relevant surface states.

3.10.2 Doping and screening of prototypical topological surface states

P. Löptien, L. Zhou, J. Wiebe, A. A. Khajetoorians, M. Bianchi, R. C. Hatch, Z. Li, F. Song, J.-L. Mi, B. B. Iversen, Z. M. Abd El-Fattah, J. W. Wells, Ph. Hofmann, and R. Wiesendanger

Rubidium adsorption on the surface of the topological insulator Bi_2Se_3 is found to induce a strong downward band bending, leading to the appearance of a quantum-confined two-dimensional electron gas state (2DEG) in the conduction band. The 2DEG shows a strong Rashba-type spin-orbit splitting, and it has previously been pointed out that this has relevance to nanoscale spintronics devices. The adsorption of Rb atoms, on the other hand, renders the surface very reactive, and exposure to oxygen leads to a rapid degrading of the 2DEG.

We have shown that intercalating the Rb atoms into the van der Waals gaps in the quintuple layer structure of Bi_2Se_3 by deposition and subsequent annealing above room temperature, drastically reduces the surface reactivity while not affecting the promising

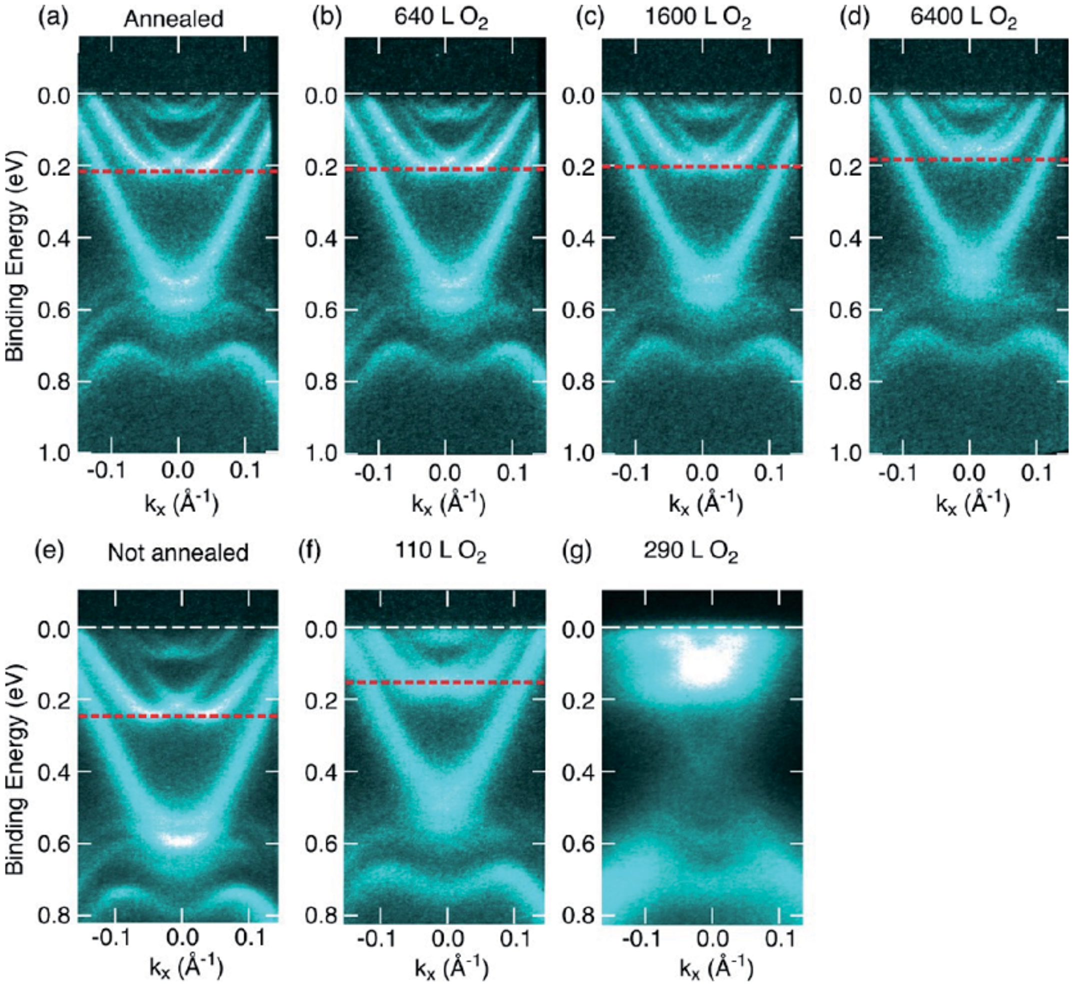

Figure 3.61: ARPES measurements of Ca-doped Bi_2Se_3 (a) after deposition of 0.23 monolayer Rb at 190 K and annealing for one minute to 350 K and (b, c, and d) following exposure to 640, 1600, and 6400 L of oxygen, respectively. (e) Similar sample after a similar deposition of Rb at 190 K, but without subsequent annealing and (f and g) the same non-annealed sample following exposure to 110 and 290 L of oxygen, respectively. Data are collected at 70 K using a photon energy of 16 eV. In each case, a red dotted line indicates the approximate position of the first Rashba-split 2DEG, such that a comparison of the extent of doping is easier [2].

electronic structure as measured by ARPES (Fig. 3.61): the 2DEGs are already formed when the Rb atoms are adsorbed on the surface, and they are not severely changed by the intercalation of Rb below the surface. Intercalating the highly reactive Rb atoms, on the other hand, protects them from interaction with the residual gas, and the surface electronic structure is not even affected by a massive exposure to oxygen. Real-space studies by STM show that one of the factors driving the intercalation process is the Coulomb repulsion between the Rb atoms. This leads to a stronger tendency

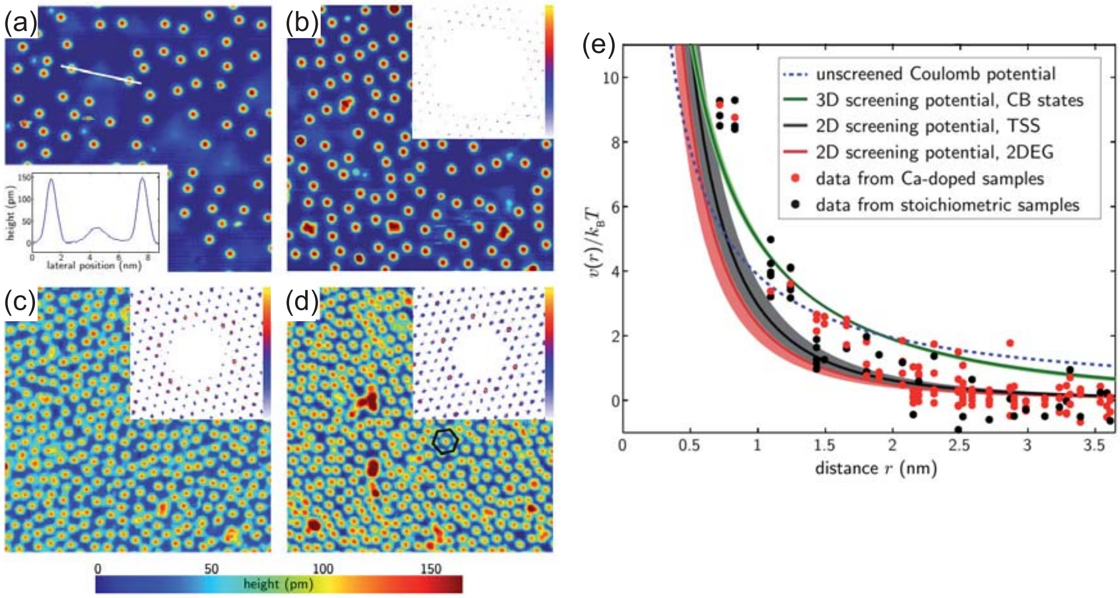

Figure 3.62: STM topographs of Rb single atoms on stoichiometric and Ca-doped Bi$_2$Se$_3$ (30 nm x 30 nm). (a) Stoichiometric Bi$_2$Se$_3$ with a 1.2% ML coverage of Rb. The inset indicates a cross section along the line in (a) that depicts the apparent heights of a Se vacancy and two Rb atoms. (b) Ca doped Bi$_2$Se$_3$ with 2.0% ML Rb. (c) Stoichiometric Bi$_2$Se$_3$ with 5.8% ML Rb. (d) Stoichiometric Bi$_2$Se$_3$ with 6.9% ML Rb. The small hexagon depicts the ($\sqrt{12}\times\sqrt{12}R10^\circ$ superstructure. Insets in (b-d): Autocorrelation plots of the atoms' positions (5 nm x 5 nm; each vector starts at the center. The number of the individual counts is plotted logarithmically using the depicted color scale). (e) The reduced pair potential for various Rb coverages and for stoichiometric and Ca-doped Bi$_2$Se$_3$, is fitted with different unscreened and screened Coulomb potentials, where the shaded regions indicate the error bars [3].

for intercalation at higher surface coverage and to a uniform distribution of the Rb dopants. Such control of the dopant uniformity is advantageous if spin-transport in these systems is to be exploited.

Moreover, we used STM to study the screening behavior produced by the positively charged Rb atoms (Fig. 3.62). By analyzing the pair correlation functions, the screened Coulomb potential between the surface Rb atoms is extracted, from which the electrostatic properties of the topological insulator are determined. By varying the surface and bulk doping, we show that the charge screening is mainly provided by the two-dimensional electron systems, residing in both the topological surface state and the surface band bending induced quantum well states, resulting in a surprisingly small screening length. With that knowledge, we even demonstrated the ability to engineer the potential landscape, in which the topological surface state resides, by atomic manipulation of individual Rb atoms.

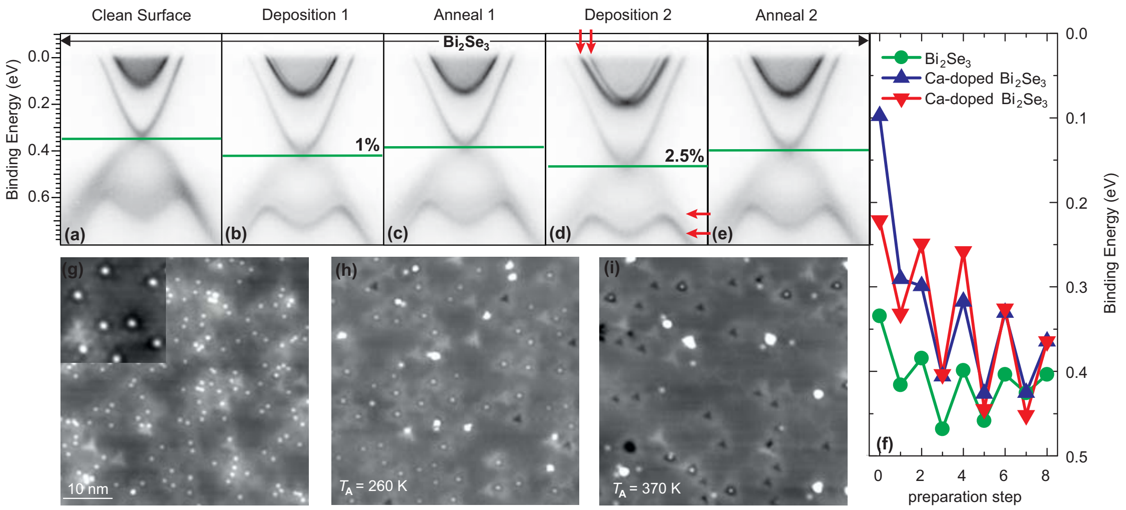

Figure 3.63: (a-e) Series of ARPES measurements for pristine Bi_2Se_3 samples after different Fe deposition and annealing steps. (a) Initial spectrum after *in-situ* cleaving. Subsequent cycles of cold deposition of Fe ($T \approx 150$K, % ML Fe as indicated) and annealing at $T_A \approx 370$K followed. The Dirac point extracted from the spectra is marked by a green and red horizontal line, respectively. Red arrows indicate quantum well states induced from band bending. (f) The resulting binding energy of the DP is plotted in dependence of the preparation step number for a pristine (circles) and two differently Ca-doped samples (up and down triangles). Preparation step number 0 indicates the freshly cleaved substrate without Fe, preparation step 1 (1%), 3 (2.5%), 5 (5%), 7 (10%), and 2, 4, 6, 8 subsequent annealing steps. (g-i) STM images of differently prepared samples of Fe on Bi_2Se_3 ($I_t = 50$pA, $V_b = 0.25$V). (g) Cold deposited Fe ($\approx 1\%$ of a ML) on pristine Bi_2Se_3. Inset: magnified view showing 8 individual Fe adatoms (10nm $\times$ 10nm, $V_b = -0.3$V, $I_t = 1$nA). (h), (i) Samples prepared as in (g) annealed to $T_A \approx 260$ K and 370 K, respectively [4].

3.10.3 Magnetic doping of prototypical topological insulators

T. Schlenk, T. Eelbo, J. Wiebe, A. A. Khajetoorians, J. Honolka, V. Sessi, T. O. Wehling, S. Stepanow, G. Bihlmayer, J.-L. Mi, B. B. Iversen, N. B. Brookes, A. I. Lichtenstein, Ph. Hofmann, K. Kern, M. Koleini, O. Pietzsch, T. Frauenheim, A. Balatsky, M. Waśniowska, M. Sikora, M. Dobrzański, A. Kozłowski, A. Pulkin, G. Autès, I. Miotkowski, O. V. Yazyev, and R. Wiesendanger

Fe adatoms and dopants at the $Bi_2Se_3(111)$ surface

A method where neutral magnetic impurities can be introduced into the surface of topological insulators and magnetically interact with the topological surface state, while only weakly perturbing the band structure, is highly desirable. We demonstrated a way to control the charge state of a magnetic impurity such that this is achieved. STM experiments illustrate that Fe atoms that are adsorbed on the surface (adatoms) of Bi_2Se_3, which act as surface donors, diffuse into subsurface sites upon thermal annealing (Fig. 3.63). Such bulk doping via the surface can be realized for a large range of coverages [4]. Complementary ARPES studies illustrate that annealing reduces the downwards band-bending, initially produced by Fe adatoms, and restores the Dirac point near its initial location before Fe adsorption. These effects are seen regardless of the initial location of the Dirac point, namely for both pristine (n-doped) and Ca-doped (nearly intrinsic) substrates. The difference in doping behavior of Fe adatoms compared to incorporated subsurface Fe atoms at different lattice sites is further studied by first principles calculations within density functional theory. The calculations reveal that the doping character changes from electron donor for Fe adatoms towards neutral for Fe incorporated into Bi. Moreover, these Fe substitutional impurities retain a large magnetic moment thus presenting an alternative scheme for magnetically doping the topological surface state.

In addition to the magnetic behaviour of the substituting Fe atoms, we also studied the properties of the Fe *adatoms* in detail. The conduction band 2DEG which forms due to the downwards band bending induced by many different adsorbates (Rb, Fe, ...) coexists with the topological surface state. For strong band bending this 2DEG shows a strong Rashba spin splitting (Figs. 3.61 and 3.64(a)). We have shown that the occurrence of simultaneous quantized valence band states leads to gap-like features in the ARPES spectra around the Dirac point, which can hamper the interpretation of gaps that are predicted to occur under certain circumstances as a result of exchange interaction of magnetic adatoms with the topological surface state. Taking into account these effects, our ARPES data proves that the topological surface state and the Dirac point is robust against doping with *paramagnetic* adatoms, i.e. if the density of adatoms is in the dilute limit.

The interaction of the topological surface state electrons with magnetic impurities depends not only on the charge doping, but crucially on the magnetic anisotropy of the adatoms. Magnetic anisotropy forces the magnetic moment of the adatoms to point into certain directions in space. While magnetic moments oriented perpendicular to

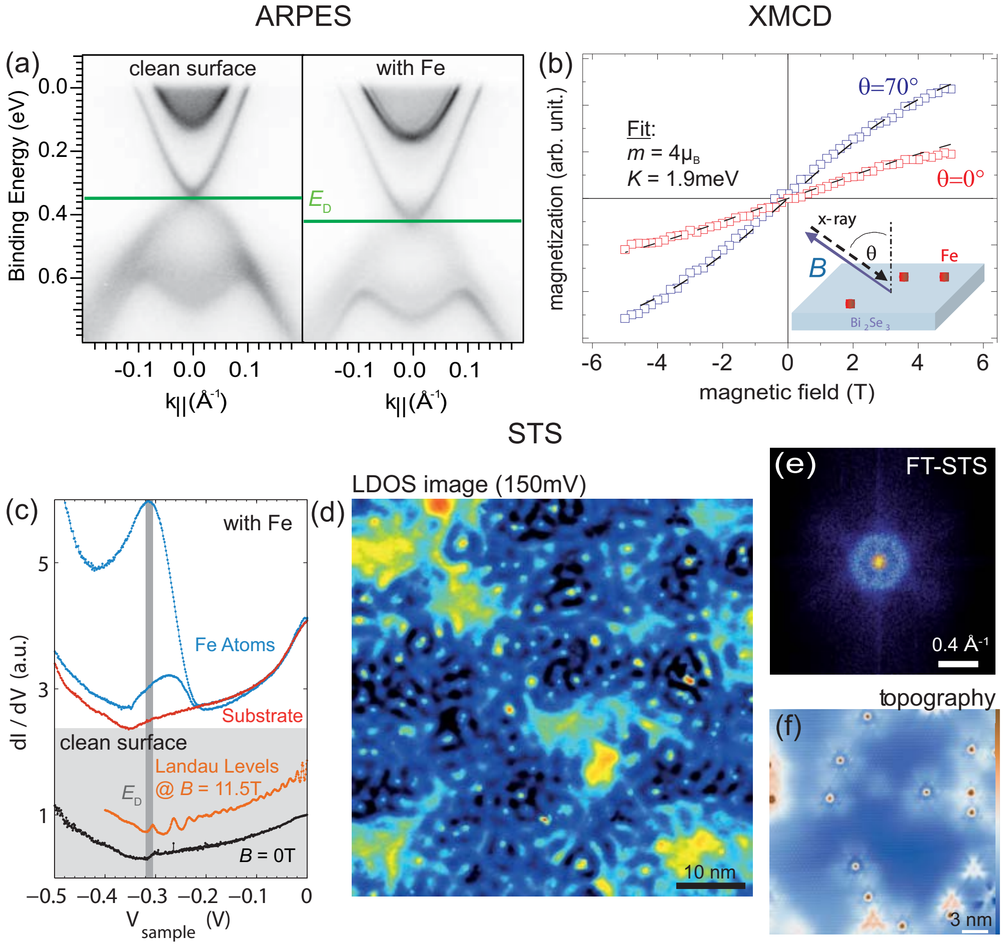

Figure 3.64: Fe adatoms on Bi_2Se_3 studied by ARPES, XMCD, and STS. (a) ARPES spectra of the Bi_2Se_3 surface before (left) and after (right) adsorption of 1% ML Fe. The Dirac point energy E_D is marked. (b) Magnetization curves $M(B)$ measured using XMCD for perpendicular and grazing direction of the magnetic field as indicated in the inset. The dashed lines represent thermodynamic fits with the indicated magnetic moment m and anisotropy K [5]. (c) Local STS measured on the Bi_2Se_3 surface before (black, bottom) and after (red, top) adsorption of Fe. The Dirac point energy E_D shifts downwards as revealed by the minimum in the spectra [5]. The spectrum taken at 11.5 T magnetic field (orange) reveals the Landau levels of the TSS. The spectra taken on top of the Fe adatoms (blue) show a resonance close to the Dirac point. (d) Spatially resolved STS (LDOS image) of the Fe covered Bi_2Se_3 shows quasi-particle interference patterns. (e) Fourier transformation of (d). (f) Constant current STM image (topography) of Fe covered Bi_2Se_3 shows the Fe atoms and the subsurface Se vacancies.

the surface plane (out-of-plane) can open a gap at the Dirac point, in-plane oriented magnetic moments cannot. XMCD measurements are ideally suited to investigate the magnetic anisotropy and ground state properties of magnetic adatoms. As shown by our work [5] using magnetic fields applied in two different orientations [Figs. 3.64(b,f)], Fe adatoms on Bi_2Se_3 clearly reveal an in-plane orientation of the magnetic moment, therefore reducing the possibility that Fe adatoms on Bi_2Se_3 can produce a gap at the Dirac point.

We have also studied the STS spectra of magnetic adatoms on different three-dimensional topological insulator surfaces, and almost always found a strong resonance close to the Dirac point localized on top of the adatom as illustrated in Fig. 3.64(c). A similar resonance has been observed at nonmagnetic impurities in Bi_2Se_3 and was attributed to the Coulomb scattering of the topological surface state at the impurity.

A particularly suited method in order to study the local electronic properties of the topological surface state of three-dimensional topological insulators is STS. Scattering of the topological surface state at step edges or defects leads to quasi-particle interference patterns in the LDOS, which can be imaged by STS as a function of the energy of the quasi-particles. The fast Fourier transformation of such an image is called FT-STS image as illustrated by our work for Fe on Bi_2Se_3 in Fig. 3.64(d,e). FT-STS images can be compared to simulated spin-dependent scattering probability images using the measured constant energy contours from ARPES and assuming an appropriate spin-dependent scattering matrix element for the topological surface state.

Co adatoms on $Bi_2Se_3(111)$

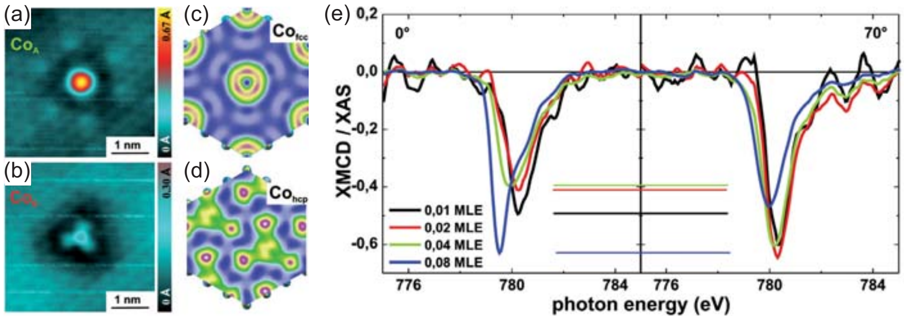

Figure 3.65: (a), (b) STM topograph of two different types of isolated Co adatoms on Bi_2Se_3 showing the affected surface in their vicinity. (c), (d) Simulations of Co atoms adsorbed in the fcc and hcp hollow site. (e) Normalized XMCD signals for a series of coverages ranging between 0.01 ML and 0.08 ML for normal (left panel) and grazing (right panel) incidence angle. The colored lines are guidelines to the eyes indicating differences between both angles [6].

We also investigated Co nanostructures on Bi_2Se_3 by means of STM/STS, XMCD and calculations using the density functional theory (Fig. 3.65). For this system, we found two different adsorption sites by STM in the single adatom regime. Our calculations revealed these to be the fcc and hcp hollow sites of the substrate. STS showed a pronounced peak for only one species of the Co adatoms indicating different electronic properties of both types. These were explained on the basis of our DFT calculations by different hybridizations with the substrate. Using XMCD we found a coverage dependent spin reorientation transition from easy-plane toward out-of-plane [Fig. 3.65(e)]. We suggest clustering to be the predominant cause for this observation.

Fe adatoms on $Bi_2Te_3(111)$

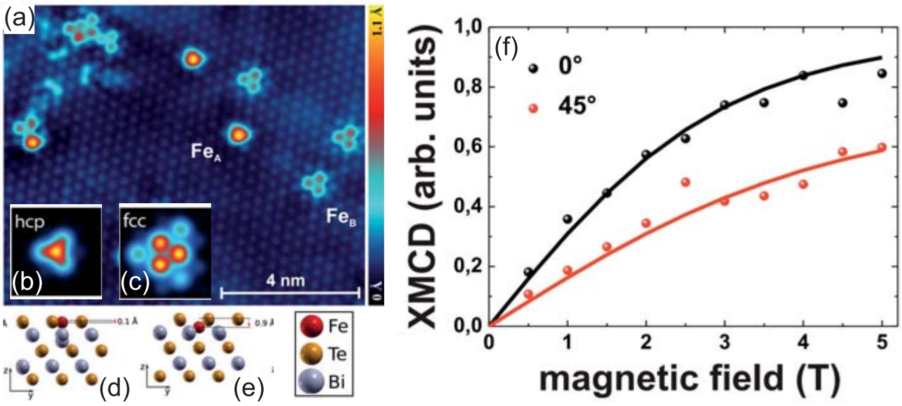

Figure 3.66: (a) Atomically resolved STM constant current map of the Bi_2Te_3 surface covered by 0.01 ML of Fe adatoms showing two different Fe adatoms (Fe_A and Fe_B) occupying different adsorption sites. (b,c) Simulated STM images of Fe adatoms in the hcp and fcc sites as calculated from first principles. (d,e) Side views of the calculated atomic configurations of Fe atoms adsorbed in the fcc and hcp adsorption sites. (f) Element selective magnetization curves for the Fe adatoms at varying angles. The data points represent the Fe XMCD intensity measured at the L3-edge while the solid lines depict the best fit profiles. The y-axis has been scaled relative to the saturation magnetization determined by the fitting procedure [7].

The electronic and magnetic properties of individual Fe atoms adsorbed on the (111) surface of Bi_2Te_3 were investigated (Fig. 3.66). STM and STS prove the existence of two distinct types of Fe species, while our first-principles calculations assign them to Fe adatoms in the hcp and fcc hollow sites. The combination of X-ray magnetic circular dichroism measurements and angular dependent magnetization curves reveals out-of-plane anisotropies for both species with anisotropy constants of $K_{fcc} = (10 \pm 4)$ meV/atom and $K_{hcp} = (8 \pm 4)$ meV/atom. These values are well in line with the results of calculations.

References

[1] S. V. Eremeev, G. Landolt, T. V. Menshchikova, B. Slomski, Y. M. Koroteev, Z. S. Aliev, M. B. Babanly, J. Henk, A. Ernst, L. Patthey, A. Eich, A. A. Khajetoorians, J. Hagemeister, O. Pietzsch, J. Wiebe, R. Wiesendanger, P. M. Echenique, S. S. Tsirkin, I. R. Amiraslanov, J. H. Dil, and E. V. Chulkov, Atom-specific spin mapping and buried topological states in a homologous series of topological insulators, Nature Comm. **3**, 635 (2012).

[2] M. Bianchi, R. C. Hatch, Z. Li, Ph. Hofmann, F. Song, J.-L. Mi, B. B. Iversen, Z. M. Abd El-Fattah, P. Löptien, L. Zhou, A. A. Khajetoorians, J. Wiebe, R. Wiesendanger, and J. W. Wells, Robust Surface Doping of Bi_2Se_3 by Rubidium Intercalation, ACSNano **6**, 7009 (2012).

[3] P. Löptien, L. Zhou, J. Wiebe, A. A. Khajetoorians, J.-L. Mi, B. B. Iversen, Ph. Hofmann, and R. Wiesendanger, Screening and atomic-scale engineering of the potential at a topological insulator surface, submitted (2013).

[4] T. Schlenk, M. Bianchi, M. Koleini, A. Eich, O. Pietzsch, T. O. Wehling, T. Frauenheim, A. Balatsky, J.-L. Mi, B. B. Iversen, J. Wiebe, A. A. Khajetoorians, Ph. Hofmann, and R. Wiesendanger, Controllable Magnetic Doping of the Surface State of a Topological Insulator, Phys. Rev. Lett. **110**, 126804 (2013).

[5] J. Honolka, A. A. Khajetoorians, V. Sessi, T. O. Wehling, S. Stepanow, J.-L. Mi, B. B. Iversen, T. Schlenk, J. Wiebe, N. B. Brookes, A. I. Lichtenstein, Ph. Hofmann, K. Kern, and R. Wiesendanger, In-Plane Magnetic Anisotropy of Fe Atoms on $Bi_2Se_3(111)$, Phys. Rev. Lett. **108**, 256811 (2012).

[6] T. Eelbo, M. Sikora, G. Bihlmayer, M. Dobrzański, A. Kozłowski, I. Miotkowski, and R. Wiesendanger, Co atoms on Bi_2Se_3 revealing a coverage dependent spin reorientation transition, New J. Phys. **15**, 113026 (2013).

[7] T. Eelbo, M. Waśniowska, M. Sikora, M. Dobrzański, A. Kozłowski, A. Pulkin, G. Autès, I. Miotkowski, O. V. Yazyev, and R. Wiesendanger, Strong Out-of-Plane Magnetic Anisotropy of Fe Adatoms on Bi_2Te_3, (submitted 2013).

Chapter 4

Collaborations

4.1 Research Partners

- Institute of Applied Physics and MARCH, University of Hamburg:
  Prof. Dr. W. Hansen, Prof. Dr. U. Merkt, Prof. Dr. H. P. Oepen

- I. Institute of Theoretical Physics, University of Hamburg:
  Prof. Dr. A. Lichtenstein, Prof. Dr. D. Pfannkuche, Prof. Dr. M. Potthoff, Prof. Dr. M. Thorwart, Jun.-Prof. Dr. F. Lechermann

- Institute for Laser Physics, University of Hamburg:
  Prof. Dr. K. Sengstock

- Institute for Physical Chemistry, University of Hamburg:
  Prof. Dr. H. Weller

- Institute for Inorganic and Applied Chemistry, University of Hamburg:
  Prof. Dr. J. Heck, Prof. Dr. C. Herrmann, Jun.-Prof. Dr. M. H. Prosenc

- Department of Computer Science, University of Hamburg:
  Prof. Dr. J. Zhang

- University of Kiel:
  Prof. Dr. R. Berndt, Prof. Dr. S. Heinze, Dr. P. Ferriani

- HGF-Forschungszentrum Jülich:
  Prof. Dr. S. Blügel, Prof. Dr. P. H. Dederichs, Dr. N. Atodiresei, Dr. G. Bihlmayer

- MPI for Solid State Research, Stuttgart:
  Dr. S. Roth, Dr. J. Smet, Dr. U. Starke

- University of Karlsruhe:
  Prof. Dr. M. Ruben, Dr. H. Hölscher

- University of Marburg:
  Prof. Dr. M. Bröring
- RWTH Aachen:
  Prof. Dr. M. Morgenstern
- University of Konstanz:
  Prof. Dr. P. Leiderer
- Center for Computational Nanoscience, Vienna, Austria:
  Prof. Dr. P. Weinberger
- University of Bialystok, Poland:
  Prof. Dr. A. Maziewski
- University of Trieste, Italy:
  Prof. Dr. S. Modesti
- National Nanotechnology Laboratory, Lecce, Italy:
  Dr. G. Maruccio
- University of Zaragoza, Spain:
  Prof. Dr. J. I. Arnaudas, Dr. D. Serrate
- University of Madrid, Spain:
  Dr. N. Mikuszeit
- University College London, GB:
  Prof. Dr. A. Shluger
- Trinity College Dublin, Ireland:
  Prof. Dr. S. Sanvito
- University of Iowa, USA:
  Prof. Dr. M. E. Flatté
- University of Ohio, Athens, USA:
  Prof. Dr. S.-W. Hla, Prof. Dr. A. R. Smith
- University of Michigan, East Lansing, USA:
  Prof. Dr. D. Tománek, Dr. S. Berber
- University of California, Irvine, USA:
  Prof. Dr. D. L. Mills, Dr. S. Lounis
- Columbia University, New York, USA:
  Prof. Dr. C. J. Chen

- Los Alamos National Laboratory, USA:
  Dr. A. V. Balatsky

- National Institute for Materials Science (NIMS), Tsukuba, Japan:
  Dr. M. Aono

- Tohoku University, Sendai, Japan:
  Dr. K. Hashimoto

- Samsung, South-Korea:
  Dr. U. H. Pi

Chapter 5

Theses

5.1 Bachelor Theses

1. Benjamin Ehlers (2011):
   Untersuchung thermischen Schaltens magnetischer Nanoinseln auf W(110) mittels spinpolarisierter Rastertunnelmikroskopie

2. Julian Hagemeister (2011):
   Strukturelle Charakterisierung des Topologischen Isolators PbBi4Te7 mit einem temperaturvariablen Rastertunnelmikroskop

3. Jonas Harm (2011):
   Untersuchung von Feldemissionsresonanzen über Fe/W(110) Nanoinseln

4. Niklas Romming (2011):
   Untersuchung dünner Mangan-Filme auf verschiedenen Wolfram-Substraten

5. Jonas Warmuth (2011):
   Softwareentwicklung für automatisierte Magnetisierungsmessungen mittels spinpolarisierter Rastertunnelmikroskopie

6. Cornelius Eder (2012):
   Strukturelle Charakterisierung von epitaktisch gewachsenem Bismut auf Bismutselenid mittels Rastertunnelmikroskopie

7. Tobias Pohlmann (2012):
   Untersuchung des Wachstums von Eisen auf Re(0001) mittels Rastertunnelmikroskopie

8. Michael Nitschke (2013):
   Aufbau und Test eines Doppelgoniometers zum Ausrichten zweier Glasfasern

5.2 Diploma Theses

1. Arne Köhler (2011):
   Rasterkraftmikroskopie an Monolagen von Co auf W(001) und Graphen auf Ru(0001)

2. Qingchui Zhu (2011):
   Magnetische Dissipation in der Austauschkraftmikroskopie

3. Christian Hanneken (2011):
   Development and Characterization of Cr Bulk Tips for SP-STM

4. André Engel (2011):
   Präparation und Charakterisierung von Chrom-Volumenspitzen zur Untersuchung magnetischer Eigenschaften bei hohen Strömen und hohen Spannungen

5. Josef Grenz (2011):
   Untersuchung des Anfangsstadiums des Wachstums von Co-Salen auf NiO(001)

5.3 Master Theses

1. Benjamin Ehlers (2012):
   Einfluß von Temperatur, Strukturgröße und Spannung beim strominduzierten Schalten mittels spinpolarisierter Rastertunnelmikroskopie
2. Johannes Friedlein (2012):
   Optimierung eines spinpolarisierten Rastertunnelmikroskops für Experimente mit hoher Zeitauflösung
3. David Vincent Altwein (2012):
   Kollektives Schaltverhalten superparamagnetischer Teilchen in magnetischen Nanoensembles
4. Niklas Romming (2013):
   Einfluss nicht-magnetischer Adlagen auf nicht-kollineare magnetische Zustände
5. Gotthold Viktor Fläschner (2013):
   Opto-Mechanical Systems in a Cryogenic Environment
6. Lasse Cornils (2013):
   Aufbau und Test eines 4K-2-Achsen-Magnetkryostatsystems für ein Rasterkraftmikroskop
7. Jan Peter Hermenau (2013):
   Magnetoelektrische Kopplung und Pump-Probe-Experimente auf atomarer Skala
8. Julian Claudius Hagemeister (2013):
   Statische und dynamische Prozesse in nichtkollinearen Spinstrukturen

5.4 Ph. D. Theses

1. Knud Lämmle (2011):
   Rasterkraftmikroskopie und -spektroskopie am magnetischen Molekül Co-Salen
2. Gabriela Herzog (2011):
   Heat assisted spin-transfer torque manipulation on the nanoscale using a spin-polarized scanning tunneling microscope
3. René Schmidt (2011):
   Magnetic exchange force microscopy and spectroscopy on Fe/W(001)
4. Jens Brede (2011):
   Spin-Polarized Scanning Tunneling Microscopy and Spectroscopy of Phthalocyanine Molecules deposited on Surfaces
5. Bruno Chilian (2011):
   Single and Coupled Magnetic Atoms Investigated by Low-Temperature STM and Model Calculations
6. Matthias Menzel (2011):
   Non-collinear magnetic ground states observed in iron nanostructures on iridium surfaces
7. Mike Gyamfi (2012):
   Scanning Tunneling Microscopy and Spectroscopy of Adatoms on Graphene
8. Liudmila Vasiljewna Dzemiantsova (2013):
   Magnetic Coupling of Individual Atoms through Non-magnetic Spacer Layers
9. Tobias Schlenk (2013):
   Spin-Resolved and Inelastic Scanning Tunneling Spectroscopy of Magnetic Atoms and Clusters
10. Anika Schlenhoff (2013):
    Imaging and Switching Individual Nanomagnets with Spin-Polarized Scanning Field Emission Microscopy
11. Peter Löptien (2013):
    Charge screening in topological insulators and low-dimensional superconductivity investigated by scanning tunneling microscopy
12. Thomas Eelbo (2013):
    Interaction of Transition Metal Adatoms and Dirac Materials investigated by Scanning Tunneling Microscopy and X-ray Magnetic Circular Dichroism

Chapter 6

Scientific Publications

6.1 Book Contributions

1. Oswald Pietzsch and Roland Wiesendanger, Fundamentals of Picoscience (ed. by Klaus D. Sattler), CRC Press p. 413-445 (2013): *Atomic Scale Magnetism Studied by Spin-Polarized Scanning Tunneling Microscopy.*

6.2 Original Articles

1. K. Hashimoto, J. Wiebe, T. Inaoka, Y. Hirayama, R. Wiesendanger, and M. Morgenstern, Journal of Physics: Conference Series **334**, 012008 (2011): *Real-space mapping of a disordered two-dimensional electron system in the quantum Hall regime*
2. B. Chilian, A. A. Khajetoorians, S. Lounis, A. T. Costa, D. L. Mills, J. Wiebe, and R. Wiesendanger, Phys. Rev. B **84**, 212401 (2011): *Anomalously large g-factor of single atoms adsorbed on a metal substrate*
3. L.V. Dzemiantsova, M. Karolak, F. Lofink, A. Kubetzka, B. Sachs, K. von Bergmann, S. Hankemeier, T.O. Wehling, R. Frömter, H.P. Oepen, A.I. Lichtenstein, and R. Wiesendanger, Phys. Rev. B **84**, 205431 (2011): *Multiscale magnetic study of Ni(111) and graphene on Ni(111)*
4. J. Wiebe, L. Zhou, and R. Wiesendanger, J. Phys. D: Appl. Phys. **44**, 464009 (2011): *Atomic magnetism revealed by spin-resolved scanning tunnelling spectroscopy*
5. S. Krause, G. Herzog, A. Schlenhoff, A. Sonntag, and R. Wiesendanger, Phys. Rev. Lett. **107**, 186601 (2011): *Joule heating and spin-transfer torque*

investigated on the atomic scale using a spin-polarized scanning tunneling microscope

6. M. Gyamfi, T. Eelbo, M. Wasniwoska, and R. Wiesendanger, Phys. Rev. B **84**, 113403 (2011): *Fe adatoms on graphene/Ru(0001): Adsorption site and local electronic properties*
7. J. E. Bickel, F. Meier, J. Brede, A. Kubetzka, K. von Bergmann, and R. Wiesendanger, Phys. Rev. B **84**, 054454 (2011): *Magnetic properties of monolayer Co islands on Ir(111) probed by spin-resolved scanning tunneling microscopy*
8. R. Wieser, Phys. Rev. B **84**, 054411 (2011): *Role of quadratic terms in the Heisenberg model for quantum spin dynamics*
9. N. Mikuszeit, S. Meckler, R. Wiesendanger, and R. Miranda, Phys. Rev. B **84**, 054404 (2011): *Magnetostatics and the rotational sense of cycloidal spin spirals*
10. S. Heinze, K. von Bergmann, M. Menzel, J. Brede, A. Kubetzka, R. Wiesendanger, G. Bihlmayer, S. and Blügel, Nature Physics **7**, 713 (2011): *Spontaneous atomic-scale magnetic skyrmion lattice in two dimensions*
11. O. Pietzsch and R. Wiesendanger, Pure and Applied Chemistry **83**, 1981 (2011): *Non-Collinear Magnetic Order in Nanostructures Investigated by Spin-Polarized Scanning Tunneling Microscopy*
12. T. Stapelfeldt, R. Wieser, E. Y. Vedmedenko, and R. Wiesendanger, Phys. Rev. Lett. **107**, 027203 (2011): *Domain Wall Manipulation with a Magnetic Tip*
13. J. Wiebe, A. A. Khajetoorians, B. Chilian, and R. Wiesendanger, Physik in unserer Zeit **42**, 162 (2011): *Logik aus atomaren Spins*
14. R. Schmidt, C. Lazo, U. Kaiser, A. Schwarz, S. Heinze, and R. Wiesendanger, Phys. Rev. Lett. **106**, 257202 (2011): *Quantitative Measurement of the Magnetic Exchange Interaction across a Vacuum Gap*
15. G. Teobaldi, K. Lämmle, T. Trevethan, M. Watkins, A. Schwarz, R. Wiesendanger, and A. Shluger, Phys. Rev. Lett. **106**, 216102 (2011): *Chemical Resolution at Ionic Crystal Surfaces Using Dynamic Atomic Force Microscopy with Metallic Tips*
16. B. Chilian, A. A. Khajetoorians, J. Wiebe, and R. Wiesendanger, Phys. Rev. B **83**, 195431 (2011): *Experimental variation and theoretical analysis of the inelastic contribution to atomic spin excitation spectroscopy*
17. A. A. Khajetoorians, J. Wiebe, B. Chilian, and R. Wiesendanger, Science **332**, 1062 (2011): *Realizing All-Spin-Based Logic Operations Atom by Atom*

18. M. Gyamfi, T. Eelbo, M. Waśniowska, and R. Wiesendanger, Phys. Rev. B **83**, 153418 (2011): *Inhomogeneous electronic properties of monolayer graphene on Ru(0001)*

19. E. Y. Vedmedenko, N. Mikuszeit, T. Stapelfeldt, R. Wieser, M. Potthoff, A. I. Lichtenstein and R. Wiesendanger, Eur. Phys. J. B **80**, 331 (2011): *Spin-spin correlations in ferromagnetic nanosystems*

20. P. Weinberger, E. Y. Vedmedenko, R. Wieser, and R. Wiesendanger, Philosophical Magazine **91**, 2248 (2011): *A multi-scale model of domain wall velocities based on ab initio parameters*

21. R. Wieser, E. Y. Vedmedenko, and R. Wiesendanger, Phys. Rev. Lett. **106**, 067204 (2011): *Indirect Control of Antiferromagnetic Domain Walls with Spin Current*

22. F. Meier, S. Lounis, J. Wiebe, L. Zhou, S. Heers, P. Mavropoulos, P. H. Dederichs, S. Blügel, and R. Wiesendanger, Phys. Rev. B **83**, 075407 (2011): *Spin-polarization of platinum (111) induced by the proximity to cobalt nanostripes*

23. R. Wiesendanger, Current Opinion in Solid State and Materials Science **15**, 1 (2011): *Single-atom magnetometry*

24. A. A. Khajetoorians, S. Lounis, B. Chilian, A. T. Costa, L. Zhou, D. L. Mills, J. Wiebe, and R. Wiesendanger , Phys. Rev. Lett. **106**, 037205 (2011): *Itinerant Nature of Atom-Magnetization Excitation by Tunneling Electrons*

25. M. Hortamani and R. Wiesendanger, Phys. Rev. B **86**, 235437 (2012): *Role of hybridization in the Rashba splitting of noble metal monolayers on W(110)*

26. J. Brede and R. Wiesendanger, Phys. Rev. B **86**, 184423 (2012): *Spin-resolved characterization of single cobalt phthalocyanine molecules on a ferromagnetic support*

27. R. Schmidt, A. Schwarz, and R. Wiesendanger, Phys. Rev. B **86**, 174402 (2012): *Magnetization switching utilizing the magnetic exchange interaction*

28. K. von Bergmann, M. Menzel, D. Serrate, Y. Yoshida, S. Schröder, P. Ferriani, A. Kubetzka, R. Wiesendanger, and S. Heinze, Phys. Rev. B **86**, 134422 (2012): *Tunneling anisotropic magnetoresistance on the atomic scale*

29. L. V. Dzemiantsova, M. Hortamani, C. Hanneken, A. Kubetzka, K. von Bergmann, and R. Wiesendanger, Phys. Rev. B **86**, 094427 (2012): *Magnetic coupling of single Co adatoms to a Co underlayer through a Pd spacer of variable thickness*

30. K. Hashimoto, T. Champel, S. Florens, C. Sohrmann, J. Wiebe, Y. Hirayama, R. A. Römer, R. Wiesendanger, and M. Morgenstern, Phys. Rev. Lett. **109**, 116805 (2012): *Robust Nodal Structure of Landau Level Wave Functions Revealed by Fourier Transform Scanning Tunneling Spectroscopy*
31. B. Wolter, Y. Yoshida, A. Kubetzka, S.-W. Hla, K. von Bergmann, and R. Wiesendanger, Phys. Rev. Lett. **109**, 116102 (2012): *Spin Friction Observed on the Atomic Scale*
32. A. Schlenhoff, S. Krause, A. Sonntag, and R. Wiesendanger, Phys. Rev. Lett. **109**, 097602 (2012): *Individual Atomic-Scale Magnets Interacting with Spin-Polarized Field-Emitted Electrons*
33. M. Bianchi, R. C. Hatch, Z. Li, P. Hofmann, F. Song, J. Mi, B. B. Iversen, Z. M. Abd El-Fattah, P. Löptien, L. Zhou, A. A. Khajetoorians, J. Wiebe, R. Wiesendanger, and J. W. Wells, ACS Nano **6**, 7009 (2012): *Robust Surface Doping of* Bi_2Se_3 *by Rubidium Intercalation*
34. J. Schwöbel, Y. Fu, J. Brede, A. Dilullo, G. Hoffmann, S. Klyatskaya, M. Ruben, and R. Wiesendanger, Nature Communications **3**, 953 (2012): *Real-space observation of spin-split molecular orbitals of adsorbed single-molecule magnets*
35. H. Fuchs and R. Wiesendanger, Nanotechnologie Aktuell , (2012): *Rechnen mit magnetischen Atomen*
36. Y. Fu, J. Schwöbel, S.-W. Hla, A. Dilullo, G. Hoffmann, S. Klyatskaya, M. Ruben, and R. Wiesendanger, Nano Lett. **12**, 3931 (2012): *Reversible chiral switching of Bis(phthalocyaninato) Terbium(III) on a metal surface*
37. J. Honolka, A. A. Khajetoorians, V. Sessi, T. O. Wehling, S. Stepanow, J.-L. Mi, B. B. Iversen, T. Schlenk, J. Wiebe, N. B. Brookes, A. I. Lichtenstein, Ph. Hofmann, K. Kern, and R. Wiesendanger, Phys. Rev. Lett. **108**, 256811 (2012): *In-plane magnetic anisotropy of Fe atoms on* Bi_2Se_3*(111)*
38. M. Gyamfi, T. Eelbo, M. Waśniowska, and R. Wiesendanger, Phys. Rev. B **85**, 205434 (2012): *Impact of intercalated cobalt on the electronic properties of graphene on Pt(111)*
39. E. Y. Vedmedenko, Q. Zhu, U. Kaiser, A. Schwarz, and R. Wiesendanger, Phys. Rev. B **85**, 174410 (2012): *Atomic-scale magnetic dissipation from spin-dependent adhesion hysteresis*
40. M. Menzel, Y. Mokrousov, R. Wieser, J.E. Bickel, E. Vedmedenko, S. Blügel, S. Heinze, K. von Bergmann, A. Kubetzka, and R. Wiesendanger, Phys. Rev. Lett. **108**, 197204 (2012): *Information Transfer by Vector Spin Chirality in Finite Magnetic Chains*

41. A. DiLullo, S.-H. Chang, N. Baadji, K. Clark, J.-P. Klöckner, M.H. Prosenc, S. Sanvito, R. Wiesendanger, G. Hoffmann, and S.-W. Hla, Nano Lett. **12**, 3174 (2012): *Molecular Kondo chain*

42. A. A. Khajetoorians, J. Wiebe, B. Chilian, S. Lounis, S. Blügel, and R. Wiesendanger, Nature Physics **8**, 497 (2012): *Atom-by-atom engineering and magnetometry of tailored nanomagnets*

43. M. Gyamfi, T. Eelbo, M. Waśniowska, T. O. Wehling, S. Forti, U. Starke, A. I. Lichtenstein, M. I. Katsnelson, and R. Wiesendanger, Phys. Rev. B **85**, 161406(R) (2012): *Orbital selective coupling between Ni adatoms and graphene Dirac electrons*

44. A. Schumann, P. Szary, E. Y. Vedmedenko, and H. Zabel, New J. Phys. **14**, 035015 (2012): *Magnetic dipole configurations in honeycomb lattices: order and disorder*

45. Y. Yoshida, S. Schröder, P. Ferriani, D. Serrate, A. Kubetzka, K. von Bergmann, S. Heinze, and R. Wiesendanger, Phys. Rev. Lett. **108**, 087205 (2012): *Conical spin-spiral state in an ultra-thin film driven by higher-order spin interactions*

46. Y.-S. Fu, Q.-K. Xue, and R. Wiesendanger, Phys. Rev. Lett. **108**, 087203 (2012): *Spin-resolved splitting of Kondo resonances in the presence of RKKY-type coupling*

47. S. Meckler, O. Pietzsch, N. Mikuszeit, and R. Wiesendanger, Phys. Rev. B **85**, 024420 (2012): *Micromagnetic description of the spin spiral in Fe double-layer stripes on W(110)*

48. S. V. Eremeev, G. Landolt, T. V. Menshchikova, B. Slomski, Y. M. Koroteev, Z. S. Aliev, M. B. Babanly, J. Henk, A. Ernst, L. Patthey, A. Eich, A. A. Khajetoorians, J. Hagemeister, O. Pietzsch, J. Wiebe, R. Wiesendanger, P. M. Echenique, S. S. Tsirkin, I. R. Amiraslanov, J. H. Dil, and E. V. Chulkov, Nat. Commun. **3**, 635 (2012): *Atom-specific spin mapping and buried topological states in a homologous series of topological insulators*

49. R. Wieser, T. Stapelfeldt, E. Y. Vedmedenko, and R. Wiesendanger, Europhys. Lett. **97**, 17009 (2012): *Manipulation of domain walls using a spin-polarized STM*

50. M. Bazarnik, J. Brede, R. Decker, and R. Wiesedanger, ACS Nano **7**, 11341 (2013): *Tailoring Molecular Self-Assembly of Magnetic Phthalocyanine Molecules on Fe- and Co-Intercalated Graphene*

51. T. Eelbo, M. Sikora, G. Bihlmayer, M. Dobrzanski, A. Kozlowski, I. Miotkowski, and R. Wiesendanger, New Journ. Phys. **15**, 113026 (2013): *Co atoms on* Bi_2Se_3 *revealing a coverage dependent spin reorientation transition*

52. A. A. Khajetoorians, T. Schlenk, B. Schweflinghaus, M. dos Santos Dias, M. Steinbrecher, M. Bouhassoune, S. Lounis, J. Wiebe, and R. Wiesendanger, Phys. Rev. Lett. **111**, 157204 (2013): *Spin Excitations of Individual Fe Atoms on Pt(111): Impact of the Site-Dependent Giant Substrate Polarization*

53. C. Hanneken, and N. Romming, Spektrum der Wissenschaft **Okt. 2013**, 22 (2013): *Magnetische Knoten auf der Festplatte*

54. N. Romming, C. Hanneken, M. Menzel, J. E. Bickel, B. Wolter, K. von Bergmann, A. Kubetzka, and R. Wiesendanger, Science **341**, 6146 (2013): *Writing and Deleting Single Magnetic Skyrmions*

55. Jong-Kwon Lee, S. Yamazaki, Hoyeol Yun, Jinwoo Park, G. P. Kennedy, Gyu-Tae Kim, O. Pietzsch, R. Wiesendanger, SangWook Lee, Suklyun Hong, U. Dettlaff-Weglikowska, and S. Roth, Nano Letters **13**, 3494-500 (2013): *Modification of Electrical Properties of Graphene by Substrate-Induced Nanomodulation*

56. E.Y. Vedmedenko, M. Schult, J. Kronjäger, R. Wiesendanger, K. Bongs, and K. Sengstock, New Journ. Phys. **15**, 063033 (2013): *Collective magnetism in arrays of spinor Bose-Einstein condensates*

57. T. Eelbo, M. Waśniowska, M. Gyamfi, S. Forti, U. Starke, and R. Wiesendanger, Phys. Rev. B **87**, 205443 (2013): *Influence of the degree of decoupling of graphene on the properties of transition metal adatoms*

58. R. Wieser, Phys. Rev. Lett. **110**, 147201 (2013): *Comparison of Quantum and Classical Relaxation in Spin Dynamics*

59. T. Eelbo, M. Waśniowska, P. Thakur, M. Gyamfi, B. Sachs, T. O. Wehling, S. Forti, U. Starke, C. Tieg, A. I. Lichtenstein, and R. Wiesendanger, Phys. Rev. Lett. **110**, 136804 (2013): *Adatoms and Clusters of 3d Transition Metals on Graphene: Electronic and Magnetic Configurations*

60. T. Schlenk, M. Bianchi, M. Koleini, A. Eich, O. Pietzsch, T. O. Wehling, T. Frauenheim, A. Balatsky, J.-L. Mi, B. B. Iversen, J. Wiebe, A. A. Khajetoorians, Ph. Hofmann, and R. Wiesendanger, Phys. Rev. Lett. **110**, 126804 (2013): *Controllable Magnetic Doping of the Surface State of a Topological Insulator*

61. A. Schwarz, D. Z. Gao, K. Lämmle, J. Grenz, M. B. Watkins, A. L. Shluger, and R. Wiesendanger, J. Phys. Chem. C **117**, 1105 (2013): *Determining Adsorption Geometry, Bonding, and Translational Pathways of a Metal-Organic Complex on an Oxide Surface: Co-Salen on NiO(001)*

62. K. Them, T. Stapelfeldt, E.Y. Vedmedenko, and R. Wiesendanger, New Journ. Phys. **15**, 013009 (2013): *Non-equilibrium finite temperature dynamics of magnetic quantum systems: applications to spin-polarized scanning tunneling microscopy*

63. R. Wieser, V. Caciuc, C. Lazo, H. Hölscher, E. Y. Vedmedenko, and R. Wiesendanger, New Journal of Physics **15**, 013011 (2013): *A theoretical study of the dynamical switching of a single spin by exchange forces*

64. R. Decker, J. Brede, N. Atodiresei, V. Caciuc, S. Blügel, and R. Wiesendanger , Phys. Rev. B **87**, 041403 (2013): *Atomic-scale magnetism of cobalt-intercalated graphene*

65. A. A. Khajetoorians, B. Baxevanis, C. Hübner, T. Schlenk, S. Krause, T. O. Wehling, S. Lounis, A. Lichtenstein, D. Pfannkuche, J. Wiebe, and R. Wiesendanger, Science **339**, 6115 (2013): *Current-Driven Spin Dynamics of Artificially Constructed Quantum Magnets*

Chapter 7

Talks and Posters

7.1 Invited Talks

25.1.2011: R. Wiesendanger, International Symposium on Deposition and Characterization of Nanomagnets on Surfaces, Bielefeld (Germany): *Imaging and Manipulating Single and Interacting Spins on Surfaces: Towards Atomic-Scale Spin Devices*

10.2.2011: R. Wiesendanger, 5th International Conference on Advanced Materials and Nanotechnology, AMN-5, Wellington (New Zealand): *Probing Spins Atom-by-Atom: 20 Years of Spin-Polarized Scanning Tunneling Microscopy*

11.2.2011: R. Wiesendanger, 5th International Conference on Advanced Materials and Nanotechnology, AMN-5, Wellington (New Zealand): *Atomic Spin Logic Devices*

28.2.2011: R. Wiesendanger, 2nd International Workshop on Advanced Atomic Force Microscopy Techniques, Karlsruhe (Germany): *Probing Magnetic Exchange Interactions and Forces on the Atomic Scale*

2.3.2011: E. Y. Vedmedenko, International Workshop "Open Statistical Physics", Open University, Milton Keynes (UK): *Critical Temperatures of Finite Samples at Finite Observation Times*

16.3.2011: S. Heinze, K. von Bergmann, M. Menzel, J. Brede, A. Kubetzka, R. Wiesendanger, G. Bihlmayer, and S. Blügel, 75th Annual Meeting of the DPG and combined DPG Spring Meeting 2011, Dresden (Germany): *Discovery of an atomic-scale skyrmion lattice in an ultrathin magnet*

22.3.2011: R. Wiesendanger, APS March Meeting 2011, Dallas (USA): *Imaging and Manipulating Single and Interacting Spins on Surfaces: Towards Atomic-Scale Spin Devices*

23.3.2011: A. A. Khajetoorians, APS March Meeting 2011, Dallas, Texas (USA): *Realizing Spin Logic Atom by Atom*

24.3.2011: J. Wiebe, APS March Meeting 2011, Dallas, Texas (USA): *Detecting excitation and magnetization of individual dopants in a semiconductor two-dimensional electron gas*

13.4.2011: R. Wiesendanger, Internat. Workshop on Atomic and Molecular Level Devising of Functional Nanostructures for Magnetic and Catalytic Applications, Zakopane (Poland): *Atomic Spin Logic Devices*

23.5.2011: R. Wiesendanger, Internat. Conf. on Novel Phenomena in Frustrated Systems, Santa Fé (USA): *Spin Spiral States in Low-dimensional Magnets Studied by Low-Temperature Spin-Polarized Scanning Tunneling Spectroscopy*

27.5.2011: R. Wiesendanger, Internat. Workshop on Spin Chirality and Dzyaloshinskii-Moriya Interaction, St. Petersburg (Russia): *Spin Spiral States in Low-dimensional Magnets Studied by Low-Temperature Spin-Polarized Scanning Tunneling Spectroscopy*

31.5.2011: R. Wiesendanger, Internat. Workshop on Functional Metalorganics, Uppsala (Sweden): *Spin-Resolved Scanning Tunneling Microscopy Study of Metalorganic Molecule-Surface Interaction with Intramolecular Resolution*

20.6.2011: R. Wiesendanger, Internat. Scanning Probe Microscopy Confer. ISPM 2011, Munich (Germany): *Computing with Atoms: Towards Atomic Spin Logic Devices*

27.6.2011: R. Wiesendanger, Internat. Workshop on Magnetoelectric Composites and Future Biomagnetic Interfaces, Kiel (Germany): *Imaging and Manipulating Single and Interacting Spins on Surfaces: Towards Atomic-Scale Spin Devices*

2.7.2011: E. Y. Vedmedenko, International Workshop on Novel Trends in Optics and Magnetism of Nanostructures, Augustow (Poland): *High switching frequency of magnetic nanoparticles*

4.7.2011: R. Wiesendanger, 5th Polish Conference on Nanotechnology NANO 2011, Gdansk (Poland): *Spin-based Logic Operations at the Atomic Level*

6.7.2011: J. Wiebe, Workshop on "Novel Trends in Optics and Magnetism of Nanostructures", Augustow (Poland): *Spin Excitation and Magnetometry of Artificial Nanostructures Built Atom by Atom.*

29.7.2011: J. Wiebe, SPIRE-Workshop "‘The Spin Triangle"’, Hamburg (Germany): *Magnetic dopants in semiconductors*

14.8.2011: E. Y. Vedmedenko, International Conference on Special Functions and their Applications, Decin (Czech Republic): *Skyrmion Lattices*

23.8.2011: R. Wiesendanger, Nordic Conference on Correlated Electron Systems, Strömsberg (Sweden): *Correlation Effects in Single-Atom Spectroscopy by STM and SPSTM*

1.9.2011: R. Wiesendanger, ECOSS-28, Breslau (Poland): *Computing with Atoms on Surfaces: Towards Atomic Spin Logic Devices*

8.9.2011: J. Wiebe, International Conference on Energy-Aware High Performance Computing, Hamburg (Germany): *Towards Atomic-Spin Based Computation: Realizing Logic Operations Atom by Atom.*

28.9.2011: J. Wiebe, 4th Nanospintronics Network Meeting, Fagerudd (Sweden): *Bottom-up engineering and magnetometry of model nanomagnets by spin-resolved scanning tunneling microscopy*

28.9.2011: G. Herzog, 1st International School on Surface Science "Technologies and Measurements on Atomic Scale", Veliky Novgorod (Russia): *Spin mapping and manipulation at the nanoscale*

14.10.2011: R. Wiesendanger, 3rd TMS Workshop on Spectroscopic Characterization, Burgstädt (Germany): *Spin-Resolved Scanning Tunneling Microscopy Study of Metalorganic Molecule-Surface Interaction with Intramolecular Resolution*

27.10.2011: R. Wiesendanger, SLONANO 2011, Ljubljana (Slovenia): *Computing with Atoms on Surfaces: Towards Atomic Spin Logic Devices*

30.10.2011: E. Y. Vedmedenko, 56th International Conference on Magnetism and Magnetic Materials, Scottsdale, Arizona (USA): *Manipulation of magnetic domain walls in nanowires and nanoparticles*

28.11.2011: J. Wiebe, 493. WE-Heraeus-Seminar, Bad Honnef (Germany): *Magnetometry of Single Atoms and Bottom-Up Nanostructures using Spin-Polarized Scanning Tunneling Spectroscopy*

28.11.2011: Kirsten von Bergmann, 493. WE-Heraeus-Seminar on Scanning Probe Techniques, Bad Honnef (Germany): *Complex magnetic structures on the atomic scale revealed by spin-polarized STM*

29.11.2011: A. Schwarz, 493. WE-Heraeus-Seminar on "Latest Developments in Scanning Probe Techniques focused on Nanotechnology", Bad Honnef (Germany): *Magnetic Exchange Force Microscopy and Spectroscopy*

30.11.2011: E. Y. Vedmedenko, International Symposium on High Performance Computing in Nano-Spintronics, Hamburg (Germany): *Multipolar Approach for Large-Scale Simulations of Magnetic Arrays*

7.12.2011: A. Schwarz, IOP Workshop "Nanomaterials: Characterisation, Simulation and Application meeting", London (U.K.): *Real Space Imaging of Magnetic Nanostructures*

12.2.2012: R. Wiesendanger, 17th Winter-School on New Developments in Solid State Physics, Mauterndorf (Austria): *Towards Atom-by-Atom Engineering of Tailored Nanomagnets and Atomic Spin Logic Devices*

26.3.2012: A.A. Khajetoorians, 76th Spring Conference, Deutsche Physikalische Gesellschaft, Berlin (Germany): *Spin LEGOs*

29.3.2012: S. Krause, 76th Spring Conference, Deutsche Physikalische Gesellschaft, Berlin (Germany): *Spin-current manipulation of atomic-scale magnets using SP-STM*

3.4.2012: R. Wiesendanger, 103. MNU Bundeskongress, Freiburg i. Brsg. (Germany): *Von der Nanophysik zu atomaren Bauelementen*

10.4.2012: J. Wiebe, 1st International Workshop on Scanning Probe Microscopies, Laboratory of Advanced Microscopies (LMA), Zaragoza (Spain): *Atom-by-atom fabrication and magnetometry of model magnetic systems*

23.4.2012: R. Wiesendanger, 3rd Nordic Workshop on Spintronics and Nanomagnetism, Varberg (Sweden): *Atom-by-Atom Engineering of Tailored Nanomagnets and Atomic-Scale Spintronic Devices*

4.5.2012: R. Wiesendanger, 3rd Internat. Conf. on Superconductivity and Magnetism, Istanbul (Turkey): *From Single-Atom Magnetometry to Tailor-Made Magnets and Atomic-Scale Spintronic Devices*

16.5.2012: A. Schwarz, Physics Boat 2012 "Atomic structure of nanosystems from first-principles simulations and microscopy experiments", Helsinki, Stockholm (Finland, Sweden): *Magnetic Exchange Force Microscopy and Spectroscopy*

29.5.2012: E. Y. Vedmedenko, International Workshop on "Statistical Physics and Low Dimensional Systems", Nancy (France): *Properties of frustrated low-dimensional magnets with pentagonal symmetry*

29.5.2012: R. Wiesendanger, Summer School of Metrology 2012, Burg Warberg (Germany): *Single-Atom Magnetometry*

30.5.2012: E. Y. Vedmedenko, International Symposium on the Dynamics of Domain Walls, Hamburg (Germany): *Atomic-level control of the domain wall dynamics*

25.6.2012: R. Wiesendanger, 4th Internat. Conf. on Nano-Structures Self-Assembly, S. Margherita di Pula, Sardinia (Italy): *From Model-Type Nanomagnets to Atomic Spin Logic Devices*

26.6.2012: E. Y. Vedmedenko, Journées complexité et désordre, Paris (France): *Magnetricity in Quasicrystals*

2.7.2012: E. Y. Vedmedenko, International Conference on Mathematics of Distances and Applications, Varna (Bulgaria): *Magnetricity in Quasicrystals*

3.7.2012: J. Wiebe, 7th International Workshop on Nano-Scale Spectroscopy and Nanotechnology (NSS-7), ETHZ and PSI, Zürich (Switzerland): *Tailoring ground states and dynamics of bottom-up engineered nanomagnets*

11.7.2012: R. Wiesendanger, 19th Internat. Conf. on Magnetism, ICM 2012, Busan (S.-Korea): *From Single-Atom Magnetometry to Tailored Nanomagnets and Atomic-Scale Spintronic Devices*

15.7.2012: R. Wiesendanger, Public Lecture, Harbin (China): *Exploring Magnetism in the Nanoworld*

23.7.2012: R. Wiesendanger, Internat. Conf. on Nanoscience and Technology, ICN+T 2012, Paris (France): *Atom-by-Atom Engineering of Tailored Nanomagnets and Atomic-Scale Spintronic Devices*

25.7.2012: A. Schwarz, International Conference on Nanoscience + Technology 2012, Paris (France): *Prospects of Magnetic Exchange Force Microscopy and Spectroscopy*

27.8.2012: R. Wiesendanger, 11th Int. Conf. on Nanostructured Materials, NANO 2012, Rhodes (Greece): *Atom-by-Atom Engineering of Tailored Nanomagnets*

5.9.2012: R. Wiesendanger, CMD-24 and ECOSS-29, Edinburgh (U. K.): *Imaging and Manipulating Single and Interacting Spins on Surfaces: Towards Atomic-Scale Spintronic Devices*

11.9.2012: J. Wiebe, 6th International Conference on SPS and 4th International Workshop on SP-STM, Timmendorfer Strand (Germany): *Tailoring ground states and dynamics of bottom-up engineered nanomagnets*

11.9.2012: A.A. Khajetoorians, 6th International Conference on SPS and 4th International Workshop on SP-STM, Timmendorfer Strand (Germany): *Probing the magnetization dynamics of artifically constructed nanomagnets*

8.11.2012: A.A. Khajetoorians, Fabrication and Properties of Nanostructures, Alicante (Spain): *Tailoring nanomagnetism atom by atom*

7.12.2012: R. Wiesendanger, 6th Internat. Meeting on Molecular Electronics ElecMol'12, Grenoble (France): *Real-space observation of spin-split molecular orbitals of adsorbed single-molecule magnets*

15.1.2013: A.A. Khajetoorians, MMM/InterMag, Chicago (USA): *Current-driven spin dynamics of artificially constructed quantum magnets*

16.1.2013: R. Wiesendanger, 12th Joint MMM - Intermag Conference, Chicago (USA): *Atomically Tailored Nanomagnets and their Use for Atomic-Level Spintronics*

21.1.2013: R. Wiesendanger, 40th Conference on the Physics and Chemistry of Surfaces and Interfaces, PCSI-40, Waikoloa, Hawaii (USA): *Recent Developments in Interface-Driven Magnetism*

11.2.2013: A. Schwarz, Towards Reality in in Nanomaterials, Levi (Finland): *Magnetic Exchange Force Microscopy and Spectroscopy - A Novel Technique to Study Magnetism with Atomic Resolution*

4.3.2013: E. Y. Vedmedenko, Heraeus Workshop "Magnetism on curved surfaces", Bad Honnef (Germany): *Properties of frustrated low-dimensional magnets*

13.3.2013: A.A. Khajetoorians, 77th Spring Conference, Deutsche Physikalische Gesellschaft, Regensburg (Germany): *Magnetization dynamics derived from excitations of single magnetic atoms on surfaces*

13.3.2013: K. von Bergmann, 77th Spring Conference, Deutsche Physikalische Gesellschaft, Regensburg (Germany): *Gaede-Prize talk: Complex magnetic order on the atomic scale*

14.3.2013: A. Schlenhoff, 77th Spring Conference, Deutsche Physikalische Gesellschaft, Regensburg (Germany): *Spin-polarized scanning field emission microscopy and spectroscopy*

3.4.2013: J. Wiebe, MRS Spring Meeting 2013, San Francisco (USA): *Tailoring Ground States and Dynamics of Bottom-Up Engineered Arrays of Atomic Spins*

4.4.2013: R. Wiesendanger, MRS Spring Meeting 2013, San Francisco (USA): *Atomic-Scale Studies of Magnetic Oxides by Spin-Polarized STM and Magnetic Exchange Force Microscopy*

10.4.2013: R. Wiesendanger, 10th Latin American Workshop on Magnetism, Magnetic Materials and their Applications, X-LAW3M, Buenos Aires (Argentina): *Atomically Tailored Nanomagnets and their Use for Atomic-Level Spintronics*

23.4.2013: R. Wiesendanger, NanoSpain 2013, Bilbao (Spain): *Exploring Magnetism in the Nanoworld*

23.5.2013: A.A. Khajetoorians, Otto Stern Symposium, Hamburg (Germany): *From Magnetic Moments of Single Atoms on Surfaces to Atomic-Scale Spin Logic Devices*

27.6.2013: R. Wiesendanger, 42nd "Jaszowiec" Internat. School and Conference on the Physics of Semiconductors, Wisla (Poland): *Revealing Magnetic Properties and Interactions on the Atomic Scale*

5.7.2013: R. Wiesendanger, Laserion 2013, Tegernsee (Germany): *Spin-Resolved Studies of Individual Molecules on Surfaces*

17.7.2013: R. Wiesendanger, Hayashi Conference, Hayama (Japan): *The Role of Surfaces and Interfaces for Nano-Scale Magnetism and Spintronics*

27.8.2013: R. Wiesendanger, JEMS 2013, Rhodes (Greece): *Towards Computation with Single Skyrmions and Single Spins*

2.9.2013: R. Wiesendanger, Internat. Conf. on Nanoscale Magnetism, ICNM 2013, Istanbul (Turkey): *Atomically Tailored Nanomagnets and their Use for Atomic-Level Spintronic*

5.9.2013: R. Wiesendanger, ECME 2013, London (U. K.): *Spintronics at the Single-Molecule Level*

9.9.2013: R. Wiesendanger, 42nd Polish Physical Society Meeting, Poznan (Poland): *Atomically Tailored Nanomagnets and their Use for Atomic-Level Spintronics*

11.9.2013: K. von Bergmann, ICN+T, Paris (France): *Spin spirals and magnetic skyrmions studied with spin-polarized STM*

12.9.2013: A.A. Khajetoorians, ICN+T/IVC-19, Paris (France): *Spin LEGOs - Bottom-up fabrication of model magnetic systems*

23.9.2013: A. Schwarz, Forces and Photons Workshop, FU Berlin , Berlin (Germany): *Forces, Tips, Cantilevers and Light*

9.10.2013: A. Schwarz, 1st German-French Summer School on Noncontact AFM, Porquerolles (France): *Magnetic sensitive force microscopy*

19.10.2013: A.A. Khajetoorians, Heraeus Seminar, Bad Honnef, "Electron Transport through Atoms, Molecules and Nanowires: Advances in Experiment and Theory", Bad Honnef (Germany): *Spin LEGOs - dynamic characterization of bottom-up fabricated atomic magnets*

30.10.2013: M. Bazarnik, Open lecture at Adam Mickiewicz University, Poznan (Poland): *Surface physico-chemistry analysis methods used for porous materials research*

6.11.2013: A.A. Khajetoorians, ACSIN-12/ICSPM21, Tsukuba (Japan): *Spin LEGOs - Bottom-up fabrication of model magnetic systems*

7.11.2013: S. Krause, 58th Annual Conference On Magnetism And Magnetic Materials, Denver, CO (USA): *Current-Driven Spin Dynamics of Artificially Constructed Quantum Magnets*

8.11.2013: R. Wiesendanger, Int. Conf. on Friction and Energy Dissipation in Man-made and Biological Systems, Trieste (Italy): *Atomic-Scale Spin Friction*

12.11.2013: A.A. Khajetoorians, Heraeus Seminar, Bad Honnef, "Interactions with the Nanoworld: Local Probes with High Time, Energy and Force Resolution", Bad Honnef (Germany): *Atomic Spin LEGOs*

25.11.2013: R. Wiesendanger, Leopoldina-INSA Symposium on Nanoscience, Halle (Saale) (Hermany): *Nano-Scale Spintronic Devices for Logic and Memory Applications*

12.12.2013: R. Wiesendanger, NANO SACLAY Nanoelectronics Workshop 2013, Paris (France): *Spintronics at the Single-Molecule Level*

7.2 Conference Contributions and Talks at Other Institutes

7.2.1 Talks

11.1.2011: H. Fuchs, Ringvorlesung "Physik im Alltag", Hamburg (Germany): *Nanotechnologie in Wissenschaft und Alltag*

25.1.2011: T. Stapelfeldt, R. Wieser, E. Y. Vedmedenko, and R. Wiesendanger, SFB668 Kolloquium, Hamburg (Germany): *Manipulation of Magnetic Domain Walls with an STM Tip*

14.3.2011: J. Schwöbel, Y. Fu, A. Dilullo, J. Brede, S. Klayatskaya, M. Ruben, G. Hoffmann, and R. Wiesendanger, 75th Spring Conference, Deutsche Physikalische Gesellschaft, Dresden (Germany): *Spin-sensitive tunneling through individual Terbium-Phtalocyanine Molecules by Spin-polarized Scanning Tunneling Microscopy*

14.3.2011: R. Wieser, E. Y. Vedmedenko, and R. Wiesendanger, 75th Spring Conference, Deutsche Physikalische Gesellschaft, Dresden (Germany): *Indirect control of antiferromagnetic domain walls with spin current*

14.3.2011: B. Wolter, Y. Yoshida, A. Kubetzka, K. von Bergmann, S.-W. Hla, and R. Wiesendanger, 75th Spring Conference, Deutsche Physikalische Gesellschaft, Dresden (Germany): *Imaging atomic-scale magnetic structures by means of lateral atom manipulation with an STM tip*

14.3.2011: M. Menzel, Y. Mokrousov, R. Wieser, K. von Bergmann, E. Vedmedenko, S. Blügel, S. Heinze, A. Kubetzka, and R. Wiesendanger, 75th Spring Conference, Deutsche Physikalische Gesellschaft, Berlin (Germany): *SP-STM study of biatomic Fe chains on* $(5 \times 1) - Ir(001)$

14.3.2011: R. Schmidt, C. Lazo, A. Schwarz, S. Heinze, and R. Wiesendanger, 75th Spring Conference, Deutsche Physikalische Gesellschaft, Berlin (Germany): *Magnetic Exchange Force Spectroscopy on antiferromagnetic Fe/W(001)*

15.3.2011: A. Schwarz, K. Lämmle, R. Wiesendanger, T. Trevethan, M. Watkins, and A. Shluger, 75th Spring Conference, Deutsche Physikalische Gesellschaft, Dresden (Germany): *Determining the Exact Adsorption Configuration of a Chiral Metal-Organic Complex on a Bulk Insulator*

16.3.2011: J. Wiebe, A. A. Khajetoorians, S. Lounis, B. Chilian, A. T. Costa, L. Zhou, D. Mills, S. Schuwalow, F. Lechermann, and R. Wiesendanger, 75th Spring Conference, Deutsche Physikalische Gesellschaft, Dresden (Germany): *Itinerant Nature of Atom-Magnetization Excitation by Inelastic Scanning Tunneling Spectroscopy*

16.3.2011: A. A. Khajetoorians, B. Chilian, J. Wiebe, and R. Wiesendanger, 75th Spring Conference, Deutsche Physikalische Gesellschaft, Dresden (Germany): *Realizing Spin Logic Atom by Atom*

16.3.2011: J. Bickel, F. Meier, J. Brede, A. Kubetzka, K. von Bergmann, and R. Wiesendanger, 75th Spring Conference, Deutsche Physikalische Gesellschaft, Dresden (Germany): *Extremely high coercivity of Co Islands on Ir(111) probed by SP-STM*

16.3.2011: T. Stapelfeldt, R. Wieser, E. Y. Vedmedenko, and R. Wiesendanger, 75th Spring Conference, Deutsche Physikalische Gesellschaft, Dresden (Germany): *Domain Wall Manipulation With a Magnetic Tip*

17.3.2011: S. Yamazaki, T. Spitz, O. Pietzsch, and R. Wiesendanger, 75th Spring Conference, Deutsche Physikalische Gesellschaft, Dresden (Germany): *Local transport measurements on folding graphite and multi-layer graphene on SiO2 by a four-probe scanning tunneling microscope*

17.3.2011: L. Dzemiantsova, A. Kubetzka, K. von Bergmann, and R. Wiesendanger, 75th Spring Conference, Deutsche Physikalische Gesellschaft, Dresden (Germany): *SP-STM study on bulk nickel (111) surface*

17.3.2011: Y. Mokrousov, M. Menzel, R. Wieser, K. von Bergmann, E. Vedmedenko, A. Kubetzka, R. Wiesendanger, S. Blügel, and S. Heinze, 75thSpring Conference, Deutsche Physikalische Gesellschaft, Dresden (Germany): *Chiral spin-structure of biatomic Fe chains on Ir(001)*

17.3.2011: Y. Fu, J. Schwöbel, A. Dillulo, G. Hoffmann, J. Brede, S. Klyatskaya, M. Ruben, and R. Wiesendanger, 75th Spring Conference, Deutsche Physikalische Gesellschaft, Dresden (Germany): *Switching behavior of double-decker single molecule magnets on a metal surface*

17.3.2011: T. Eelbo, M. Gyamfi, M. Waśniowska, and R. Wiesendanger, 75th Spring Conference, Deutsche Physikalische Gesellschaft, Dresden (Germany): *Electronic properties and localization of Fe atoms on bilayer graphene on Ru(0001)*

18.3.2011: A. Schlenhoff, A. Sonntag, S. Krause, and R. Wiesendanger, 75th Spring Conference, Deutsche Physikalische Gesellschaft, Dresden (Germany): *Observation of superparamagnetism in image potential states using SP-STM*

18.3.2011: S. Krause, G. Herzog, A. Schlenhoff, A. Sonntag, and R. Wiesendanger, 75th Spring Conference, Deutsche Physikalische Gesellschaft, Dresden (Germany): *Quantification of spin torque and Joule heating using SPSTM*

7.4.2011: R. Wieser, Group seminar, The Computational Magnetism Group, Prof. R. Chantrell, University of York, York (U.K.): *Current and Field driven domain wall motion*

10.5.2011: J. Wiebe, Seminar at the Uppsala University UniMolecular Electronics Center, Uppsala (Sweden): *Spin Excitation and Magnetometry of Artificial Nanostructures Built Atom by Atom*

12.5.2011: O. Pietzsch, Short Course on Physical Characterization of Nanostructures, Leuven (Belgium): *Spin-Polarized Scanning Tunneling Microscopy: Studying Magnetism of Nanostructures*

16.6.2011: J. Bickel, Debye-Ornstein Colloquium, Utrecht (Netherlands): *Spin-polarized STM of high coercivity Co nanostructures on Ir*

30.8.2011: J. Bickel, F. Meier, J. Brede, A. Kubetzka, K. von Bergmann, and R. Wiesendanger, ECOSS 28, Wroclaw (Poland): *Spin-polarized STM of high coercivity Co nanostructures on Ir*

31.8.2011: M. Menzel, Y. Mokrousov, R. Wieser, K. von Bergmann, E. Vedmedenko, S. Blügel, S. Heinze, A. Kubetzka, and R. Wiesendanger, ECOSS-28, Wroclaw (Poland): *Atomic-scale spin spiral observed in individual metallic chains*

2.9.2011: M. Gyamfi, T. Eelbo, M. Waśniowska, T. Wehling, A. Lichtenstein, S. Forti, U. Starke, and R. Wiesendanger, ECOSS-28, Wroclaw (Poland): *Ni atoms on graphene: electronic properties and phonon excitations*

19.9.2011: R. Schmidt, A. Schwarz, and R. Wiesendanger, NCAFM 2011, Lindau (Germany): *Properties of Magnetic Tips for Magnetic Exchange Force Microscopy and Spectroscopy*

1.11.2011: R. Wieser, T. Stapelfeldt, E. Y. Vedmedenko, and R. Wiesendanger, 56th Annual Conference on Magnetism and Magnetic Materials, Scottsdale (Arizona, USA): *Manipulation of transverse domain walls using a spin-polarized STM*

3.11.2011: R. Wiesendanger, Zernike-Colloquium, Groningen (The Netherlands): *Exploring the Spin in the Nanoworld*

17.11.2011: A. A. Khajetoorians, Seminar, Copenhagen (Denmark): *Atom-by-atom engineering and magnetometry of tailored nanomagnets*

13.12.2011: R. Wieser, M. Menzel, Y. Mokrousov, J. Bickel, E. Y. Vedmedenko, S. Blügel, S. Heinze, K. von Bergmann, A. Kubetzka and R. Wiesendanger, Seminars zur Theorie der Kondensierten Materie, Aachen (Germany): *Theoretical studies on the complex magnetism of bi-atomic Fe-chains on (5x1)-Ir(001)*

1.2.2012: A. Schwarz, SFB 677 Kolloquium CAU, Kiel (Germany): *Magnetic Molecules on Bulk Insulators*

28.2.2012: J. Bickel, M. Menzel, K. von Bergmann, A. Kubetzka, and R. Wiesendanger, 2012 APS March Meeting, Boston (USA): *Magnetic Structure and Stability of 1D Co/Fe Wires*

1.3.2013: R. Wiesendanger, CNR NANO Seminar, Modena (Italy): *Imaging and Manipulating Single and Interacting Spins on Surfaces: Towards Atomic-Scale Spintronic Devices*

1.3.2012: J. Wiebe, A. A. Khajetoorians, B. Chilian, R. Wiesendanger, S. Lounis, A. T. Costa, and D. L. Mills, 2012 APS March Meeting, Boston, Massachusetts (USA): *Anomalously large* g*-factor of single atoms adsorbed on a metal substrate*

2.3.2012: A.A. Khajetoorians, J. Wiebe, S. Lounis, B. Chilian, S. Bluegel, R. Wiesendanger, APS March Meeting 2012, Boston (USA): *Atom-by-atom engineering and atomic magnetometry of tailored nanomagnets with SP-STM*

7.3.2012: A. Schwarz, R. Schmidt, and R. Wiesendanger, NCAFM 2012, Cesky Krumlov (Czech Republic): *Observation and quantitative evaluation of superparamagnetic behavior utilizing magnetic exchange force microscopy and spectroscopy*

26.3.2012: B. Wolter, Y. Yoshida, K. von Bergmann, A. Kubetzka, S.-W. Hla, and R. Wiesendanger, 76^{th} Spring Conference, Deutsche Physikalische Gesellschaft, Berlin (Germany): *Spin friction observed on the atomic scale*

26.3.2012: J. Honolka, A. A. Khajetoorians, V. Sessi, T. O. Wehling, S. Stepanow, J. Mi, B. B. Iversen, T. Schlenk, J. Wiebe, N. Brookes, A. I. Lichtenstein, P. Hofmann, K. Kern, and R. Wiesendanger, 76^{th} Spring Conference, Deutsche Physikalische Gesellschaft, Berlin (Germany): *In-plane anisotropy of Fe atoms on* Bi_2Se_3*(111)*

26.3.2012: A.Eich, S. V. Eremeev, G. Landolt, T. V. Menshchikova, B. Slomski, Yu. M. Koroteev, Z. S. Aliev, M. B. Babanly, J. Henk, A. Ernst, L. Patthey, A. A. Khajetoorians, J. Hagemeister, O. Pietzsch, J. Wiebe, R. Wiesendanger, P. M. Echenique, S. S. Tsirkin, I. R. Amiraslanov, J. H. Dil and E. V. Chulkov, 76^{th} Spring Conference, Deutsche Physikalische Gesellschaft, Berlin (Germany): *STM studies on the ternary topological insulator* $PbBi_4Te_7$

26.3.2012: J. Grenz, A. Schwarz, and R. Wiesendanger, 76^{th} Spring Conference, Deutsche Physikalische Gesellschaft, Berlin (Germany): *Density driven solidification of a 2D molecule gas on a bulk insulator: Co-Salen on NiO(001)*

26.3.2012: E. Y. Vedmedenko, Q. Zhu, U. Kaiser, A. Schwarz, and R. Wiesendanger, 76^{th} Spring Conference, Deutsche Physikalische Gesellschaft, Berlin (Germany): *Atomic Scale Magnetic Dissipation from Spin-Dependent Adhesion Hysteresis*

27.3.2012: M. Gyamfi, T. Eelbo, M. Waśniowska, T. O. Wehling, S. Forti, U. Starke, A. I. Lichtenstein, M. I. Katsnelson, and R. Wiesendanger, 76^{th} Spring Conference, Deutsche Physikalische Gesellschaft, Berlin (Germany): *Electronic properties of Ni adatoms on graphene*

27.3.2012: T. Eelbo, M. Gyamfi, S. Forti, U. Starke, M. Waśniowska, and R. Wiesendanger, 76^{th} Spring Conference, Deutsche Physikalische Gesellschaft, Berlin (Germany): *Visualizing quantum interference nearby individual magnetic impurities on graphene*

28.3.2012: M. Menzel, Y. Mokrousov, R. Wieser, J. Bickel, E. Vedmedenko, S. Blügel, S. Heinze, K. von Bergmann, A. Kubetzka, and R. Wiesendanger, 76^{th} Spring Conference, Deutsche Physikalische Gesellschaft, Berlin (Germany): *Micromagnetic simulations of the spin spiral state in bi-atomic Fe chains on Ir(001)*

28.3.2012: T. Eelbo, M. Sikora, M. Waśniowska, M. Dobrzański, M. Gyamfi, G. Bihlmayer, I. Miotkowski, A. Kozlowski, and R. Wiesendanger, 76^{th} Spring Conference, Deutsche Physikalische Gesellschaft, Berlin (Germany): *Electronic properties and magnetic anisotropy of individual Co adatoms adsorbed on topological insulator surfaces*

28.3.2012: K. von Bergmann, M. Menzel, D. Serrate, Y. Yoshida, A. Kubetzka, R. Wiesendanger, and S. Heinze, 76^{th} Spring Conference, Deutsche Physikalische Gesellschaft, Berlin (Germany): *Tunneling anisotropic magnetoresistance on the atomic scale*

28.3.2012: R. Decker, J. Brede, N. Atodiresei, V. Caciuc, S. Blügel, and R. Wiesendanger, 76^{th} Spring Conference, Deutsche Physikalische Gesellschaft, Berlin (Germany): *Spin-polarized STM of Co-intercalated graphene on Ir(111)*

28.3.2012: L. Dzemiantsova, A. Kubetzka, K. von Bergmann, and R. Wiesendanger, 76^{th} Spring Conference, Deutsche Physikalische Gesellschaft, Berlin (Germany): *SP-STM study of individual Co atoms on Pd/Co/Ir(111)*

28.3.2012: A. Schwarz, R. Schmidt, and R. Wiesendanger, 76^{th} Spring Conference, Deutsche Physikalische Gesellschaft, Berlin (Germany): *Observation and quantitative evaluation of superparamagnetic behavior utilizing magnetic exchange force microscopy and spectroscopy*

29.3.2012: J. Brede, R. Decker, J. Schwöbel, S. Klyatskaya, M. Ruben, and R. Wiesendanger, 76^{th} Spring Conference, Deutsche Physikalische Gesellschaft, Berlin (Germany): *Spin resolved measurements of magnetic molecules on surfaces*

29.3.2012: R. Wieser, V. Caciuc, C. Lazo, H. Hölscher, E. Y. Vedmedenko, R. Wiesendanger, and S. Heinze, 76^{th} Spring Conference, Deutsche Physikalische

Gesellschaft, Berlin (Germany): *Theoretical study of dynamical switching of a single spin by exchange forces*

29.3.2012: S. Lounis, A. T. Costa, B. Chilian, A. A. Khajetoorians, J. Wiebe, R. Wiesendanger, and D. L. Mills 76th Spring Conference, Deutsche Physikalische Gesellschaft, Berlin (Germany): *First-principles investigation of g-shifts and damping of dynamical magnetic excitations in adatoms on surfaces*

29.3.2012: J. Wiebe, A. A. Khajetoorians, S. Lounis, A. T. Costa, B. Chilian, D. L. Mills, and R. Wiesendanger, 76th Spring Conference, Deutsche Physikalische Gesellschaft, Berlin (Germany): *Anomalously large* g*-factor of single atoms adsorbed on a metal substrate*

29.3.2012: A. Schlenhoff, A. Sonntag, S. Krause, and R. Wiesendanger, 76th Spring Conference, Deutsche Physikalische Gesellschaft, Berlin (Germany): *Spin-transfer torque and Joule heating of field-emitted electrons*

29.3.2012: A. Sonntag, S. Krause, G. Herzog, A. Schlenhoff, and R. Wiesendanger, 76th Spring Conference, Deutsche Physikalische Gesellschaft, Berlin (Germany): *Spin-transfer torque switching efficiency in SP-STM experiments*

4.6.2012: R. Wieser, Theory group seminar Prof. S. Heinze, Kiel (Germany): *Thermal and quantum fluctuations in spin spiral structures induced by Dzyaloshinsky-Moriya interaction*

4.6.2012: T. Eelbo, M. Gyamfi, S. Forti, U. Starke, M. Waśniowska, and R. Wiesendanger, Graphene Week 2012, Delft (Netherlands): *Visualizing electron scattering on graphene around Co adatoms by means of STM*

12.6.2012: A. Schlenhoff, SFB616 "Energiedissipation an Oberflaechen" Seminar, Universität Duisburg-Essen, Duisburg (Germany): *Individual atomic-scale magnets interacting with spin-polarized field-emitted electrons*

2.7.2012: J. Grenz, A. Schwarz, D. Gao, M. Watkins, A. Shluger, and R. Wiesendanger, 15th International Conference on Noncontact Atomic Force Microscopy (NCAFM 2012), Ceský Krumlov (Czech republic): *Co-Salen on NaCl(001) and NiO(001): Substrate influence on adsorption geometry and growth*

11.7.2012: A. Schwarz, R. Schmidt, C. Lazo, S. Heinze, and R. Wiesendanger, International Conference on Magnetism (ICM), Busan (Republic of Korea): *Probing the Distance Dependence of the Magnetic Exchange Interaction with Atomic Resolution*

12.7.2012: J. Brede, J. Schwöbel, R. Decker, A. Dilullo, G. Hoffmann, S. Klyatskaya, M. Ruben and R. Wiesendanger, International Conference on Magnetism (ICM), Busan (Republic of Korea): *Spin resolved measurements of single molecular magnets on surfaces*

12.7.2012: A. Schlenhoff, A. Sonntag, S. Krause, and R. Wiesendanger, International Conference on Magnetism (ICM), Busan (Republic of Korea): *Spin-transfer torque and Joule heating of field-emitted electrons*

12.7.2012: Y. Yoshida, S. Schroeder, P. Ferriani, D. Serrate, K. von Bergmann, A. Kubetzka, S. Heinze, and R. Wiesendanger, International Conference on Magnetism (ICM), Busan (Republic of Korea): *Conical spin-spiral state in an ultra-thin film driven by higher-order spin interactions*

12.7.2012: S. Krause, G. Herzog, A. Schlenhoff, A. Sonntag, and R. Wiesendanger, International Conference on Magnetism (ICM), Busan (Republic of Korea): *Joule heating and spin-transfer torque investigated on the atomic scale using SP-STM*

12.7.2012: R. Schmidt, A. Schwarz, and R. Wiesendanger, International Conference on Magnetism (ICM), Busan (Republic of Korea): *Magnetization switching utilizing the magnetic exchange interaction*

12.7.2012: M. Menzel, Y. Mokrousov, R. Wieser, J. E. Bickel, E. Y. Vedmedenko, S. Blügel, S. Heinze, K. von Bergmann, A. Kubetzka, and R. Wiesendanger, International Conference on Magnetism (ICM), Busan (Republic of Korea): *Non-collinear magnetic ground state in finite metallic chains*

24.7.2012: A.A. Khajetoorians, J. Wiebe, S. Krause, T. Schlenk, B. Baxevanis, Chr. Huebner, D. Pfannkuche, T.O. Wehling, S. Lounis, A. Lichtenstein, R. Wiesendanger, International Conference on Nanoscience and Technology (ICN+T), Paris (France): *Probing magnetization dynamics of single atom systems with SP-STM*

24.7.2012: Y. Yoshida, S. Schröder, P. Ferriani, D. Serrate, A. Kubetzka, K. von Bergmann, S. Heinze, and R. Wiesendanger, International Conference on Nanoscience and Technology (ICN+T), Paris (France): *Conical Spin Spiral State in an ultra-thin Film driven by higher-order Spin Interactions*

24.7.2012: J. Schwöbel, R. Decker, A. Dilullo, G. Hoffmann, S. Klyatskaya, M. Ruben, and R. Wiesendanger, International Conference on Nanoscience and Technology (ICN+T), Paris (France): *Spin resolved measurements of single molecular magnets on surfaces*

24.7.2012: T. Eelbo, M. Sikora, M. Waśniowska, M. Dobrzanski, A. Kozlowski, M. Gyamfi, G. Bihlmayer, I. Miotkowski, and R. Wiesendanger, International Conference on Nanoscience and Technology (ICN+T), Paris (France): *Electronic and Magnetic Properties of Co Adatoms on the* Bi_2Se_3 *Surface*

25.7.2012: A. Schlenhoff, S. Krause, A. Sonntag, and R. Wiesendanger, International Conference on Nanoscience and Technology (ICN+T), Paris (France): *Spin-transfer torque and Joule heating of field-emitted electrons*

25.7.2012: B. Wolter, Y. Yoshida, A. Kubetzka, S.-W. Hla, K. von Bergamnn, and R. Wiesendanger, International Conference on Nanoscience and Technology (ICN+T), Paris (France): *Spin Friction Observed on the Atomic Scale*

25.7.2012: S. Krause, G. Herzog, A. Schlenhoff, A. Sonntag, and R. Wiesendanger, International Conference on Nanoscience and Technology (ICN+T), Paris (France): *Joule heating and spin-transfer torque investigated on the atomic scale using SP-STM*

25.7.2012: M. Ashino and R. Wiesendanger, International Conference on Nanoscience and Technology (ICN+T), Paris (France): *Unusual Elastic and Inelastic Behavior of Carbon Nanotubes due to Molecular Encapsulation: Dynamic Force Microscopy and Spectroscopy Studies*

26.7.2012: R. Decker, J. Brede, N. Atodiresei, V. Caciuc, S. Blügel, and R. Wiesendanger, International Conference on Nanoscience and Technology (ICN+T), Paris (France): *Structure and magnetism of cobalt intercalated graphene on Ir(111) studied by spin-polarized STM*

26.7.2012: L. Dzemiantsova, A. Kubetzka, K. von Bergmann, and R. Wiesendanger, International Conference on Nanoscience and Technology (ICN+T), Paris (France): *SP-STM study of individual Co atoms on Pd/Co/Ir(111)*

26.7.2012: A.A. Khajetoorians, J. Wiebe, S. Lounis, B. Chilian, S. Blügel, and R. Wiesendanger, International Conference on Nanoscience and Technology (ICN+T), Paris (France): *Atom-by-atom engineering and atomic magnetometry of tailored nanomagnets with SP-STM*

26.7.2012: K. von Bergmann, M. Menzel, D. Serrate, Y. Yoshida, A. Kubetzka, R. Wiesendanger, and S. Heinze, International Conference on Nanoscience and Technology (ICN+T), Paris (France): *Tunneling anisotropic magnetoresistance on the atomic scale*

3.8.2012: J. Wiebe, J. Honolka, A. A. Khajetoorians, V. Sessi, T. O. Wehling, S. Stepanow, J.-L. Mi, B. B. Iversen, T. Schlenk, N. Brookes, A. I. Lichtenstein, Ph. Hofmann, K. Kern, and R. Wiesendanger, 31st International Conference on the Physics of Semiconductors (ICPS 2012), Zurich (Switzerland): *In-Plane Magnetic Anisotropy of Fe Atoms on* Bi_2Se_3*(111)*

5.9.2012: A. Schlenhoff, S. Krause, A. Sonntag, and R. Wiesendanger, European Conference on Surface Science (ECOSS-29), Edinburgh (U.K.): *Spin-transfer torque and Joule heating generated by spin-polarized field-emitted electrons*

10.9.2012: R. Decker, J. Brede, N. Atodiresei, V. Caciuc, S. Blügel, and R. Wiesendanger, 6th International Conference on SPS and 4th International Workshop on

SP-STM, Timmendorfer Strand (Germany): *Atomic-scale view of an intercalated ferromagnet-graphene heterostructure*

10.9.2012: M. Bazarnik, A. Wykrota, L. Jurczyszyn, M.W. Radny, K. Morgenstern, R. Czajka, 6^{th} International Conference on SPS and 4th International Workshop on SP-STM, Timmendorfer Strand (Germany): *Molecular functional units on Si(100)*

10.9.2012: J. Brede, R. Decker, J. Schwöbel, A. Dilullo, G. Hoffmann, S. Klyatskaya, M. Ruben, and R. Wiesendanger, 6^{th} International Conference on SPS and 4th International Workshop on SP-STM, Timmendorfer Strand (Germany): *Spin resolved measurements of single molecular magnets on surfaces*

11.9.2012: A. Schlenhoff, S. Krause, A. Sonntag, and R. Wiesendanger, 6^{th} International Conference on SPS and 4th International Workshop on SP-STM, Timmendorfer Strand (Germany): *Spin-transfer torque and Joule heating generated by spin-polarized field-emitted electrons*

11.9.2012: M. Menzel, Y. Mokrousov, R. Wieser, J. Bickel, E. Vedmedenko, S. Blügel, S. Heinze, K. von Bergmann, A. Kubetzka, and R. Wiesendanger, 6^{th} International Conference on SPS and 4th International Workshop on SP-STM, Timmendorfer Strand (Germany): *Non-collinear magnetic ground state in finite metallic chains*

11.9.2012: K. von Bergmann, M. Menzel, D. Serrate, Y. Yoshida, A. Kubetzka, R. Wiesendanger, and S. Heinze, 6^{th} International Conference on SPS and 4th International Workshop on SP-STM, Timmendorfer Strand (Germany): *Tunneling Anisotropic Magnetoresistance on the Atomic Scale*

11.9.2012: L. Dzemiantsova, A. Kubetzka, K. von Bergmann, and R. Wiesendanger, 6^{th} International Conference on SPS and 4th International Workshop on SP-STM, Timmendorfer Strand (Germany): *SP-STM study of individual Co atoms on Pd/Co/Ir(111)*

12.9.2012: L. Zhou, P. Löptien, A. A. Khajetoorians, J. Wiebe, M. Bianchi, R. Hatch, Z. S. Li, Ph. Hofmann, F. Song, J. Mi, B. B. Iversen, M. Z. Abd El-Fattah, J. W. Wells, and R. Wiesendanger, 6^{th} International Conference on SPS and 4th International Workshop on SP-STM, Timmendorfer Strand (Germany): *Coulomb-repulsion driven surface doping of Bi2Se3 with Rb*

12.9.2012: T. Schlenk, J. Honolka, A. A. Khajetoorians, V. Sessi, T. O. Wehling, S. Stepanow, J.-L. Mi, B. B. Iversen, J. Wiebe, N. Brookes, A. I. Lichtenstein, Ph. Hofmann, K. Kern, and R. Wiesendanger,, 6^{th} International Conference on SPS and 4th International Workshop on SP-STM, Timmendorfer Strand (Germany): *In-Plane Magnetic Anisotropy of Fe Atoms on* Bi_2Se_3*(111)*

12.9.2012: T. Eelbo, M. Waśniowska, M. Sikora, G. Bihlmayer, M. Gyamfi, M. Dobrzanski, A. Kozlowski, Z. Kakol, I. Miotkowski, R. Wiesendanger, 6^{th} International Conference on SPS and 4th International Workshop on SP-STM, Timmendorfer Strand (Germany): *Co atoms on* Bi_2Se_3*: electronic and magnetic properties*

9.10.2012: J. Brede, R. Decker, J. Schwöbel, A. Dilullo, G. Hoffmann, S. Klyatskaya, M. Ruben, and R. Wiesendanger, The 13^{th} International Conference on Molecule-based Magnets, Orlando, Florida (USA): *Spin Resolved Measurements of Single Molecular Magnets on Surfaces*

1.11.2012: R. Wiesendanger, 59^{th} AVS Symposium, Tampa (USA): *Spin Friction Observed on the Atomic Scale*

16.11.2012: R. Wiesendanger, University of Bonn, Colloquium, Bonn (Germany): *Atomically Tailored Nanomagnets and their Use for Atomic-Level Spintronics*

24.11.2012: A.A. Khajetoorians, Department of Physics Seminar, Göttingen (Germany): *Interactions between atomic moments and bath electrons: experimental insight at the atomic level*

13.12.2012: R. Wiesendanger, UCL Graduate School and DAAD Masterclass Colloquium, London (U. K.): *Nanotechnology: Past, Present, and Future*

8.1.2013: B. Ehlers, Ringvorlesung "Physik im Alltag", Hamburg (Germany): *Nanotechnologie in Forschung und Alltag*

4.3.2013: R. Wieser, Computational Engineering and Design (CED) Group seminar, Southampton (Great Britain): *Magnetization dynamics in classical and quantum Heisenberg spin systems*

11.3.2013: K. Hashimoto, T. Champel, S. Florens, C. Sohrmann, J. Wiebe, Y. Hirayama, R.A. Römer, R. Wiesendanger, and M. Morgenstern 77^{th} Spring Conference, Deutsche Physikalische Gesellschaft, Regensburg (Germany): *Robust Nodal Structure of Landau Level Wave Functions Revealed by Fourier Transform Scanning Tunneling Spectroscopy*

12.3.2013: J. Wiebe, T. Schlenk, A. A. Khajetoorians, and R. Wiesendanger, 77^{th} Spring Conference, Deutsche Physikalische Gesellschaft, Regensburg (Germany): *Magnetism of Fe on Pt(111) Revisited by Inelastic Scanning Tunneling Spectroscopy*

12.3.2013: A. Schwarz, R. Schmidt, E. Y. Vedmedenko, and R. Wiesendanger, 77^{th} Spring Conference, Deutsche Physikalische Gesellschaft, Regensburg (Germany): *Detecting and Interpreting Spin-Dependent Dissipation Observed with Magnetic Exchange Force Microscopy and Spectroscopy*

13.3.2013: P. Löptien, L. Zhou, J. Wiebe, A. A. Khajetoorians, and R. Wiesendanger, 77th Spring Conference, Deutsche Physikalische Gesellschaft, Regensburg (Germany): *Charge screening at the surface of a topological insulator: Rb on* Bi_2Se_3

13.3.2013: R. Decker, J. Brede, N. Atodiresei, V. Caciuc, S. Blügel, and R. Wiesendanger, 77th Spring Conference, Deutsche Physikalische Gesellschaft, Regensburg (Germany): *Magnetism of graphene on Ir(111) intercalation systems*

13.3.2013: A. Eich, T. Schlenk, M. Bianchi, M. Koleini, O. Pietzsch, T.O. Wehling, T. Frauenheim, A. Balatsky, J.-L. Mi, B.B. Iversen, J. Wiebe, A.A. Khajetoorians, Ph. Hofmann and R. Wiesendanger , 77th Spring Conference, Deutsche Physikalische Gesellschaft, Regensburg (Germany): *Controllable magnetic doping of the surface state of a topological insulator*

14.3.2013: L. Dzemiantsova, M. Hortamani, C. Hanneken, A. Kubetzka, K. von Bergmann, and R. Wiesendanger, 77th Spring Conference, Deutsche Physikalische Gesellschaft, Regensburg (Germany): *Magnetic coupling of single Co adatoms through Pd spacer layers*

14.3.2013: J. Grenz, A. Schwarz, D. Gao, M. Watkins, A. Shluger, and R. Wiesendanger, 77th Spring Conference, Deutsche Physikalische Gesellschaft, Regensburg (Germany): *Co-Salen on NaCl(001) and NiO(001): Substrate influence on adsorption geometry and growth*

14.3.2013: J. Brede, M. Bazarnik, R. Decker, J. Schwöbel, and R. Wiesendanger, 77th Spring Conference, Deutsche Physikalische Gesellschaft, Regensburg (Germany): *Spin-resolved measurements of single molecular magnets on graphene*

22.3.2013: R. Wiesendanger, Distinguished iNANO Lecture, Åarhus (Denmark): *Exploring Magnetism in the Nanoworld*

24.4.2013: A.A. Khajetoorians, TU Delft Seminar, Delft (Netherlands): *Magnetization dynamics derived from excitations of single magnetic atoms on surfaces*

2.5.2013: A.A. Khajetoorians, IPCMS Strasbourg visit, Strasbourg (France): *Magnetization dynamics derived from excitations of single magnetic atoms on surfaces*

14.6.2013: K. von Bergmann, Seminar of Prof. A. Rosch, University of Köln, Germany, Köln (Germany): *Spin spirals and magnetic skyrmions studied with spin-polarized STM*

14.6.2013: A. Schlenhoff, Seminar of Prof. M. Weinelt, Free University of Berlin, Berlin (Germany): *Nanomagnets interacting with spin-polarized electrons from Stark-shifted image-potential states*

19.6.2013: A.A. Khajetoorians, MPI Stuttgart Visit, Stuttgart (Germanz): *Spin LEGOs - dynamic characterization of bottom-up fabricated atomic magnets*

8.8.2013: Alexander Schwarz, Arne Köhler, Josef Grenz, Roland Wiesendanger, NCAFM 2013, Maryland University (USA): *Contrast Formation on Adsorbed CO Molecules Imaged with Metallic Tips*

9.9.2013: L. Zhou, International Conference on Nanoscience and Technology, Paris (France): *Charge screening at the surface of a topological insulator: Rb adatoms on* $Bi_2Se_3(111)$

9.9.2013: M. Bazarnik, J. Brede, R. Decker, J. Schwöbel, and R. Wiesendanger, XLII Meeting of Polish Physicists, Poznan (Poland): *Spin-resolved measurements of single molecular magnets on graphene*

11.9.2013: H. von Allwörden, K. Ruschmeier, A. Schwarz, and R. Wiesendanger, International Conference on Nanoscience and Technology, Paris (France): *A high resolution AFM operated at about 300 mK in up to 10 T under UHV-conditions*

11.9.2013: J. Wiebe, A. A. Khajetoorians, T. Schlenk, M. Steinbrecher, B. Schweflinghaus, M. dos Santos Dias, M. Bouhassoune, S. Lounis, and R. Wiesendanger, International Conference on Nanoscience and Technology ICN+T, Paris (France): *Magnetism of Fe on Pt(111) Revisited by Inelastic Scanning Tunneling Spectroscopy*

11.9.2013: Y. Yoshida, B. Wolter, A. Kubetzka, S.-W. Hla, K. von Bergmann, and R. Wiesendanger, International Conference on Nanoscience and Technology ICN+T, Paris (France): *Spin-depend friction observed on the atomic scale by using atomic manipulation and spin-polarized scanning tunneling microscopy*

12.9.2013: N. Romming, C. Hanneken, M. Menzel, J.E. Bickel, B. Wolter, K. von Bergmann, A. Kubetzka, and R. Wiesendanger, International Conference on Nanoscience and Technology, Paris (France): *Tuning non-collinear magnetic states with non-magnetic adlayers*

13.9.2013: A. Schlenhoff, S. Krause, and R. Wiesendanger, International Conference on Nanoscience and Technology, Paris (France): *Microscopic origin of Joule heating studied by SP-STM*

8.11.2013: S. Krause, A. Sonntag, A. Schlenhoff, J. Hermenau, J. Friedlein and R. Wiesendanger, 58th Annual Conference On Magnetism And Magnetic Materials, Denver CO (USA): *Electric-field induced manipulation of the magnetic anisotropy using SP-STM*

8.11.2013: A. Schlenhoff, S. Krause, A. Sonntag, and R. Wiesendanger, 58th Annual Conference On Magnetism And Magnetic Materials, Denver CO (USA): *Individual atomic-scale magnets interacting with spin-polarized field-emitted electrons*

12.11.2013: N. Romming, C. Hanneken, M. Menzel, J.E. Bickel, B. Wolter, K. von Bergmann, A. Kubetzka, and R. Wiesendanger, 544. WE-Heraeus-Seminar: Interactions with the Nanoworld, Bad Honnef (Germany): *Writing and deleting single magnetic skyrmions*

18.11.2013: R. Wiesendanger, MPI für Physik komplexer Systeme (Colloquium), Dresden (Germany): *Complex Spin States in Nanostructures*

3.12.2013: J. Wiebe, Seminar des GrK 1621, Dresden (Germany): *Spin-resolved and inelastic scanning tunneling spectroscopy of nanostructures built atom by atom*

5.12.2013: R. Wiesendanger, University of Hannover, Germany (GDCh-Weihnachts-Kolloquium), Hannover (Germany): *Spin-resolved studies of individual molecules on surfaces: Towards single-molecule spintronics*

6.12.2013: A. Schlenhoff, Seminar of Prof. M. Donath and Dr. D. Wegner, University of Münster, Münster (Germany): *Imaging and switching individual nanomagnets with spin-polarized scanning field emission microscopy*

7.2.2 Posters

15.3.2011: P. Löptien, F. Meier, L. Zhou, J. Wiebe, and R. Wiesendanger, 75th Spring Conference, Deutsche Physikalische Gesellschaft, Dresden (Germany): *A sub-Kelvin facility for cross-sectional scanning tunneling spectroscopy of metal-semiconductor heterostructures*

15.3.2011: S.-H. Chang, A. Scarfato, C. Kleeberg, M. Bröring, G. Hoffmann, and R. Wiesendanger, 75th Spring Conference, Deutsche Physikalische Gesellschaft, Dresden (Germany): *Scanning tunneling microscopy study of asymmetric Pd pincer complexes on a Cu(111) Surface*

15.3.2011: T. Eelbo, M. Gyamfi, M. Waśniowska, and R. Wiesendanger, 75th Spring Conference, Deutsche Physikalische Gesellschaft, Dresden (Germany): *Growth mode and evolution of electronic properties for* $Bi_{1-x}Sb_x alloys on W(110)$

15.3.2011: A. Köhler, R. Schmidt, A. Schwarz, and R. Wiesendanger, 75th Spring Conference, Deutsche Physikalische Gesellschaft, Dresden (Germany): *Structural Phases and Magnetism of the Co Monolayer on W(001)*

16.3.2011: M. Gyamfi, T. Eelbo, M. Waśniowska, and R. Wiesendanger, 75th Spring Conference, Deutsche Physikalische Gesellschaft, Dresden (Germany): *Inhomogeneous electronic properties of monolayer graphene on Ru(0001)*

16.3.2011: J. Grenz, A. Schwarz, J. Hattendorff, and R. Wiesendanger, 75th Spring Conference, Deutsche Physikalische Gesellschaft, Dresden (Germany): *Growth of Co-Salen on NiO(001) at submonolayer coverages: A non-contact atomic force microscopy study*

18.3.2011: A. Engel, A. Schlenhoff, A. Sonntag, S. Krause, and R. Wiesendanger, 75th Spring Conference, Deutsche Physikalische Gesellschaft, Dresden (Germany): *Preparation of bulk Chromium tips for SP-STM*

18.3.2011: A. Sonntag, A. Schlenhoff, G. Herzog, S. Krause, B. Ehlers, and R. Wiesendanger, 75th Spring Conference, Deutsche Physikalische Gesellschaft, Dresden (Germany): *Thermal magnetization reversal of small Fe-nanoislands on W(110)*

26.4.2011: M. Gyamfi, T. Eelbo, M. Waśniowska, T. Wehling, A. Lichtenstein, S. Forti, U. Starke, and R. Wiesendanger, Graphene Week 2011, Obergurgl (Austria): *Ni atoms on graphene: electronic properties and phonon excitations*

23.8.2011: T. Stapelfeldt, R. Wieser, E.Y. Vedmedenko, and R. Wiesendanger, European School on Magnetism, Targoviste (Romania): *Domain Wall Manipulation With A Magnetic Tip*

23.8.2011: T. Stapelfeldt, R. Wieser, E.Y. Vedmedenko, and R. Wiesendanger, European School on Magnetism, Targoviste (Romania): *Domain Wall Manipulation With A Magnetic Tip*

19.9.2011: A. Köhler, R. Schmidt, A. Schwarz, and R. Wiesendanger, 14th International Conference on Noncontact Atomic Force Microscopy (NCAFM 2011), Lindau (Germany): *Structural Phases of the first Co layers on W(001)*

19.9.2011: J. Grenz, K. Ruschmeier, A. Schwarz, R. Wiesendanger, 14th International Conference on Noncontact Atomic Force Microscopy (NCAFM 2011), Lindau (Germany): *Molecular dynamics of Co-Salen on NiO(001) at submonolayer coverages*

20.9.2011: H. von Allwörden, K. Ruschmeier, A. Schwarz, and R. Wiesendanger, 14th International Conference on Noncontact Atomic Force Microscopy (NCAFM 2011), Lindau (Germany): *Design and construction of a 300 mK, 10 Tesla, UHV facility for AFM*

29.11.2011: A. Eich, S. V. Eremeev, G. Landolt, T. V. Menshchikova, B. Slomski, Yu. M. Koroteev, Z. S. Aliev, M. B. Babanly, J. Henk, A. Ernst, L. Patthey, A. A. Khajetoorians, J. Hagemeister, O. Pietzsch, J. Wiebe, R. Wiesendanger, P. M. Echenique, S. S. Tsirkin, I. R. Amiraslanov, J. H. Dil and E. V. Chulkov, 493. WE-Heraeus-Seminar: Latest developments in Scanning Probe Techniques focused on Nanotechnology, Bad Honnef (Germany): *STM studies on the ternary topological insulator* $PbBi_4Te_7$

27.3.2012: Lihui Zhou, Peter Löptien, Focko Meier, Jens Wiebe, and Roland Wiesendanger, 76th Spring Conference, Deutsche Physikalische Gesellschaft, Berlin (Germany): *A low-temperature facility for spin-polarized scanning tunneling microscopy*

27.3.2012: C. Hanneken, A. Kubetzka, K. von Bergmann, and R. Wiesendanger, 76th Spring Conference, Deutsche Physikalische Gesellschaft, Berlin (Germany): *Chromium Bulk Tips for Spin-Polarized Scanning Tunneling Microscopy*

27.3.2012: J. Friedlein, A. Sonntag, B. Ehlers, S. Krause, and R. Wiesendanger, 76th Spring Conference, Deutsche Physikalische Gesellschaft, Berlin (Germany): *An oxygen annealing chamber for the preparation of clean hard metal substrates*

27.3.2012: A. Eich, A.A. Khajetoorians, J. Hagemeister, O. Pietzsch, J. Wiebe and R. Wiesendanger, 76th Spring Conference, Deutsche Physikalische Gesellschaft, Berlin (Germany): *STM studies on the ternary topological insulator* $PbBi_4Te_7$

30.3.2012: B. Ehlers, G. Herzog, J. Friedlein, S. Krause, and R. Wiesendanger, 76th Spring Conference, Deutsche Physikalische Gesellschaft, Berlin (Germany): *Switching the magnetization of nanomagnets using SP-STM*

30.3.2012: M. Menzel, K. von Bergmann, S. Heinze, Y. Mokrousov, G. Bihlmayer, J. Bickel, J. Brede, R. Wieser, E. Vedmedenko, S. Blügel, A. Kubetzka, and R. Wiesendanger, 76th Spring Conference, Deutsche Physikalische Gesellschaft, Berlin (Germany): *Complex magnetic ground states observed in Fe nanostructures on different Ir surfaces*

30.3.2012: T. Stapelfeldt, R. Wieser, E. Y. Vedmedenko, and R. Wiesendanger, 76th Spring Conference, Deutsche Physikalische Gesellschaft, Berlin (Germany): *Domain Wall Manipulation With a Magnetic Tip*

30.3.2012: K. Them, T. Stapelfeldt, E. Y. Vedmedenko, and R. Wiesendanger, 76th Spring Conference, Deutsche Physikalische Gesellschaft, Berlin (Germany): *Quantum-Mechanical Model of Spin Polarized STM*

19.5.2012: M. Bazarnik, L. Jurczyszyn, M.W. Radny, R. Czajka, K. Morgenstern, Electron Controlled Chemical Lithography Meeting 2012, Stykkishólmur (Iceland): *Molecular photo-switch on Si(100)*

7.6.2012: R. Decker, J. Brede, N. Atodiresei, V. Caciuc, S. Blügel, and R. Wiesendanger, Graphene week, Delft (Netherlands): *Structure and magnetism of cobalt intercalated graphene on Ir(111)*

3.7.2012: K. Ruschmeier, A. Schwarz, and R. Wiesendanger, 15th International Conference on Noncontact Atomic Force Microscopy (NCAFM 2012), Ceský Krumlov (Czech Republic): *Evaluation of thermal noise spectra recorded below 1 K with an interferometric detection*

12.7.2012: A. Sonntag, A. Schlenhoff, S. Krause, G. Herzog, and R. Wiesendanger, International Conference on Magnetism (ICM), Busan (Republic of Korea): *Bulk Cr tips with full spatial magnetic sensitivity for spin-polarized scanning tunneling microscopy*

12.7.2012: S. A. Nepijko, D. Kutnyakhov, I. E. Protsenko, H. J. Elmers, R. Wiesendanger, and G. Schoenhense, International Conference on Magnetism (ICM), Busan (Republic of Korea): *Preparation of chains of single-domain Ni nanoparticles with collinear direction of magnetization*

24.7.2012: T. Eelbo, M. Gyamfi, M. Waśniowska, and R. Wiesendanger, International Conference on Nanoscience and Technology, Paris (France): *Graphene on Pt(111) intercalated by Cobalt studied with STM and STS*

16.8.2012: J. Wiebe, J. Honolka, A. A. Khajetoorians, V. Sessi, T. O. Wehling, S. Stepanow, J.-L. Mi, B. B. Iversen, T. Schlenk, A. Eich, O. Pietzsch, N. Brookes, A. I. Lichtenstein, Ph. Hofmann, M. Bianchi, K. Kern, and R. Wiesendanger, International CECAM Workshop "Topological Materials", Bremen (Germany): *In-plane magnetic anisotropy of Fe atoms on* Bi_2Se_3*(111)*

10.9.2012: B. Ehlers, G. Herzog, J. Friedlein, S. Krause, and R. Wiesendanger, 6th International Conference on SPS and 4th International Workshop on SP-STM, Timmendorfer Strand (Germany): *Switching the magnetization of nanomagnets using SP-STM*

10.9.2012: C. Hanneken, A. Kubetzka, K. von Bergmann, S.-W. Hla, and R. Wiesendanger, 6th International Conference on SPS and 4th International Workshop on SP-STM, Timmendorfer Strand (Germany): *Chromium Bulk Tips for Spin-Polarized Scanning Tunneling Microscopy*

10.9.2012: A. Kubetzka, K. von Bergmann, M. Menzel, J. Brede, R. Wiesendanger, G. Bihlmayer, S. Blügel, and S. Heinze, 6th International Conference on SPS and 4th International Workshop on SP-STM, Timmendorfer Strand (Germany): *Magnetism of fcc and hcp Fe atomic layers on Ir(111)*

10.9.2012: A. Schwarz, R. Schmidt, and R. Wiesendanger, 6th International Conference on SPS and 4th International Workshop on SP-STM, Timmendorfer Strand (Germany): *Magnetic Exchange Force Spectroscopy with Atomic Resolution*

10.9.2012: P. Löptien, L. Zhou, A. A. Khajetoorians, J. Wiebe, and R. Wiesendanger, 6th International Conference on SPS and 4th International Workshop on SP-STM, Timmendorfer Strand (Germany): *Superconductivity in thin lanthanum films*

10.9.2012: S. Krause, A. Sonntag, G. Herzog, A. Schlenhoff, and R. Wiesendanger, 6th International Conference on SPS and 4th International Workshop on SP-STM, Timmendorfer Strand (Germany): *Spin-transfer torque switching efficiency in SP-STM experiments*

10.9.2012: A. Eich, J. Honolka, A. A. Khajetoorians, V. Sessi, M. Koleini, T. O. Wehling, S. Stepanow, J.-L. Mi, B. B. Iversen, A. Balatsky, T. Schlenk, J. wiebe, O. Pietzsch, N. Brookes, A. I. Lichtenstein, Ph. Hofman, M. Bianci, K. Kern and R. Wiesendanger, 6th International Conference on SPS and 4th International Workshop on SP-STM, Timmendorfer Strand (Germany): *Properties of magnetically doped topological insulator* Fe/Bi_2Se_3

10.9.2012: J. Friedlein, A. Sonntag, B. Ehlers, S. Krause, and R. Wiesendanger, 6th International Conference on SPS and 4th International Workshop on SP-STM, Timmendorfer Strand (Germany): *An oxygen annealing chamber for the preparation of clean hard metal substrates*

10.9.2012: A. Sonntag, A. Schlenhoff, S. Krause, G. Herzog, and R. Wiesendanger, 6th International Conference on SPS and 4th International Workshop on SP-STM, Timmendorfer Strand (Germany): *Bulk Cr tips with full spatial magnetic sensitivity for spin-polarized scanning tunneling microscopy*

10.9.2012: M. Gyamfi, T. Eelbo, M. Waśniowska, and R. Wiesendanger, 6th International Conference on SPS and 4th International Workshop on SP-STM, Timmendorfer Strand (Germany): *Bistability of Adatoms on Graphene*

10.9.2012: N. Romming, Y. Yoshida, S. Schröder, P. Ferriani, D. Serrate, A. Kubetzka, K. von Bergmann, S. Heinze, and R. Wiesendanger, 6th International Conference on SPS and 4th International Workshop on SP-STM, Timmendorfer Strand (Germany): *Conical Spin-Spiral State in an Ultrathin Film*

10.9.2012: T. Stapelfeldt, R. Wieser, E.Y. Vedmedenko, and R. Wiesendanger, 6th International Conference on SPS and 4th International Workshop on SP-STM, Timmendorfer Strand (Germany): *Domain Wall Manipulation With A Magnetic Tip*

4.3.2013: M. Bazarnik, R. Decker, J. Brede, and R. Wiesendanger, International Winterschool on Electronic Properties of Novel Materials 2013, Kirchberg (Austria): *Fe and Co intercalation of epitaxial graphene on Ir(111)*

9.3.2013: G. Fläschner, K. Ruschmeier, R. Bakhtiari, A. Schwarz, R. Wiesendanger, and M. Thorwart, 77th Spring Conference, Deutsche Physikalische Gesellschaft, Regensburg (Germany): *Nonlinear response of an optomechanical system studied via the noise power spectrum*

11.3.2013: L. Zhou, P. Löptien, A. Khajetoorians, J. Wiebe, and R. Wiesendanger, 77th Spring Conference, Deutsche Physikalische Gesellschaft, Regensburg (Germany): *Superconductivity in Thin La Films*

12.3.2013: J. Friedlein, A. Schlenhoff, A. Sonntag, S. Krause, and R. Wiesendanger, 77th Spring Conference, Deutsche Physikalische Gesellschaft, Regensburg (Germany): *Nanomagnets affected by spin-polarized tunneling and field-emission*

13.3.2013: A. Köhler, A. Schwarz, and R. Wiesendanger, 77th Spring Conference, Deutsche Physikalische Gesellschaft, Regensburg (Germany): *Investigation of single Co atoms on Mn/W(001)*

15.3.2013: D. Altwein, E. Vedmedenko, R. Wieser, and R. Wiesendanger, 77th Spring Conference, Deutsche Physikalische Gesellschaft, Regensburg (Germany): *Collective Switching of Nanoparticles in Magnetic Arrays*

15.3.2013: N. Romming, Y. Yoshida, S. Schröder, P. Ferriani, D. Serrate, A. Kubetzka, K. von Bergmann, S. Heinze, and R. Wiesendanger, 77th Spring Conference, Deutsche Physikalische Gesellschaft, Regensburg (Germany): *Conical Spin-Spiral State in an Ultrathin Film*

18.3.2013: A. Bick, C. Staarmann, P. Christoph, P. Rothfos, P. Windpassinger, C. Becker, K. Sengstock, H. Zhong, G. Fläschner, A. Schwarz, and R. Wiesendanger , 77th Spring Conference, Deutsche Physikalische Gesellschaft, Regensburg (Germany): *Towards coupling a BEC to a micromechanical oscillator*

30.5.2013: A. B. Butenko, A. N. Bogdanov, and U. K. Rössler, Workshop "Dzyaloshinskii-Moriya Interaction and Exotic Spin Structures", Veliky Novgorod (Russian Federation): *Surface- and defect-induced Dzyaloshinskii-Moriya interactions: influence on vortex states in magnetic nanodots*

7.8.2013: J. Grenz, A. Schwarz, and R. Wiesendanger, 16th International Conerence on Non-Contact Atomic Force Microscopy (NCAFM '13), University of Maryland College Park, Maryland (USA), University of Maryland College Park, Maryland (USA): *Co adatoms on NiO(001)*

8.10.2013: A. Köhler, A. Schwarz and R. Wiesendanger, 1st German-French Summer School on noncontact atomic force microscopy, Porquerolles (France): *CO adsorbed on Mn/W(001)*

8.10.2013: K. Ruschmeier, H. von Allwörden, A. Schwarz, and R. Wiesendanger, 1st German-French Summer School on noncontact atomic force microscopy, Porquerolles (France): *A high resolution UHV - 300mK - 10T - Atomic Force Microscope*

8.10.2013: J. Wiebe, P. Löptien, L. Zhou, A. A. Khajetoorians, J.-L. Mi, B. B. Iversen, Ph. Hofmann, and R. Wiesendanger, Kickoff meeting of DFG-SPP 1666, Frankfurt (Germany): *Screening and Atomic-Scale Engineering of the Potential at a Topological Insulator Surface*

12.11.2013: J. Friedlein, A. Sonntag, J. Harm, S. Krause, and R. Wiesendanger, 544. WE-Heraeus-Seminar: Interactions with the Nanoworld, Bad Honnef (Germany): *Toward a multiprobe- high frequency- spin-polarized scanning tunneling microscope*

12.11.2013: A. Schwarz, A. Köhler, J. Grenz, and R. Wiesendanger , 544. WE-Heraeus-Seminar: Interactions with the Nanoworld: Local Probes with High Time, Energy and Force Resolution, Bad Honnef (Germany): *Carbon Monoxide: Contrast Formation in Non-Contact Atomic Force Microscopy Imaging*

Chapter 8

Lectures and Courses at the University of Hamburg

- Nanostrukturphysik I und II
- Magnetismus und Oberflächenphysik
- Einführung in die Rastersondenmikroskopie und -spektroskopie
- Ringvorlesung Physik im Alltag
- Seminar über Nahfeldgrenzflächenphysik und Nanotechnologie
- Seminar über aktuelle Probleme der Rastersensorphysik
- Proseminar über Visionen der Festkörperforschung
- Proseminar über Theorie und Praxis der Rastersensormethoden
- Proseminar über Magnetismus und Oberflächenphysik
- Übungen zur Nanostrukturphysik I und II
- Übungen zu Magnetismus und Oberflächenphysik
- Übungen zur Einführung in die Rastersondenmikroskopie und -spektroskopie
- Physikalisches Praktikum für Fortgeschrittene
- TU - Praktikum
- Studienarbeiten zur Rastersondenmikroskopie
- Bachelorarbeiten zur Grenzflächen- und Tieftemperaturphysik
- Schwerpunktpraktikum Grenzflächen- und Tieftemperaturphysik
- Diplompraktikum bzw. Masterarbeiten zur Grenzflächen- und Tieftemperaturphysik

Chapter 9

Contributions to International Organizations

- Organizer of the International Workshop on "Ultrafast Dynamics on the Atomic Scale" (Hamburg 2011)
- Co-Organizer of the SPIRE-Workshop "The Spin Triangle" (Hamburg 2011)
- Member of the International Program Advisory Board of the "6th International Symposium on Surface Science ISSS-6" (Tokyo, Japan 2011)
- Co-Organizer of the International Workshop on "Spin Dynamics and Kondo Effects in STM" (Hamburg 2011)
- Member of the International Scientific Committee of the "International Conference on Nanostructures and Self-Assembly NANOSEA 2012" (Sardinia, Italy 2012)
- Member of the International Steering Committee of the "International Conference on Nanoscience and Technology ICN+T 2012" (Paris, France 2012)
- Co-Chairman of the "6th International Conference on Scanning Probe Spectroscopy SPS'12" (Timmendorfer Strand, Germany 2012)
- Chairman of the "4th International Workshop on Spin-Polarized Scanning Tunneling Microscopy SPSTM-4" (Timmendorfer Strand, Germany 2012)
- Member of the International Advisory Committee of the "International Symposium on Macro- and Supramolecular Architectures and Materials MAM-12" (Coimbatore, India 2012)
- Member of the International Advisory Committee of the "International Conference on Advances in Metrology AdMet-2013" (New Delhi, India 2013)
- Member of the International Committee of the "Latin American Workshop on Magnetism, Magnetic Materials, and their Applications LAW3M" (Buenos Aires, Argentina 2013)

- Organizer of the Otto-Stern-Symposium 2013 (Hamburg 2013)
- Member of the International Advisory Committee of the "1st Hayashi Conference on Next Decades of Surface Science" (Tokyo, Japan 2013)
- Member of the International Steering Committee of the "19th International Vacuum Congress IVC-19" (Paris, France 2013)
- Chair of the Nanoscience and Technology Committee of the "19th International Vacuum Congress IVC-19" (Paris, France 2013)

Chapter 10

How to reach us

... by mail	write to University of Hamburg, Institute of Applied Physics, Jungiusstraße 11, D-20355 Hamburg, Germany.
... by phone	call (++49) 40 42838 5244.
... by fax	send to (++49) 40 42838 6188.
... by e-mail	send to `wiesendanger@physnet.uni-hamburg.de`
... within the WWW	`www.nanoscience.de`
... personally	


11